NOTICE

AVIS

The quality of this microform is heavily dependent upon the quality of the original thesis submitted for microfilming. Every effort has been made to ensure the highest quality of reproduction possible.

La qualité de cette microforme dépend grandement de la qualité de la thèse soumise au microfilmage. Nous avons tout fait pour assurer une qualité supérieure de reproduction.

If pages are missing, contact the university which granted the degree.

S'il manque des pages, veuillez communiquer avec l'université qui a conféré le grade.

Some pages may have indistinct print especially if the original pages were typed with a poor typewriter ribbon or if the university sent us an inferior photocopy.

La qualité d'impression de certaines pages peut laisser à désirer, surtout si les pages originales ont été dactylographiées à l'aide d'un ruban usé ou si l'université nous a fait parvenir une photocopie de qualité inférieure.

Canadä

UNIVERSITY OF ALBERTA

Lateral Energy Transport In Laser-Produced Plasmas

By

Douglas Wade Vick

A thesis submitted to the Faculty of Graduate Studies and Research in partial fulfillment of the requirements for the degree of Doctor of Philosophy.

Department of Electrical Engineering

Edmonton, Alberta

Fall 1993

The author has granted an irrevocable non-exclusive licence allowing the National Library of Canada to reproduce, loan, distribute or sell copies of his/her thesis by any means and in any form or format, making this thesis available to interested persons.

The author retains ownership of the copyright in his/her thesis. Neither the thesis nor substantial extracts from it may be printed or otherwise reproduced without his/her permission.

L'auteur a accordé une licence irrévocable et non exclusive permettant à la Bibliothèque nationale du Canada de reproduire, prêter, distribuer ou vendre des copies de sa thèse de quelque manière et sous quelque forme que ce soit pour mettre des exemplaires de cette thèse à la disposition des personnes intéressées.

L'auteur conserve la propriété du droit d'auteur qui protège sa thèse. Ni la thèse ni des extraits substantiels de celle-ci ne doivent être imprimés ou autrement reproduits sans son autorisation.

Canada

Institute of Laser Engineering

Osaka University
2-6 Yamada-oka
Suita Osaka, 565, Japan

June 5, 1993

To whom it may concern:

We permit Mr. Doug Vick at the University of Alberta to use the figure, showing the configuration of the GEKKO IV glass laser system. The figure includes the layout of the oscillator amplifiers and experimental vacuum chamber.

Sincerely,

Kazuo A. Tanaka

Associate Professor

UNIVERSITY OF ALBERTA
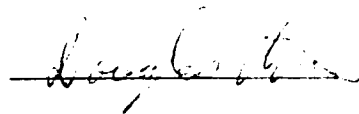
RELEASE FORM

NAME OF AUTHOR: Douglas Wade Vick

TITLE OF THESIS: Lateral Energy Transport In Laser-Produced Plasmas

DEGREE: Doctor of Philosophy

YEAR THIS DEGREE WAS GRANTED: 1993

Permission is hereby granted to the University of Alberta Library to reproduce single copies of this thesis and to lend or sell such copies for private, scholarly or scientific research purposes only.

The author reserves all other publication and other rights in association with the copyright in the thesis, and except as hereinbefore provided neither the thesis nor any substantial portion thereof may be printed of otherwise reproduced in any material form whatever without the author's prior written permission.

102-10531 85 Ave.
Edmonton, Alberta
T6E 2K5

Oct 8/1993

UNIVERSITY OF ALBERTA

FACULTY OF GRADUATE STUDIES AND RESEARCH
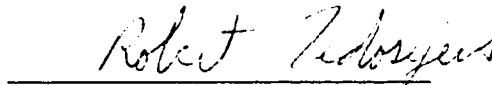
The undersigned certify that they have read, and recommended to the Faculty of Graduate Studies and Research for acceptance, a thesis entitled **Lateral Energy Transport In Laser-Produced Plasmas** submitted by Douglas Wade Vick in partial fulfillment of the requirements for the degree of Doctor of Philosophy.

Dr. A. A. Offenberger

Dr. C. E. Capjack

Dr. R. Fedosejevs

Dr. P. R. Smy

Dr. W. Rozmus

Dr. A. M. Robinson

Dr. B. Ahlborn

Oct 4, 1993

To my parents

Abstract

A study of lateral energy transport in planar targets irradiated by 0.53 μm laser light was conducted over an intensity range of 3×10^{12}-3×10^{14} W/cm^2 and for laser pulse widths varying from 170 to 860 picoseconds. Spatially- 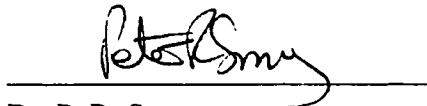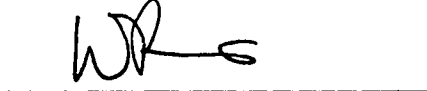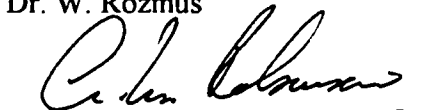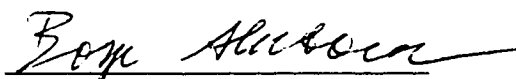and spectrally- resolving x-ray diagnostics were used to obtain the profiles of target emission in the energy bands from 60 - 250 eV and above 1 keV. The beam focus configurations adopted were of two basic types, consisting of (a) spatially modulated intensity spots (diameter ~300 μm) and (b) a tight focus spots (diameter ~100 μm). In both cases the aim was to assess the degree of lateral energy transport which occurs outside the nominal laser focus. To this end, special targets were constructed which consisted of plastic substrates with buried tracer layers, or tracer patterns deposited onto the substrate outside the laser focus. The x-ray signature emission recorded from the tracer material allowed the determination of plasma conditions existing in the lateral regions of the target. Observations indicated that only a small fraction of the incident laser energy was available for heating of the lateral substrate. Lateral x-ray signals were dominated by a hot expanding underdense plasma which coupled weakly to the lateral substrate. Under spatially-modulated irradiation conditions, this plasma formed a collisional structure between the laser hot spots at early stages in the interaction which persisted throughout the laser pulse.

A two dimensional particle-in-a-cell code was used to aid in interpreting the experiments. The code incorporated models for classical flux-limited electron thermal transport, average ion atomic physics, diffusion-approximated radiation transport, and transport inhibition by magnetic fields. The predicted electron temperatures, density scale lengths and x-ray emission profiles were in good agreement with experimental measurements done with both focal spot configurations.

Acknowledgement

This project could not have been undertaken without the support of many people. I would like to thank my supervisors Dr. Offenberger and Dr. Capjack for their advice and encouragement during and after my experiments, and my dissertation committee for a prompt and thorough reading of the thesis and for numerous useful suggestions. A special thanks is reserved for Dr. Fedosejevs who guided me during my first years as an experimentalist. On this side of the Atlantic, I have benefited from the excellent technical assistance of Blair Harwood, Alois Haromy, and Kevin Houston. Thanks to fellow grad students Ying Tsui, Jim Broughton, Rob Newton, Masayuki Fujita, Chihiro Yamanaka, and Yanmin Li for fond memories of many late working and symposium nights.

The complete list of individuals who aided me during my sojourn in Japan would be lengthy indeed. The full facilities of the Institute of Laser Engineering were kindly made available to me by Dr. Nakai and his co-workers. Dr. Tanaka supervised my stay in Japan and successfully sought out funding for the research. Again, special thanks is reserved for Dr. Kado for sharing his expertise concerning the operation of the GEKKO IV system and the various diagnostics, and especially for many hours of assistance during the experiments. I am also grateful to fellow students H. Yamamoto, M. Tsukamoto, H. Sugio, and T. Hagihara for their assistance and support. Thanks to Dr. Nishiguchi for discussions concerning the simulations, and to Dr. Takagi for his advice in the target fabrication lab. During his visits to ILE, Dr. M. C. Richardson provided me with a good deal of fatherly advice and encouragement.

Table of Contents

List of Tables

List of Figures

1. Introduction

Laser-produced plasmas have long been recognized as small, efficient sources of x-ray radiation. The x-ray spectra from such sources exhibit characteristic signatures which are sensitive indicators of the temperatures, densities, and fractional ion populations of the emitting sources. Therefore, such plasmas have engendered interest from a purely theoretical point of view, by providing a test of atomic physics models and allowing, for example, the creation of astrophysical-type conditions in the laboratory. As x-ray sources, however, plasmas have found practical applications as well, particularly in the field of diagnostics for controlled fusion research. As laser technology advances, x-ray lithography and microscopy may be expected to join the list of applications. In order to introduce the present work, a brief overview of some of the current research involving laser-produced plasmas (LPPs) follows.

The first two decades of research on LPPs was motivated largely by the inertial confinement fusion (ICF) program. Since its introduction into the de-classified literature (Nuckolls et al., 1972), this field has remained an important motivating drive for the development of diagnostics for quantifying x-ray emission sources or, alternatively, using these x-ray sources as a diagnostic tool for characterizing other physical variables in ICF experiments. A review of the recent status of ICF and outstanding issues remaining in the field is presented by Yamanaka (1991).

In the directly laser-driven scheme a spherical shell of low Z material enclosing a fuel of liquid or solid deuterium (DT) is symmetrically compressed to densities

1

sufficiently high to initiate a fusion reaction at the core of the pellet. The driving force of this compression is supplied by the blowoff plasma which is formed by the laser-induced heating and ablation of the outer shell or pusher. A simple rocket model of the hydrodynamic efficiency of the implosion (Yamanaka, op. cit.) may be used to argue that target shells of large aspect ratio $R_0/\Delta R_0$ (where R_0 and ΔR_0 are initial shell radius and thickness) are preferred since they place less stringent requirements on the ablation pressure. Mass ablation rates (and thus ablation pressure) have been found to increase with shorter wavelength. Other attractive features of short wavelength drivers include reduced hot electron production and higher intensity thresholds for the onset of parametric instabilities. For such reasons laser fusion drivers are envisioned to operate at 0.35 or 0.25 μm, assuming that several physics and engineering issues (some of which are mentioned below) are successfully resolved.

In order to ensure a return on the invested energy, a viable fusion reactor pellet must deliver an overall energy gain (here defined as the ratio of thermonuclear energy output to laser energy input) of 100 or more. Bodner (1981) showed that several conditions had to be met to achieve this situation:

(i) The energy coupling efficiency of the laser to the DT fuel must exceed 5%.

(ii) Preheat of the pellet core, i.e., energy deposited prior to the arrival of the ablatively driven shock, must be less than 10 eV. Suprathermal electrons and high energy x-rays produced in the outer plasma are potentially the chief offenders here.

(iii) The radius of the compressed core must be less than $\frac{1}{30}$ of the initial radius.

(iv) The density of the compressed fuel must be larger than 200 g/cm^3.

(v) The temperature of the ignition zone must reach 10 keV.

(vi) The radius of the compressed fuel must be larger than the mean free path of the alpha particles produced by the fusion reaction. This condition is necessary for α-particle heating and nuclear burn to propagate throughout the entire fuel volume.

Recent implosion experiments on targets with cryogenically cooled DT fuel cores have resulted in promising reports of fuel densities of 20 - 40 g/cm³ and 100 g/cm³ (McCrory et al., 1988; Nakai et al. 1990).

In order to achieve the six conditions listed above, the pellet compression must proceed very symmetrically. Driver uniformity remains one of the outstanding physics issues for the direct drive scheme. Numerical and analytic studies have established that the intensity variations on ICF targets should not exceed an rms value of 1 % in order to result in a sufficiently symmetric implosion. Small phase errors in the near field wavefront pattern of the driver beam result in high intensity hot spots on the target. Furthermore, some degree of non-uniformity in multibeam systems is unavoidable due to beam imbalance created by differences in the pumping efficiencies and optical properties of the amplifier chains (Bradley et al., 1989). Over the preceding decade a good deal of progress has been made to alleviate the forementioned problems via beam smoothing techniques such as induced spatial incoherence (ISI) and smoothing by spectral dispersion (SSD) (Knox, 1989). Some small and large scale irradiation non-uniformities may be expected to remain even when these techniques are applied. Furthermore, at the laser intensities and plasma scale lengths expected in fusion targets, beam filamentation instabilities (Epperlein 1990, 1991) may seriously degrade the uniformity of the driver. Recently, filamentation (Young et al., 1988) and self focusing of ISI-smoothed beams (Afshar-rad et al., 1992) have been observed in long-scale-length LPPs. The degree to which lateral thermal, hydrodynamic, or radiation transport could alleviate or aggravate these deleterious effects remains a topic of interest to the fusion community.

Throughout the 1980s, an increasing proportion of laser plasma research was motivated towards the goals of nano-fabrication and microscopy. Such research has, in part, been fueled by a technological revolution in x-ray optics, including multilayer

3

mirrors and zone plate lenses (Ceglio 1989, 1991), providing a number of new possibilities for manipulating x-rays, . As of 1990, the smallest lateral structures that could be manufactured by lithographic methods were about 1 µm in size, making possible microcomponent densities up to 10^7 per microchip. Through the 1990s, the push towards 1 Gigabyte random access memory chips will eventually require the dimensions of these structures to be reduced to 0.2 µm. Quantum effect devices (for example resonant tunneling and superlattice devices) will require even more stringent demands of 60 nm or less (Smith and Craighead, 1990). Soft x-ray sources are attractive candidates for the lithographic production of such structures since the inherent resolving limits imposed by diffraction are much smaller than those of visible optical systems. Synchrotrons or undulators provide reasonably efficient, narrow-bandwidth x-ray sources. However, these facilities are expensive and have potentially large down times. LPPs represent a viable alternative since they are smaller, relatively inexpensive, and potentially highly reliable. Lithographic systems relying on LPPs may be expected to be developed once a number of technical hurdles have been overcome (Silfvast et al., 1992).

In the field of biological and medical research, x-ray sources promise to improve upon the resolution currently available using optical microscopes. The high penetration depth of x-rays should allow the imaging of specimens several microns thick, which is not possible in electron microscopes. By using x-ray wavelengths which fall within the water window of 23 - 44 Å (defined by the absorption K edges of carbon and oxygen) it should be possible to produce high contrast images of biological structures *in vitro*, a capability not possible with electron microscopy. The two approaches in this field are contact x-ray microscopy (CXM) and scanning transmission x-ray microscopy (STXM). In CXM a biological specimen is placed in contact or close proximity to an x-ray resist (typically polymethylmetacrylate or

4

PMMA) and irradiated by an x-ray source. The resist is then developed and viewed by using another device such as an electron microscope. Impressive results have been achieved by CXM imaging using an undulator x-ray source - for example the imaging of human chromosome samples to ~10 nm resolution (Shinohara, 1989). In STXM, a zone plate is used to focus the x-ray radiation down to a tiny probe spot which is then scanned across the specimen. As with the case of lithography, LPPs present the same attractive features when considered as sources for microscopy, namely their small scale, affordability, and reliability which would allow them to be placed in smaller laboratories. A summary of the potential of LPPs for microscopy has been presented by Michette (1990).

A final area of active research in LPPs is the development of laboratory x-ray lasers (LXRLs). The motivation for this research is also geared partly toward biological applications. In addition LXRLs would represent an ideal diagnostic for holographic probing of high density plasmas, a tool which would be of particular value to the laser fusion community. Great progress has been made towards the LXRL since 1984 when the first reports amplification of x-ray lines in the vicinity of 200 $\overset{o}{A}$ were published (see Rosen, 1990, and references therein). More recently, gain has been measured at a wavelength of 45 $\overset{o}{A}$ near the important water window. Typical LXRL experiments have been conducted with thin exploding targets using high power facilities such as the NOVA laser (Keane et al., 1989). The development of tabletop, ultrashort pulse lasers is currently opening a new range of topics in laser-plasma phenomena; among these is including direct optical pumping of cold atoms to the upper levels of x-ray lasing transitions, which would allow the x-ray laser research to make the move into smaller laboratories. One of the central points stressed by Rosen (op. cit.) is that detailed knowledge of the plasma conditions are necessary in order to successfully complete the LXRL program. A list of mechanisms which may produce

deleterious effects in the lasing medium (all of which are mentioned in the Rosen paper) would include: laser beam filamentation due to ponderomotive and thermal self-focusing effects; heat flow and radiative cooling instabilities; local magnetic fields; Rayleigh-Taylor-, Kelvin-Helmholtz-, and Rayleigh-Bénard- type instabilities; and anomalous heating by stimulated Brilliouin scattering or ion acoustic turbulence. This list serves to illustrate the complexities in the full treatment of laser-plasma interaction and the need for good 2D modeling of laser plasma physics.

The bulk of the literature dealing with the dynamics of laser plasmas has been restricted to 1D characterization of the physics. Experimental measurements of plasma temperatures, densities and ablation rates have generally been interpreted using 1D models or simulation codes. The 1D treatment has been found to be adequate for providing a first-order approximation to the energy transport processes occurring near the target surface. Furthermore, the 1D situation is amenable to analytic and numerical modeling. When one proceeds to the more realistic 2D situation an analytic treatment of the problem becomes formidable, and experiments must necessarily rely to a greater degree upon 2D numerical codes to aid in the interpretation of results. The complexity (both physical and numerical) and numerical resources required tend to scale geometrically with the dimensions of the simulation. As computing resources available to users have increased, the sophistication of codes and the demand put upon the computers have kept pace and may be expected to do so into the foreseeable future. Currently several sophisticated 2D fluid codes exist which are capable of modeling hydrodynamic, thermal and radiative transport, magnetic fields, and laser beam propagation. Experimental studies must remain the benchmarks against which the credibility and reliability of such codes are evaluated.

This thesis summarizes a study in the lateral structure of the x-ray emission features from plasmas produced in planar targets irradiated by 0.53 μm laser light.

The motivation for the study may be drawn from the foregoing discussion. First, in the field of ICF, there is the need to characterize the 2D nature of the transport mechanisms near the ablation surface of targets and in the laser absorption region. One specific aim of the experimental study was an assessment of the degree to which energy may be transported laterally beyond the laser absorption region and coupled into the target. Second, for applications which require small x-ray sources, such as CXM or point projection x-ray shadowgraphy diagnostics for ICF (Kondo, 1991), the resolution achievable is limited by the size of the emitter which may be influenced by lateral expansion of the plasma. Therefore, lateral transport from the ablation region is of interest even if energy coupling into the surrounding target is weak. A final and equally important objective was the database against which the 2D hydrocodes could be tested.

Some of the transport mechanisms which come into play when a laser beam is focused at high intensity onto a target are sketched in Fig. 1.1 . The laser beam and nominal focal region are defined by the dotted lines in the figure and the hot ablated plasma by the shaded area. The lateral expansion of the plasma creates a heat reservoir which extends beyond the focal spot and may couple energy into the target substrate. Electron thermal conduction (labeled as $\kappa\nabla T$ in the figure) can widen the ablation front (the crater shaped depression in the target) and transfer heat from the expanding plasma to the cold lateral target substrate. Radiative processes in the plasma (labeled $h\nu$) can also heat this region. Electric fields generated by space charge effects (labeled by ---- and ++++) can induce electron currents which return to the target surface along the edge of the expanding sheath and propagate back to the focal spot. Highly energetic electrons may also be produced by a number of processes such as resonance absorption. These electrons are ejected from the focus and may redeposit their energy in remote lateral regions of the target. The electron currents generate and are

influenced by strong magnetic fields which form at the edges of laser spots. These fields, in addition to bending the electron trajectories, may strongly inhibit the local thermal transport. Finally, the high pressures created by the ablation process drives a shock which undergoes an expansion into the target compressing and heating the material there.

vacuum

laser

e

e

$B \otimes$

$\odot B$

$\kappa \nabla T$ $\kappa \nabla T$ $\kappa \nabla T$

hv

target

shock front
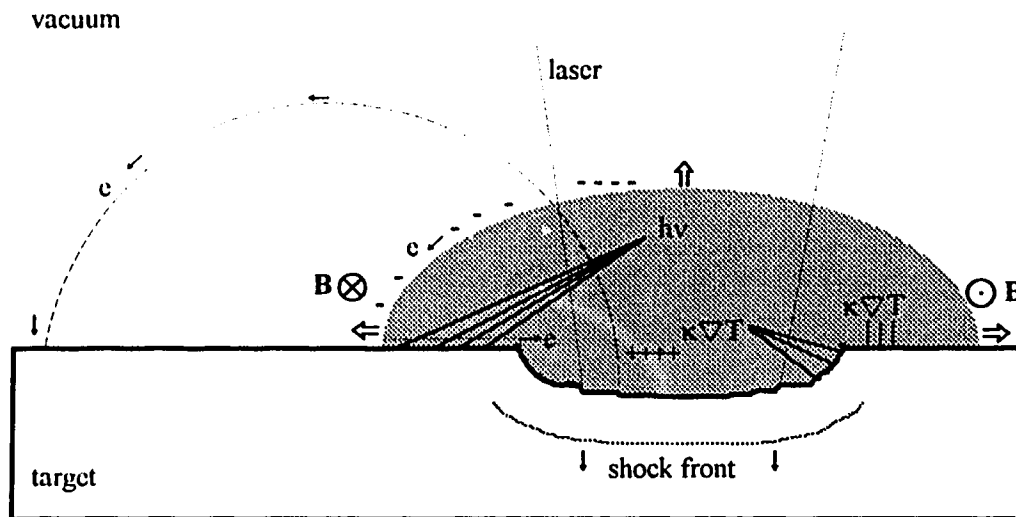
Figure 1.1. Various lateral transport mechanisms which may occur in a laser-produced plasma.

Most of the previous work on lateral transport has involved either measurements of the shock breakout from the rear side (i.e., that side opposite to the laser focus) of planar foils, or measurements characterizing the remote deposition of energy at the front side of targets. Studies aimed at characterizing transport in the immediate vicinity of the focal spot are few in number and have yielded somewhat conflicting conclusions. The need therefore remains for more work on this subject in order to enhance our understanding of the complicated three dimensional situation prevalent in real laboratory plasmas.

8

The study summarized in this thesis incorporated several techniques which had not previously been applied to the lateral transport problem. The incorporation of spatially resolving spectrometers into the diagnostics made possible the identification of specific ion states and allowed temperature estimates of the lateral regions to be made. A second feature of the experiments was the use of multilayer and special tracer targets used to identify those regions of the target which gave rise to the x-ray emission. Also in contrast to previous work, a number of different beam target configurations were tried, in order to compare the effects of outward directed transport from a single laser spot with the effects of inward directed transport between two laser spots. A novel method of measuring the laser energy distribution on target was also introduced in this study. The method made possible an accurate assessment of beam spillover, which was essential for a proper interpretation of the observations. Finally, a direct comparison of the x-ray emission recorded by the diagnostics, and the degree of lateral transport implied by these measurements, were compared with the predictions of a 2D hydrodymamics code which incorporated laser absorption, electron thermal transport, atomic physics, radiation transport, and magnetic fields.

The experiments were conducted at the Institute of Laser Engineering (ILE) in Suita, Japan. The full ILE facilities were kindly made available to the author by Dr. Nakai and his associates. These resources included the GEKKO IV laser system, the x-ray diagnostics, and the target fabrication facility.

The remainder of this thesis is structured as outlined below.

In Chapter 2 an overview of the dominant physical processes and energy transport mechanisms expected in the experiments is presented. The role of laser absorption, thermal transport, and ablation processes are considered. One-dimensional analytic models that have proved useful in characterizing the temperature, hydrodynamics, and density profiles are introduced, and the limitations of these models

noted. This is followed by a review of the atomic physics processes which give rise to the x-ray signals recorded by the diagnostics, and of the nature of radiation transport in LPPs.

Chapter 3 deals with physical transport mechanisms which may be important when the more realistic 2D case is considered. These include beam diffraction, thermal smoothing, generation of magnetic fields and their inhibiting effect on transport coefficients, hot electrons, and radiation transport. A review of previous related work in lateral transport is presented in parallel with this discussion.

An outline of the experimental method follows in Chapter 4. A description of the GEKKO IV laser and the experimental support facilities at the Institute of Laser Engineering is presented. The x-ray and optical diagnostics used in the study are also described here.

The following four chapters deal with the experimental results and analysis. Chapter 5 is devoted to the experimental characterization of the laser focal conditions of the target experiments. The lateral transport experiments are the subject of the three subsequent chapters and may be classified into two types - those involving a low to moderate-intensity, spatially-modulated laser spot (~300 μm dia.), and those involving a medium to high-intensity, tight focus laser spot (~110 μm dia.). The modulated intensity and tight focus experiments are discussed in Chapters 6 and 7 respectively. In both chapters, the data is interpreted with post-processed output from the 2D fluid particle code IZANAMI which was developed at ILE. Chapter 8 is devoted to the description of collisional structures which were observed in the coronas of targets during the modulated intensity experiments.

The thesis concludes with some closing interpretive remarks on the experiments and suggestions for future research.

2. Energy Transport in Laser-Produced Plasmas: 1D Models

In this chapter we shall be concerned with the dominant energy transport mechanisms thought to play a role in the experiments described in later chapters. These mechanisms include laser light absorption, electron thermal conduction, advection from the ablating target, and the emission and transport of x-rays. In particular we are interested in identifying the dominant absorption processes, characteristic temperature and density profiles, and expected mass ablation rates. To this end a number of one dimensional (1D) models which have proved successful in describing laser-target interactions will be reviewed; two dimensional (2D) transport effects will be reserved for the next chapter. The final section of the chapter will be devoted to a discussion of the atomic physics, x-ray emission and radiation transport processes of particular relevance to the diagnostics used in the experiments.

The laser ablation of a target is a complex interaction involving electromagnetic radiation, atomic physics, hydrodynamics and kinetic processes. When intense laser light is focused onto a solid in vacuum, a plasma quickly forms as a result of collisional or multiphoton ionization. A thermal wave is quickly driven into the solid, heating and ionizing the material behind the thermal front. The hydrodynamic pressure of this heated material creates an expansion into the vacuum, while simultaneously driving a shock into the solid. Typically the shock will quickly overtake the thermal front, creating a situation shown in Figure 2.1 (it is assumed that the solid is thick enough to prevent total ablation over the time span of interest, which

is normally on the order of the laser pulse duration). Four regions may be identified in the interaction. The leftward traveling shock front forms the boundary between the unperturbed solid I and the shocked material II. The ablation front separates the dense solid from the conduction zone III, which is characterized by sharp temperature and density gradients. In this region the heating and outward advection of material to the right is balanced by thermal conduction to the left. The boundary between the conduction zone and the corona IV, which is characterized by high temperatures and low densities, is termed the critical surface and represents the point beyond which the laser can not propagate.
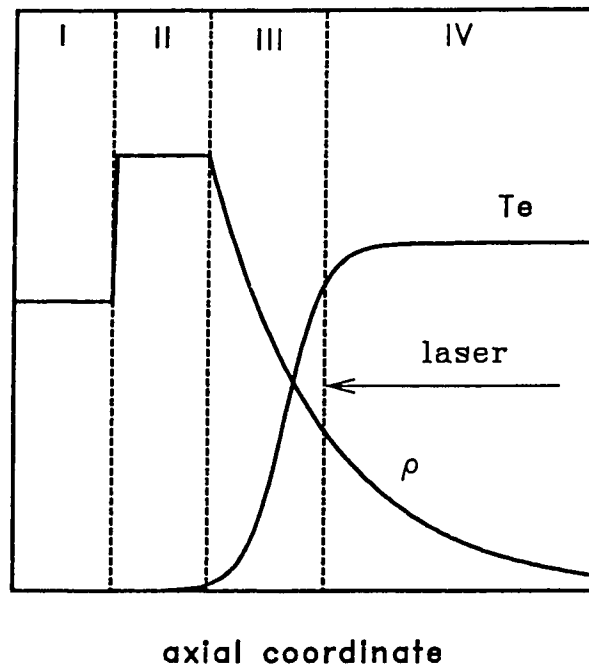
Figure 2.1. A representation of temperature and density profiles characteristic of a laser-target interaction. The interaction may be zoned into (I) the unperturbed target, (II) the shocked, dense target material, (III) the supercritical ablation region where thermal transport dominates, and (IV) the underdense corona where laser absorption occurs.

Collisional Processes

Collisional processes figure predominantly in all of the transport mechanisms mentioned above. For this reason a brief discussion on collisions between the charged species in a plasma is in order. Much of plasma behavior is influenced by the fact that the ion and electron species differ greatly in mass. This disparity determines the relative equilibration times between two systems of comparable temperature. These times are related in terms of the electron and ion masses by

$$\tau_{ee} : \tau_{ii} : \tau_{ei}^{Eq} = 1 : \left(\frac{m_i}{m_e}\right)^{1/2} : \left(\frac{m_i}{m_e}\right) \qquad 2.1.$$

Thus electrons exchange energy on a much shorter time scale than ions do, and similar species exchange energy on a much shorter time scale than different species do.

Equation 2.1 and the ratio of ion to electron masses have important consequences. First, energy transport processes involving collisions, such as thermal conduction, tend to be electron-dominated, while hydrodynamic phenomenon, such as transport by advection, tend to be dominated by the more massive ions. Second, the coupling between ions and electrons may be often assumed to be weak over the time scales of interest (e.g., the length of the laser pulse). It is therefore common in numerical modeling to treat the electrons and ions as independent fluids, interacting through a collisional coupling term, subject to the constraint of charge neutrality. Strong collisional coupling between the ions and electrons occurs only where particle densities are sufficiently high; hence (over time scales of interest in this study) ion heating tends to be restricted to regions near to the target surface.

The functional form of the collision rates are stated below, for the case in which the ion and electron species are both near equilibrium (but not necessarily with each other), and in which the ion temperature is less than the electron temperature.

13

Under such conditions there are two characteristic rates, given by (Shkarofsky et al., 1966)

$$\nu_{ei} = \frac{4\sqrt{2\pi}}{3} \frac{\overline{Z}^2 n_i e^4 \ln \Lambda}{m_e^{1/2} T_e^{3/2}} = 2.91 \times 10^{-6} \frac{\overline{Z}(n_e cm^3) \ln \Lambda}{(T_e/eV)^{3/2}} \; sec^{-1} \qquad 2.2a$$

$$\nu_{ii} = \frac{4\sqrt{\pi}}{3} \frac{\overline{Z}^4 n_i e^4 \ln \Lambda}{m_i^{1/2} T_i^{3/2}} \qquad 2.2b.$$

The coulomb logarithm, introduced to account for screening effects (Spitzer, 1956), may be estimated by (Balescu, 1988)

$$\ln \Lambda = \begin{cases} 25.3 - \ln\left(\frac{(n_e cm^3)^{1/2}}{(T_e/eV)} \right), & T_e > 10Z^2 \; eV \\ 23 - \ln\left(\frac{(n_e cm^3)^{1/2} Z}{(T_e/eV)^{-3/2}} \right), & otherwise \end{cases} \qquad 2.3$$

which is valid for $n_e \lambda_D^2 >> 1$, where λ_D is the Debye length (Book, 1987)

$$\lambda_D = 7.43 \times 10^2 \left(\frac{T_e/eV}{n_e cm^3} \right)^{1/2} cm \qquad 2.4.$$

Assuming the ions to be cold, the energy relaxation time for electron-ion collisions may be estimated to be

$$\tau_{ei}^{Eq} = \frac{m_i}{2 m_e \nu_{ei}} = 3.15 \times 10^8 \frac{A(T_e/eV)^{3/2}}{Z n_e cm^3 \ln \Lambda} \; sec \qquad 2.5.$$

Taking as an example a CH plasma at 500 eV and 4.0×10^{21} cm^{-3} (the critical electron density for a 0.53 μm laser wavelength), the relaxation time is ~250 ps. For comparable temperatures and densities below 1.0×10^{21} cm^{-3}, the relaxation time exceeds typical laser pulse lengths used in the experiments, indicating that the

14

electrons and ions were effectively decoupled in the corona for the target shots of this study.

Inverse Bremmstrahlung

One collisional process of importance is classical inverse bremmstrahlung, which is the dominant mechanisms of laser absorption in a plasma for wavelengths below 1 μm and intensities below 10^{15} W/cm^2. Craxton and McCrory (1980) have performed numerical studies of the laser absorption efficiency for this intensity and wavelength regime assuming inverse bremsstrahlung as the only absorption mechanism and have successfully reproduced a number of experimental results (Atzeni, 1987, and references therein). Essentially, the absorption process involves the damping of the propagating electromagnetic wave through electron ion collisions. The electromagnetic fields in a plasma obey Maxwell's equations

$$\nabla \cdot \mathbf{E} = \frac{\rho}{\varepsilon_0} \qquad \text{2.6a}$$

$$\nabla \cdot \mathbf{B} = 0 \qquad \text{2.6b}$$

$$\nabla \times \mathbf{B} = \mu_0 \left(\varepsilon \frac{\partial \mathbf{E}}{\partial t} + \mathbf{J} \right) \qquad \text{2.6c}$$

$$\nabla \times \mathbf{E} = -\frac{\partial \mathbf{B}}{\partial t} \qquad \text{2.6d}$$

where the dielectric function ε is a property of the local plasma conditions. A simple 1D model may be used to derive an expression for ε from the electron equation of motion (Shearer 1970, 1971; Duderstadt and Moses, 1982):

$$\dot{w} = -\frac{eE}{m_e} - v_{ei}w \qquad \text{2.7}$$

15

Here the electron acceleration $\dot{w}$ has been collisionally damped through an expression of the form (2.2a). This equation may be solved with the two Maxwell equations (2.6c) and (2.6d) under the assumptions that the solutions of the E field and electron velocity are of the form

$$E(z,t) = E(z)e^{i(kz+\omega t)} \; \hat{x} \qquad\qquad 2.8a$$

$$w(z,t) = w(z)e^{i(kz+\omega t)} \; \hat{x} \qquad\qquad 2.8b.$$

Here the laser is assumed to propagate in the negative z direction into a plasma corona which extends along the positive z direction, as envisioned in Fig. 2.1. The current density **J** is assumed to originate from electron density perturbations in a fixed ion background:

$$J = -n_e ew \qquad\qquad 2.9.$$

In the limit $\omega >> v_{ci}$ it can be shown using the equations above that the dielectric function of the plasma may be written

$$\varepsilon = \left(\frac{kc}{\omega}\right)^2 = 1 - \frac{n_e}{n_c} - i\frac{n_e}{n_c}\frac{v_{ci}}{\omega} \qquad\qquad 2.10$$

where the critical density n_c is given by

$$n_c = \frac{\varepsilon_0 m_e \omega^2}{e^2} \qquad\qquad 2.11.$$

This represents the electron density above which the laser light cannot propagate. The power absorption coefficient may be obtained from expression (2.10)

$$\alpha = -2\,\mathrm{Im}(k) = \frac{n_e v_{ci}/n_c c}{\left(1 - n_e/n_c\right)^{1/2}} \qquad\qquad 2.12.$$

If we assume a density profile of the form $n_c e^{-z/L}$, as in the self-similar isothermal model discussed later, the flux attenuation from infinity to a point z is

$$\exp\left[-\int_{+\infty}^{z}\frac{e^{-2z'/L}v_c}{\left(1 - e^{-2z'/L}\right)^{1/2}}dz'\right] \qquad\qquad 2.13$$

16

where ν_c is the collisional frequency at critical density

$$\nu_c = \frac{n_c}{n_e}\nu_{ei}$$ $\quad$ 2.14.

The intensity at z is determined from (2.13) to be

$$I(z) = I_{inc}\exp\left[-\frac{4\nu_c L}{c}\left(1-\left(1-e^{-z/L}\right)^{1/2}\left(1+1/2\,e^{-z/L}\right)\right)\right]$$ $\quad$ 2.15

The total absorption fraction for the wave traveling up to critical density and back to infinity, assuming total reflection of the wave at the critical surface, is

$$A = 1 - \exp\left[-\frac{8\nu_c L}{3c}\right]$$ $\quad$ 2.16.

If a linear density profile is assumed, it may be shown that the functional form of the predicted absorption is preserved, but with the numerical factor 8/3 replaced by 32/15.

The Hydrodynamic Equations

We begin this section with the concept of the distribution function $f(x,w,t)$ which describes a system of particles (most generally these may be ions, electrons, photons, etc.) and represents the density of particles within a phase volume element $(d^3x\,d^3w\,dt)$ of phase space at the coordinates $(x_1,x_2,x_3,w_1,w_2,w_3,t)$. The spatial density of particles at any point in space is represented by an integral over the particle velocities w:

$$n(x,t) = \iiint_w f(x,w,t)d^3w$$ $\quad$ 2.17.

An important example of such a distribution function is the Maxwellian, which describes a system of massive particles in thermal equilibrium

$$f(x,w) = n(x)\left(\frac{m}{2\pi T}\right)^{3/2}\exp\left[-w^2/2T\right]$$ $\quad$ 2.18

17

where m and T are the particle mass and the temperature in energy units.

The time evolution of the system of particles is described by the kinetic equation

$$\frac{df}{dt} = \frac{\partial f}{\partial t} + \frac{\partial \mathbf{x}}{\partial t} \bullet \frac{\partial f}{\partial \mathbf{x}} + \frac{\partial \mathbf{w}}{\partial t} \bullet \frac{\partial f}{\partial \mathbf{w}} = S(\mathbf{x}, \mathbf{w}, t) \qquad 2.19.$$

where S is a source term which describes the interaction of the system with external environment or with another system. For a system of plasma particles (electrons or ions) this interaction typically takes the form of a collisional coupling term, in which case the time development of the system is described by the Boltzmann equation

$$\frac{df}{dt} = \frac{\partial f}{\partial t} + (\mathbf{w} \bullet \nabla_x)f + \left(\frac{\mathbf{F}}{m} \bullet \nabla_w\right)f = \left(\frac{\partial f}{\partial t}\right)_{coll} \qquad 2.20$$

in which the particle trajectories are influenced by the local Lorentz acceleration

$$\frac{\mathbf{F}}{m} = q(\mathbf{E} + \mathbf{w} \times \mathbf{B}) \qquad 2.21$$

where q, $\mathbf{E}$, and $\mathbf{B}$ are the particle charge and the electric and magnetic fields.

The Navier-Stokes equations may be recovered by taking various moments of the variable $\mathbf{w}$ of the Boltzmann equation over velocity space (Spitzer, 1956; Braginskii, 1965). Defining

$$\overline{Q}(\mathbf{x}, t) = \int_{-\infty}^{+\infty} \int_{-\infty}^{+\infty} \int_{-\infty}^{+\infty} Q(\mathbf{w}) f(\mathbf{x}, \mathbf{w}, t) d^3\mathbf{w} \qquad 2.22$$

then, for Q=1, Q=mw, and Q=mww/2, and dropping the subscript on the spatial divergence, we recover respectively the equations for mass conservation, motion, and energy conservation:

$$\frac{\partial n}{\partial t} + \nabla \bullet (n\mathbf{v}) = 0 \qquad 2.23$$

$$mn\left[\frac{\partial \mathbf{v}}{\partial t} + (\mathbf{v} \bullet \nabla)\mathbf{v}\right] = qn(\mathbf{E} + \mathbf{v} \times \mathbf{B}) - \nabla P \qquad 2.24$$

18

$$\frac{\partial}{\partial t}\left(\rho e + \frac{\rho v^2}{2}\right) + \nabla \bullet \left(\rho v\left[h + \frac{v^2}{2}\right]\right) = -\nabla \bullet q + qnE \bullet v + C \quad 2.25$$

where ρ is the mass density, v the fluid velocity, P the pressure, $\nabla \bullet q$ the thermal conduction term, C the equilibration term (originating from the right hand side of 2.20), and e and h the specific internal energy density and enthalpy, related through

$$h = e + \frac{P}{\rho} \quad\quad 2.26.$$

For the case of an ideal gas e and h are given by

$$e = C_v T = \left(\frac{1}{\gamma - 1}\right)\frac{P}{\rho} \quad\quad 2.27a$$

$$h = C_p T = \left(\frac{\gamma}{\gamma - 1}\right)\frac{P}{\rho} \quad\quad 2.27b$$

It is often the case that the kinetic energy term in (2.25) is eliminated using the first 2 hydrodynamic equations (2.23) and (2.24). By doing so we arrive at the form most commonly used in numerical simulations of plasmas. The electron and ion equations are both stated below:

$$\rho C_{ve}\left(\frac{\partial}{\partial t} + v \bullet \nabla\right)T_e = -\nabla \bullet q_e - P_e\nabla \bullet v - en_e E \bullet v - \frac{2m_e}{m_i} v_{ei}\left(T_e - T_i\right) + L + \mathcal{R}$$

$$2.28a$$

$$\rho C_{vi}\left(\frac{\partial}{\partial t} + v \bullet \nabla\right)T_i = -\nabla \bullet q_i - P_i\nabla \bullet v + q_i n_i E \bullet v + \frac{2m_e}{m_i} v_{ei}\left(T_e - T_i\right) + \mathcal{R}_i$$

$$2.28b.$$

The equilibration term has been written explicitly in terms of the collision rate, and laser absorption and radiative loss terms L and $\mathcal{R}$ added as is typically done for numerical modeling.

Absorption and Ablation models

Using the results of the previous discussion we now return to the laser target interaction represented in Fig. 2.1, and present some estimates pertaining to the conditions in the conduction zone and the corona.

It is apparent from (2.23-2.25) that a steady-state solution in region IV is not possible since there is no way of satisfying the condition that n and P must both tend to zero at great distances from the target. The 1D self-similar isothermal expansion model (Mora and Pellat, 1979) has proved successful in describing the hydrodynamics of the corona. The assumptions of this model are:

1. The plasma may be adequately described by a two fluid description in which the ions obey hydrodynamic equations

$$\frac{\partial n_i}{\partial t} + \frac{\partial}{\partial x}(n_i v) = 0 \qquad\qquad 2.29$$

$$\left(\frac{\partial}{\partial t} + v_i \frac{\partial}{\partial x}\right) v_i = -\frac{Ze}{m_i} \frac{\partial \Phi}{\partial x} \qquad\qquad 2.30$$

which are seen to be special cases of equations (2.23) and (2.24). In particular, the ions are assumed to be cold so that the local gradient of Coulomb potential Φ dominates over the pressure term.

2. The electrons are characterized by a single temperature, and are collisionally uncoupled to the ions, obeying the Vlasov equation

$$\frac{\partial f}{\partial t} + w_e \frac{\partial f}{\partial x} + \frac{e}{m_e} \frac{\partial \Phi}{\partial x} \frac{\partial f}{\partial w_e} = 0 \qquad\qquad 2.31$$

with a distribution function given by a Maxwellian (2.18) plus a perturbation term. The electron and ion densities are related through the quasi-neutrality condition

$$n_e = \overline{Z} n_i \qquad\qquad 2.32$$

where $\overline{Z}$ is the average ionization state of the plasma.

20

3. The plasma is assumed to expand from an unperturbed region in which the ion density is fixed at n_0.

Under these assumptions the solutions to the equations above may be written in terms of the dimensionless similarity variable $x/C_s t$, where the isothermal sound speed C_s is given by

$$C_s = \sqrt{\frac{ZT_e}{m_i}} \qquad\qquad 2.33.$$

The solutions are

$$n_i = n_0 \exp\left(- v_i/C_s\right) \qquad\qquad 2.34$$

$$v_i = C_s + x/t \qquad\qquad 2.35$$

$$e\Phi = -T_e\left(1 + x/C_s t\right) \qquad\qquad 2.36$$

If the unperturbed region lies to the left of the critical layer then the density profile in region IV may be rewritten in the reference frame for which the origin coincides with critical density

$$n_i = n_c \exp\left(-x'/C_s t\right) \qquad\qquad 2.37.$$

Note that this profile is consistent with that assumed in deriving the laser absorption term (2.16). From equation (2.37) one can identify a time-dependent absorption scale length for the plasma, $L(t) = C_s t$. We may also define a characteristic scale length for the entire interaction in terms of the laser pulse width τ,

$$L(\tau) = C_s \tau \qquad\qquad 2.38.$$

Assuming inverse bremmstrahlung absorption, and a self-similar model of expansion, Mora (1982) developed a self-consistent set of predictions for the corona absorption and hydrodynamics. By equating the absorbed intensity to the energy required to drive the isothermal expansion, the argument of the exponential in (2.16) was shown to scale as $I\lambda^5$. Consequently, the model predicts a transition flux given by

$$\left(\frac{I^*}{4.8 \times 10^{11} \ W/cm^2}\right) = \left(\frac{\lambda}{1.06\,\mu m}\right)^{-5} \left(\frac{2Z}{A}\right)^{5/4} \left[\frac{1}{Z}\left(\frac{\ln \Lambda}{6}\right)\left(\frac{\tau}{100\,ps}\right)\right]^{3/2} \quad 2.39$$

below which absorption is very strong. At the transition flux the predicted absorption fraction (2.16) is 71%, while for $I = 0.38\ I^*$ this quantity is 90%.

Anticipating the experimental sections to follow later, we will use some typical laser and target parameters for the estimates that follow. The experiments were conducted on planar targets of low to moderate Z. The laser wavelength was 0.53 μm, and pulse widths varied from 300 ps to 900 ps. By changing the focal conditions on target, incident intensities in the range of $(1 \times 10^{13} - 4 \times 10^{14})$ W/cm^2 were achieved. In the following table we present values of I^* for typical parameters of the experiments (for $\ln \Lambda = 7$).

TABLE 2.1 Transition Flux (Mora model)		
Target Type	τ **(ps)**	$I^*\left(W/cm^2\right)$
CH (Z=3.5,A=6.5)	860	3.5×10^{15}
NaF (Z=10,A=21)	860	1.5×10^{16}
CH	400	1.1×10^{15}
NaF	400	4.6×10^{15}

Since these intensities are all much higher than those reached experimentally, the Mora model predicts that the absorption fraction will be high for all experiments. In fact, long before these intensities are reached, othe absorption mechanisms such as non-linear inverse bremmstrahlung and parametric decays are expected to come into play.

When the absorption is strong, as expected in these experiments, it may be no longer valid to assume that the laser energy reaches the critical surface. If most of the laser is absorbed in the region where the denominator in expression (2.12) is

22

approximately unity, and assuming the density profile in the absorption region is of the form (2.38), then the laser may be assumed to dump its energy in the vicinity where the density is given by

$$n_M \approx 2 n_c \left(c / v_c L \right)^{1/2} \qquad\qquad 2.40$$

The corona in this case is not strictly isothermal, but exhibits a peak temperature in the vicinity of density n_M, which, when written in terms of the definitions (2.40) is given by

$$n_M / n_c \approx 0.60 \left(\frac{I_{inc}}{4.8 \times 10^{11} \; W/cm^2} \right)^{1/4} \left(\frac{\lambda}{1.06 \, \mu m} \right)^{-3/4} \left(\frac{2Z}{A} \right)^{-5/16} \left[\overline{Z} \left(\frac{\ln \Lambda}{6} \right) \left(\frac{\tau}{100 \, ps} \right) \right]^{3/8}$$

$$2.41$$

where I_{inc} is the incident laser intensity. If we take typical values for the tight focus experiments of $I_{inc} = 3.0 \times 10^{14}$ W/cm^2 and $\tau = 400$ ps, the expression above is greater than unity for both CH and NaF plasmas. A fraction of the laser may be expected to reach the critical surface under these conditions.

We now consider the conduction zone III. Assuming the dominant energy transport processes are thermal transport and advection, the boundary conditions in the frame of the ablation front will obey the Rankine Hugoniot relations

$$\rho_- v_- = \rho_+ v_+ \qquad\qquad 2.42$$

$$P_- + \rho_- v_- = P_+ + \rho_+ v_+ \qquad\qquad 2.43$$

$$h_- + \frac{v_-^2}{2} + \frac{q}{\rho_- v_-} = h_+ + \frac{v_+^2}{2} + \frac{q}{\rho_+ v_+} \qquad\qquad 2.44$$

where the subscripts $+$ and $-$ denote the conditions in front of and behind the ablation front. Three cases may be identified based on the relation between the heat wave velocity $V_{HW} \sim q/\rho_+ h_-$ and the shock wave velocity $V_{sh} \sim (P_-/\rho_+)^{1/2}$:

1. When the heat front velocity exceeds the shock wave velocity a supersonic thermal wave results. It can be shown that such a wave can not exist in materials of

constant thermal conductivity (Zel'dovich and Raizer, 1966) but is possible in laser-produced plasmas for which thermal conduction is a strong function of temperature. This is the situation which exists at very early times during the pulse. In this case, the shock zone of Fig 2.1 does not exist and the thermal wave propagates directly into the unperturbed target.

2. If the shock speed exceeds the thermal front speed, then a subsonic deflagration results.

3. The limiting case when the two velocities are equal is known as the Chapman-Jouget deflagration.

The conduction zone may be modeled by a steady state solution (Manheimer et al., 1982; Fabbro et al., 1985) if some simplifying assumptions are made:

1. The ablation process is determined by the balance between thermal conduction, laser absorption, and the outward advection.

2. The solution in region IV is assumed to obey the isothermal model described above.

3. The matter may be described by a perfect gas equation of state with specific energy and enthalpy given by equations (2.27-2.28).

4. The absorbed laser energy is assumed to be deposited at the critical surface.

5. A single-temperature plasma is assumed.

5. The error incurred by neglecting the accelerated reference frame of the target is negligible.

This model will be hereafter referred to as the isothermal Chapman Jouget (CJ) model.

For steady state the following relations must be satisfied at the critical surface:

$$[\rho v] = 0 \qquad\qquad 2.45$$

$$[\rho v^2 + \rho C_s^2] = 0 \qquad\qquad 2.46$$

$$\dot{m}[v^2/2 + 5C_s^2/2] + [q] = I_{abs} \qquad\qquad 2.47$$

where $\dot{m}$ is the mass ablation rate and I_{abs} the absorbed intensity. The classical heat conduction term (discussed in greater detail below) is given by

$$q = -K_0 T^{5/2} \frac{dT}{dx} \qquad 2.48.$$

When equations (2.45) and (2.46) are integrated from the ablation surface to the critical surface the following expressions result

$$\dot{m} = \rho_0 C_{sc} \qquad 2.49$$

$$v = C_{sc} - \left(C_{sc}^2 - C_s^2 \right)^{1/2} \qquad 2.50$$

if the velocity is taken to be zero at the ablation front. The local velocity of the plasma is subsonic in the ablation region and equals C_{sc}, the sound speed, at the critical surface . The maximum temperature is also reached at this point. The solution is consistently matched to an isothermal expansion if the boundary is made equal to the critical layer.

The energy needed to supply the isothermal expansion may be found by integrating the energy in the corona from the critical surface to infinity

$$\frac{dE_{IV}}{dt} = \frac{d}{dt} \int_0^\infty \rho \left(v^2/2 + e \right) dx = 4\rho C_{sc}^3 \qquad 2.51$$

The energy equation evaluated at the boundary in region III yields

$$q_{III} = -3\rho_c C_{sc}^3 \qquad 2.52$$

which represents the thermal heat flux into the conduction zone. It is evident that, in addition to the energy flux from the conduction zone ($-q_{III}$), and outward heat flux of $q_{IV} = \rho_c C_{sc}^3$ must be supplied to maintain the isothermal expansion (2.51). If the hydrodynamic variables are continuous across the boundary then the absorbed intensity and heat flux are related by

$$I_{abs} = q_{IV} - q_{III} = 4\rho_c C_{so}^3 \qquad 2.53$$

One fourth of the laser energy is therefore needed to maintain the isothermal expansion. One can then immediately write predictions for the coronal temperatures, ablation pressure, and mass ablation rate:

$$T_e = \left[\frac{m_i}{(\bar{Z} + 1)}\right]\left(\frac{I_{abs}}{4\rho_c}\right)^{2/3} \qquad 2.54$$

$$P_a = 2\rho_c C_{sc}^2 = 12\left(\frac{I_{abs}}{10^{14}\ W/cm^2}\right)^{2/3}\left(\frac{\lambda}{\mu m}\right)^{-2/3}\left(\frac{A}{2Z}\right)^{1/3}\ Mbar \qquad 2.55$$

$$\dot{m} = \rho_c C_{sc} = 1.50 \times 10^5 \left(\frac{I_{abs}}{10^{14}\ W/cm^2}\right)^{1/3}\left(\frac{\lambda}{\mu m}\right)^{-4/3}\left(\frac{A}{2Z}\right)^{2/3}\ \frac{gm}{cm^2 s} \qquad 2.56$$

The temperature in region III is obtained by integrating the energy equation along the spatial coordinate x from the critical density to the ablation point

$$T = \left(T_c^{5/2} - \frac{25}{4}\frac{\bar{Z} + 1}{\bar{Z}A}\frac{n_{cc}C_{sc}}{K_o} x\right)^{2/5} \qquad 2.57$$

where the x origin has been taken at the critical surface. The position of the ablation surface may be identified as the point where the temperature becomes zero:

$$D = \frac{4\bar{Z}K_o T_c^{5/2}}{25(\bar{Z} + 1)n_{cc}C_{sc}} \qquad 2.58.$$

The quantity D is termed the standoff distance and is an important parameter in the interpretation of thermal smoothing measurements discussed in Chapter 3. In order to estimate D, the thermal conductivity of the plasma must be known.

If the laser radiation is absorbed before reaching critical density, an isothermal model can not describe the zone IV. A steady-state solution for the conduction zone (2.45-2.47) may then be matched to the point of density n_M. This solution is known as the self-regulating model and exhibits temperature and pressure scalings of

$$T_c \approx 60.5\left(\frac{I_{inc}}{4.8 \times 10^{11}\ W/cm^2}\right)^{1/2}\left(\frac{\lambda}{1.06\mu m}\right)^{1/2}\left(\frac{2Z}{A}\right)^{-1/8}\left[\frac{1}{\bar{Z}}\left(\frac{\ln\Lambda}{6}\right)\left(\frac{\tau}{100ps}\right)\right]^{1/4}\ eV$$

$$2.59$$

$$P_a \approx 0.22 \left(\frac{I_{inc}}{4.8 \times 10^{11}\ W/cm^2} \right)^{3/4} \left(\frac{\lambda}{1.06\mu m} \right)^{-1/4} \left(\frac{2Z}{A} \right)^{-7/16} \left[\bar{z} \left(\frac{\ln \Lambda}{6} \right) \left(\frac{\tau}{100ps} \right) \right]^{1/8} Mbar$$

<div align="right">2.60</div>

$$\dot{m} = \rho_M C_M \approx 7.62 \times 10^3 \left(\frac{I_{inc}}{4.8 \times 10^{11}\ W/cm^2} \right)^{1/2} \left(\frac{\lambda}{1.06\mu m} \right)^{-5/2}$$

$$x \quad \left(\frac{\bar{Z}}{A} \right)^{-1/2} \left(\frac{2Z}{A} \right)^{-3/8} \left[\bar{z} \left(\frac{\ln \Lambda}{6} \right) \left(\frac{\tau}{100\ ps} \right) \right]^{-1/4} \frac{gm}{cm^2 sec}$$

<div align="right">2.61</div>

To conclude this section, two tables are presented showing predictions of the preceding ablation models for typical laser intensities and pulse widths. To calculate the absorbed intensity, the following expression based on experimental work (Key et al., 1983) at 0.53 μm was used:

$$\frac{I_{abs}}{I_{inc}} \approx 0.90 \left(\frac{I_{inc}}{10^{13}\ W/cm^2} \right)^{-0.08}$$

<div align="right">2.62.</div>

For the case of intensities below 5×10^{13} W/cm^2 and laser pulse lengths of about a nanosecond, these models provide an adequate first approximation for the parameters of the interaction. The characteristic scale lengths $C_s\tau$ are somewhat less than the experimental focal spot size (~300 μm), and the 1D models retain some validity. Experimental temperatures were typically in the range 500 - 650 eV, which resides between the values predicted by the two models. Experimentally determined mass ablation rates (Key, op. cit.) exhibit agreement with the isothermal CH model both in scaling and in magnitude; for example at an intensity of 3×10^{13} W/cm^2, the experimental value is ~2.0×10^5 gm/cm^{2}sec. The agreement is probably due in part to the weak scaling of the hydrodynamic velocity with intensity, since the assumption that the absorbed laser intensity is deposited at the critical surface is not accurate. For

example, if (2.15) is evaluated for a CH plasma of scale length 50 μm and temperature 500 eV, the absorption region (where the laser intensity falls from 90% to 10% of the incident value) lies between 28 μm and 104 μm from the critical surf .

We shall see that, for the case of the high intensity, short pulse case, the values from the table cannot be expected to be accurate since there is insufficient time to set up the steady-state conditions assumed by the model. Also the smaller (~110) focal spot diameter of the high intensity experiments places more severe restraints on the validity of the 1D models. Indeed, both temperatures and scale lengths are severely over predicted.

TABLE 2.2			ISOTHERMAL-CJ MODEL	
Target Type	CH (Z=3.5,A=6.5)	NaF (Z=10,A=21)	CH (Z=3.5,A=6.5)	NaF (Z=10,A=21)
τ (ps)	860	860	400	400
$I_{inc}\left(W/cm^2\right)$	3.0×10^{13}	3.0×10^{13}	3.0×10^{14}	3.0×10^{14}
$I_{abs}\left(W/cm^2\right)$	2.5×10^{13}	2.5×10^{13}	2.0×10^{14}	2.0×10^{14}
$T_c(eV)$	437	532	1800	2200
P(Mbar)	7.0	7.3	29	30
C_{sc}(cm/sec)	1.7×10^7	1.6×10^7	3.5×10^7	3.3×10^7
$\dot{m}(gm/cm^2\,sec)$	2.1×10^5	2.3×10^5	4.3×10^5	4.6×10^5
$\dot{d}(\mu m/n\,sec)$	1.9	0.82	3.8	1.7
$C_s\tau(\mu m)$	147	132	138	141

TABLE 2.3 SELF-REGULATING MODEL		
Target Type	CH (Z=3.5,A=6.5)	NaF (Z=10,A=21)
τ (ps)	860	860
$I_{inc}\left(W/cm^2\right)$	3.0×10^{13}	3.0×10^{13}
n_M/n_c	0.73	0.51
$T_c(eV)$	816	1080
P(Mbar)	3.6	3.3
C_{sm}(cm/sec)	2.1×10^7	2.2×10^7
$\dot{m}(gm/cm^2 sec)$	1.8×10^5	1.6×10^5
$\dot{d}(\mu m/n sec)$	1.7	0.57
$C_{sm}\tau(\mu m)$	177	191

Thermal Conduction and Flux Inhibition

The thermal conduction term q may be derived from the Boltzmann equation. The term may be written in terms of the distribution function as (Boyd and Sanderson, 1969)

$$q = \int\int\int_{-\infty-\infty-\infty}^{+\infty+\infty+\infty}\left(m_e w^2/2\right)wfd^3w \qquad 2.63.$$

In deriving the functional form of q, the distribution function is assumed to be a slowly varying function of temperature and density which may be expanded in terms of T_c and n_e as

$$f = f^0 + f^1 + f^2 + ... \qquad 2.64.$$

The first order correction term f^1, linear in the temperature and density gradients, is assumed to be a sufficient correction to f^0, which is taken to be locally Maxwellian (2.17). A steady state condition $(\partial f/\partial t = 0)$ is assumed to prevail. Furthermore the conductivity is normally evaluated under the assumption of constant pressure, allowing the local temperature and density gradients to be related through

$$P_e = n_e k_B T_e \qquad\qquad 2.65.$$

The Boltzmann equation in one dimension under these assumptions becomes

$$eEf^0 \frac{w_x}{k_B T_e} + f^0 w_x \frac{\partial T_e}{\partial x}\left(\frac{mw^2}{2k_B T_e^2} - \frac{5}{2T_e}\right) = -\nu_{ee}\left(f - f^0\right) = -\nu_{ee}f^1 \qquad 2.66.$$

Here the gradients have been assumed to exist in the x direction only. The collision term is a simplified one and is more correctly treated by Braginskii (1965). The integral (2.63) vanishes for $f = f^0$ and therefore q may be obtained by substitution of the correction term f^1 into (2.63). One still needs an expression for the electric field. This is normally provided by forcing the local current density to zero:

$$j = \int\limits_{-\infty}^{+\infty}\int\limits_{-\infty}^{+\infty}\int\limits_{-\infty}^{+\infty} ewfd^3w = \sigma E + \alpha\nabla T_e = 0 \qquad\qquad 2.67$$

where σ is the conductivity and α is the Seebeck coefficient. We quote the final expression obtained by Braginskii (1965):

$$K = \frac{n_e \tau_e k_B T_e}{m_e}\frac{\gamma_o'(Z)}{\delta_o(Z)} = K_o T_e^{5/2} = \frac{96.9\left(T_e/eV\right)^{5/2}}{\ln\Lambda\overline{Z}}\frac{\gamma_o'(Z)}{\delta_o(Z)}\frac{W}{eV cm} \qquad 2.68$$

where the collision time

$$\tau_e = \frac{3m_e^{1/2}T_e^{3/2}}{4\sqrt{2\pi}\ln\Lambda e^4\overline{Z}^2 n_i} = \frac{3.44\times10^5\left(T_e/eV\right)^{3/2}}{\ln\Lambda\overline{Z}^2\left(n_i cm^3\right)}\ s \qquad\qquad 2.69$$

has been used to arrive at the numerical coefficient in (2.68). The Braginskii coefficients γ_o' and δ_o arise when a more thorough treatment of the collision term in the kinetic equation is performed.

Using the expression (2.68) and suitable values for γ'_o and δ_o (Nishiguchi, 1983), values for the standoff distance of a steady-state ablating CH plasma (2.58) may now be estimated and are presented in Table 2.4. Also presented is an estimate of the time required to establish the conduction zone and set up a steady-state situation

$$t_D = 494\left(\frac{I_{abs}}{10^{14}\ W/cm^2}\right)\ ps \qquad\qquad 2.70.$$

TABLE 2.4 ISOTHERMAL-CJ MODEL (CH Plasma) Standoff Distance (D) and Duration of Transient Phase (t_D)		
$I_{inc}\left(W/cm^2\right)$	3.0×10^{13}	3.0×10^{14}
$I_{abs}\left(W/cm^2\right)$	2.5×10^{13}	2.0×10^{14}
$D(\mu m)$	12	195
$t_D(ps)$	122	1020

Thus for intensities well below 10^{14} W/cm^2 and laser pulse widths on the order of a nanosecond, the standoff distance is on the order of 10 μm, and the time required to form the steady-state standoff distance is a fraction of the laser pulse length. The steady-state ablation models can be expected to provide an approximate description of the ablation process. For the case of high intensity, short pulse conditions, a steady-state situation in the conduction zone never develops, and the steady-state models cannot be expected to describe the interaction well.

The model for conductivity presented above is accurate for plasmas in which the scale length of the local temperature gradient $T/\nabla T$ does not exceeds the mean free path of the energy carrying electrons. This condition can be violated in laser-produced plasmas and a heuristic procedure known as flux limiting is applied in

modeling the heat flow. The conduction term is set equal to the harmonic mean of the classical expression $K\nabla T$ and the free streaming flux

$$\frac{1}{q_{fl}} = \frac{1}{q_{cl}} + \frac{1}{q_{fs}}$$ 2.71

$$q_{fs} = fn_e kT_e v_{th} = fn_e k_B T_e (T_e/m_e)^{1/2}$$ 2.72.

The corrected thermal conductivity K^* may be defined by

$$q_{fl} = K^* \nabla T_e = \frac{K\nabla T_e}{1 + \left|\dfrac{K\nabla T_e}{q_{fs}}\right|}$$ 2.73.

The large body of experimental work on ablation rates (Delettrez, 1986, and references therein) indicates that values of f from 0.03-0.1 must be incorporated into the conductivity calculations of numerical codes in order to reproduce the observations. Fabbro and co-workers (op. cit.) showed that a steady state solution in the conduction zone, in which the classical conductivity term in (2.48) was replaced by the flux-limited term, could be matched to an isothermal expansion if a temperature and density discontinuity were assumed to exist at the critical density. It can be shown that the coronal temperatures, ablation pressures, and mass ablation rates (2.54-2.56) are corrected by the factors $\left(\dfrac{\phi}{0.6}\right)^{-2/3}$, $\left(\dfrac{\phi}{0.6}\right)^{1/3}$, and $\left(\dfrac{\phi}{0.6}\right)^{2/3}$, respectively, where

$$\phi = \frac{\overline{Z}A^{1/2}}{0.12 f(\overline{Z}+1)^{3/2}}$$ 2.74

If ϕ exceeds the value 0.6 in this model, the hydroflow is found not to be inhibited and the correction terms do not apply. As an example, if we take for a CH plasma $Z=3.5$ and $f=0.1$, then ϕ is 0.78 and the flow is not inhibited. Taking $Z=10$ and $f=0.03$, we find ϕ is 0.31, resulting in correction factors of 1.5, 0.81, and 0.65 to the temperature, pressure, and ablation rate.

32

Various mechanisms have been proposed to account for flux limitation, including ion-wave turbulence, electric fields generated by electron return currents, and magnetic-field-induced inhibition. More precise treatments of the Fokker Planck equation than that outlined earlier have been found to predict flux limitation without the need to postulate any of the physical mechanisms listed above (Yamanaka, 1991). Essentially, it is predicted that the component of the electron distribution function responsible for transporting most of the heat decouples from that component involved in energy absorption. The result is that the absorbed energy is not as effectively transported away from the absorption regions as would be expected by simpler treatments. The first practical predictions for the non-local flux, proposed by Luciani and co-workers (1983) was

$$q(x) = \int_{-\infty}^{+\infty} \frac{q_{SH}(x')}{2\Lambda(x')} \exp\left[-\frac{|x - x'|}{\Lambda(x')}\right] dx' \qquad 2.75$$

$$\Lambda(x) = 116(\overline{Z} + 1)^{1/2} \lambda_s(v_{th}) \qquad 2.76$$

with λ_s the free mean path of electron ion scattering. This model has more recently been shown to be subject to numerical instability when implemented in codes (Prasad and Kershaw, 1989). Recent progress towards improving on (2.75) have been made by Epperlein and Short (1991) and Prasad and Kershaw (1991).

The modeling used in this thesis will rely upon the conventional treatment of thermal conduction (2.68, 2.73).

Atomic Models, X-ray Emission and Transport

The chief diagnostics used in the experiments of this thesis were x-ray measurements. The use of spatially- and spectrally- resolved x-rays are a well

established diagnostic of LPPs (Kilkenney, 1980). Therefore some introductory discussion about x-ray generation and emission from LPPs is in order. In general, one is concerned with the emission of radiation from highly excited states of atoms, whose populations are in turn a function of the local temperature and density of the plasma. Thus x-ray emission from a plasma may be used to infer these populations and provide a measurement of local plasma conditions.

Models of x-ray emission generally begin with a calculation of the atomic level populations of the various excited states and ionization species as a function of temperature and density. If an atomic species is assumed to have N states, which include all the excited and ionization levels, then the equations governing the time development of the system may be written in the form

$$\frac{dn_i}{dt} = \sum_{j \neq i=1}^{N} R_{ji}(T_e, n_e)n_j - \sum_{j \neq i=1}^{N} R_{ij}(T_e, n_e)n_i \qquad 2.77$$

where R_{ji} is the transition rates from state j into state i and R_{ij} is the transition rate from state i to state j. A non-trivial solution to equation (2.77) requires that the relation

$$\sum_{i=1}^{N} z_i n_i = n_e \qquad 2.78$$

be satisfied, where z_i is the ionization of state i. Equation (2.77) may be expressed in the form of a matrix equation

$$\frac{dn}{dt} = R(T_e, n_e) \circ n \qquad 2.79$$

where R is an NxN rate matrix. Ideally one would like to include time-dependent atomic physics equations represented by (2.77) to be solved simultaneously with the hydrodynamics and radiation transport equation. Due to the considerable demand put upon the resources of computers this ideal has not yet been achieved but is an ongoing area of research. Where kinetic codes have been developed, they are typically run as

34

post-processors to the hydrodynamic simulations, using local Maxwellian electron distributions based on the temperatures predicted by the hydrocodes. Kinetic codes essentially involve the solution of the time-dependent rate equations given by equation (2.79) over all the atomic states to be modeled using one of a number of methods such as Guassian elimination or conjugate gradient methods (Kaushik, 1990). Consistency is checked by comparing the average ionization state and electron densities predicted by the kinetic simulations to those predicted by the steady-state models used in the hydrodynamic simulations. Discrepancies of less than a few per cent can regularly be achieved for simulations of experiments involving 300-600 μm diameter focal spots and 1 ns laser pulse lengths (Kauffman et al. 1987).

Results from time-dependent codes suggest that for many applications the time-independent solutions provide adequate estimates of the population levels in a plasma. An example of such a model is the RATION code (Lee and Whitten, 1984; Lee et al.;1985), which solves for the population levels for elements of Z = 5 to 26. The algorithm makes use of a Gaussian elimination technique with back-solving. Considerable simplification of the rate matrix can be made by grouping states of similar ionic charge together; the resultant matrix then consists of a series of overlapping blocks situated along the diagonal. In the RATION code, detailed level populations are solved for the hydrogen-like, helium-like and lithium-like species. Each of the species of lower ionic charge are represented by their ground state populations.

A fully collisional-radiative model must be used to cover the wide range of densities and temperatures that exist in LPPs. The atomic processes which determine population levels may be categorized as collisional or radiative. They are summarized below, coupled with their inverse processes.

Collisional processes:

$$X(z) + e \xrightleftharpoons[\text{3 body recombination}]{\text{collisional ionization}} X(z+1) + 2e \qquad \text{2.80a}$$

$$X_l + e \xrightleftharpoons[\text{collisional deexcitation}]{\text{collisional excitation}} X_u + e \qquad \text{2.80b}$$

$$X^{**}(z) + e \xrightleftharpoons[\text{electron capture}]{\text{autoionization}} X^*(z+1) + 2e \qquad \text{2.80c}$$

Radiative processes:

$$X(z+1) + e \xrightleftharpoons[\text{photoionization}]{\text{radiative recombination}} X(z) + h\nu \qquad \text{2.80d}$$

$$X_u \xrightleftharpoons[\text{photoexcitation}]{\text{radiative decay}} X_l + h\nu \qquad \text{2.80e}$$

$$X(z+1) + e + h\nu \xrightarrow{\text{stimulated recombination}} X(z) + 2h\nu \qquad \text{2.80f}$$
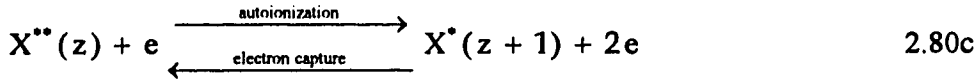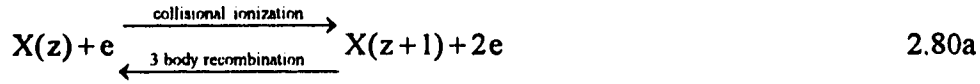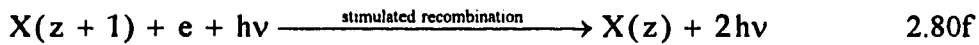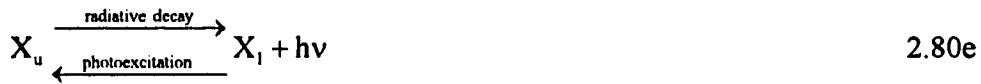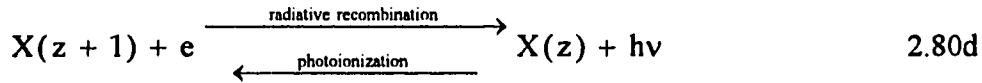
Here the terms in parentheses denote the ionization stage of species X, the subscripts u and l denote the upper and lower states of bound-bound transitions, and the asterisk and double asterisk denote respectively excited and doubly-excited states.

A significant body of work pertaining to the calculation of collisional and radiative rates predates laser-plasma physics, since the topic has long been of interest to other fields, notably astrophysics. A brief summary of the rates follows. More detailed discussions with references may be found in Colombant and Tonon, (1973); Lee (1985); and Eidmann (1989).

Collisional ionization (2.80a) rates have been investigated by Lotz (1967;1968;1969) and may be expressed as

$$R_{CI} = 2.97 \times 10^{-6} \frac{\xi E_1 (E_{ion}/T_e)}{(E_{ion}/eV)(T_e/eV)^{1/2}} \quad \frac{cm^3}{s} \qquad \text{2.81}$$

36

where E_{ion} is the ionization potential from the bound state, ξ is the number of electrons in the outer shell of the ionizing species and E_1 the exponential integral of the first kind.

The collisional excitation (2.76b) rate for hydrogenic ions has the form (Van Regemorter, 1962)

$$R_{CE} = 2.50 \times 10^{-5} \frac{\exp[-E_{ul}/T_e] f_{lu}}{(E_{ul}/eV)(T_e/eV)^{1/2}} \quad \frac{cm^3}{s}$$

2.82

where E_{ul} is the energy separation between the levels and f_{ul} the absorption oscillator strengths. The excitation rates for helium- and lithium-like ions exhibit similar functional form with suitable Gaunt factor corrections (Vinogradov et al., 1975; Cochrane and McWhirter, 1983; Lee, op. cit.).

The autoionization process (2.80c) involves doubly-excited states, produced by excitation and electron capture, which are of higher energy than the ground state of the next ionization level. Such states may undergo radiative decay giving rise to satellite lines lying on the long wavelength side of resonance lines and, as such, have attracted attention as a temperature diagnostic (Mewe, 1988). Alternatively, doubly-excited states may decay by autoionization into the ground state of the next ionization level. There is no convenient functional form for the rates but the numerical predictions of various authors (Gabriel, 1972; Vainstein and Safranova 1978) may be used.

The rates for the inverse collisional processes are found through application of the principle of detailed balancing, which states that in the special case of local thermodynamic equilibrium (LTE), the rate of population of a level by process R must be balanced by the rate of depopulation due to the inverse process R^{INV}.

$$n_i R_{ij} = n_j R_{ji}^{INV}$$

2.83

Under LTE conditions the level populations are related by the Boltzmann relation

$$\left(\frac{n_i}{n_j}\right)_{LTE} = \frac{g_i}{g_j}\exp\left[E_{ij}/T_e\right]$$ 2.84

where g_i and g_j are the statistical weights and E_{ij} the energy separation of the levels. A special case of this equation which relates populations of successive ionization stages is the Saha-Boltzmann equation:

$$\left(\frac{n_z}{n_{z+1}}\right)_{LTE} = 1.66\times10^{-22}\left(n_e cm^3\right)\frac{g_z}{g_{z+1}}\frac{\exp\left[E_{ion}/T_e\right]}{\left(T_e/eV\right)^{3/2}}$$ 2.85

Using these relations the inverse rates can be determined:

Three body recombination:

$$R_{3B} = 4.93\times10^{-28}\frac{g_z\xi\,\exp\left[E_{ion}/T_e\right]E_1\left(E_{ion}/T_e\right)}{g_{z+1}E_{ion}\left(T_e/eV\right)^2}\quad\frac{cm^6}{s}$$ 2.86

Collisional deexcitation:

$$R_{CD} = 2.50\times10^{-5}\frac{\left(g_u/g_l\right)f_{lu}}{\left(E_{ul}/eV\right)\left(T_e/eV\right)^{1/2}}\quad\frac{cm^3}{s}$$ 2.87

Electron capture

$$R_{EC} = 1.66\times10^{-22}\frac{g_a\,\exp\left[-E_a/T_e\right]R_{AI}}{g_{gr}\left(T_e/eV\right)^{3/2}}\quad\frac{cm^6}{s}$$ 2.88

where g_a and g_{gr} are the statistical weights of the autoionizing level and initial ground state, E_a is the ionization energy for the autoinizing state, and R_{AI} is the autoionization rate for the inverse process.

Rates involving radiation introduce the additional complication of the radiation field. The radiation field enters the expressions for the radiative rates through the mean intensity $J(\nu)$. This may defined in terms of the specific intensity $I(\nu,\Omega)$, which represents the local energy flux per unit frequency per unit solid angle, as

$$J(\nu) = \int_\Omega I(\nu,\Omega)d\Omega$$ 2.89.

38

In general, this quantity cannot be solved for locally, it requires a self-consistent solution of the radiative transfer equation (discussed below), along with an atomic physics model to account for emission, absorption and scattering. This formidable problem is an ongoing area of research. One method used to approximate radiation effects, and that adopted in the RATION code, is the assumption of a local Planck radiation field of characteristic temperature T_r:

$$J(v) = \frac{2hv^3}{c^2} \frac{1}{\exp[hv/T_r] - 1} \qquad 2.90$$

Turning now to the radiative processes, the radiative recombination rate is given by Spitzer (1948)

$$R_{RR} = 5.20 \times 10^{-14} Z \left(E_{ion}/T_e \right)^{3/2} \exp[E_{ion}/T_e] E_1 \left(E_{ion}/T_e \right) \frac{cm^3}{s} \qquad 2.91$$

where Z is the charge on the initial ion. Seaton (1959) presents an expression for the special case of hydrogenic species. The photoionization rate (Mihalis, 1982) is

$$R_{PI} = \int \alpha_{z,z+1} J(v) \frac{dv}{hv} \qquad 2.92$$

where $\alpha_{z,z+1}$ is the bound-free cross section

$$\alpha_{z,z+1} = 4.12 \times 10^{26} \frac{\left(E_{ion}/eV \right)^{5/2}}{Z^5 (v \, sec)^3} \, cm^2 \qquad 2.93.$$

A bound state u will undergo radiative decay (2.80e) to a lower state l at the rate given by the Einstein coefficient (Woodgate, 1980)

$$A_{ul} = \frac{2e^2 \omega_{ul}^2}{mc^3} \frac{g_l}{g_u} f_{lu} = \frac{6.65 \times 10^{15}}{\left(\lambda_{ul}/\overset{\circ}{A} \right)^2} \frac{g_l}{g_u} f_{lu} \, sec^{-1} \qquad 2.94$$

where the statistical weight for a state g_i in terms of its total angular momentum number J is 2J+1. Oscillator strengths for hydrogen-like, helium-like and lithium-like

ions have been tabulated by several investigators (see Lee, op. cit.). The inverse process of photoexcitation proceeds according to

$$R_{PE} = \int \alpha_{lu} J(v) \frac{dv}{hv}$$ 2.95

$$\alpha_{lu} = \frac{\pi e^2}{mc} f_{lu} \phi(v)$$ 2.96

where $\phi(v)$ is the normalized line profile function for the transition. The stimulated recombination rate (2.80f) is given by

$$R_{SR} = \left(\frac{n_z}{n_{z+1}}\right)_{LTE} \int \alpha_{z,z+1} \left(J(v) + \frac{2hv^3}{c^2}\right) \exp[-hv/T_e] \frac{dv}{hv}$$ 2.97

To summarize the foregoing discussion, the characteristics of x-ray emission from the plasma are determined by the relative populations of the atomic states existing in the plasma. These are in turn functions of the local electron temperature and density of the plasma, and therefore provide a means of measuring local state parameters. To utilize x-rays as a diagnostic, however, we must consider the emission, absorption and transport of radiation within and away from the plasma.

The radiation transport equation may be derived from a photon distribution function in a manner analogous to that used to arrive at the Boltzmann equation (2.20) for massive particles (Pomraning, 1973). The photon distribution function is a function of 7 variables: the spatial coordinate vector r, the unit vector Ω (or equivalently the angular variables $[\mu=\cos\theta,\phi]$) which specify the direction of propagation of the photons, the photon frequency v, and the time coordinate t. The time evolution of the system is described by the equation

$$\frac{df(r,\Omega,v,t)}{dt} = \chi(r,\Omega,v,t)$$ 2.98

The right hand side of (2.98) is a source term which represents the emission, absorption and scattering of photons, i.e., the local interaction of the radiation with matter. The left hand side of (2.98) when written explicitly becomes

$$\frac{df(r, \mu, \phi, \nu, t)}{dt} = \left(\dot{x} \frac{\partial}{\partial x} + \dot{y} \frac{\partial}{\partial y} + \dot{z} \frac{\partial}{\partial z} + \dot{\mu} \frac{\partial}{\partial \mu} + \dot{\phi} \frac{\partial}{\partial \phi} + \dot{\nu} \frac{\partial}{\partial \nu} \right) f$$

2.99

The time derivatives $\dot{x}, \dot{y}, \dot{z}$ represent the x-component of the photon velocity, i.e

$$\dot{x} = c\Omega_x, \quad \dot{y} = c\Omega_y, \quad \dot{z} = c\Omega_z \qquad 2.100$$

The time derivatives $\dot{\nu}, \dot{\mu}, \dot{\phi}$ are non-zero when the refractive nature of the medium must be taken into account. In such a case the photons will experience a shift in frequency as they propagate through the medium. For the energies of interest in this study, these effects are negligible and the corresponding terms may be dropped.

The source term may be divided into emission, absorption, and scattering terms. The introduction of photon scattering into the equation considerably complicates the transport problem, particularly when the scattering processes are not elastic. Since absorption processes dominate scattering in the soft x-ray region, the scattering term is not considered here. A more thorough treatment may be found in Pomraning (op. cit.). The source term is written in terms of an emissivity function $\varepsilon(r, \nu, t)$ and opacity function $\kappa(r, \nu, t)$

$$\chi(r, \Omega, \nu, t) = \frac{\varepsilon(r, \nu, t)}{h\nu} - c\kappa(r, \nu, t) f(r, \Omega, \nu, t) \qquad 2.101$$

The spatial and temporal dependence of the emissivity and opacity functions enter implicitly through the atomic level populations, which are in turn determined by the local plasma conditions through the rate equations of the previous section.

Using the relation between the specific intensity and the distribution function

$$I(r, \mu, \phi, \nu) = c\, h\nu\, f(r, \mu, \phi, \nu) \qquad 2.102$$

equations (2.99-2.101) combine to give

41

$$\frac{1}{c}\frac{\partial I}{\partial t}+\Omega\cdot\nabla I=\varepsilon-\kappa I=\kappa(S-I)\qquad\qquad 2.103$$

where the source function $S=\varepsilon/\kappa$ has been introduced. From an experimentalist's viewpoint, one is often interested in the transport along a single line of sight, namely, a line through the plasma towards the instrument recording the emission. Since the time scales involved in the propagation of the radiation through the plasma are much less than those which are characteristic of the hydrodynamic evolution of the plasma conditions, one approximates the transport using the time-independent version of (2.103) with a single spatial dependence. The intensity observed along a single ray through an emitting and absorbing region of length ℓ is then (Zeldovich and Raizer, 1966)

$$I_\nu(\ell)=\int_0^\ell \varepsilon(x,\nu)\exp\left[-\int_x^\ell \kappa(x',\nu)dx'\right]dx\qquad\qquad 2.104$$

assuming that no intensity is entrant at the boundary point x=0. If the functions have no spatial dependence then (2.104) reduces to the simple form

$$I_\nu=S(\nu)\left(1-e^{-\kappa\ell}\right)\qquad\qquad 2.105$$

The x-ray emission processes may be categorized into bound-bound, free-bound and free-free. The emissivity due to a bound-bound transition (radiative decay) of energy $h\nu$, is

$$\varepsilon_{\nu(bb)}=n_u\frac{h\nu}{4\pi}A_{ul}\phi(\nu)\qquad\qquad 2.106$$

where $\phi(\nu)$ is the normalized lineshape of the transition, A_{ul} the Einstein coefficient, and n_u the population density of the upper level. The emissivity associated with the free-bound process (radiative recombination) into a level with ionization energy E_{ion} is

$$\varepsilon_{v(fb)} = 1.01 \times 10^{-42} \left(n_e cm^3\right)\left(n_{i+1} cm^3\right) \frac{g_i}{g_{i+1}} \frac{\left(E_{ion}/eV\right)^{5/2} G}{Z\left(T_e/eV\right)^{3/2}} \exp\left[\left(E_{ion} - h\nu\right)/T_e\right] \frac{ergs}{cm^3 sec\, Hz\, sterad}$$

$$h\nu > E_{ion} \qquad\qquad 2.107$$

The free-free process (bremmstrahlung) results in an emissivity of

$$\varepsilon_{v(ff)} = 5.05 \times 10^{-41} \frac{\left(n_e cm^3\right)}{\left(T_e/eV\right)^{1/2}} \sum_i z_i \left(n_i cm^3\right) \exp\left[-h\nu/T_e\right] \frac{ergs}{cm^3 sec\, Hz\, sterad} \qquad 2.108$$

The opacities associated with these emission processes are

$$\kappa_{v(bb)} = n_l \frac{\pi e^2}{mc}\left(1 - \frac{n_u g_l}{n_l g_u}\right) f_{lu} \phi(\nu)\; cm^{-1} \qquad\qquad 2.109$$

$$\kappa_{v(fb)} = 4.13 \times 10^{26} \frac{\left(n_i cm^3\right)\left(E_{ion}/eV\right)^{5/2} G}{Z_i \left(\nu\, sec\right)^3}\left[1 - 1.66 \times 10^{22} \frac{n_{i+1} g_i \left(n_e cm^3\right)}{n_i g_{i+1}\left(T_e/eV\right)^{3/2}} \exp\left[\left(E_{ion} - h\nu\right)/T_e\right]\right] cm^{-1}$$

$$h\nu > E_{ion} \qquad 2.110$$

$$\kappa_{v(ff)} = 3.43 \times 10^6 \frac{n_e cm^3}{\left(T_e/eV\right)^{1/2}} \sum_i \frac{\left(n_i cm^3\right) z_i^2}{\left(\nu\, sec\right)^3}\left(1 - \exp\left[-h\nu/T_e\right]\right) cm^{-1} \qquad 2.111.$$

Here G is the Gaunt factor, and the other terms take on the meanings previously defined.

We conclude this section with a specific example pertinent to the experiments. We consider the most prominent sodium and aluminum transitions recorded by the x-ray spectrometers, summarized in the table following. The population levels for the upper and lower states of these transitions predicted by RATION are shown in Figure 2.2. The electron density assumed in the calculation used for both graphs was 10^{21} cm^{-3}. In Figure 2.3 the bound-bound opacities for the same lines are presented for representative temperatures. The top graph shows the opacities of the K-shell lines of sodium and aluminum as a function of electron density for a 600 eV plasma. The

opacity of the lithium-like aluminum transitions at temperatures of 70 eV and 600 eV is presented in the lower graph. The strong temperature dependence evident in the lower graph is due primarily to the marked shift in relative populations of the lithium, helium and hydrogen-like species as evident in Figure 2.2.

Calculations of the sort used for these graphs will enter in the analysis of the x-ray spectra obtained during the experiments.

TABLE 2.5 Prominent Line Transitions of Sodium and Aluminum				
ion species	configuration	$\lambda\left(\overset{\circ}{A}\right)$	terms	$A_{ul}\left(s^{-1}\right)$
Na^{9+}	$1s^2-1s2p$	11.0027	$g^1S-^1P^0$	1.35×10^{13}
Na^{10+}	$1s-2p$	10.02(3|9)	$g^2S-^2P^0$	9.59×10^{12}
Al^{11+}	$1s^2-1s2p$	7.7571	$g^1S-^1P^0$	2.76×10^{13}
Al^{12+}	$1s-2p$	7.17(1|6)	$g^2S-^2P^0$	1.80×10^{13}
Al^{10+}	$1s^22s-1s^23p$	48.(297|338)	$g^2S-^2P^0$	5.67×10^{11}
Al^{10+}	$1s^22p-1s^23d$	52.(299|446)	$^2P^0-^2D$	9.78×10^{11}
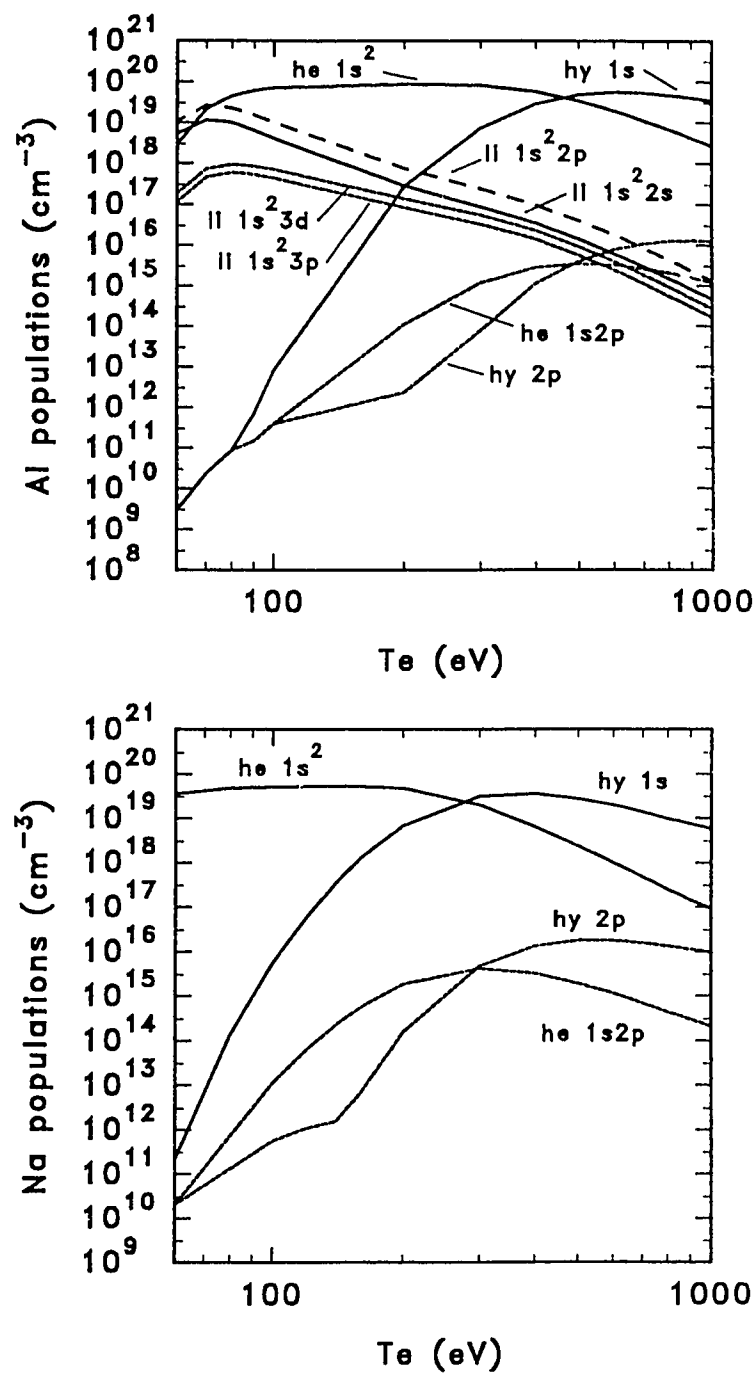
Figure 2.2. RATION predictions for the population densities of selected states as a function of electron temperature for an electron density of 10^{21} cm^{-3}.
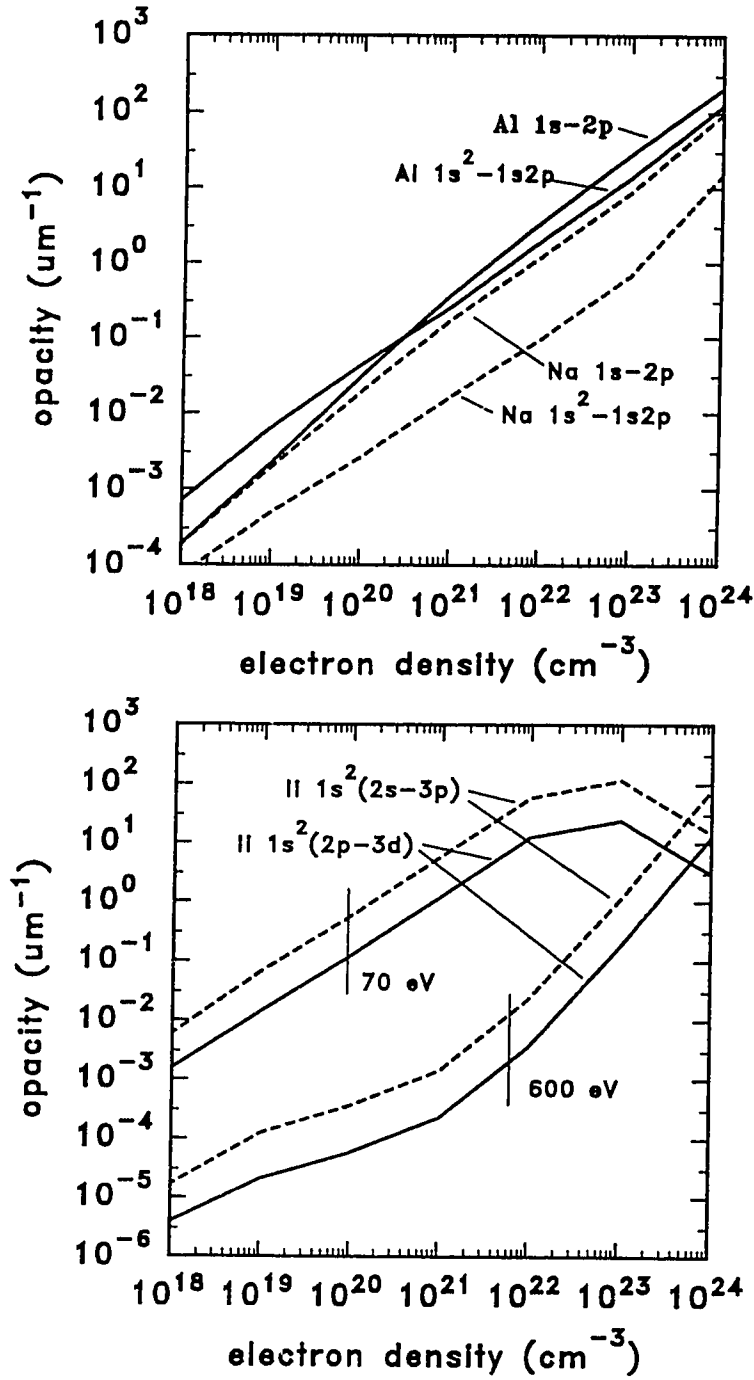
Figure 2.3. Top: RATION predictions for the bound-bound opacities of the dominant K-shell transitions of Al^{11+}, Al^{12+}, Na^{9+}, Na^{10+} ions as a function of electron density for a 600 eV plasma. Bottom: bound-bound opacities for the dominant Al^{10+} lines for a 70 eV and 600 eV plasma.

3. Lateral Energy Transport Mechanisms

In this chapter a brief review of lateral transport mechanisms and previous studies related to them is presented in order to place the present study in context. We begin with some very general comments about the nature of the problem.

A description of laser plasma interaction is considerably more complicated when one proceeds to the three dimensional situation, and must of necessity involve the use of sophisticated computer codes. The 3D hydrodynamic flow away from the focal spot has been characterized by Pert (1989) under the assumption that flow at the target is planar. Quite generally one may expect the plasma expansion to become three dimensional after a time $t=D_{spot}/C_s$, where the D_{spot} is the laser spot size and C_s the ion velocity near at the critical surface. If the laser pulse length exceeds this value one cannot expect 1D models to accurately represent the latter stages of the flow.

At the edge of the focal spot the flow will deviate from the planar situation, expanding outwards and along the target surface forming a hot plasma sheath. Due to the high conductivity of the corona, this plasma may heat the substrate outside the main focus. The extent of this coupling will depend strongly on the local temperature and density of the plasma, on competing transport mechanisms such as advection, and flux inhibition mechanisms.

The laser may also contribute to heating of the target outside the nominal focal spot. In addition to the possible presence of focused residual ASE light or, for the case of lasers that rely upon frequency upconversion, residual first harmonic light, the

47

density profile of the expanding plasma can refract the laser laterally. The propagation is described by the equation

$$\left(\frac{\partial^2}{\partial z^2} + \nabla_\perp^2 + \frac{\omega^2}{c^2} \varepsilon(\mathbf{r}, t) \right) E(\mathbf{r}, t) = \frac{\partial^2}{\partial t^2} E(\mathbf{r}, t) \qquad 3.1$$

where z is the laser axial coordinate and ε the density dependent dielectric function of the plasma (2.10).

Thermal Smoothing. Measurements from the Rear Sides of Targets.

One lateral energy transport issue which has attracted considerable interest is the thermal smoothing of ablation non-uniformities due to lateral heat transport in the supercritical zone. It has already been noted in the introductory chapter that the inertial confinement scheme for laser fusion imposes stringent requirements on the uniformity of coupling between the target and driver. Here the quantity of interest is the ablation pressure or equivalently the ablation temperature. A first approximation in assessing the contribution of this process is the cloudy day model (Brueckner and Jorna, 1974; Gardner and Bodner, 1981) in which the steady state thermal transport equation

$$\nabla \bullet \kappa \nabla T = 0 \qquad 3.2$$

is solved over a semi-infinite plane (x>0) with a boundary condition periodic in y. The periodic variations in the y direction are damped along the x direction according to the decay of the lowest spatial mode $\exp[-kx]$, where $k=2\pi/L$ is the wave number of the spatial modulation at the boundary. By extension of this model, lateral thermal perturbations along the critical layer of an ablating target may be expected to decay to the ablation front by a factor $\exp[-kD]$ where D is the standoff distance.

Manheimer, Colombant, and Gardner (1982) presented an improved model in which the hydrodynamic equations were solved self consistently under the assumption that all variables exhibited the x dependence predicted by the 1D steady state CJ model outlined in chapter 2, plus small lateral perturbations proportional to $\exp[-iky]$. In such a model, the laterally propagating pressure perturbations enhance the damping factor, which is predicted to be $\exp[-1.34kD]$. To take a specific numerical example, if we demand the thermal perturbations to be damped by a factor of $1/100$, the cloudy day and Manheimer models require minimum values of D/L of 0.73 and 0.55 respectively.

Experimental studies of thermal smoothing have typically involved measurement of the rear side of planar foils. In order to create the non-uniform irradiation conditions needed to assess the smoothing mechanism, opaque/neutral density strips or optical wedges were inserted into the beam path. The earliest research of this type was performed by Obenschain and co-workers (1980; 1981) using 1.05 μm light at intensities to 10^{14} W/cm^2 and pulse lengths of 3-4 ns. By using Doppler shift or impact foil techniques, the velocity non uniformity of planar foils was seen to decrease as the laser intensity increased, indicating that significant lateral smoothing was occurring. It was reported that for an intensity of 1.5×10^{13} W/cm^2, the effect of spatial modulations of period 140 μm were nearly eliminated. Cole et al. (1982a; 1982b) used X-ray shadography to compare lateral images of thin ablating CH targets under 1.05 μm and 0.53 μm radiation. A significant reduction in the smoothing was observed in the case of the shorter wavelength. A similar experiment performed with 0.35 μm light achieved qualitatively similar results (Bocher et al., 1984). In addition, the use of high Z layers coated onto low Z substrates improved the uniformity of the foil acceleration. This effect was attributed to the transport of x-ray emission from the high Z layer. The decreased smoothing with shorter wavelengths is

expected since the standoff distance D exhibits wavelength scaling. For example, in the 1D steady state model the scaling implied by (2.53), (2.54), and (2.58) is

$$D \propto I_{abs}^{4/3} \lambda^{14/3} \qquad\qquad 3.3.$$

More recent smoothing experiments have relied on time resolved measurements of the optical emission due to the breakout of the ablatively driven shock from the rear side $\cdots$ illuminated by 0.53 μm light (Shepard and Campbell, 1989; Kado $\cdots$ $\cdots$ both experiments the rear side of the target foils were re-imaged $\cdots$ $\cdots$ $\cdots$ slit of an optical streak camera. The principle of these measurements relies on the relation between the shock speed and ablation pressure (Zeldovich and Raizer, 1966)

$$v_{sh}^2 = \frac{P_{abl}}{\rho_+ \left(1 - \rho_+/\rho_-\right)} \qquad\qquad 3.4$$

where the subscripts + and - again denote conditions ahead and behind the shock front. For strong shocks the ratio ρ_+/ρ_- is approximately constant. Thus if a pressure non-uniformity ΔP exists at the ablation front

$$\frac{\Delta P}{P} = 2 \frac{\Delta v_{sh}}{\overline{v}_{sh}} \qquad\qquad 3.5.$$

The quantity Δv_{sh} may be obtained from the thickness of the foil and the interval between the shock breakout times under different ablation conditions. Similarly the shock velocity may be determined by measuring the transit time of the shock across targets of various thickness under similar irradiation conditions. Using pressure scaling laws of the form $P \propto I^\alpha$ from 1D models, one can define a smoothing factor Γ as the ratio of the measured pressure differences to those expected without any smoothing

$$\Gamma = \left(\frac{\Delta P}{P}\right)_{exp} \bigg/ \left(\frac{\Delta P}{P}\right)_{1D} = \frac{\Delta v_{sh}}{\overline{v}_{sh}} \frac{I_{max}^\alpha + I_{min}^\alpha}{I_{max}^\alpha - I_{min}^\alpha} \qquad\qquad 3.6.$$

Shepard and Campbell (op. cit.) used a novel beam/target configuration in which a high intensity focus of 40 μm diameter was positioned within a lower intensity focus of 250 μm diameter. Significant smoothing was reported for intensities above 5×10^{13} W/cm^2. The highest spatial resolution (~1μm) was achieved using an ultraviolet Schwarzschild microscope (Kado et al., op. cit.). Smoothing factors calculated for several target shots taken over a laser intensity range $2-8 \times 10^{13}$ W/cm^2 all fell between values predicted by the cloudy day model and the Manheimer model.

Measurements from the Ablation Sides of Targets.

The extent to which rear side measurements accurately reflect the conditions at the ablation surface have been questioned. Two dimensional simulations of double foil experiments indicate that velocity modulations of the ablation foils undergo additional smoothing as they coast to the impact foils (Cole, 1982b). Furthermore, the shock fronts propagating through ablating foils will exhibit some 2D spreading. For this reason, corresponding studies of the front side of ablating targets are of interest. One such study performed at 0.27 μm wavelengths, based on soft x-ray pinhole images (hv > 1.5 keV) from CH overcoated aluminum substrates (Matsushima, 1985), revealed no lateral smoothing of the ablation front under modulated laser intensity.

The idealized steady state situation assumed in the cloudy day and Manheimer models may not be realized in many laser target experiments since the establishment of a quasi-stationary conduction zone requires a finite amount of time. During this early phase of the interaction, known as the transient regime there may be little lateral transport even over short scale lengths. Recent numerical simulations suggest that even with beams smoothed by induced spatial incoherence techniques, early shocks

generated in the transient phase create persistent density perturbations which seed Rayleigh Taylor instabilities during the remainder of the laser pulse (M. H. Emery et al., 1991). Recent measurements performed by Desselberger and co workers with 0.53 μm laser radiation tend to confirm these predictions (1992). In this work, high resolution 2D x-ray images (hv~98 eV) of medium and high Z targets recorded using a multilayer mirror show persistent non uniformities formed during the transient phase. The features were found to be smoothed if a preformed plasma was produced before the onset of the main pulse. The reason for the persistence of these structures if no preformed plasma was present is as yet unclear.

A study done by Mead et al. (1984) with 1.06 and 0.35 μm wavelengths on beryllium coated aluminum planar substrates was partially aimed at quantifying lateral transport effects. The focal region of the target (250 μm dia.) was surrounded by titanium shields of inner diameter 340 μm which provided a high efficiency x-ray emitter. A four channel x-ray microscope was unable to detect significant lightup from the shield even in the sub keV region for the case of 0.35 μm irradiation. For the case of longer wavelength x-rays, images were consistent with a small amount of lateral heating of the target. Some lateral inhibition mechanism was required to account for the results at 1.06 μm.

In constrast to the Mead study, xuv images recorded from aluminum planar targets under tight focus (60 μm dia.), high intensity ($0.5\text{-}1\times10^{15}$ W/cm^2) irradiation conditions exhibited emission features along the target surface at wavelengths of 155 Å and 187 Å which extended to diameters of 350 μm (Benattar and Godard, 1984; 1986). These features were seen under 1.05 , 0.53 , and 0.27 μm irradiation. Lateral heating of the substrate by suprathermal electrons was postulated as a cause of these features.

An interesting experiment performed by Key and co-workers reported significant lateral transport at high intensities and longer wavelengths. The study was compiled over a wide range of intensities (10^{13} W/cm^2 - 2×10^{15} W/cm^2) for the laser wavelengths of 1.06, 0.53, and 0.35 μm and pulse lengths of 0.6 -1.5 ns. An array of Faraday cups were used to record the angular and temporal ion emission from the ablation region. Estimates of the integrated kinetic energy recorded indicated that most of the absorbed energy of the laser was converted to kinetic energy of expansion and exhibited only weak nonlinear dependence on absorbed energy. However, as the absorbed intensity increased, time-resolved x-ray measurements indicated that the fraction of ions recovered from the nominal focal spot area decreased rapidly. These two relationships were interpreted as evidence for an area of ablation lying outside the focus, possibly due to an extended heat conducting zone of plasma outside the laser focus. The lateral transport exhibited a strong wavelength dependence of $\lambda^{2.5}$ between 1.06 and 0.53 μm

The Role of Magnetic Fields; Hot Electron Transport

Faraday rotation measurements have revealed the presence of strong toroidal magnetic fields around the edge of the laser focus in target experiments (Stamper and Ripin, 1975; Stamper et al., 1978; Raven et al., 1978; Raven et al. 1979; Burgess et al., 1985). Such structures have been used to explain the 2 peak structure commonly recorded by ion diagnostics (S. R. Goldman and R. F. Schmalz, 1987). The presence of B fields, which may reach megagauss strengths under some conditions, can strongly inhibit thermal transport.

Braginskii (1965) solved the Fokker Planck equation with the inclusion of the B field under the assumption that a single correction to the distribution function f[1] was sufficient. By substitution of f[1] into the expressions for the various flux terms the transport equations were closed self-consistently. Inclusion of the B field in the modeling of laser plasma interactions requires the addition of the magneto-hydrodynamic equation into the system (Nishiguchi, 1984a)

$$\frac{\partial B}{\partial t} = \nabla \times (v \times B) + \frac{c}{e} \nabla \times \frac{\nabla P_e}{n_e} - \frac{c}{4\pi e} \nabla \times \left[\frac{(\nabla \times B) \times B}{n_e}\right] - \frac{c}{e} \nabla \times \left[\frac{R_T + R_U}{n_e}\right] \qquad 3.7$$

Here v is the fluid velocity, B the magnetic field, and R_T and R_U are the thermal and frictional forces. (The fourth term is considerably complicated and will not be written out in detail here).

The presence of the B field in effect creates three local thermal conductivities which act along different directions:

$$q = -\kappa_{\parallel} \nabla_{\parallel} T_e - \kappa_{\perp} \nabla_{\perp} T_e - \kappa_{\otimes} \left(\hat{B} \times \nabla T_e\right) \qquad 3.8.$$

The expressions for the conductivities are

$$\kappa_{\parallel} = \frac{n_e \tau_e T_e}{m_e} \frac{\gamma_0'}{\delta_0} \qquad 3.9$$

$$\kappa_{\perp} = \frac{n_e \tau_e T_e}{m_e} \frac{\gamma_0' + \gamma_1'(\omega_e \tau_e)^2}{\delta_0 + \delta_1'(\omega_e \tau_e)^2 + (\omega_e \tau_e)^4} \qquad 3.10$$

$$\kappa_{\otimes} = \frac{n_e \tau_e T_e}{m_e} \frac{\omega_e \tau_e \left(\gamma_0'' + \gamma_1''(\omega_e \tau_e)^2\right)}{\delta_0 + \delta_1'(\omega_e \tau_e)^2 + (\omega_e \tau_e)^4} \qquad 3.11$$

where ω_e is the Lamour frequency

$$\omega_e = \frac{qB}{cm_e} = 1.77 \times 10^7 \left(\frac{B}{gauss}\right) s^{-1} \qquad 3.12.$$

As the magnitude of the magnetic field tends to zero, expression (2.66) is recovered from (3.9)- (3.11). The Braginskii coefficients δ, γ are functions of the atomic number Z. Nishiguchi (1984b) obtained polynomial fits to the coefficients for arbitrary Z by using the incomplete tabulations presented by Braginskii (op. cit.):

$$\xi_{Brag.} = \xi_\infty + a/Z + b/Z^2 + c/Z^3 + d/Z^4 \qquad 3.13.$$

The Braginskii coefficients are typically of order unity so that the flux inhibition is determined mainly by the parameter $\omega_e \tau_e$. From (3.12) and (2.69) we may write

$$\omega_e \tau_e = \frac{6.1 \times 10^{12} \left(T_e / eV \right)^{3/2} \left(B / gauss \right)}{\ln \Lambda \bar{Z} \left(n_e cm^3 \right)} \qquad 3.14$$

Taking as an example a fully ionized 500 eV CH plasma at density $n_{crit}/10$, $\omega_e \tau_e = 6.2(B/Mgauss)$, fields on the order of a megaguass will strongly inhibit transport in the corona.

Several mechanisms have been postulated to explain the growth and saturation of magnetic fields in LPPs. One of the most important mechanisms is the $\nabla n \otimes \nabla T$ effect (Max, 1980), which may be identified with the second term in (3.7). The effect arises from the presence of high electron pressure gradients in the plasma, which create a charge separation field. Such fields have been postulated to account for optical shadowgraphy observations of electrical breakdown in plexiglass targets during the initial phase of shock wave propagation (Amirinov et al., 1985). The field may be written in terms of temperature and density gradients

$$E = -\frac{1}{en_e} \nabla P_e = -\frac{k_B}{e} \left(\nabla T_e + \frac{T_e}{n_e} \nabla n_e \right) \qquad 3.15.$$

The source term of interest follows from the Maxwell equation (2.6d)

$$\frac{\partial B}{\partial t} = -c\nabla x E = \frac{ck_B}{e} \left(\nabla \ln n_e x \nabla T_e \right) \qquad 3.16.$$

55

Saturation in the growth of the field will be due to the other terms in 3.7, notably the convective term $\nabla \times (v \times B)$. Conditions at the edge of the laser spot are ideal for the manifestation of this effect, featuring high density gradients toward and normal to the target and high temperature gradients inward and parallel to the target.

Other mechanism have been proposed as candidates for large scale B field generation, including the ejection of hot electrons generated by resonance absorption, and an anisotropic electron pressure. In addition to these mechanisms, thermal and Weibel instabilities and laser filamentation may create small scale magnetic field structures (see Max, op. cit., and references therein).

Besides their effect on the local transport coefficients, the B-fields have a marked effect on the trajectories of energetic charged particles. Hot electrons predominantly emitted in the corona through resonance absorption or parametric processes, and accelerated predominantly down the coronal density gradient, can be deflected by the B-fields and redeposit their energy over a radius several mm beyond that of the focal spot. This is known as the fountain effect and has been reported by many investigators (Yates et al. 1982; Shiraga et al., 1982; Villeneuve et al., 1983; Terai et al., 1985). An additional mechanism which may account for such observations involves the existence of a polarized fast ion sheath which expands rapidly beyond the focal region and transports hot electron return currents to the target surface and back to the focal area (Jaanimagi et al, 1981). A representative study was done on tight focus ($\sim 120 \mu m$ dia.) CO_2 LPPs by Keiffer and co-workers (1983). They measured the angular distribution of the high energy spectrum from high Z tracer discs bombarded by hot electrons using K-edge filtered diagnotics. The tracer discs were of various diameters in order to characterize the lateral features and extent of the emission. The essential results of these investigations were: 1) For the relatively long wavelength of 10.6 μm, up to 9% of the incident laser energy may be re-transported in this fashion; 2) Evidence of hot

electron transport can be seen up to several mm away from the focal spot; 3) The energy of electrons and the angle of incidence with which they collide with the target both increase as a function of radius; 4) Lower intensity ($\sim 5 \times 10^{12}$ W/cm^2) x-ray emission features are consistent with a normally incident distribution of electrons. At higher intensities the spectral and angular distributions agree with that expected from a semi-isotropic distribution of incident electrons; 5) Observations (3) and (4) can be explained through the increased production of hot electrons with higher intensities along with a B-field structure which modifies the trajectories of these electrons, as predicted by theoretical models (Forslund and Brackbill, 1982, Fabbro and Mora, 1982).

In general the contribution of energetic particles to the non-local transport may be expected to decrease with the laser wavelength, since inverse bremsstrahlung absorption becomes increasingly predominant over resonance absorption, and the intensity thresholds for parametric processes higher as the laser wavelength decreases.

Non-Local Thermal Transport and Radiation Transport

The issue of non-local electron thermal transport has already been touched upon in the previous chapter. Due to the complexity of the problem and the considerable computational demands involved, most of the work in this area has relied on 1D models. However, an interesting letter presented by Epperlein, Rickard, and Bell (1988) employed a 2D Fokker Planck code to compare the predictions of the non-local algorithm with that of classical flux limited fluid code. An example was presented for a simulation representing non-uniformly irradiated low Z target. The results indicated that although average temperatures predicted by the two codes

compared closely, the fluid codes may severely overestimate the degree of lateral smoothing for distances less than $80\lambda_{fmp}$. Using equation (2.67) we may write

$$\lambda_{fmp}^{ee} = \left(\frac{T_e}{m_e}\right)^{1/2} \tau_e = 1.44 \times 10^{17} \frac{(T_e/eV)^2}{\ln \Lambda \bar{Z}(n_e cm^3)} \ \mu m \qquad 3.17$$

Taking as an example a fully ionized CH plama at critical density with a nominal temperature of 500 eV, we find $\lambda_{fmp} = 0.39\mu m$ or $80\lambda_{fmp} = 31\mu m$, which is within the range of interest in this study.

A significant fraction of the energy in LPPs can be converted into x-rays and transported to the colder regions of the target. The x-ray conversion efficiency generally increases with the atomic number of the target and decreases with laser wavelength (Mochizuki et al., 1986; Kodama et al., 1986; Popil et al., 1987; Kodama 1990). For 0.53 μm radiation, one may expect approximate conversion efficiencies of 5%, 10% and 50% respectively for CH, Al and Au plasmas for nanosecond range pulse lengths.

The x-ray opacity of materials also increases with atomic number. This has the effect that, for high Z targets, absorption and re-emission of radiation by material immediately surrounding the high temperature plasma may redistribute energy laterally. X-ray images of high Z plasmas taken in different x-ray bands exhibit different lateral extents (Chaker et al., 1989). This effect has been postulated to explain discrepancies between numerically generated non LTE gold spectra and experimentally obtained spectra (Kiyokawa et al., 1983; Nishimura et al., 1991).

For the majority of targets used in this experiment the x-ray conversion should not exceed 10%, which sets an upper bound on the contribution of x-rays to the lateral heating. The hot, optically thin expanding corona will provide the source for most of this emission. Although the peak x-ray emissivity occurs in the dense supercritical conduction zone adjacent to the ablation layer, the aspect ratio of this region and its

relative orientation with respect to the target surface make it an unlikely candidate for

coupling with the colder regions outside the laser focus.

.

4. Experimental Method and Instrumentation

Outline of the Experiments

The experiments were performed using the GEKKO IV Nd-glass laser and target facilities at the Institute of Laser Engineering, Osaka, Japan. The objective of the study was to assess the extent to which the energy deposited by a laser onto a solid target is transported laterally to regions outside the laser focus. In order to accomplish this objective, the spatial distribution of the target x-ray emission was recorded over selected wavelength bands. The chief diagnostics employed for this purpose included a Bragg crystal spectrometer, an XUV grazing incidence spectrometer, and an x-ray pinhole camera. The spectrometers provided time-integrated, spectrally-resolved images over the spectral ranges 5 -12 $\overset{o}{A}$ and 50 - 200 $\overset{o}{A}$. All three instruments used x-ray-sensitive film as the recording medium.

The majority of the data was recorded from massive planar CH foils. By the term 'massive', we mean that the target is several times thicker than the final ablation depth reached by the laser. In order to record the x-ray emission originating from specific locations of the interaction area, the technique of tracer layers was adopted (Herbst, 1982). The tracer layers were principally composed of aluminum (Al) or sodium flouride (NaF)., A limited number of targets with gold tracers were also tried. The tracer materials Al and NaF were chosen because the highly-ionized species (Al^{11+}, Al^{12+}, Na^{9+}, Na^{10+}) emit K shell lines within the spectral range of the crystal spectrometer, and because both materials could be easily vacuum-deposited onto CH

substrates. The tracer layer patterns typically consisted of discs centered around the laser axis or rectangular bars or annuli located outside the laser focus. Typically the tracers were buried under an additional layer of CH. The crystal spectrometer and pinhole instrument were filtered with beryllium foil which effectively attenuated most of the x-ray emission from the CH substrates. In this manner it was possible to record the time-integrated emission history of material originating from differing locations of the laser/target interaction area. The presence or absence of tracer signature emission was then used to infer the conditions prevailing at various locations in the target. A second advantage of using tracer layers is that opacity effects due to self absorption of x-ray radiation are reduced, since a thin emitting layer presents a smaller areal density along the line of sight of a recording diagnostic than would a solid target of tracer material under the same irradiation conditions.

The targets were fabricated in the pellet factory at ILE. With few exceptions, the target foils were supported by M2 (inner diameter 2 mm) washers which were in turn fixed to 0.9 mm diameter glass stalks. A description of the target fabrication procedure may be found in Appendix 1.

The experiments may be categorized into two groups based on the laser focal conditions. In the first configuration, a nominal spot size of 300 μm was used and intensity modulations along one direction were imposed within this diameter by inserting a set of opaque strips into the laser beam before the focusing lens. In this series of shots the objective was to assess the amount of lateral energy transport between highly-irradiated regions. In the second series of shots the laser focus was tightened to produce the smallest spot and highest intensities available. In this case the objective was to study lateral transport outside the immediate vicinity of a laser spot.
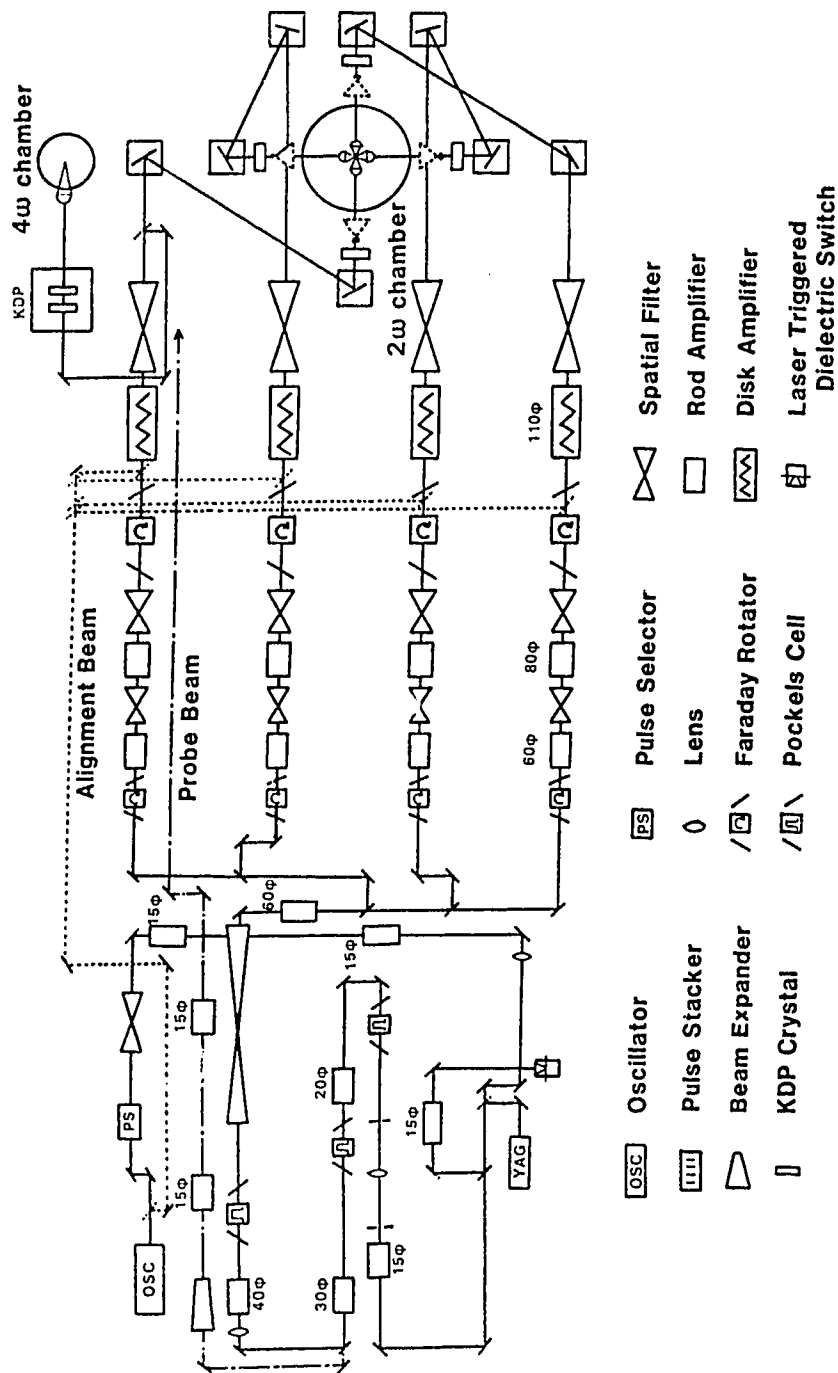
61

Figure 4.1. The GEKKO IV laser system.

The GEKKO IV Laser Facility

The GEKKO IV system has been operational since March 1978, and has undergone several modifications minor since its inception (Kato et. el. 1977; 1978a; 1978b; 1980; 1982). The laser was designed to deliver four terawatt beams of 9.5 cm diameter with low prepulse and ASE levels and a shot to shot stability of better than 10%. The layout of the four beam glass phosphate system is depicted in Figure 4.1. The system consists of a common front end (shown at left in the figure) followed by four main amplifier stages.. The experiments described in the present work were primarily performed using the D chain (the bottom chain shown in the figure).

The essential components of the oscillator and pulse selector are shown in Figure 4.2. The oscillator is an actively mode-locked Q-switched resonator which produces pulse trains of approximately 1 ms in length at a repetition rate of 5 per second. The active medium consists of a neodymium-doped crystalline yttrium lithium flouride (Nd:YLF) rod of length 75 nm and diameter 6 mm. The rod is cut at the Brewster angle to eliminate optical losses, and is pumped by a linear flashlamp with a pulse duration of 400 ms. In order to maximize pumping efficiency, the rod and flashlamp are located at the foci of a gold-plated elliptically shaped cavity. A 2 mm diameter aperture selects a single transverse mode of the oscillator. Mode locking is accomplished by means of an acousto-optic modulator (AOM). The AOM consists of a quartz crystal positioned to Bragg reflect the amplified beam and is driven by a 50 MHz rf driver, and is set to oscillate with a period equal to the round trip time of light in the oscillator cavity (2L/c). Q switching is accomplished by another AOM which is activated 300 ms into the flashlamp pulse. The widths of the individual pulse train component pulses are selectable from within a range of 170 ps - 900 ps Full Width
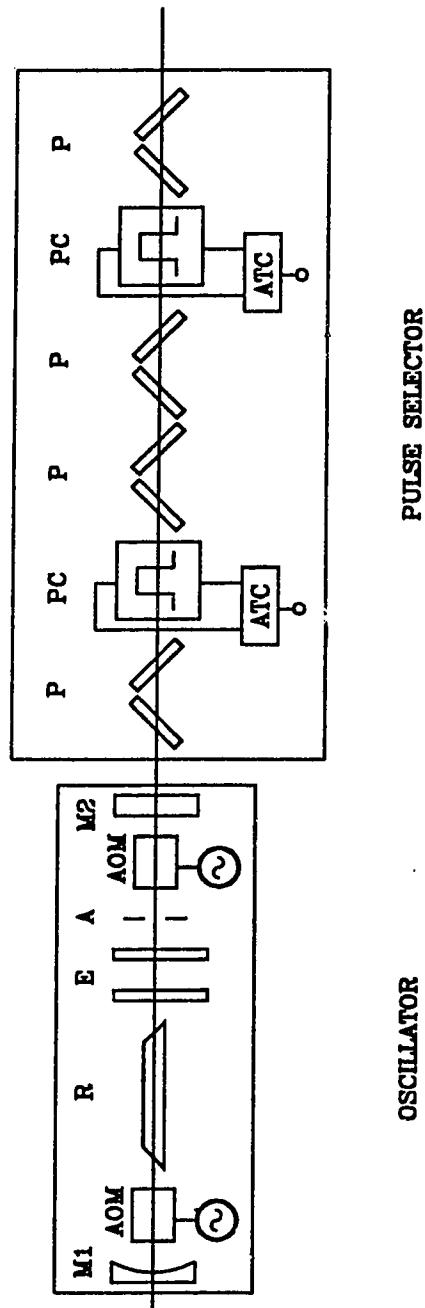
Figure 4.2. The components of the GEKKO IV oscillator and pulse selector. The 100% and 60% reflecting mirrors M1 and M2 define the oscillator cavity. Other components of the systems include the rod (R), etalon (E), aperture (A), acoustic optical modulators (AOM), polarizers (P), Pockels Cells (PC), and avalanche transistor circuits (ATC).

Half Maximum (FWHM) by means of etalons of suitable thickness inserted into the laser cavity. The stability of the output energy of the oscillator has been measured to be better than 5%.

After exiting the oscillator, a single pulse component is selected from the pulse train by two dual crystal Pockels cells used in conjunction with dielectric polarizers. The Pockels cells consist of birefringent crystals whose dielectric properties change when an electric field is placed across them. When not activated, the overall passive attenuation of the selector is better than 10^{-7}. Electrically-triggered avalanche circuits induce fast rise time (ns) pulses which are propagated through two cables to either side of the Pockels cells. By using cable delays a temporally square-shaped voltage pulse across the cells are created, allowing for the selection of a single pulse component near the peak of the pulse train.

After exiting the pulse selector the beam is then amplified and expanded in stages all the way down the remainder of the chain to the final output lens. The amplifier chain consists of a sequence of glass rods of increasing diameter and a final disk amplifier. All amplifiers are pumped by cylindrical arrays of Xe filled linear flashlamps enclosed by elliptically-crenulated sheets of polished aluminum. The disk amplifier features six elliptical glass disks mounted in a staggered configuration at the Brewster angle. The rod amplifiers are sealed within a transparent water jacket through which coolant is circulated after each laser shot. The disk amplifiers are cooled by a nitrogen gas flow.

LHG-7 phosphate glass was chosen as the lasing medium of the amplifiers since it possesses a relatively large cross section for stimulated emission and a relatively weak dependence of the refractive index with temperature. The maximum repetition rate of the laser at full pump settings (approximately 1 hour) is determined by the latter effect, and thus consequently by the thermal conductivity of the glass

which determines the rate of cooling of the glass. Apart from the choice of lasing medium, a number of other features were incorporated into the amplifiers. The disks are anti-reflection coated to suppress parasitic oscillations. The flashlamp assembly and reflectors are positioned for optimum efficiency and uniform pumping. The entire amplifier chain is covered with a dust cover which prevents air currents from inducing non-uniformities in the beam. Finally, regular maintenance overhauls are scheduled in which the flashlamps and windows are inspected and cleaned to ensure optimum uniformity and energy extraction.

Parasitic oscillations and counter-propagating reflections are eliminated by isolating the stages of the system from each other through the use of Pockels cells and Faraday rotators. These components also reduce the ASE propagating through the system. The Pockels cells are triggered by a Laser Triggered Dielectric Switch (LTDS) activated by a fraction of the beam split off from the main beam after the initial stages of the amplification.

The other essential components of the chain are the vacuum spatial filters which are maintained at pressures of 5×10^{-3} torr. By use of the filters, in which the propagating beam is focused through pinholes of typical diameter 200 μm, the beam diameter may be controlled and beam diffraction effects reduced. The effects of ASE, and wave front distortion due to non-uniform pumping are also reduced. Finally the higher spatial frequencies in the beam are eliminated thus smoothing the intensity profile of the output beam.

The final output beam is relayed to the target chamber by two turning mirrors. The intensity profile may be well approximated by a flat-top of diameter 8 cm. The output beam divergence has been previously measured to be $1-2 \times 10^{-4}$ radians, and the linear peak-to peak wave front distortion estimated from interferometric measurements

to be about 1.5λ in the first harmonic. The prepulse levels have also been measured to be less than 5×10^{-7} of the main energy pulse.

Before entering the target chamber the 1.06 μm light is upconverted to 0.53 μm light by propagation through a potassium dihydrogen phosphate (KDP) type II crystal of 1 cm thickness.[1] The crystal is sandwiched between two antireflection coated BK-7 glass windows and a layer of Decalin index matching fluid. The sealed window assembly is mounted in a rotating sleeve to allow adjustment of the crystal orientation for maximum conversion efficiency. A heat absorbing filter is positioned after the KDP crystal to attenuate the residual 1.06 μm light by a factor of approximately 10^{-5}.

The power of frequency-doubled light in terms of the incident power and propagation angle scales as

$$P_{2\omega}(\theta) \propto P_\omega^2 \, \frac{\sin^2(\Delta k\ell/2)}{(\Delta k\ell/2)^2} \qquad 4.1$$

where ℓ is the thickness of the crystal and

$$\Delta k = \frac{\omega}{c}\left(2n_e^{2\omega}(\theta) - n_e^\omega(\theta) - n_o^\omega\right) \qquad 4.2$$

where θ is the angle subtended by the propagation vector and the optical axis of the crystal, and n_e and n_o are the indices of refraction for the ordinary and extraordinary polarizations at the labeled frequencies. Optimum conversion for the KDP type II crystal occurs for the phase matching angle of $59.1°$. In practice conversion efficiencies of 40% may be achieved; however, for the crystal used in these experiments a nominal efficiency of 20% was realized. One important effect of the

---

[1]A detailed discussion on second harmonic generation may be found in (Yariv, 1985). A summary of the basic physical properties of KDP was presented by Craxton et al. (1981).

Figure 4.3. The GEKKO IV target chamber area.

nonlinear dependence of the conversion efficiency is that any intensity non uniformities in the original beam are accentuated by the upconversion process.

Target Chamber and Alignment System

The target chamber is shown in Figure 4.3 and again schematically in Figure 4.4. The chamber is constructed of 12 mm thick non-magnetic stainless steel and has an inner diameter of 110 cm. It may be evacuated down to 10^{-6} torr by a turbomolecular pump of pumping speed 1000 L/sec. The four laser beams originally entered the chamber in a tetrahedral configuration. Presently, only two beam (which are shown at top in Figure 4.4) are available along the original paths. The 2ω radiation is focused to chamber center using 13 cm diameter aspheric lenses of focal length 15 cm. These are mounted on XYZ translation stages in the chamber and vacuum sealed from the outside by antireflection coated glass. Each beam port is equipped with a calorimeter for energy measurements and a beam alignment assembly (described below).

Two target monitors are mounted along orthogonal axes in the equatorial plane of the chamber. Each camera images target center by means of a relaying lens and a microscope objective, and feature low and high magnification settings (40 μm/cm or 250 μm/cm scaling on the visual monitors). Backlighting for the cameras is provided by two halogen lamps filtered in a green bandwidth. The monitors also feature fiducial crosses at the screen centers which are used to define the chamber center reference for both beam and target alignment. Two pairs of display monitors are located in the laser control and near the chamber.

GEKKO IV TARGET CHAMBER
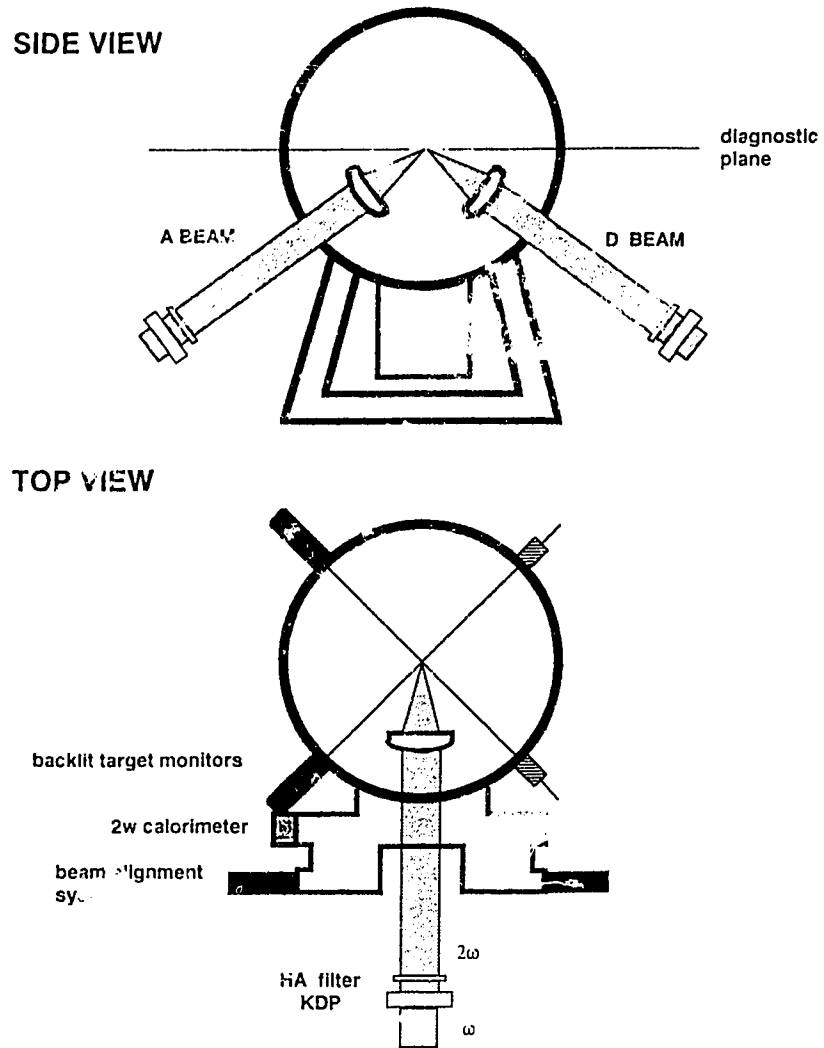
SIDE VIEW

diagnostic
plane

A BEAM   D BEAM

TOP VIEW

backlit target monitors

2w calorimeter

beam alignment
sy.

2ω

HA filter
KDP

ω

Figure 4.4 The GEKKO IV target chamber and beam orientation.

70

All targets are mounted on 0.9 mm diameter glass stalks approximately 3 cm in length. The ablation targets are inserted into mechanical pencil jackets which are in turn inserted into a rotating silo which sits below chamber center above the evacuation port. The silo is mounted on an XYZ translational stage. The targets may be raised to target center, rotated and adjusted to center to an accuracy of 10 μm manually through the use of remote manipulators fed through one of the vacuum flanges. A second target silo is located directly above the chamber. The reusable targets involved in the beam alignment procedure are housed here. They are supported by glass stalks which are in turn inserted into the ends of 880 cm-long metal rods. The rods are housed in the silo and can be lowered and raised by remote control. Stepping motors at the top of the chamber allow XYZ translation of the alignment targets.

The laser operation and diagnostics are performed by remote control in a screen room adjacent to the amplifier bay. The laser diagnostics include measurement of the coolant flow to the amplifiers, the charging status of the laser power supply, the vacuum in the spatial filters, the oscillator output and LTDS signal levels, the flashlamp currents and the energy calorimeters. The main control console is shown in Figure 4.5. The laser operation and the target and lens servomechanisms are also controlled from here; also the images from the various monitors at the chamber are relayed to the console.

The experiments placed rather stringent requirements on the accuracy with which the target and beam had to be positioned. These requirements are met by the GEKKO IV alignment system, which allow both target and beam positions to be set to 10 μm accuracy. The focusing lens is adjusted by remotely controlled servomechanisms which allow independent movement along three axes with a minimum increment of 0.6 μm. The position of the lens along the laser axis is displayed digitally on the control console and can be adjusted in precise increments.

The beam alignment was performed with the chamber under vacuum; in order to retain the pointing accuracy of the beam during experiments, the chamber was kept under vacuum conditions for each set of targets, and the beam alignment procedure repeated between each vacuum cycle.

The beam alignment system is illustrated in Figure 4.6. The beam focusing and alignment system makes use of the back reflection of low intensity laser light from a 500 μm diameter gold-coated steel ball. The beam alignment is accomplished in a series of steps. A low-energy pointing shot is first taken using the full amplifier chain
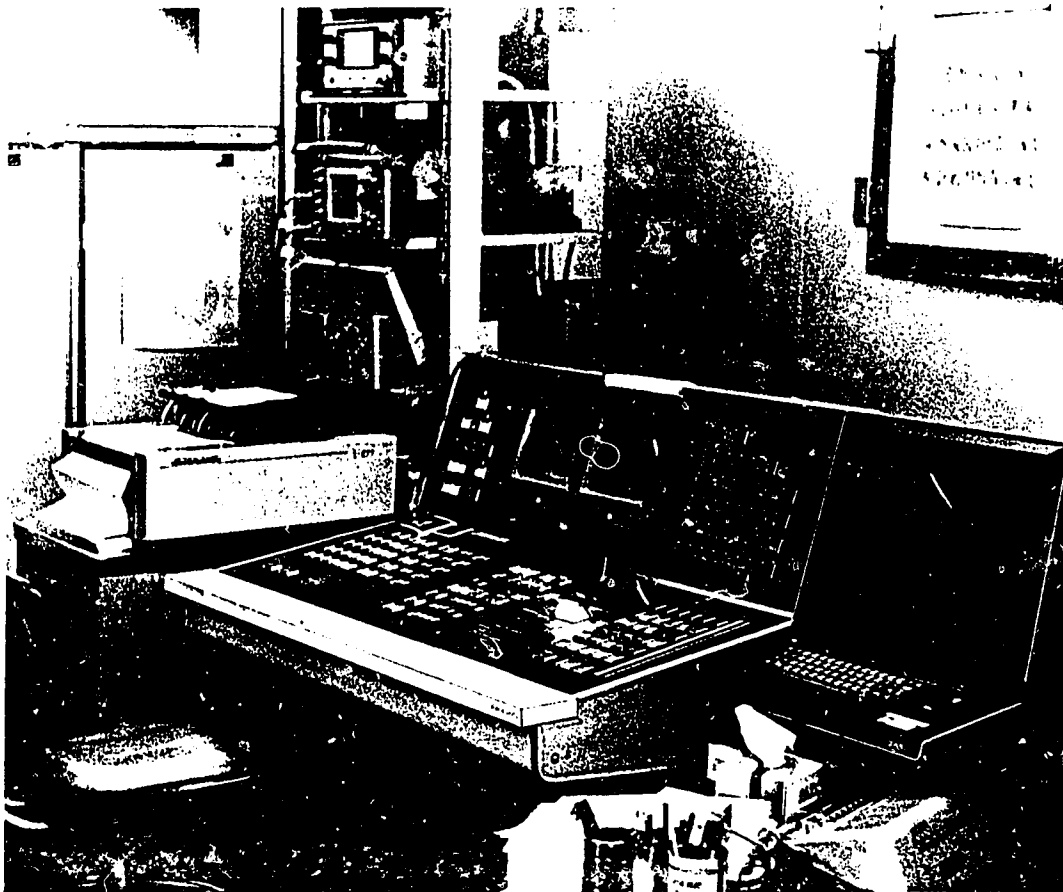
Figure 4.5. The laser control console.

72
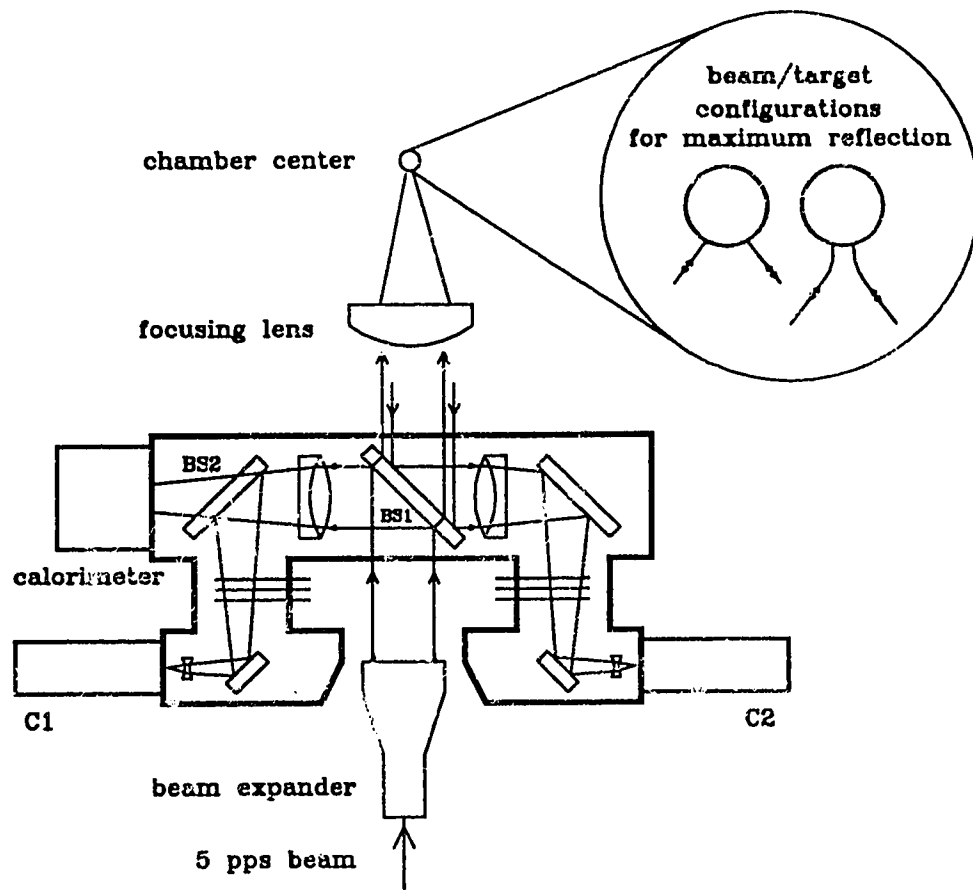
Figure 4.6. The GEKKO IV beam alignment system.

path but without the later amplifiers stages pumping. The 4% beam splitter BS1 redirects a fraction of the light into the left side of the housing where it is focused onto the video camera C1. The position of the beam is noted and marked on the monitor by the operator. Next the 5pps output from the oscillator is diverted from the amplifier path (dashed line in Figure 4.1) and aligned through a pair of apertures which straddle the final disc amplifier. In this manner the 5 pps signal is adjusted to be collinear with the beam path to within 0.1 milliradians. The diameter of the 5 pps beam is widened

by raising a beam expander into the path after the KDP crystal. The orientation of the expander is adjusted until the 5pps image on C1 is coincident with that of the pointing shot. The 5pps beam is now sufficiently collinear with the main beam path to allow accurate alignment.

The beam is next brought to chamber center in the following way. A thin fluorescent paper strip in the shape of an inverted triangle is lowered and positioned to chamber center using the backlit target monitors. The first order focus alignment is achieved by adjusting the lens position until the brightest and tightest spot may be seen on the paper. The paper is now replaced by the reflecting ball. The back reflection from the ball is reflected from S1 to the right side of the housing and sed onto camera C2. As the laser axis coordinate of the focusing lens is adjusted the brightness of the image on camera 2 passes through two 2 maxima corresponding to the configurations illustrated in Figure 4.6. Only if the optical axis of the bean intersects center of the ball do the two maxima image at the same location on C2. Using this criterion, the three coordinates of the lens are adjusted alternately until the beam focus may be brought to target center. A digital display records the position of the lens and allows it to be moved in and out of focus to an accuracy of about 1 micron. After alignment is complete the expander is lowered from the beam path and the oscillator is re-diverted back through the amplifier path.

x-ray pinhole cameras
30 um Be filtering
15 um resolution

spatially-resolving
grazing-incidence
xuv spectrometer

optical
streak
camera

spatially-resolving
x-ray crystal spectrometer
25 um Be filtering
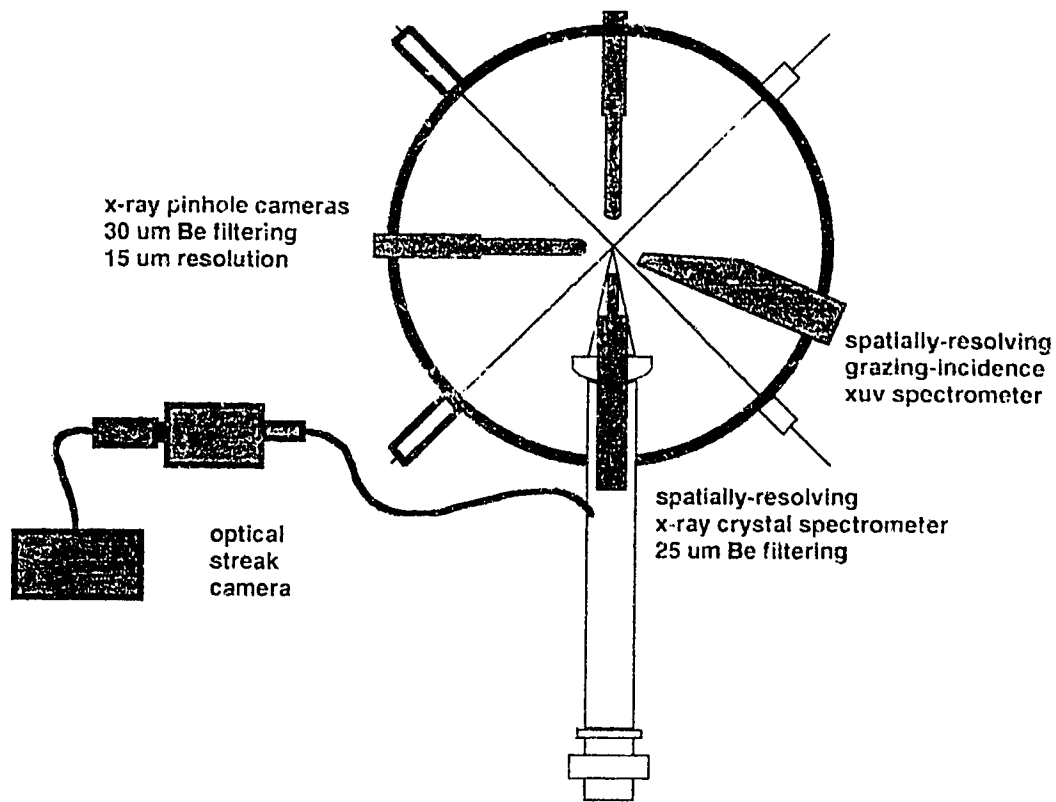
Figure 4.7 The diagnostic configuration used in the experiments.

X-ray Diagnostics

The configuration of the chief diagnostics and laser beam used in the experiments are shown in Figure 4.7. The x-ray instruments were all mounted in the equatorial plane of the chamber. Each instrument was secured to the vacuum chamber by means of its own adapter flange. The adapters featured two pairs of opposing setting bolts which allowed alignment adjustments of the instruments to be made.

The two spectrometers are shown in Figure 4.8, opened to reveal their dispersing elements. Both instruments featured light-sealed film cartridges which were attached to the end of extension assemblies allowing the film to be positioned from outside the vacuum chamber. The dispersing element .s and film planes were separated by gate valves operated from the outside of the chamber, allowing the film sides of the instruments to be leaked to atmosphere and re-evacuated without disturbing the chamber vacuum. This design feature was necessary to allow the film to be processed and replaced between successive laser target shots.

The geometry of the crystal spectrometer is illustrated in Figure 4.9. The x-rays originating from the source point S are selectively Bragg reflected from the crystal at an angle θ to a point P on the film plane according to the relation

$$m\lambda = 2d \sin \theta \qquad\qquad 4.3$$

where m is the diffraction order and d the separation between the Bragg layers. In this particular instrument the film plane and the line segment $\overline{SO}$ which is parallel to the instrumental axis define a right handed coordinate system with origin at point O. The line collinear with the surface of the crystal subtends an angle $\pi - \alpha$ with respect to the x axis. The aperture A in the form of a 35 μm wide slit provided spatial resolution in one direction (perpendicular to the plane of the figure). The slit was cut into 20 μm tantalum foil mounted onto a beryllium foil of thickness 25 μm. The beryllium foil effectively attenuated radiation below a cutoff of approximately 1 keV, and also provided a light seal for the instrument.

The dispersive properties of the spectrometer are most easily understood by considering a virtual source and aperture S' and A' defined by reflecting the segment $\overline{SR}$ about the crystal surface. If the coordinates of the virtual source are (x',y') then the wavelength dispersion along the film plane is given by
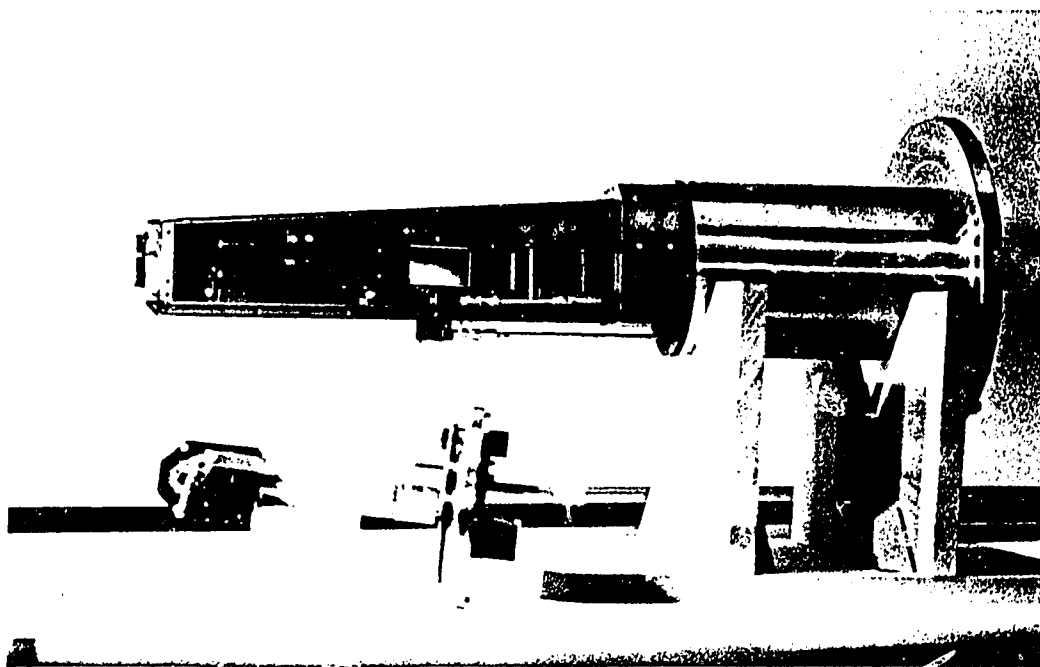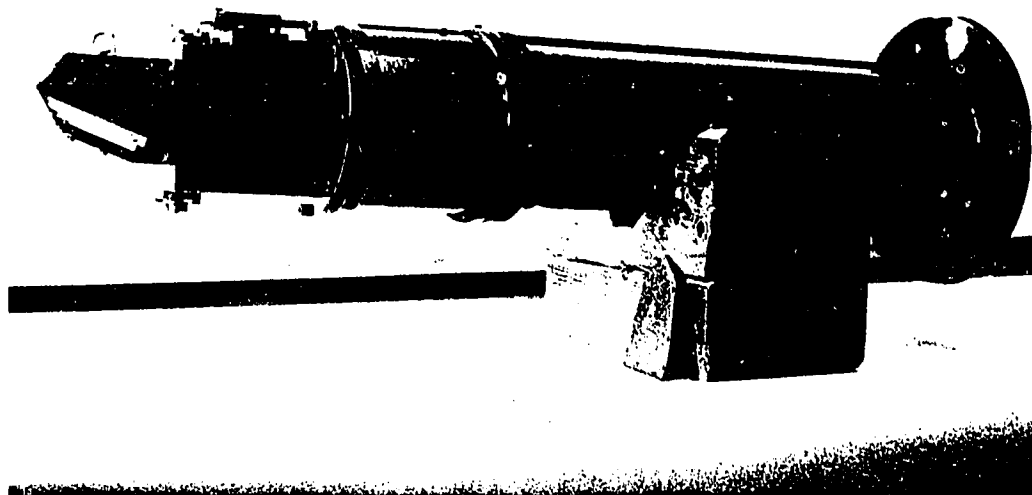
Figure 4.8. The x-ray crystal spectrometer (top) and grazing incidence spectrometer (bottom) with film cartridge.
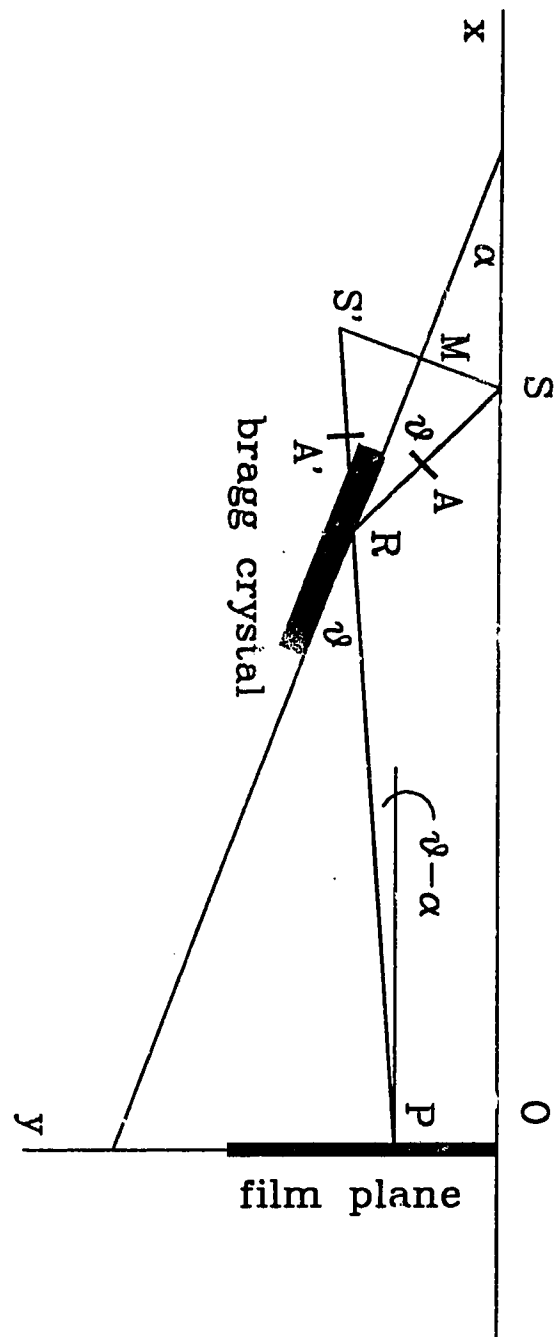
Figure 4.9. The geometry of the x-ray crystal spectrometer.

78

$$\lambda(y) = \frac{2d}{m}\left[\sin\alpha + \left(\frac{y'-y}{x'}\right)\cos\alpha\right]$$ 4.4

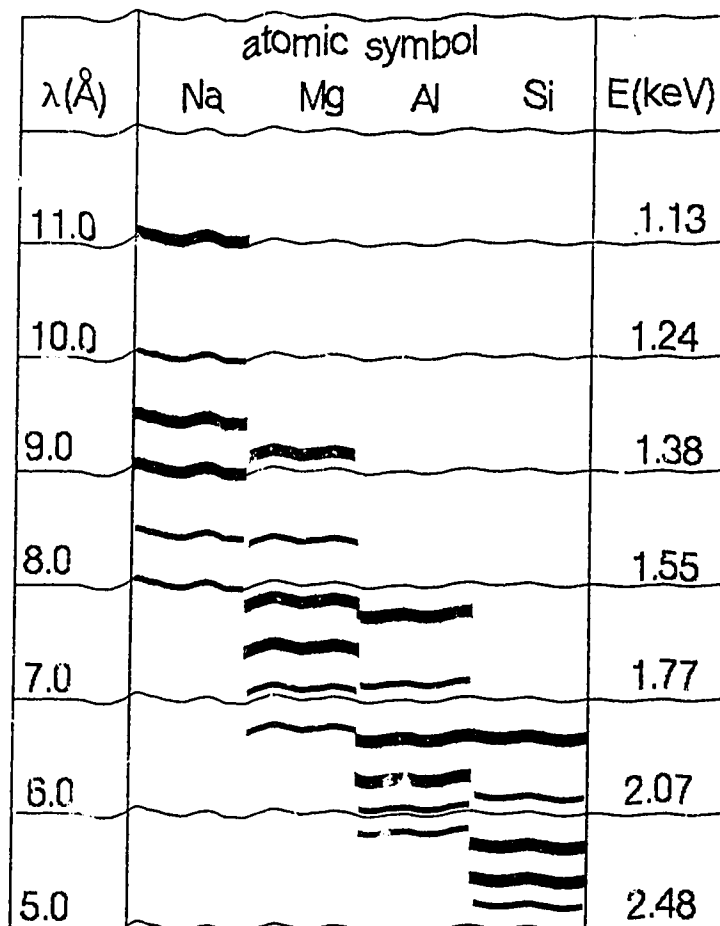where the Bragg condition (4.7) has been used. The magnification of the instrument in the spatially-resolving direction is

$$M = \frac{x'}{\ell}\sec(\theta - \alpha) - 1$$ 4.5

where ℓ is source to slit separation. Using the parameters of the instrument, namely $2d = 25.76$ Å, $\alpha = 19.5°$, $x' = 161$ mm, and $y' = 30$ mm the spectral range over the 60 mm long film plane was 4.1 Å to 13.1 Å and the linear wavelength dispersion $d\lambda/dy$ for reflection in the first order was 0.151 Å/mm. The nominal magnification of the instrument was 7.1. In Figure 4.10 the a wavelength chart of the dominant K shell x-ray lines which are found within the spectral range of the instrument is presented.

The crystal used in the spectrometer was thallium acid phthalate (TlAP), whose reflective and diffractive properties have been characterized by Henke and co-workers (1982). Reflectivity measurements (Barrus, 1981) on TlAP crystal have yielded good agreement with the predictions of the Darwin Prins model for this material. One general result of this model is diffraction effects within the crystal will disperse a collimated beam impinging on the crystal into an angular distribution of the form (Henke et al., 1990)

$$I(\Delta\theta) = \frac{R(\omega/2\pi)}{\Delta\theta^2 + (\omega/2)^2}$$ 4.6.

For TlAP crystal the Full Width Half Maximum ω varies from .2 to .7 milliradians for the spectral range of interest to this study. Since the x-rays striking the crystal were not sharply collimated in this instrument, the incident angular width embraced the whole diffraction line 4.10 and signal at the film plane was determined by the integrated reflectivity R.

atomic symbol

λ(Å)	Na	Mg	Al	Si	E(keV)
11.0					1.13
10.0					1.24
9.0					1.38
8.0					1.55
7.0					1.77
6.0					2.07
5.0					2.48

H - Like lines ⸺

He - Like lines ▬▬

Figure 4.10. The dominant K shell lines from various elements which could be recorded by the crystal spectrometer.

The resolving power of the instrument was limited by source broadening effects. Taking as a example an plasma source of dimension 100 μm radiating the resonance line of Al^{11+} ($\lambda = 7.7571$ Å) the line at the film plane will be widened to 0.012 Å, corresponding to $\lambda/\Delta\lambda=630$. The resolving power dropped accordingly in the intensity modulation experiments for which the source size was ~300 μm.

The XUV grazing incidence spectrometer was installed at an azimuthal angle of 67.5° with respect to that of the laser beam. The geometry of the instrument is shown in Figure 4.11, showing the original design presented by Nakano and co-workers (1984). The dispersing element was a mechanically ruled, 5 cm-wide concave grating of nominal groove density 1200 l/mm (Harada et al.,1980; Kita et al., 1983). A numerically controlled ruling machine was used to correct the grating for aberration. The grating was designed to collect x-rays from the source S at an incident angle α=87° and focus them to a flat field 235 mm away. The wavelength dispersion of the instrument was determined by the relations

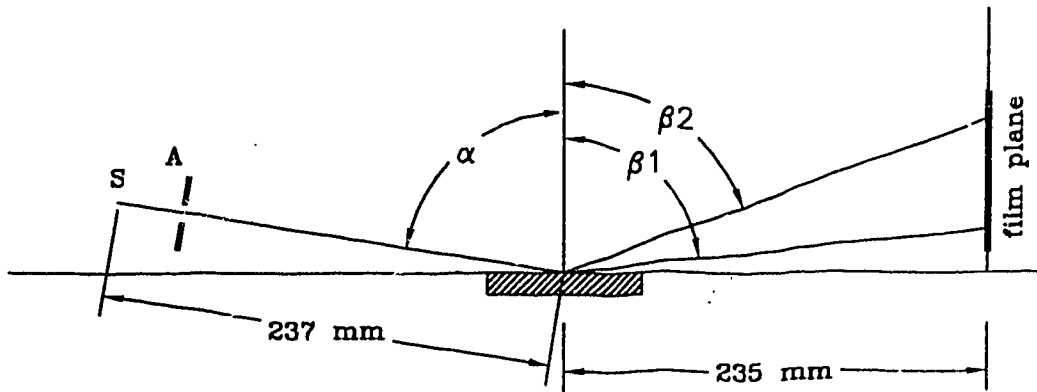Figure 4.11. The geometry of the XUV grazing incidence spectrometer.

$$m\lambda = d_0(\sin \alpha + \sin \beta) \qquad 4.7$$

$$y = 235\cot\beta \ mm \qquad 4.8$$

where d_0 is the groove periodicity.

A 50 μm diameter pinhole provided spatial resolution perpendicular to the dispersion direction. The pinhole aperture was located 25.6 mm from the source resulting in a magnification of 18.4 on the film plane. There was no additional filtering for this instrument as was the case for the crystal spectrometer. However, a pair of strong magnets was installed in the nose of the instrument to prevent ion-induced damage to the grating. The resolving power of the instrument is limited by the pinhole size. For a line at 50 $\overset{o}{A}$, a 50 μm aperture results in a broadening of $\Delta\lambda = 0.22 \overset{..}{A}$ or a resolving power of 230.

The main x-ray pinhole camera was installed at an azimuthal angle of 90° with respect to that of the laser axis in order to record the profiles of the x-rays emitted laterally from the target (an additional identical instrument installed at 180° viewed the rear side of the target and was used for a few select shots on thin foil targets). Spatial resolution in 2 directions was provided by a 15 μm diameter pinhole located 20 mm from the plasma source. The magnification of the instrument was 11. The instrument was filtered with a 30 μm beryllium foil which served as a vacuum seal between the chamber and film. The 22 mm diameter film disks were secured in open ended cylindrical cartridges and inserted into the mounted camera up to the beryllium filter. As with the spectrometers, the film could be removed and replaced between target shots.

The crystal spectrometer and pinhole data was recorded on Kodak Direct Exposure Film (DEF). Kodak 101-07 monolayer film was used in the grazing incidence spectrometer. The film was cut, loaded and processed in the GEKKO IV darkroom. DEF film possesses several attractive features, including ease of handling,

large dynamic range, and a well characterized density curve (Rockett et al. 1985; Henke et al., 1986; Oades et al., 1990). The 101 film response has been calibrated by Henke and co workers (1984b) and T. Tachi (1990). The DEF film was processed as follows:

Kodak GBX Developer	5 min @ 20° C
fresh running water (stop)	30 sec
Kodak GBX fixer	8 min
fresh running water	30 min
hang drying	12 hours

The 101 film was processed as follows:

presoak, $H_2O^\dagger$	2 min @ 20° C
Kodak D19:$H_2O^\dagger$ (1:1)	4 min, gentle agitation
$H_2O^\dagger$ stop	30 sec
Fuji Superfix	2 min
$H_2O^\dagger$ rinse	30 sec
Fuji Quick Wash	3 min
$H_2O^\dagger$ wash	30 sec
hang drying	12 hours

$\dagger$ distilled water

Laser Diagnostics

In order to characterize the focal conditions for each target shot, it was desirable to know the energy, temporal profile, and spatial distribution of the laser beam. The energy of each target shot was recorded using a volume-absorbing calorimeter of response $10\mu V/mW$ mounted outside the chamber (Fig. 4.4 and 4.6).

The output of the calorimeter was relayed to a pen recorder in the screen room. The sensitivity of the calorimeter was benchmarked against an absolutely-calibrated Apollo Series ALC calorimeter which provides the energy standard at ILE.

The temporal profile of the laser was captured using Hamamatsu C979 streak camera and temporal analyzer. The instrument was calibrated using the etalon method (Tsuchiya, 1983). A fraction of the laser front end was diverted from the oscillator room to an optical PIN diode located near the chamber to provide the timing trigger for the instrument. A Mitsubishi ST2000 multimode optical fibre was placed in the beam after the KDP crystal in order to relay the light to the streak camera slit. Small pieces of gelatin ND filters affixed to the end of the fibre provided attenuation if necessary. The streak camera was set in close proximity to the beam so that the modal dispersion $\Delta\tau_f$ of the fibre (length 150 cm) could be minimized. Based on the published properties of the fibre, $\Delta\tau_f$ was estimated to be ~64 ps. The true pulse width $\Delta\tau_1$ was estimated from the relation

$$\Delta\tau_1 = \sqrt{\Delta\tau_m^2 - \Delta\tau_f^2 - \Delta\tau_s^2} \qquad\qquad 4.9$$

where $\Delta\tau_m$ was the measured pulse width and $\Delta\tau_s$ the contribution due to the finite camera slit size.

Two typical laser pulses recorded by the streak camera are shown in Figure 4.16. The etalon of the laser oscillator was set for 900 ps and 400 ps for the case of (a) and (b) respectively.

A visible Schwarzschild microscope was used in measuring the laser intensity pattern near the vicinity of best focus (see Chapter 5). The instrument is shown in Figure 4.13. The essential optical components are the concentric mirrors M1 and M2 whose radii are related by the Schwarzschild condition (Burch, 1947; Shealy et.al., 1989)

$$\frac{R_2}{R_1} = 1.5 - \frac{R_2}{S_0} \pm \left(1.25 - \frac{R_2}{S_0}\right)^{1/2} \qquad 4.10$$

where the + sign is taken for magnifications greater than 5 and the - sign is taken for magnifications less than 5. The magnification is given by

$$M = \frac{S_i}{S_0} \qquad 4.11$$

The instrument was designed for a magnification of 15 and total working distance (source to image plane) of 1.5 meters (Kado et al., 1988 ;1991). The acceptance half solid angle of the primary mirror θ_1 was 7°. The sphericity of the mirrors has been measured using a Zygo Mark IV interferometer system to be better than $\lambda/10$ for visible wavelengths. Consequently the spatial resolution of the instrument was limited by the Rayleigh criterion (Born and Wolf, 1959)

$$\Delta r = 0.61 \frac{\lambda}{\sin \theta_1} \qquad 4.12$$

to be ~2.7 Å for visible light. As in the case of the x-ray spectrometers, the optical elements and image plane are separated by a gate valve which allows the recording end of the instrument to be leaked and evacuated while the target chamber is under vacuum.
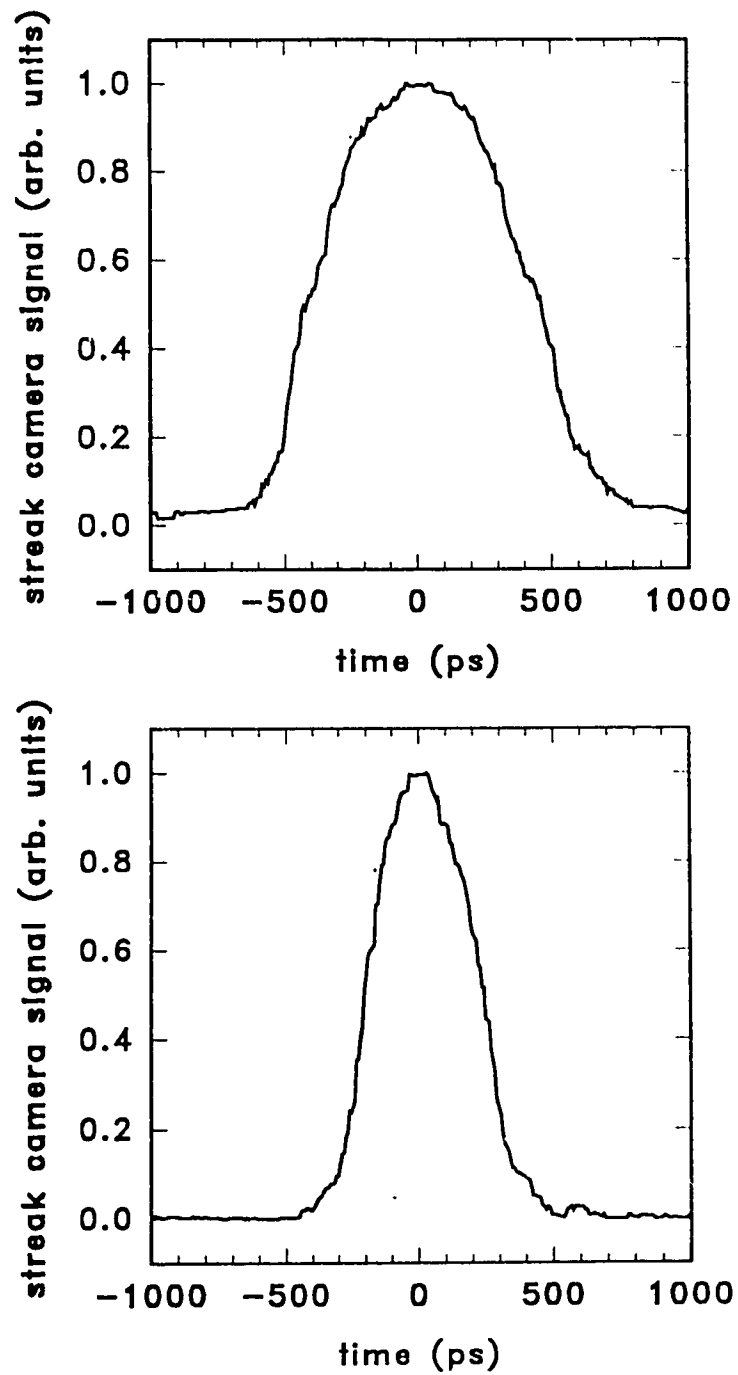
Figure 4.12. Typical optical streak camera records captured during the long pulse (top) and short pulse (bottom) experiments.
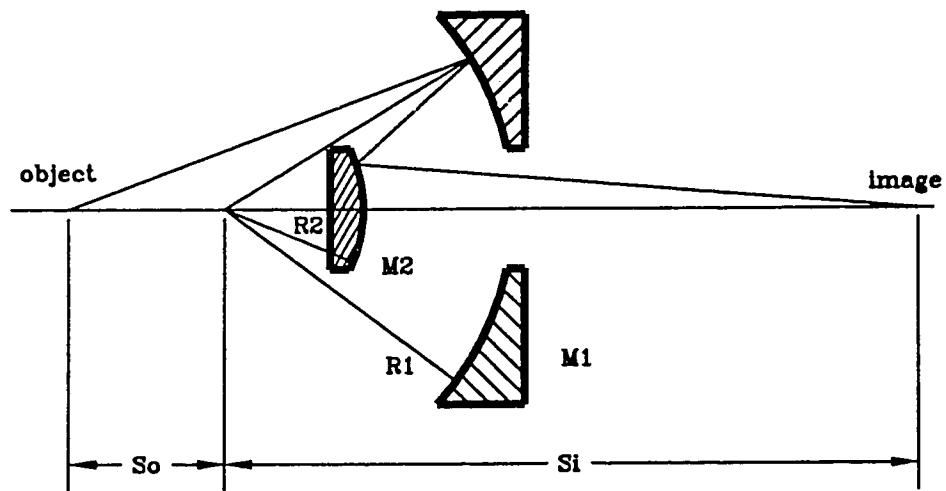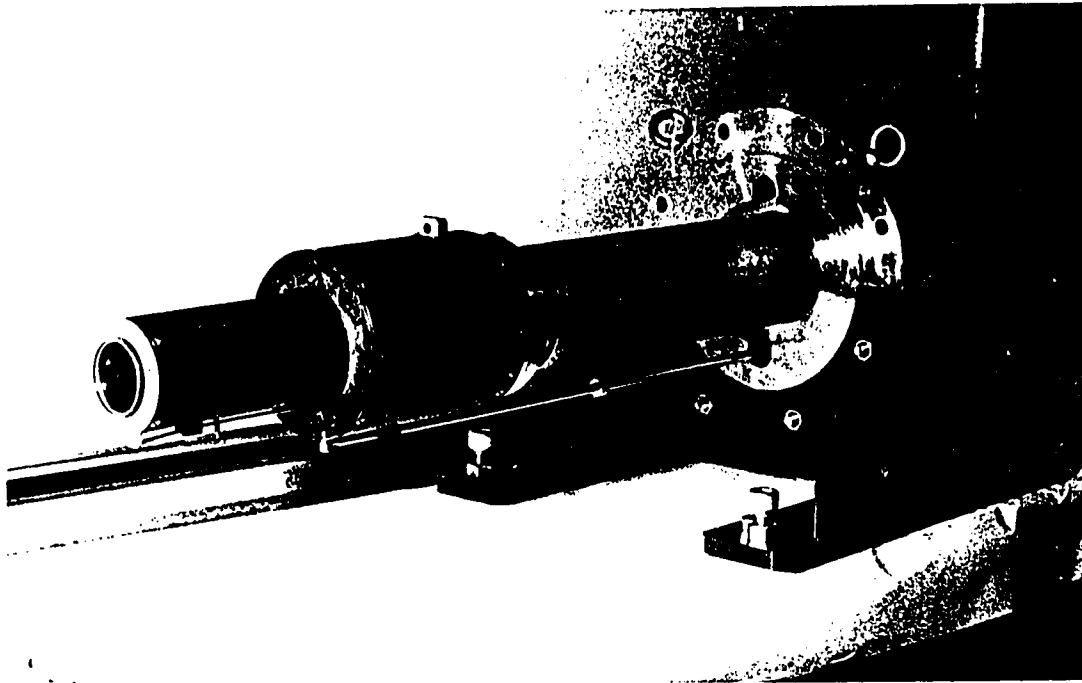
Figure 4.13. The visible Schwarzschild microscope used in the focal spot characterization, and the optical configuration of the instrument.

5. Focal Spot Characterization

In order to interpret the x-ray experiments, it was necessary to characterize the energy distribution of the focal spot as thoroughly as possible. For the case of the modulated intensity experiments, it was essential to measure the spatial periodicity of the intensity modulations and assess the amount of diffracted light which could be expected in the shadow regions of the intensity profile. Furthermore, the optimum choice for the focal spot size and the modulation mask relies on some knowledge of the behavior of the beam in the transition region between near and far field conditions. For the best focus experiments, the size and uniformity of the best focus spot and the amount of energy deposited outside the nominal focal spot radius had to be determined.

A well-established method of characterizing the focal spot involves rerouting a small fraction of the beam through a lens with optical properties equivalent to those of the primary focusing lens, and reimaging the equivalent focal plane onto film or camera. One advantage of this method is that a shot-to-shot record of the focal spot may be taken. The method requires that the primary and equivalent lenses be as near to identical as possible in order to faithfully reproduce the focal spot on target. Unfortunately the positioning of the beam alignment assembly and KDP crystal housing precluded the use of this technique. Instead, two alternative approaches were employed in which the focal spot intensity was measured at the actual target position. The resulting profiles were assumed to be representative of the intensity patterns present during target experiments.

The first method involved focusing a small amount of laser energy non-destructively onto a thin target and collecting the forward scattered laser light with the visible Schwarzschild microscope (VSM) described in Chapter 4. The orientation of the diagnostic is shown in Fig. 5.1. The VSM was mounted on the horizontal mid plane of the chamber at an angle of 22.5° with respect to the laser axis.

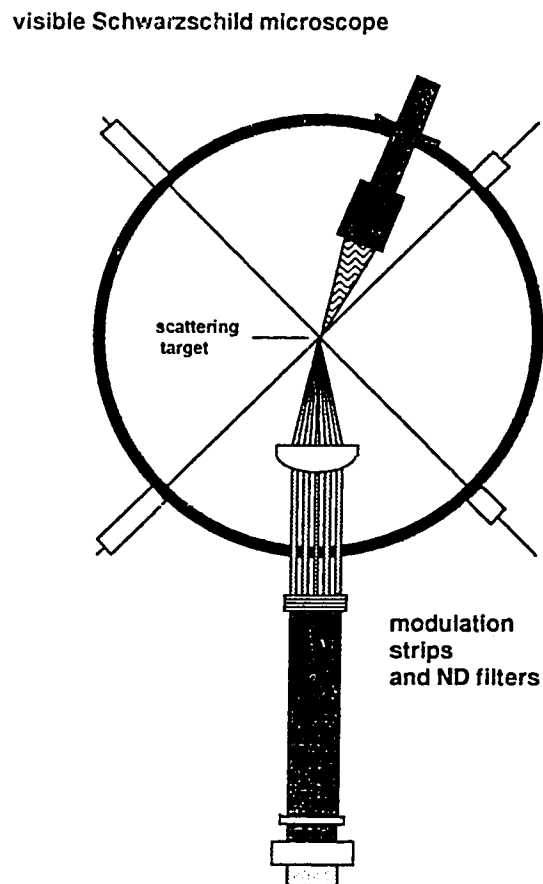**visible Schwarzschild microscope**

Figure 5.1. Configuration of the scattering experiment undertaken in order to characterize the focal spot energy distribution.

This ensured that the instrument collected only scattered light from the target and none of the laser beam re-expanding from the focal region. The fully-pumped D beam chain was used in these measurements, in order to reproduce as closely as possible the beam profile used in the actual experiments. Glass neutral density filters were positioned after the KDP crystal to strongly attenuate the beam (typically by a factor of 10^5) in order to prevent the target from ablating.

The target consisted of a thin layer of transparent adhesive tape mounted on a 2 mm diameter washer and glass stalk as described in Chapter 4. The tape, initially of 60 μm thickness, was presoaked for 12 hours in toluene; after this treatment the adhesive layer was separated from the tape recovering a substrate of thickness 45 μm. Densitometer measurements verified that only a small fraction of collimated light incident on a single layer of tape is absorbed or scattered.

In order to assess the degree to which scattering effected the resolution of the VSM measurements, pinholes covered with a single layer of tape were placed on a microscope stage, illuminated from below, and reimaged onto photographic prints. The apparent image sizes of covered pinholes increased in dimension by 10 μm over those of uncovered pinholes. Based on these measurements a spatial resolution of approximately 10 μm was assumed.

The procedure followed for the focal spot measurement consisted of three stages: the alignment and calibration of the VSM, the positioning of the focusing lens and assessment of signal levels, and the focal spot measurement proper. Once the VSM was been mounted on the chamber, the initial crude alignment was done with the chamber at atmospheric pressure. A spherical foam CH target of diameter 1 mm was positioned at target center using the backlighting monitor system, and a helium-neon laser beam was brought onto the target. The scattered light from this target was then used to align the optical axis of the instrument and adjust the focus. The chamber was

90

next sealed and evacuated, a CCD camera positioned at the image plane of the VSM, and the next iteration of alignment and focusing was done. It was necessary for the chamber to remain under vacuum from this point onward until the final measurements were finished. At this point the foam target was replaced with a precision mesh (washer mounted) of spatial periodicity 167 μm and the final focusing adjustment was made. The CCD camera was then replaced with the film cartridge for the remainder of the experiment. The magnification of the instrument was determined by imaging the mesh onto film (again by making use of scattered light from a helium-neon laser) and scanning the resulting exposure under a densitometer. In this way the magnification of the instrument was determined to be 14.0 (±3%).

Kodak 3200 35 mm black and white film was used to record the VSM images. The procedure used in processing the film was kept constant throughout the course of the measurements. The film was developed for 10 minutes in Kodak D76 developer at 20° C, followed by a 30 second rinse in fresh running water, a 15 minute fix in Fuji Superfix at 20° C, and a 30 minute wash in running water. In order to convert optical density to relative intensity, the film was calibrated by making exposures of samples placed adjacent to a wratten green filter and a neutral density step wedge under a photographic enlarger.

For the second phase of the experiment the laser was brought to target center by the method outlined in Chapter 4. At this point the tape target was introduced and aligned at chamber center. The first full energy laser shots recorded were used to establish signal levels and set a suitable filter attenuation. As there were no fiducial markings on the surface of this target, the accuracy of positioning along the laser axis was approximately 150 μm. Accordingly the target was kept fixed and the position of the focusing lens adjusted incrementally over a sequence of shots in order to establish
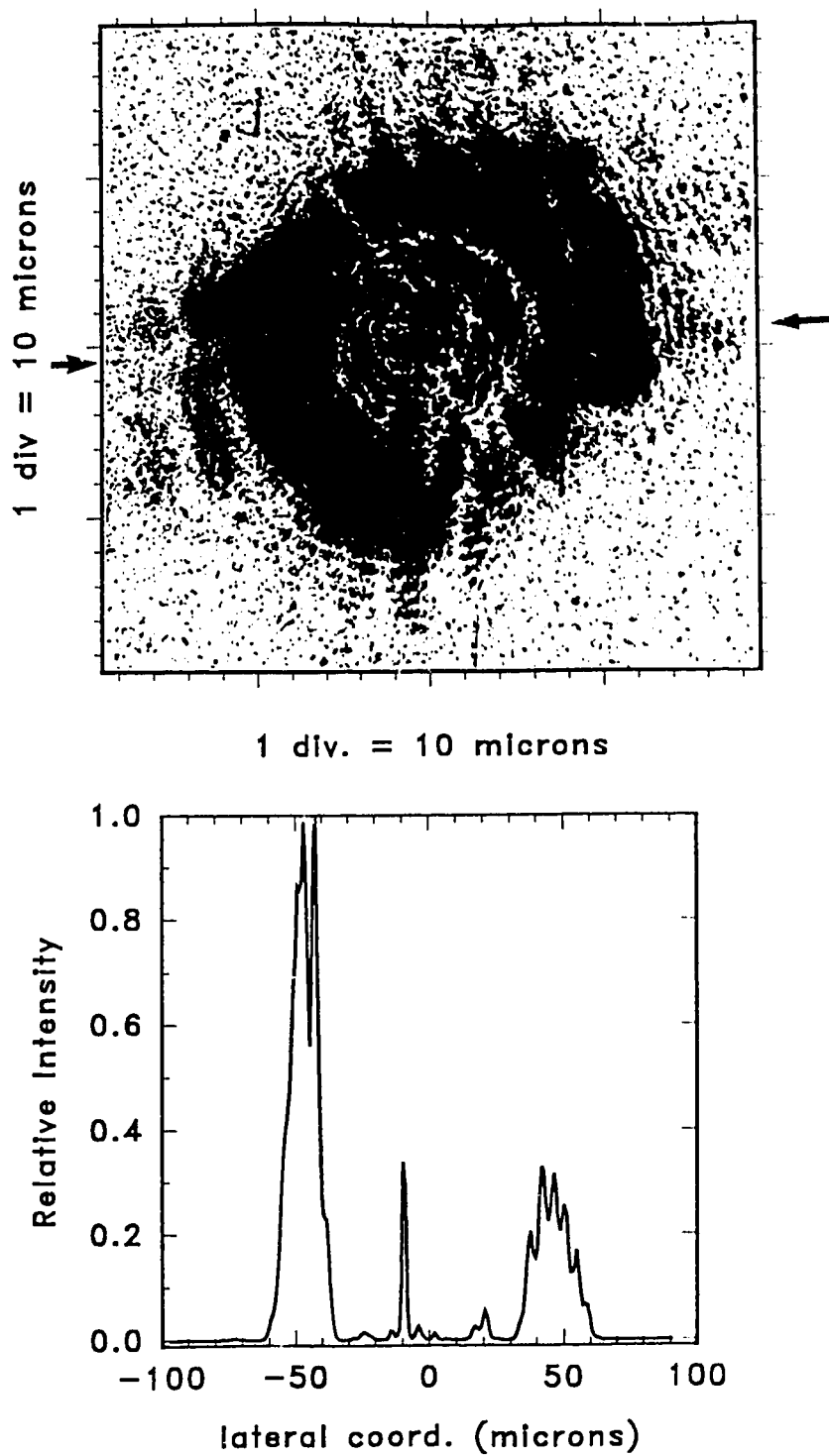
Figure 5.2. (a) Image of the GEKKO IV focal spot near best focus as recorded by the visible Schwarzschild microscope. (b) The intensity profile along the line indicated by the arrows in (a).

the best focus lens position. The VSM film images were developed immediately after each shot and the image sizes plotted against lens position to construct the dependence of the beam radius on the laser axial coordinate. The best focus spot diameter was determined to be nominally 110 μm, which is many times larger than the diffraction limited spot size (f#)xλ=1 μm. The depth of focus, defined as the length over which the focal spot size is less than $\sqrt{2}$ of the minimum spot size, was found to be 280 μm.

With the best focus lens position established, several shots were recorded at selected lens positions in order to investigate the radial and axial dependence of the beam profile. An enlargement of the best focus intensity pattern as recorded on film is shown in Fig. 5.2a. The intensity profile from a densitometer scan taken through the centerline of the focal spot indicated by the arrows in (a) is shown in Fig. 5.2(b). After conversion from optical density to relative flux it was evident that most of the energy was deposited within an annulus of inner radius 30 μm and outer radius 60 μm. In addition, there was strong azimuthal dependence in the intensity pattern. Within the limited data set of images (taken on different days and thus with slightly different lens settings and input beam structure) the details of this azimuthal structure varies, but the overall annular structure is preserved. Another notable feature is the existence of diffraction rings outside of the main focal region. The intensity of these features were less than 1% of that in the donut region. Since the intensity profiles exhibit such a well defined cutoff radius the best focus condition was judged suitable for the lateral transport experiments.

The beam structure near best focus exhibits considerable variation along the laser axis. As the beam begins to diverge on the far side of the best focus position it breaks up into filaments. Fig. 5.3 represents the focal spot pattern 63 μm on the diverging side of best focus. At positions further along from this point it continued to
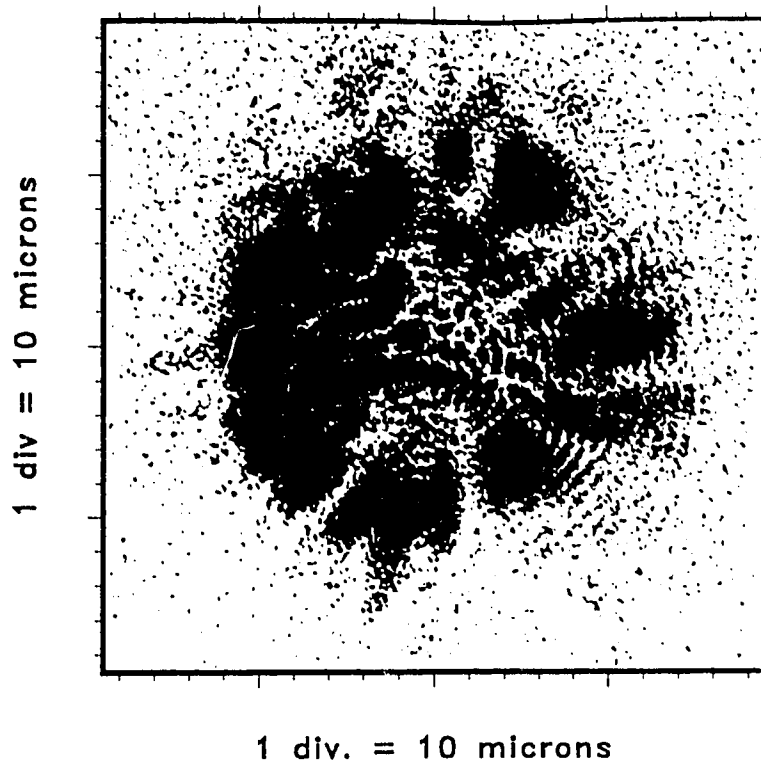
1 div. = 10 microns

Figure 5.3.   VSM image of the beam 63 on the divergent side of best focus.

exhibit such local structure, and consequently these positions were deemed unsuitable for the main experiments.   The general beam characteristics (convergence to a ring pattern and subsequent breakup) are typical for this type of laser system, and such filamentary structure has been attributed to scattering and self-focusing in the laser amplifiers (e.g. Gabl et al., 1990).

On the converging side of best focus the far field focal pattern exhibits a cup-shaped profile.   A representative profile resulting from the averaging of radial profiles from three laser shots is shown as a solid curve in Fig. 5.4.   The focal condition (which was used in the intensity modulation experiments) was 313 µm on the convergent side
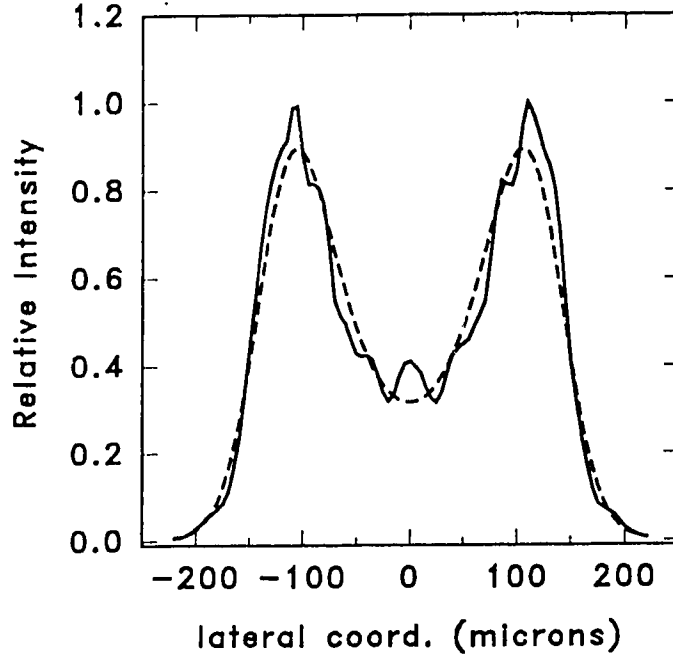
94

Figure 5.4. Experimentally obtained intensity profile (solid) obtained from VSM images for the focal condition used in the intensity modulation. The profile represents an average of three profiles. The dashed line represents an analytic fit of the form (5.1) to the experimental profile.

of best focus. The central intensity cup is consistent with the type of far-field profile expected for a flat-top beam input as is the case for GEKKO IV. The cup shape may be further enhanced by the central blind spot in the focusing lens and non-uniform amplification along the laser amplifier chain. Also shown by the dashed line in the figure is a best fit to the averaged profile for a function of the form

$$I(r) = I_0 \exp\left[c_6 r^6 + c_4 r^4 + c_2 r^2\right]$$ 5.1

This heuristic function was used to estimate the overall intensity envelope for the modulated intensity experiments.

Apart from the radial structure across the beam, the azimuthal intensity variation could be as much as a factor of two, due probably to output beam imbalance which varied from day to day on the GEKKO IV system. An unavoidable result of the radial and azimuthal dependence of the profile is that when the beam is modulated in one direction with masks, the intensity distribution within an irradiated region will not be uniform, nor will there be equal energy balance between adjacent irradiated regions. This beam characteristic had to be factored into the errors in the analysis of the x-ray experiments.

Masks consisting of opaque parallel strips were placed across the beam near the ND filters, resulting in alternating illuminated and shadowed regions of equal width in the intensity profile. Masks with spatial periods of 0.4, 1.0, 2.0, and 3.0 cm were tried . The final choice of mask and lens settings for the x-ray experiments were the strip arrays of periodicity 3.0 cm and lens setting resulting in a target position 313 μm on the convergent side of best focus. This choice represented a compromise between the desire for a maximum possible intensity on target and the quality of the intensity pattern on target, and the spatial resolution of the diagnostics. With respect to the former consideration, the wave front at -313 μm was sufficiently in the far field to reproduce well-defined intensity modulations along one direction. At -200 μm this is no longer the case; near field effects significantly distort the shape of the modulation pattern.

Figure 5.5 shows an intensity profile (solid curve) resulting from a shot taken for the same focal setting as Fig. 5.4, but with an mask of spatial period of 2.0 cm placed in the beam. The film was scanned along a line oriented at right angles to the strips and displaced 120 μm (in target coordinates) from the centerline of the focal spot image. The dashed curve represents the profile of the envelope as predicted by
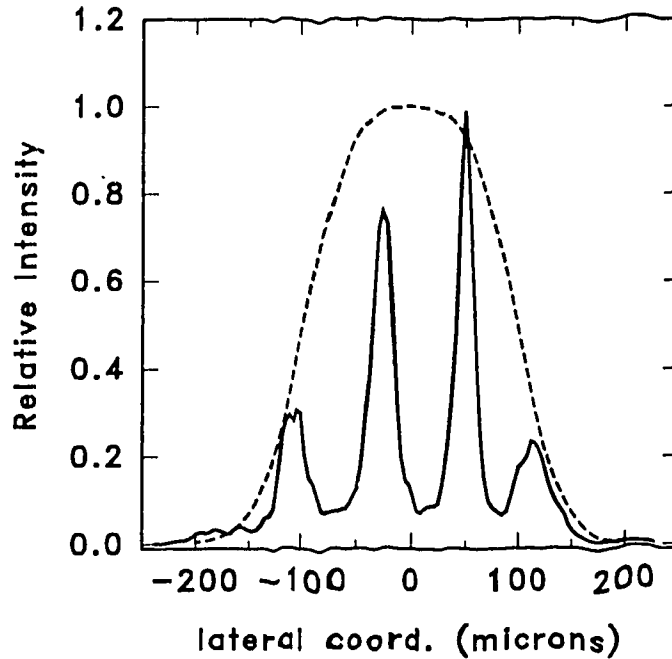
Figure 5.5. An example of an intensity profile created by placing an opaque mask of spatial period 2.0 cm in the input beam.

the function 5.1. The modulation within the envelope is not a perfect step function and some spillover of laser energy is evident in the shadow regions. This spillover may be partly an effect of the resolution of the measurements, but it was also observed in the results of the second method described below. It was concluded from these measurements that the energy incident in the shadow regions was not zero but did not exceed 10% of that in the high energy regions.

Microablation Study

The second method used to characterize the laser beam pattern involved firing low energy laser shots onto planar microablation targets, which were afterwards removed from the target chamber and photographed under a microscope. By taking a series of shots over a range of incident laser energies and comparing the ablation patterns so produced, one can reconstruct the intensity distribution in the beam. The assumption of this method is that the incident laser energy is low enough and pulse width short enough to preclude significant lateral transport in the ablating target.

The targets typically consisted of 20 μm-thick planar aluminum foils vacuum-coated with 100 $\overset{o}{A}$ of gold. These targets were oriented vertically resulting in an incident laser angle of 35°. The azimuthal orientation of the target was set to within 4 ° by using the specular reflection of the light from the halogen lamps into the target monitors. The positioning errors along the laser axis (~20 μm for both the target and laser beam) accounted for most of the error in this measurement. The procedure described in chapter 4 was used to set the beam position and focal condition at chamber center.

The laser pulse was generated by the common amplifier chain of GEKKO IV (see Fig. 4.1), which resulted in incident energies on target on the order of millijoules, and allowed a shot repetition period of 20 minutes. No attenuation of the beam was done at the target chamber; instead, the energy of the laser pulse was varied by adjusting the charging voltage of the final 60 mm diameter common amplifier. The energy reaching the target chamber was too low to record with the 2ω calorimeter. Instead the relative energy of each series of shots was obtained by replacing this calorimeter with a fast biplanar Hamamatsu R1328Ux-01 phototube. The phototube
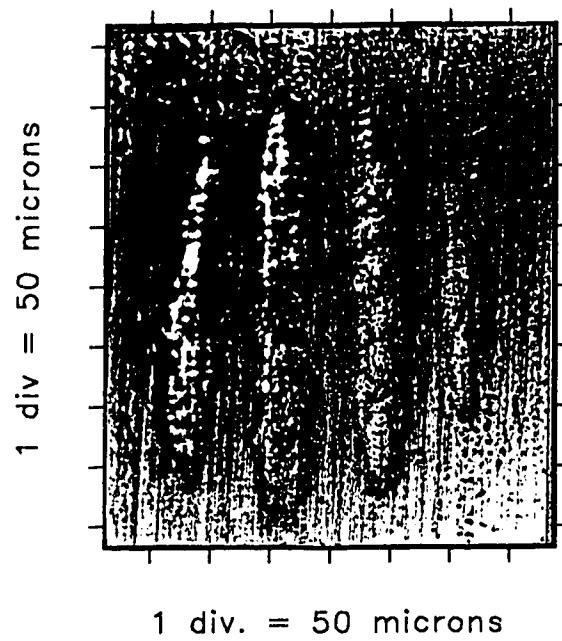
1 div. = 50 microns

Figure 5.6. Photograph of an aluminum target after irradiation by low intensity spatially-modulated laser light.

signal was captured on a Tektronix 7104 oscillosope, and the area under the photodiode pulse was estimated in order to obtain the relative energy of each shot. The photodiode signals were plotted against energies recorded by a calorimeter positioned after the last common amplifier (see Fig. 4.1), assuming an I^2 dependence due to the KDP conversion function (4.1). The resulting plot was linear with a correlation of 0.9998, thus verifying the validity of this method of energy measurement. Based on the published values of the phototube response and the beam splitter optics, typical energies of ~10 mJ reached the target.

The ablation pattern created on a pure aluminum target by a beam masked with a strip array of spatial period 2.0 cm is shown in Figure 5.6. The elliptical shape of the
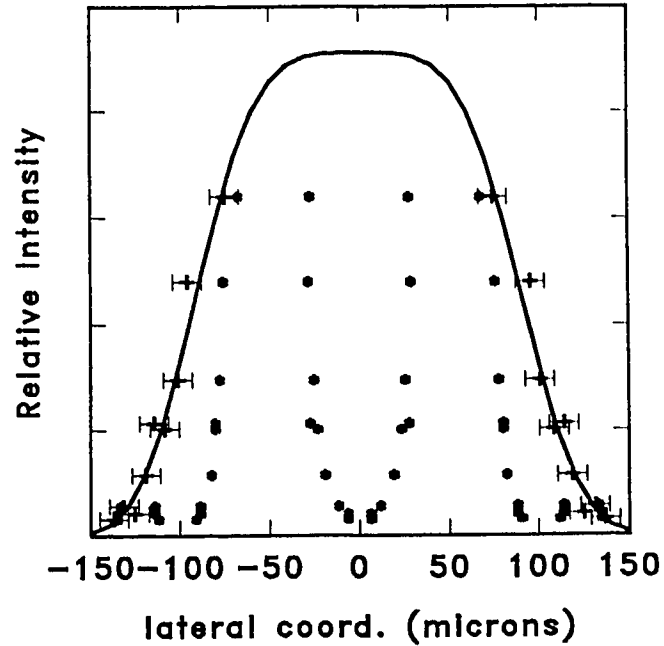
99

Figure 5.7. The intensity profile on target determined from the microablation method for a beam masked with a strip array of period 3.0. cm. The error bars are shown only for the points which define the overall envelope. A supergaussian of mode four (solid line) was found to fit this data well.

ablation pattern and the slight convergence of the ablation strips is due to the incident angle and convergence of the laser beam. Besides the strip pattern created by the beam mask, a hole in the center of the beam (caused by the focusing lens) may be seen in the ablation patterns. Long, narrow ablation features aligned parallel to the irradiation strips were observed in the masked regions. The shape and orientation of these features suggests that the beam spillover into the masked regions was due at least in part to diffraction effects originating at the strip array.

Targets used after the one of Fig. 5.6 were of improved design, featuring 100 Å layers of gold over the aluminum substrates. With this type of target a series of shots taken over a range of incident energies could be used to generate intensity profiles. Each ablated target exhibited areas within which the Au overcoat had ablated away. These areas were assumed to define regions over which the incident intensity had exceeded some threshold value I_{th}. The radial coordinates of the Au/Al boundaries along the (horizontal) center line of each ablation pattern were measured for each target. For each target i and Au/Al boundary radius r_{ij} a set of intensities defining the profile were then be generated from

$$I\left(r_{ij}\right) = \left(I_{th}E_i/E_{ref}\right) \qquad\qquad 5.2$$

where E_i and E_{ref} are the incident energies for shot i and an arbitrarily chosen reference shot. In the same manner the overall envelope of the intensity profile on target was inferred by measurement of the maximum radii of the ablation boundaries.

The profile generated from a series of shots taken with a beam masked by a strip array of period 3.0 cm is shown in Figure 5.7. Each point represents an average of two values taken from either side of a central axis parallel to the ablation bands. Error bars are shown only for the set of points defining the envelope of the beam. A supergaussian of mode 4 (solid line) was found to fit this profile quite well. The period of intensity modulations suggested by this measurement was 103 μm, which is significantly lower than the value of 112 μm implied by the scattering measurement. The discrepancy may be due to the positioning error, since a previous measurement yielded a value in agreement with the VSM results.

The beam profile is markedly different from that recorded with the VSM, exhibiting no evidence of a wide central dip. The differences were even more striking in the case of targets placed at best focus, for which the nominal focal spot diameter was found to be 40 μm. The differences may be expected since the divergence and

101

wave front structure of input beams were different for the two procedures. The scattering measurement used the full GEKKO IV amplifier chain as in the x-ray experiments, it was accordingly taken as the more appropriate measurement of the experimental conditions. The ablation measurement was nevertheless of value in that it basically verified the presence of some spillover of light into the masked portions of the beam, and set similar limits of ~10% for the fraction of energy in these regions.

Numerical Beam Models

Attempts were made to reproduce the beam profile by numerical means using the MATLAB software package[1]. Fast Fourier Transform (FFT) and beam propagation methods, which are described in Appendix 2, were both tried and were able to model the gross features of the beam profile away from the focal plane. However, both methods predicted a very sharply-peaked intensity distribution at the focal plane, with spot dimensions on the order of the diffraction limit of the lens. No modeling of optical aberrations or corrections for lens thickness were incorporated into the algorithms, which accounts at least in part for the discrepancies near the focal plane.

The profile of Fig. 5.8 represents the intensity distribution predicted at 140 μm on the convergent side of the focal plane (corresponding to approximately half the depth of focus of the real beam), as generated from a 2D FFT of a plane wave input
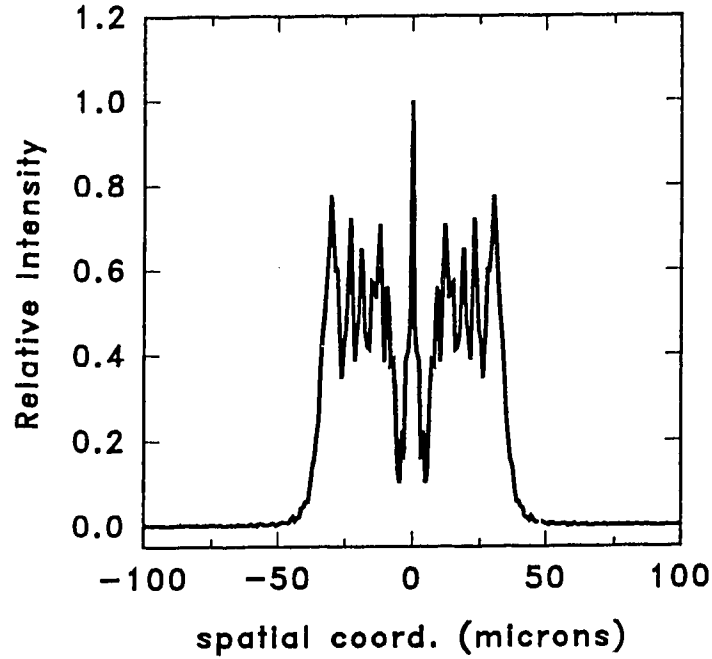
---

[1] © The Math Works 1984 -1991

Figure 5.8 A FFT reconstruction of the intensity profile 140 µm on the convergent side of the focal plane.

field hard-apertured by a hole of diameter 8 cm and focused by a lens of f=15 cm. The numerically generated curve and the measured profile (Fig. 5.2) both exhibit in common an annular ring and central spike.

In Fig. 5.9 central intensity profiles created by the beam propagation routine are displayed. An input intensity of radial dependence

$$I_{in} = \exp\left[-\left(\frac{r}{\Theta_r}\right)^{P_r}\right] \qquad 5.3$$

with Θ_r=4.0 cm and P_r=10 was expanded in terms of 33 Hermite Gaussian modes and propagated by matrix methods to the near field region. The profiles at 50, 100, 200,
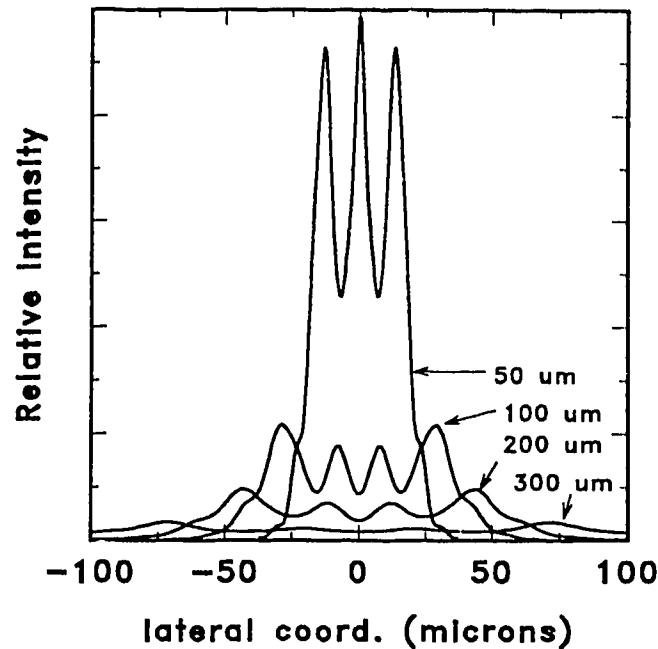
103

Figure 5.9 Intensity profiles predicted by the beam propagation routine for several positions on the convergent side of best focus.

and 300 μm on the convergent side of best focus are shown. The flat-top input results in a crater-shaped intensity profile which comes to be dominated by the central spike as the beam approaches the focal plane. The discrepancy between this calculation and the FFT algorithm could be reduced by using a larger number of input modes in the expansion, and by mixing the input phase of these modes.

It is evident that more sophisticated routines must be developed in order to construct more accurate renderings of the focused beam profile. Besides the inclusion of optical aberrations, some accounting for a forward-scattering component of the field should also be included in a full treatment of this problem.
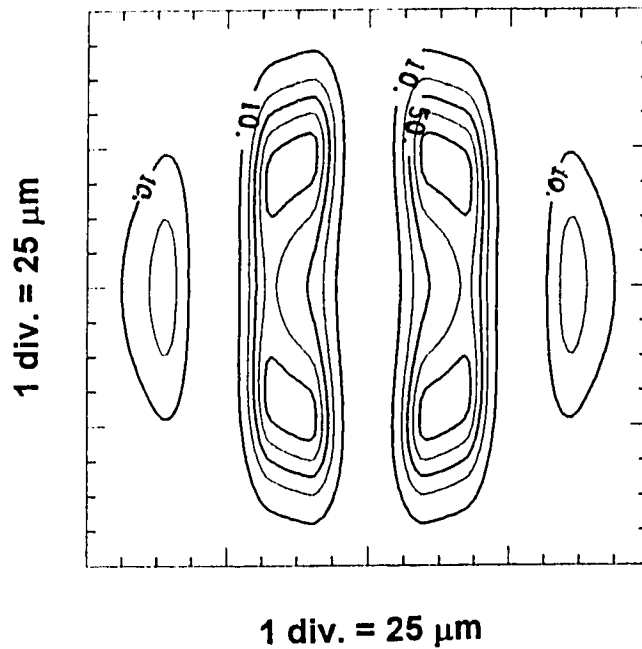
1 div. = 25 μm

Figure 5.10. Contour plot of the idealized intensity distribution incident on target for the modulated beam experiments. The contours represent 10, 30, 50, 70 and 90% of maximum.

The essential results of the measurements described in the present chapter may be summarized as follow. For the tight focus condition, the nominal focal spot size was 110 μm with less than 1% intensity beyond a radius of 60 μm. There is, however, evidence of a strong azimuthal and radial structure in the beam resulting in marked fluctuation in local intensity. The defocused spot intensity profile exhibits a more uniform angular distribution and a crater profile typical of a flat-top input beam. The spatial periodicity of the intensity modulations was determined to be 112 μm for the focal conditions used in the modulation experiments. A 7% error must be assumed in this value due chiefly to the limitations of the target positioning. The intensity

105

modulation is well approximated by a smoothed step function in which not more than 10% of the laser intensity is diffracted into the shadow regions.

Finally, a numerically-generated focal spot intensity distribution based on the VSM analysis is presented in Figure 5.10. A step profile of period 112 μm was imposed over the radial fit (5.1) to produce this pattern. The step profile was given smooth Gaussian-shaped shoulders at the step edges such that 10 % spillover of energy occurred into the low intensity strips. The result represents a reasonable, albeit idealized, representation of the incident intensity pattern for the target shots described in the next chapter.

6. Modulated Intensity Experiments

Experimental Conditions

The target experiments described in this chapter were performed with the modulated intensity focal spot described in the previous chapter. Due to the limitations of the GEKKO IV system, the peak incident laser intensities available for the experiments were about 3.3×10^{13} W/cm^2. Target shots were taken for nominal laser pulse widths of 860 ps and 410 ps (representing statistically averaged values based on the optical streak camera measurements). In general, energy extracted from the amplifiers was less for the shorter pulses with the consequence that all data fell within the same intensity range of $3 \times 10^{12} - 3 \times 10^{13}$ W/cm^2.

The targets, as described previously in Chapter 4 and in Appendix 1, were polystyrene foils coated with tracer layers and variable-thickness CH overcoats, and were positioned for normal-incidence irradiation. The first series of shots were performed with 860 ps pulses on targets with a single aluminum tracer. For the later 400 ps pulse experiments a second tracer layer of NaF was evaporated immediately after the Al layer. This double tracer configuration allowed one to record emission patterns of material originating from two depths of the same target and thus provided information about the lateral dependence of the ablation profile. The choice for the range of the CH overcoat thicknesses (0 - 1.2 μm) was determined mainly by the intensity limitations of the laser using published data on mass ablation rates (Boehly et al., 1986). The thickness of the tracer layers (approx. 0.1 μm) represented a

107

compromise between the need for adequate signal levels and the desire for a thin tracer region in order to localize the original depth of the tracer. Since the aluminum tracers were opaque to visible light, they were deposited onto the substrates as finite diameter (400 μm) discs in order to allow the targets to be positioned under the highest magnification of the backlighting target monitor system. (The NaF tracers transmitted visible light and thus presented no such problem). The apparent size of the tracer disk images on the orthogonal monitor screens were used to set the position and orientation of the targets. The azimuthal angle of the target normals were always oriented slightly away (< 4°) from that of the laser axis, so that the target substrate did not occlude the lateral x-ray emission along the line of sight of the laterally-positioned pinhole camera (see Fig. 4.7).

The beam mask used to produce the intensity modulation was an array of parallel 1.5-cm-wide strips mounted at the entrance to the beam alignment assembly. In this manner a spatial modulation of 3 cm was imposed on the incoming beam. The central strip of the mask was always positioned along the optical axis in order to eliminate the central dip in the intensity profile caused by the central hole of the focusing lens. Due to the configurations of the GEKKO IV target chamber ports and x-ray instruments, the spatially resolving directions of these instruments differed: the Bragg and XUV spectrometers spatially resolved emission in horizontal and vertical directions respectively. Consequently the orientation of the beam mask was alternated throughout the experiments to create horizontal irradiation strips (to provide XUV- and pinhole-resolved data) and vertical irradiation strips (to provide crystal-spectrometer-resolved data).
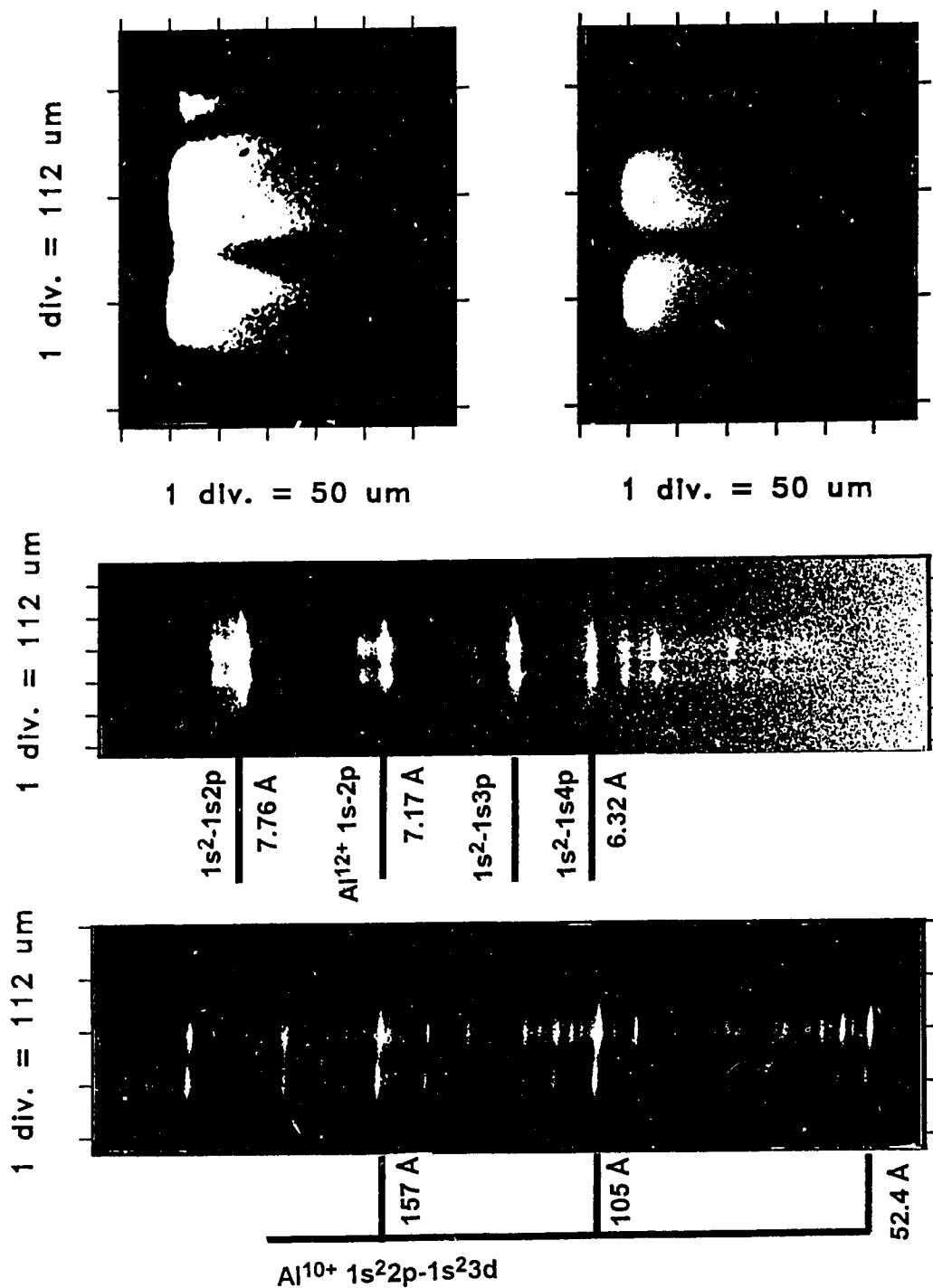
Figure 6.1. Representative x-ray film images recorded by the pinhole camera (top), crystal spectrometer (center) and grazing incidence spectrometer (bottom). The spatial dimensions of the emission region as determined from the magnifications of the instruments are also shown.

109

Descriptive Summary of the Database

A basic premise of these experiments was that the lateral transport and ablation will be reflected in the spatial profiles of the x-ray emission. Typical x-ray images as recorded by the three instruments are shown in Figure 6.1. These data were collected on different shots taken on single-tracered targets. The estimated peak intensities and CH overcoat depths for the shots were, from top to bottom, 3.3, 1.9 and 0.7 $\times 10^{13}$ W/cm^2; and 0.54, 0.48, and 0.24 μm. The pinhole image is dominated by two coronal expansion plumes originating from the directly-irradiated regions of the target. The laser here converges from the right with a bean f# of 15/8. The spectrometer images likewise exhibit two bright regions of emission which originate from the irradiated areas. The dominant features of the crystal spectrometer data are the K shell emission lines from Al^{11+} (1s^2-1snp series) and Al^{12+} (1s-np series). The continuum signal levels were generally faint for this diagnostic. The dominant features in the XUV spectra are the first few diffraction orders of the resonance line of Al^{10+} (1s^{2}2p-1s^{2}3d) at 52.38 $\overset{\text{o}}{\text{A}}$. The continuum levels recorded by the XUV diagnostic represented a significant fraction of the signal.

If the absorbed energy was uniformly redistributed into the target across the intensity modulation, we would expect lateral uniformity in the hydrodynamic flow and x-ray emission of the tracer. This situation clearly does not hold for the examples presented here and, in general, the emission patterns reflected the spatial structure of the incident laser. All three of the diagnostics, however, exhibit a spatial widening of the dominant x-ray features as the CH overcoat of the targets decreased.

In the x-ray pinhole image (top left, Fig. 6.1) one may observe a bright feature adjacent to the target surface between the expansion plumes; this may be interpreted as evidence for lateral heating and ablation in the non irradiated or 'shadow' region of the

target. This feature was not in evidence in all of the pinhole images, but was limited to the target shots of higher energy or lower overcoat depth. For example, the feature is absent from the top right pinhole image of Fig. 6.1, which was recorded from a shot of intensity 2.4×10^{13} W/cm^2 and overcoat depth 0.48 µm. Such observations are be indicative of an upper bound on the extent of lateral heating and ablation (at least to the temperatures needed to produce a significant amount of x-ray emission above 1 keV). The dominant emission features, i.e. the coronal expansion plumes, were typically wider than the irradiation regions. The widths of the plumes may be partly due to ablation occurring in the shadow region; however, the dominant fraction of this emission may be due to lateral advection of the tracer plasma into the shadow region. This becomes most apparent for the case of uncoated targets (see Chapter 8). Nevertheless the lateral profile of the ablation surface (the boundary between the bright and dark regions) also indicates that some widening beyond the nominal 56 µm width of the irradiation strips may have occurred.

The pinhole and spectrometer data were used to make estimates of the typical conditions prevailing in the corona of the targets. The pinhole images represent spectrally-integrated emission chiefly from energies above 1.5 keV, as illustrated in Figure 6.2. In the top graph the beryllium-filtered free-free and free bound continuum emission is plotted for a 500 eV aluminum plasma of electron density 10^{21} cm^{-3} (solid line), along with the transmission function of the filter (dashed line). The emission curve was calculated from equations (2.107) and (2.108) with ionization potentials taken from Kelly and Palumbo (1983). The fractional ion populations were obtained from the RATION code and the free bound emission was evaluated as a summation over the ground states of Be-like to fully stripped aluminum. This is a reasonable
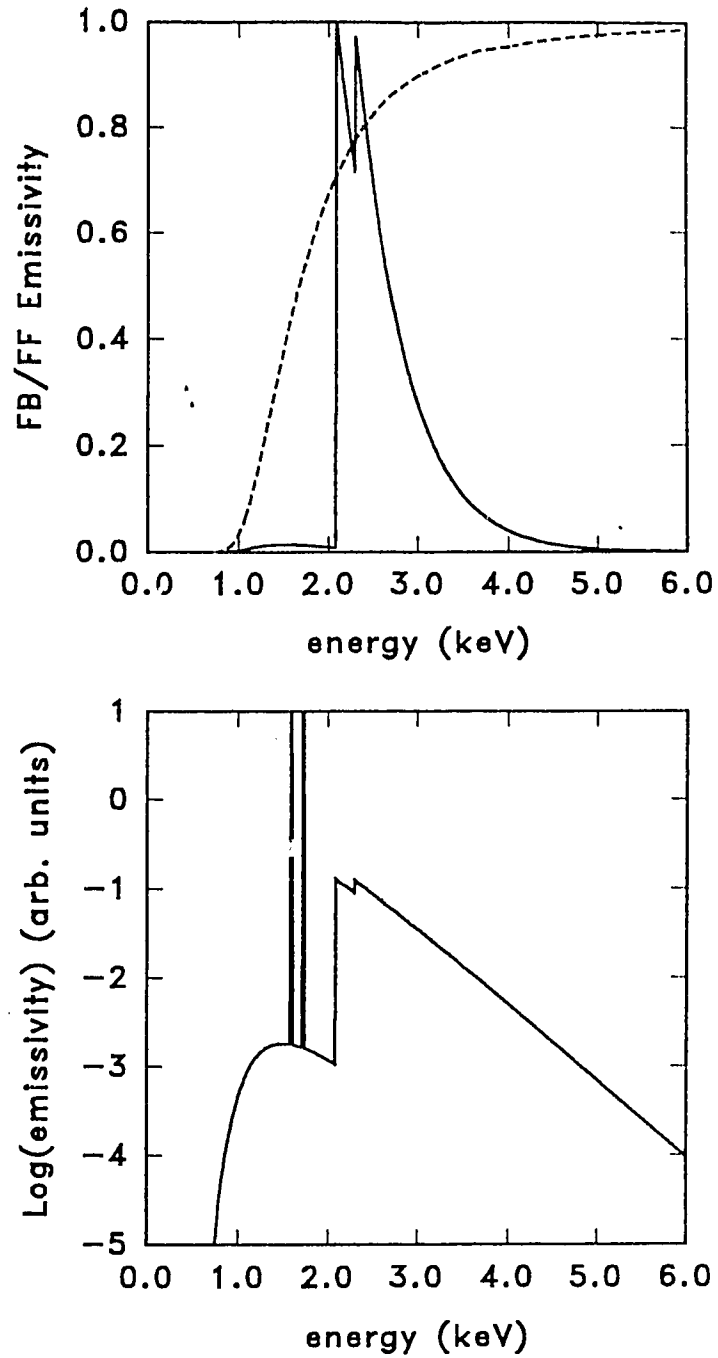
Figure 6.2. Top: continuum emission spectra from a 500 eV aluminum plasma and electron density 10^{21} cm^{-3}, attenuated by a 30 μm Be filter (transmission function shown as a dashed line). Bottom: same as top, but plotted on a logarithmic scale with the two dominant K-shell lines added.

approximation since these populations represent over 90% of the ions present at 500 eV. The larger contribution to the continuum emission originates from recombination into the highly stripped aluminum ions.

The bottom graph in Figure 6.2 shows the filtered continuum emission with the two dominant lines in the spectra (at 1.60 keV and 1.73 keV), calculated from (2.106) and table of transitions in chapter 2. These lines make up ~70% of the total line emission recorded by the pinhole camera. The estimated emissivities for the spectrally-integrated continuum, the 1s-2p line, and $1s^2$-1s2p singlet lines were 8.4, 8.7 and 8.4 $\times 10^{13}$ ergs/sec/Hz/sterad. These values may be taken as estimates of the relative contribution of the line and continuum emission in the pinhole images.

In Figure 6.3 the results from two densitometer scans of pinhole images are presented. The scans were taken in a direction parallel to that of the laser axis and through the center of one irradiation region. Optical densities were converted to photon flux using a published model for the sensitivity of the DEF film (Henke et al., 1986), assuming a monochromatic x-ray source of 2 keV. (This calculation was repeated for several energies, and the shape of the resulting profiles exhibited only a weak energy dependence for energies above 1.5 keV). The solid line is the profile from a 860 ps shot (I_p=3.3x10^{13} W/cm^2) and the dashed line that of a 400 ps pulse shot (I_p=3.8x10^{13} W/cm^2). The profiles were fit to curves of the form exp(-x/L) resulting in e-folding lengths of 51 and 32 μm. These values may be taken as estimates of n_e^2 scale lengths in the corona, where the upper levels of the line transitions are determined by the collisional processes (2.81, 2.82) and cascade decay. The contribution from the continuum emission also scales as n_e^2. The contribution of the continuum may be enhanced by line self opacity effects which will come into play at densities above 10^{19} cm^{-3}. The 1D isothermal CJ model of Chapter 2 predicts
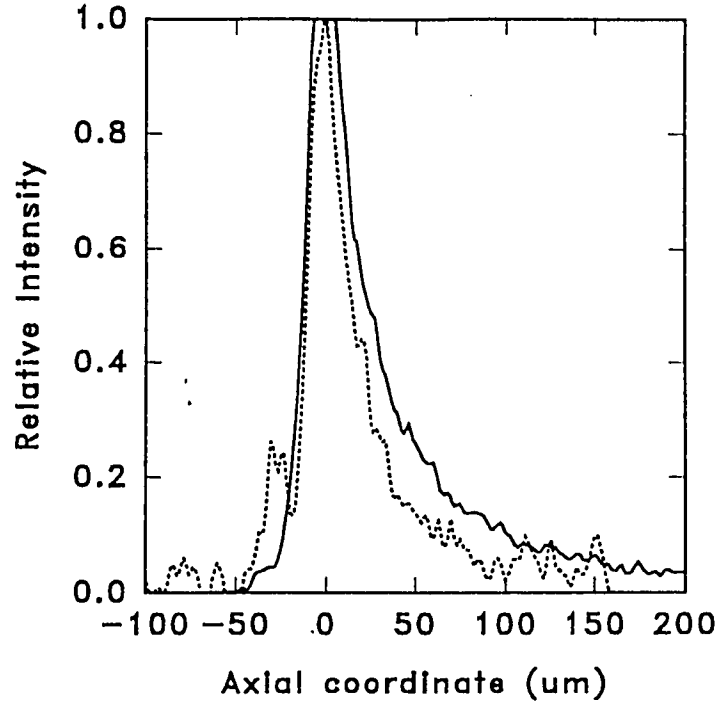
Figure 6.3. Typical axial emission profiles taken from pinhole images of targets irradiated by 860 ps (solid) and 400 ps (dashed) laser pulses.

electron temperatures and scale lengths of 463 eV, 151 μm and 505 eV, 74 μm for the long and short pulse shots, where the scale lengths have been estimated by $C_s\tau$. The corresponding predictions of the self regulating model were 855 eV, 181 μm and 758 eV, 79 μm. The overestimates are partly due to the 3D expansion of the real plasma which results in steeper profiles than would be expected for 1D hydroflow.

114
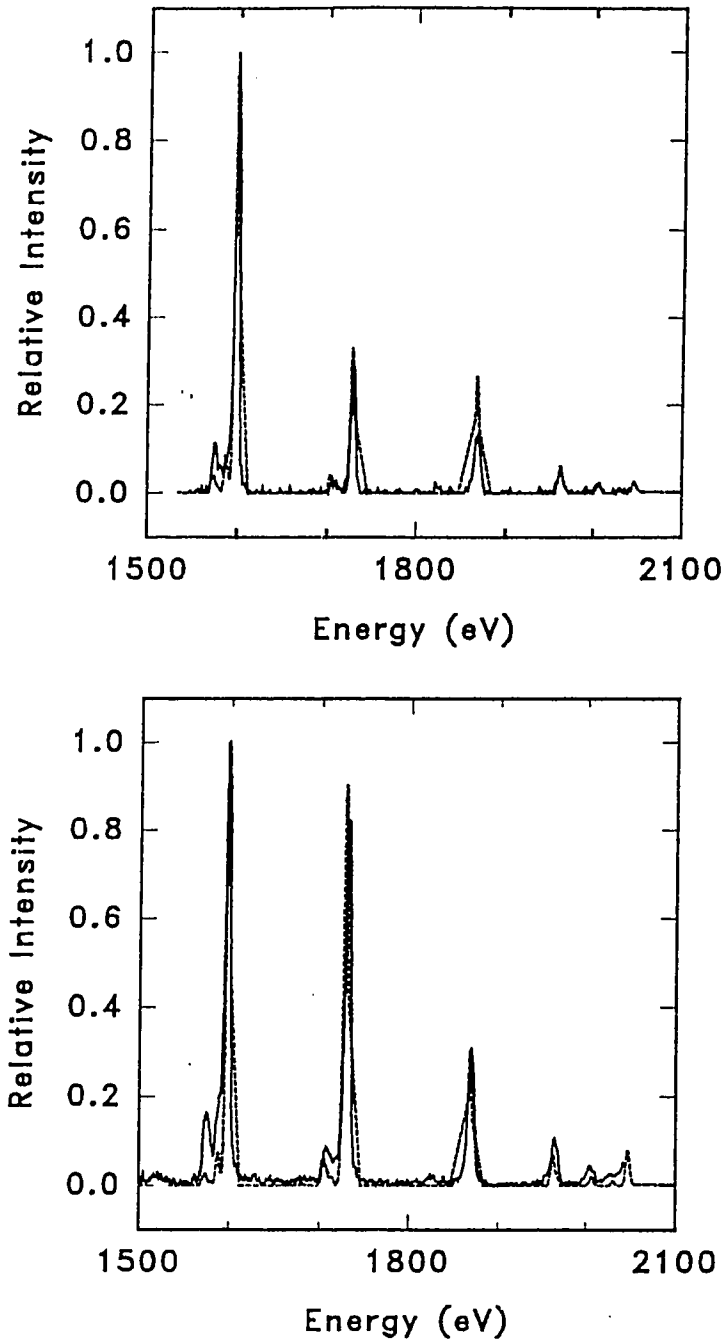
Figure 6.4. Typical aluminum K-shell spectra from targets irradiated at 1.9 and 3.3 x 10^{13} W/cm^2 (pulse width 860 ps) RATION fits to the spectra are represented by dashed lines. An instrumental width of 5 eV was used in the calculation. The best fit electron temperatures and densities were (470 eV, 580 eV) and 4×10^{20} cm^{-3}.

Typical coronal temperatures were estimated from the K-shell line spectra recorded by the crystal spectrometer, and were found to lie in the range 300 - 600 eV. In Figure 6.4 aluminum K-shell spectra are presented from target shots of intensity 1.9 and 3.3 x10^{13} W/cm^2. The x-ray emission originated from the irradiated regions of the targets. The optical densities were converted to relative energy flux and taking into account the DEF film and Be filter response curves and the wavelength dependence of the crystal reflectivity (Henke et al., 1982). The dashed lines are theoretical spectra generated by the RATION code and fitted to the experimental curves. The fits are quite reasonable considering that the spectra represent the time integrated emission from a emitter undergoing changes in temperature and density. The estimated electron densities and temperatures from the fits were 4.0 x10^{20} cm^{-3}, 470 eV, and 4.0 x10^{20} cm^{-3}, 580 eV. These temperatures lie between the predictions of the isothermal CJ model (330 eV, 463 eV) and the self regulating model (649 eV, 855 eV).

Analysis Of Lateral X-ray Emission Profiles

Lateral emission profiles from the resonance lines of Al^{11+}, Al^{12+}, Na^{9+}, and Na^{10+} were obtained by taking densitometer scans in the spatially resolving direction through the lines. The densitometer slit was apertured to collect emission from an equivalent source size of 100 μm (in the wavelength resolving direction) in order to sample a swath of plasma narrower than the focal spot diameter. After conversion to intensity the lateral profiles were deconvolved from the slit function using an algorithm presented by Jones (1967).
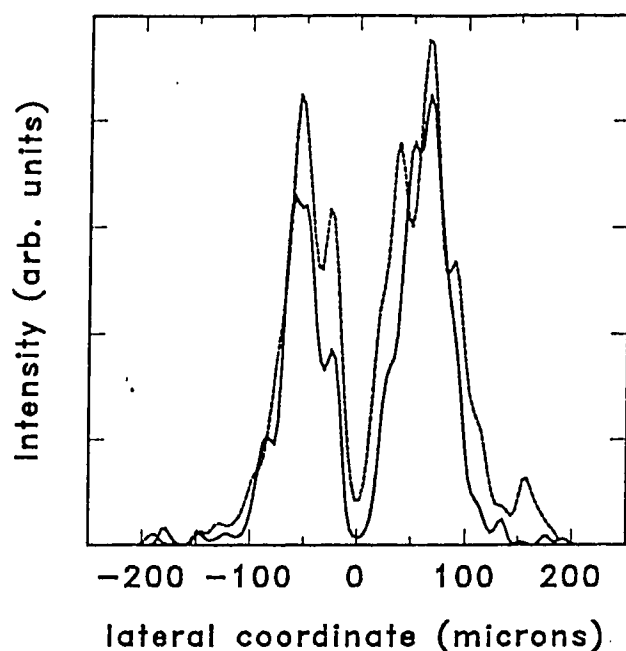
Figure 6.5. Typical lateral emission profiles for the Al^{12+} (solid) and Al^{11+} (dashed) resonance lines as recorded with the crystal spectrometer. The laser intensity and pulse width were 2.3×10^{13} W/cm^2 and 860 ps. For an indication of the intensity profile see Fig. 5.10.

A typical deconvolved intensity profile showing the relative strengths and lateral profiles of the Al^{12+} 1s-2p and Al^{11+} 1s^2-1s2p (singlet) lines are shown in Figure 6.5. Differences as large as a factor of two in the local intensity maxima (originating from the irradiated regions) were often observed in the profiles and implied that the energy of the beam profile was not symmetrically balanced across the modulations. The profiles were characteristically sharply shouldered except for targets with very thin overcoats. The profile widths of the Al^{11+} resonance lines were invariably wider than those of the Al^{12+} 1s-2p line.

The lateral widths of the profiles, defined at one e-folding of the maximum intensity, were plotted as a function of the areal density of the material overlying the tracer layer. These values should be representative of the widths of the ablation region

117

at the time the tracer is ablating. The 860 ps pulse data is shown in Fig. 6.6 with the e-foldings of the Al^{12+} line plotted at top and the Al^{11+} line plotted at bottom. Each data point represents an average of two e-foldings, i.e. one from each of the two high irradiation regions, and the error bars were generated from the discrepancies between these values. A minimum error of 7% could be expected from the target positioning error and this was also considered as a minimum error in the data. The data has also been grouped by incident laser intensity, as indicated in the figure captions.

No clear evidence for the Al^{12+} species beyond the 56 μm width of the irradiated region may be seen from the data. The e-folding of the Al^{11+} line exhibits a weak dependence on the overcoat thickness, possibly indicating lateral heating of the tracer to temperatures below 400 eV, for which fractional populations of the Al^{12+} states are expected to be very low. Clearly, however, there is no indication that there is enough transport of energy in the lateral region to create ablation conditions comparable to those in the irradiation region. This observation is one of the chief results of the experiments. For the intensities and scale lengths of this study, there is insufficient lateral transport to smooth away the effects of non-uniform irradiation.

The dashed curves in the graph illustrate the ablation expected if the beam spillover was absorbed by the lateral substrate. The curves represent the predicted widths of ablation-exposed tracer layers based on the following simple 1D model which neglects lateral transport. An illustrative definition of this width is presented in Fig. 6.7 which represents a cross section of an ablated tracer target (with the tracer layer shaded). The ablation rate is assumed to obey a relation of the form

$$\dot{\rho}_A = a\left(\frac{I_{inc}}{10^{13} \ W/cm^2}\right)^b \qquad\qquad 6.1$$

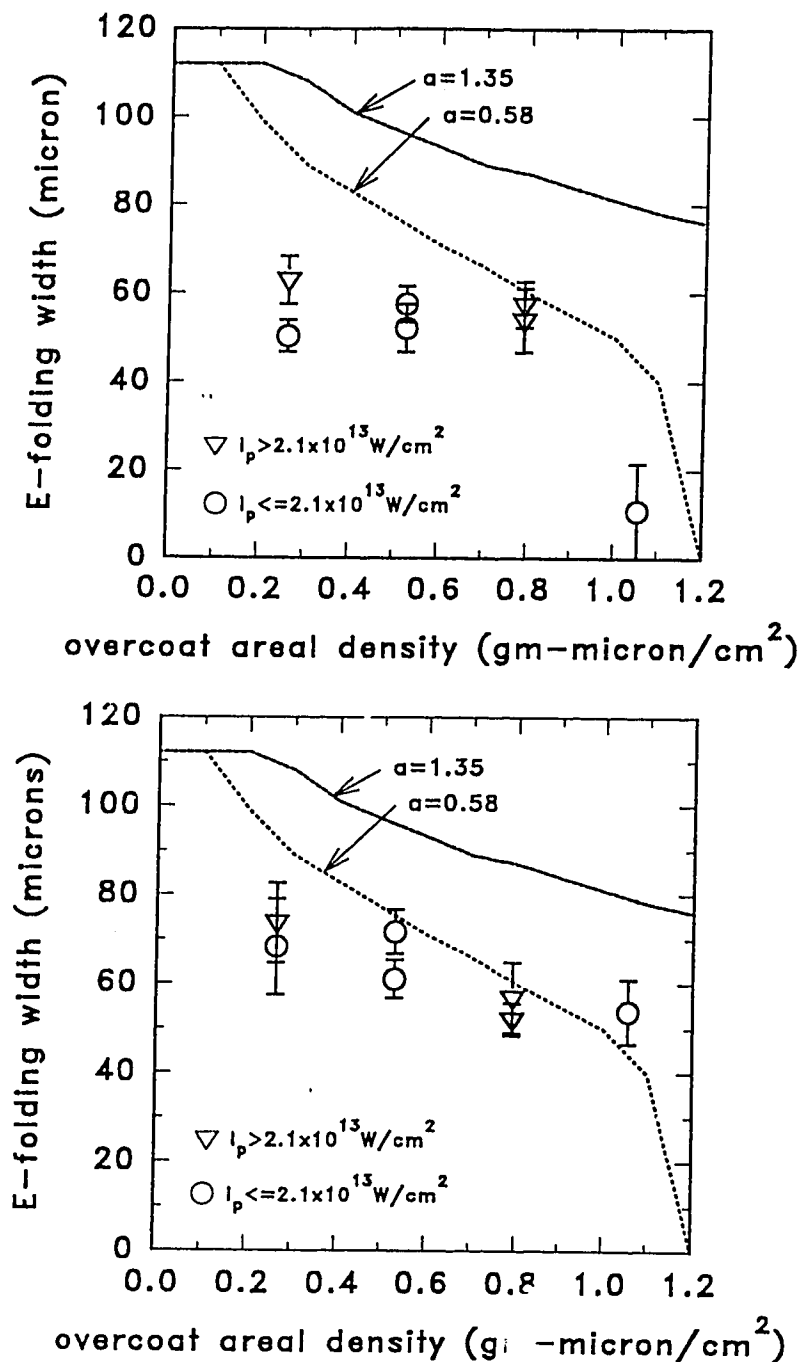which implies a final ablated areal density ρ_A of

Figure 6.6. E-folding widths of emission profiles for the Al^{12+} (top) and Al^{11+} (bottom) resonance lines as a function of the areal density of the overcoat layer. The laser pulse width was 860 ps.

$$\rho_A = \frac{a}{\sqrt{b}} \sqrt{\frac{\pi}{\ln 2}} \frac{\Delta_{FWHM}}{2} \left(\frac{I_p}{10^{13} \ W/cm^2} \right)^b \qquad 6.2$$

assuming a temporally Gaussian laser pulse of peak intensity I_p and full width half maximum Δ_{FWHM}. A spatial intensity distribution was constructed based on the focal spot pattern of Fig. 5.10 and assuming an incident energy of 6 J, (which represents a medium energy for this data base). A lateral ablation profile was constructed from (6.2) using the local intensity determined by the horizontal line through the point of maximum intensity in Fig. 5.10. The scaling parameter b was taken to be 0.33 in accordance with 1D models and experimental studies (Fabbro et al., 1982a; Key et al., 1983).
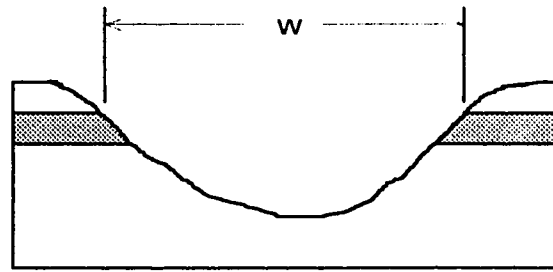

Figure 6.7. Definition of the parameter w plotted in Figs. 6.6 and 6.8.

The two curves were generated with the same intensity profile and with values of the coefficient a of 0.58×10^5 gm/s/cm^2 (suggested by the data of Boehly et al., 1986) and 1.35×10^5 gm/s/cm^2 reported by Key et al. (op. cit.). Both curves lie considerably above the data points and therefore suggest a greater degree of ablation than is implied by the data. A possible reason for this discrepancy, which supported by 2D simulations discussed below, is that the low intensity spillover laser radiation of the shadow region is effectively absorbed in the expanding corona, whose density scale

120

lengths are determined by the higher intensity of the irradiated region. The maximum ablation depths observed in the experiments seem to agree most closely with the results of Boehly et al. (op. cit.).

The corresponding plots for short pulse experiments are shown in Figure 6.8 with the emissivity e-foldings of the Na^{10+} 1s-2p line (open symbols) and Al^{11+} $1s^2$-1s2p line (filled symbols) plotted at top and those of the Na^{9+} $1s^2$-1s2p line plotted at bottom. The emission from the Al layers were generally faint and the Al 1s-2p line was generally absent, indicating somewhat lower temperatures than in the long pulse shots. The data is again grouped by energy and, in contrast with the data of Fig 6.6, exhibits some evidence of energy dependence, with wider e-foldings observed at higher incident energies. In general, the widening of the emission profiles is more marked than in the case of the longer pulse data. This may partly be due to the shorter plasma scale length which should result in more efficient coupling of the laser to target. For these short pulse target shots there was less time to set up an absorbing corona in the shadow region and the spillover irradiation may have contributed to the lateral heating of the target. The distribution of the Na^{9+} e-foldings generally follows the dashed lines, which were generated as described before, assuming a representative energy of 3 J and laser pulse width of 400 ps. If the lateral substrate is heated to temperatures below 200 eV, the fractional populations of the Na^{9+} ion will dominate those of Na^{10+} and we might expect the behavior seen in Fig. 6.8.

The XUV data which captures the emission from lower ionization states continues the trend of Fig. 6.8. Spatial modulations in the profiles of the lithium-like tracer lines are essentially smoothed away in shots of intensity exceeding 10^{13} W/cm^2. Lateral scans through the Al^{10+} $1s^22p$-$1s^23d$ line and adjacent continuum from two 860 ps shots may be seen in Fig. 6.8. The estimated intensities for these shots were 0.7 and 3.3 x10^{13} W/cm^2.

Figure 6.8. E-folding widths of emission profiles for the Na[10+] and Al[11+] (top) and Na[9+] (bottom) resonance lines as a function of the areal density of the overcoat layer. The laser pulse width was 400 ps.
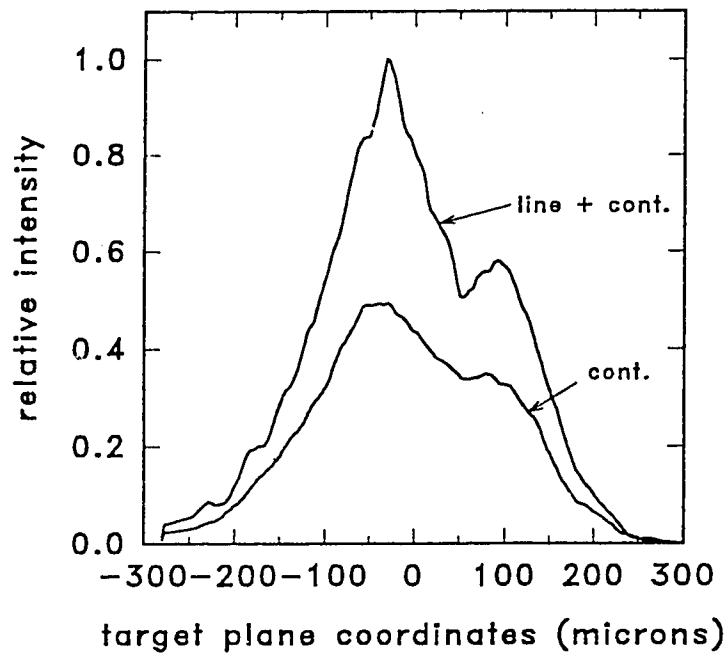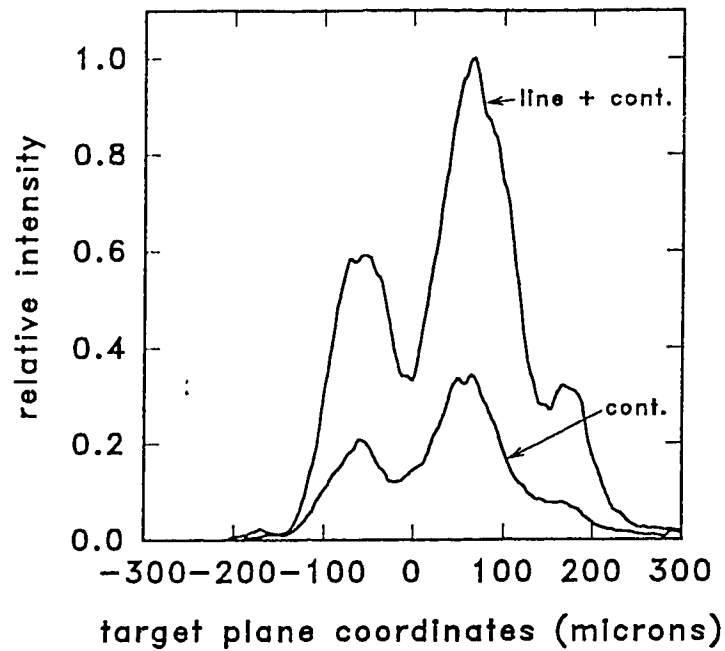
Figure 6.9. Typical lateral emission profiles for the Al^{10+} resonance line. The laser intensities for these shots were 0.7 and 3.3 $\times 10^{13}$ W/cm^2 (pulse width 860 ps). The nominal intensity profile is shown in Fig. 5.10.

IZANAMI: A 2D Fluid Particle Code

Because of the complex nature of the laser target interaction it was desirable to use 2D hydrodynamic simulations to aid in the interpretation of the measurements. For this purpose the IZANAMI fluid particle code developed at the Institute of Laser Engineering was used. This code is based on an improved particle-in-a-cell implementation of the Navier Stokes equations (Nishiguchi and Yabe, 1983). The hydrodynamic variables are defined over an Eulerian (and generally non-uniform) mesh as cell centered quantities. Mass, momentum, and energy are advected through the motion of finite sized fluid particles which have associated with them only a set of coordinates, a mass, and an equation of state.

The hydrodynamics is time stepped forward in two phases. In the first phase the local velocity and internal energy are advanced according to a finite differenced form of the momentum and energy equations (for the sake of brevity terms such as thermal conduction, laser absorption, radiative loss will not written be out). The fluid is assumed to be stationary during this phase and the advection terms are dropped. The momentum equation is advanced in time according to

$$\rho_{i,j}^n \frac{V_{xi,j}^{n+1} - V_{xi,j}^n}{\Delta t^n} = -\frac{1}{\Delta x_i^n}\left(P_{i+1/2,j}^n - P_{i-1/2,j}^n\right) \qquad 6.3$$

$$\rho_{i,j}^n \frac{V_{zi,j}^{n+1} - V_{zi,j}^n}{\Delta t^n} = -\frac{1}{\Delta z_i^n}\left(P_{i,j+1/2}^n - P_{i,j-1/2}^n\right) \qquad 6.4$$

where the indices i and j label the cells along the two spatial coordinate x and z, and n labels the timestep. Quantities evaluated at cell centers and cell boundaries have integer and integer plus 1/2 subscripts respectively. Next the energy equation is advanced in time using the velocities averaged between timesteps n and n+1:

$$\rho_{i,j}^{n} \frac{E_{i,j}^{n+1} - E_{i,j}^{n}}{\Delta t^{n}} = -\frac{\left(P^{n}\overline{V}_{x}\right)_{i+1/2,j} - \left(P^{n}\overline{V}_{x}\right)_{i-1/2,j}}{\Delta x_{i}^{n}} - \frac{\left(P^{n}\overline{V}_{z}\right)_{i,j+1/2} - \left(P^{n}\overline{V}_{z}\right)_{i,j-1/2}}{\Delta z_{j}^{n}} \qquad 6.5$$

In the second Lagrangian phase, the position of each particle p is advanced according to

$$X_{p}^{n+1} = X_{p}^{n} + V_{p}^{n+1}\Delta t^{n} \qquad\qquad 6.6$$

where V_{p}^{n+1} is an area weighted velocity which accounts for overlapping of a single particle into adjacent cells due to the finite size of the particle. As the particles are advected from one cell to another, the momentum and energy carried with them are subtracted and added to the proper Eulerian cells. In this way the basic hydrodynamic scheme is strictly momentum and energy conserving. The particular differencing scheme outlined above has been demonstrated to exhibit good numerical stability (Harlow,1964). The essential improvements added by Nishiguchi and Yabe involved the weighting algorithm applied during the Lagrangian phase of the time step, and resulted in a reduction of artificial viscosity, numerically generated noise, the number of particles needed in a simulation.

An ideal gas equation of state for the electrons and ions is assumed in IZANAMI. An average ion hybrid model developed by Itoh and co-workers (1987) is used to describe the atomic physics. The model has been shown to exhibit good agreement with steady state CR models. A diffusion model of radiation transport is also incorporated into the code.

The magnetic field behavior is also modeled in IZANAMI (Nishiguchi et al., 1984). Fields are evolved through a finite differenced version of (3.7). The Braginskii model outlined in chapter 3 is used to simulate the effect of the fields on the energy transport.

125

Simulation Results

Due to the diagnostic constraints discussed in the first section of this chapter, there was no single target shot for which the spatially-resolved emission was obtained by all instruments. Partly because of these constraints, the parameters chosen for the simulations reflect representative rather than specific beam/target conditions.

The simulations were run on a non-uniform Eulerian grid of dimension 30 radial x 69 axial cells with CH and aluminum particles initially distributed to simulate single tracer layered targets. The axial (z) and lateral (x) dimensions of the simulation domain were 730 μm and 112 μm. The spatial profile of the laser was a step function deposited in the central 56 μm of the domain. The laser pulse was temporally Gaussian (Δ_{FWHM}=860 ps) and was switched on at t=$-1.5\Delta_{FWHM}$ = -1290 ps, where the temporal origin has been defined at the peak of the pulse. The peak incident laser intensity of 3.3×10^{13} W/cm^2 corresponded to that of the higher energy shots in the data base. The laser absorption mechanism was assumed to be inverse bremsstrahlung, with 100% reflection assumed at the critical surface. Beam refraction was not modeled in the simulations due to limitations on the numerical resources. However the growth and influence of the magnetic fields was included in the simulations. A reflective boundary condition was applied at the boundaries parallel to the laser axis. Fluid particles reaching these boundaries were reflected with momentum change $P_x \rightarrow -P_x$, $P_z \rightarrow P_z$. A flux limiter of 0.1 was applied to the thermal conduction in both directions.

The remaining figures in this chapter deal with the results of a single simulation for which the CH and aluminum fluid particles were initially distributed to simulate a 0.1 μm tracer buried under 0.54 μm of CH. Contour plots of electron temperature and density and average ionization state are used to illustrate the time evolution of the

system (Fig. 6.10). These are displayed in five pages representing the simulation times t = -840, -240, +60, +360, and +810 ps. The contour plot domains for this and subsequent figures are of size 112 x 224 μm with vertical and horizontal tick spacings of 28 μm and 25 μm. The laser propagates from the right within the central 56 μm of the of the simulation.

The plots from top to bottom display T_e, n_e and $\overline{Z}$. At the beginning of the pulse, the ablating plasma quickly undergoes 2D expansion, establishing a corona in both the irradiated and shadow regions. In the first set of plots the adjacent plasmas have just begun to collide at the lateral boundaries. The electron temperatures at this point are still moderately low. In the ensuing plot one may see the growth of the temperature and density scale length. A gradual lateral smoothing of both temperature and density contours may be observed as the simulation progresses. The density e-folding at t=60 ps is consistent with the nominal value of 51 μm obtained form the x-ray pinhole image. The time history of the ablating aluminum tracer is revealed in the ionization plots. The contour $\overline{Z}$=4 may be interpreted as the boundary between the aluminum and CH which is essentially fully ionized to 3.5 in the corona. The tracer begins to ablate at about -300 ps and has finished by the time of the third plot (+60 ps). There is just sufficient lateral transport of energy to ablate away the tracer in the non-irradiated region during the falling phase of the laser pulse. The last of the tracer is ablating at t=+810 ps. By way of comparison, in a second simulation run under identical laser conditions but with a target of 0.12 μm overcoat, the lateral tracer layer ablates away 100 ps after the peak of the pulse. The ionization state of this plasma is less than 9, and the electron temperatures less than 300 eV. This would imply low population levels in the highest ionization states of the tracer which is consistent with experimental observation. Since the experimental intensities were typically less than
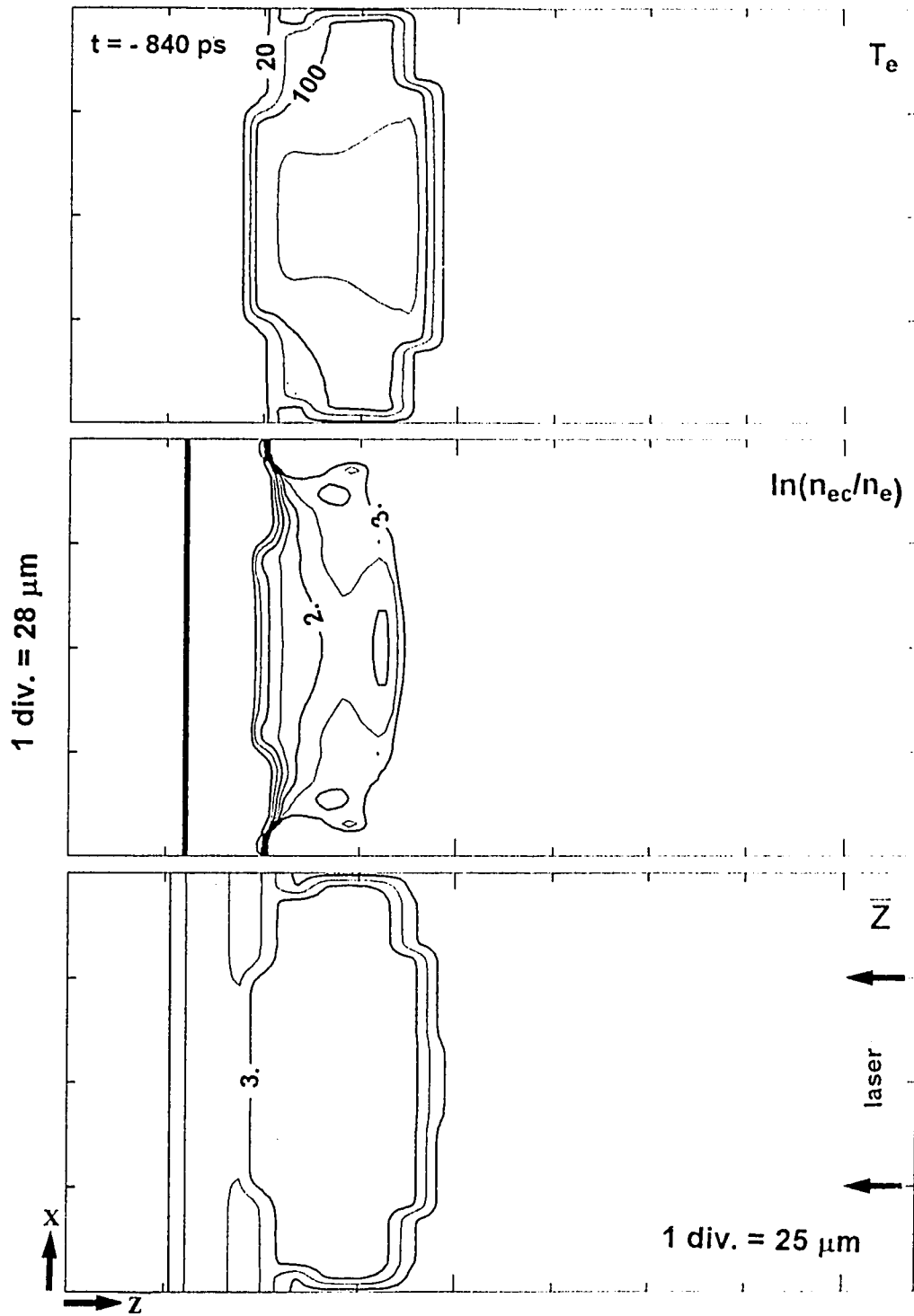
Figure 6.10. Contour plots of T_e (top), n_e (center), and $\overline{Z}$ (bottom) for five simulation times, as predicted by IZANAMI. The simulation parameters are described in the text.

128

Fig 6.10b   1 div. = 25 μm

129

Fig 6.10c

1 div. = 28 μm

1 div. = 25 μm

t = 60 ps

T_e

$\ln(n_{ec}/n_e)$

$\bar{Z}$

Fig 6.10d

1 div. = 28 μm

1 div. = 25 μm

Fig 6.10e

t = 810 ps

T_e

100

400

$\ln(n_{ec}/n_e)$

0.

1.

$\bar{Z}$

3.

5.

1 div. = 28 μm

1 div. = 25 μm

132
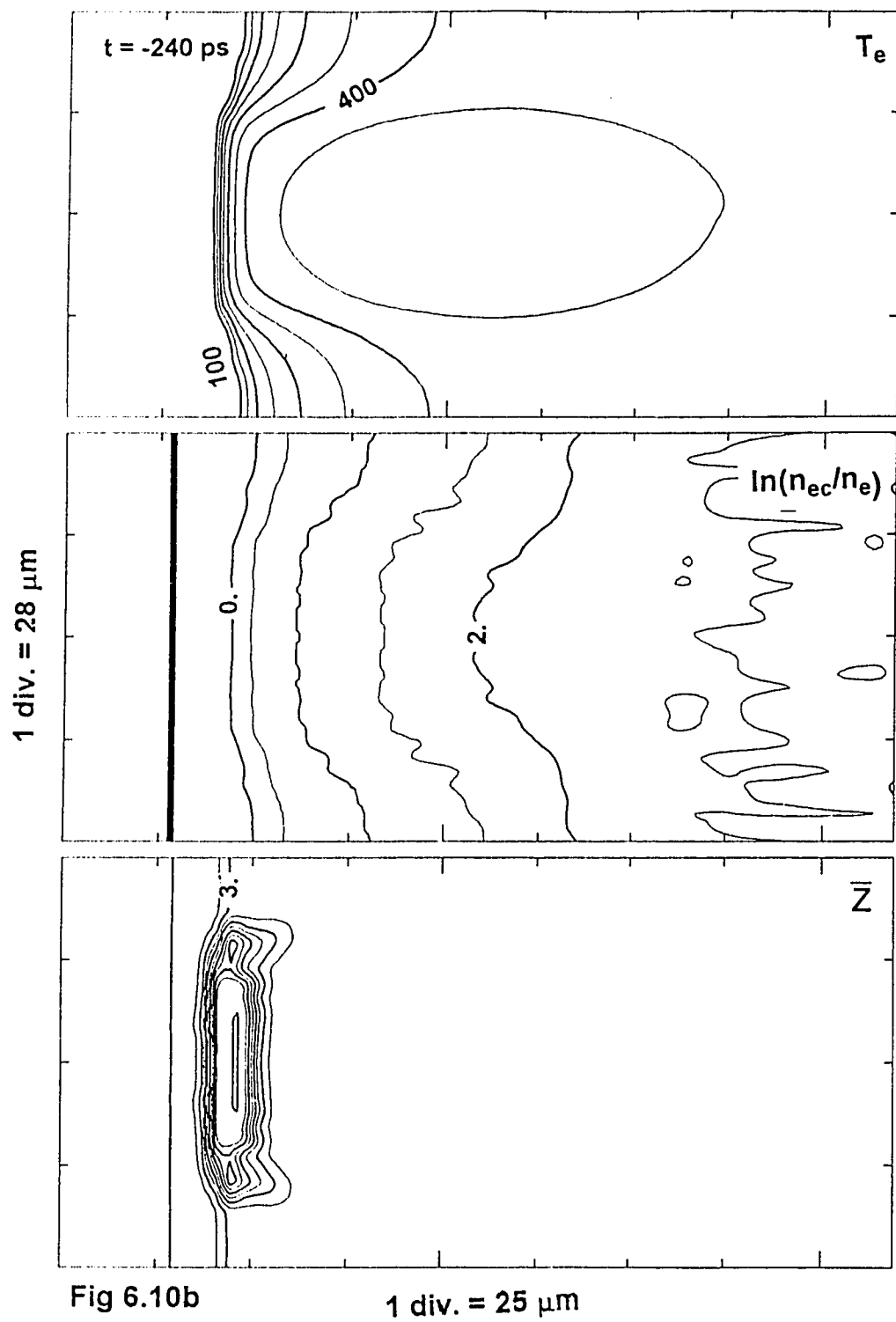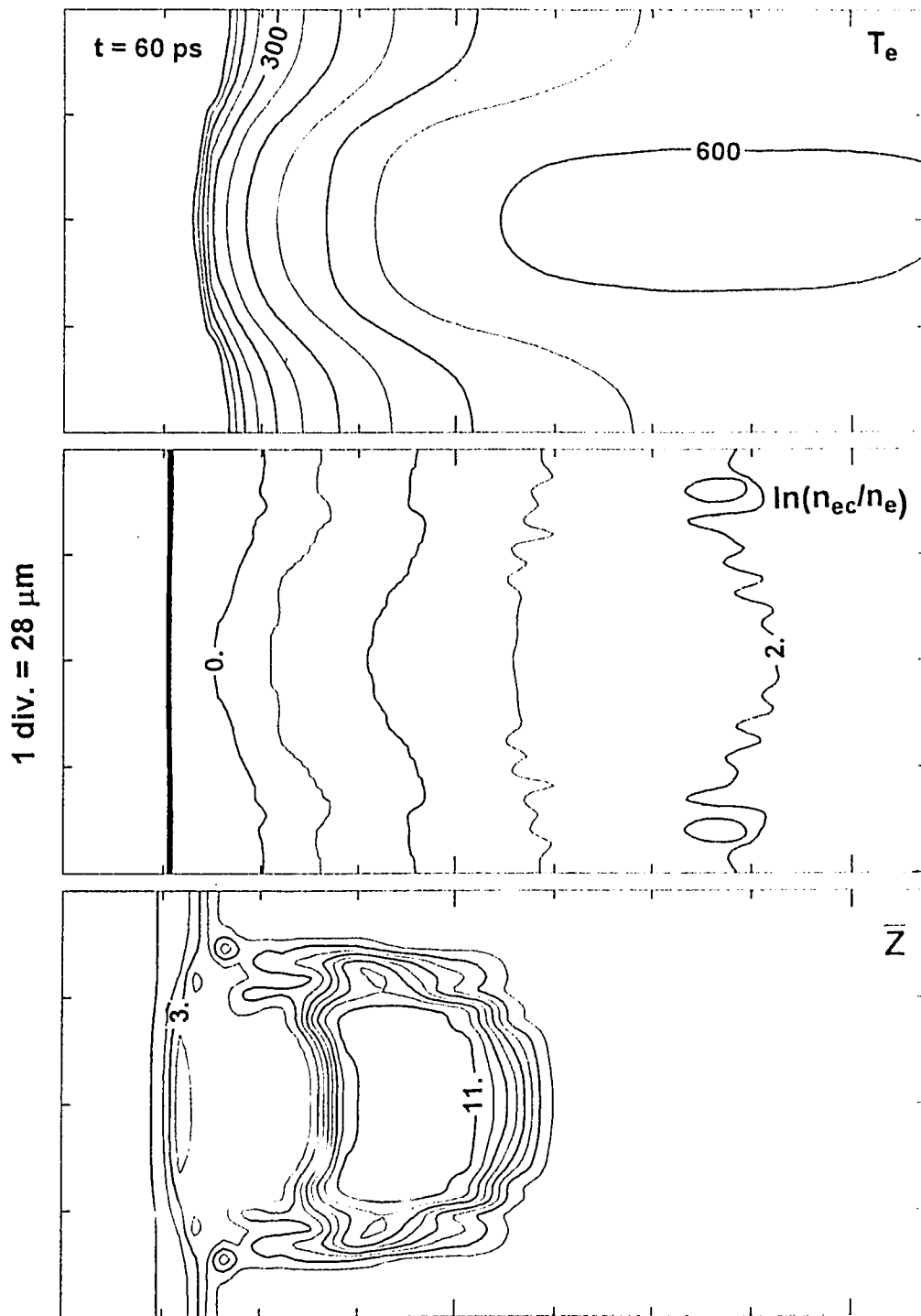
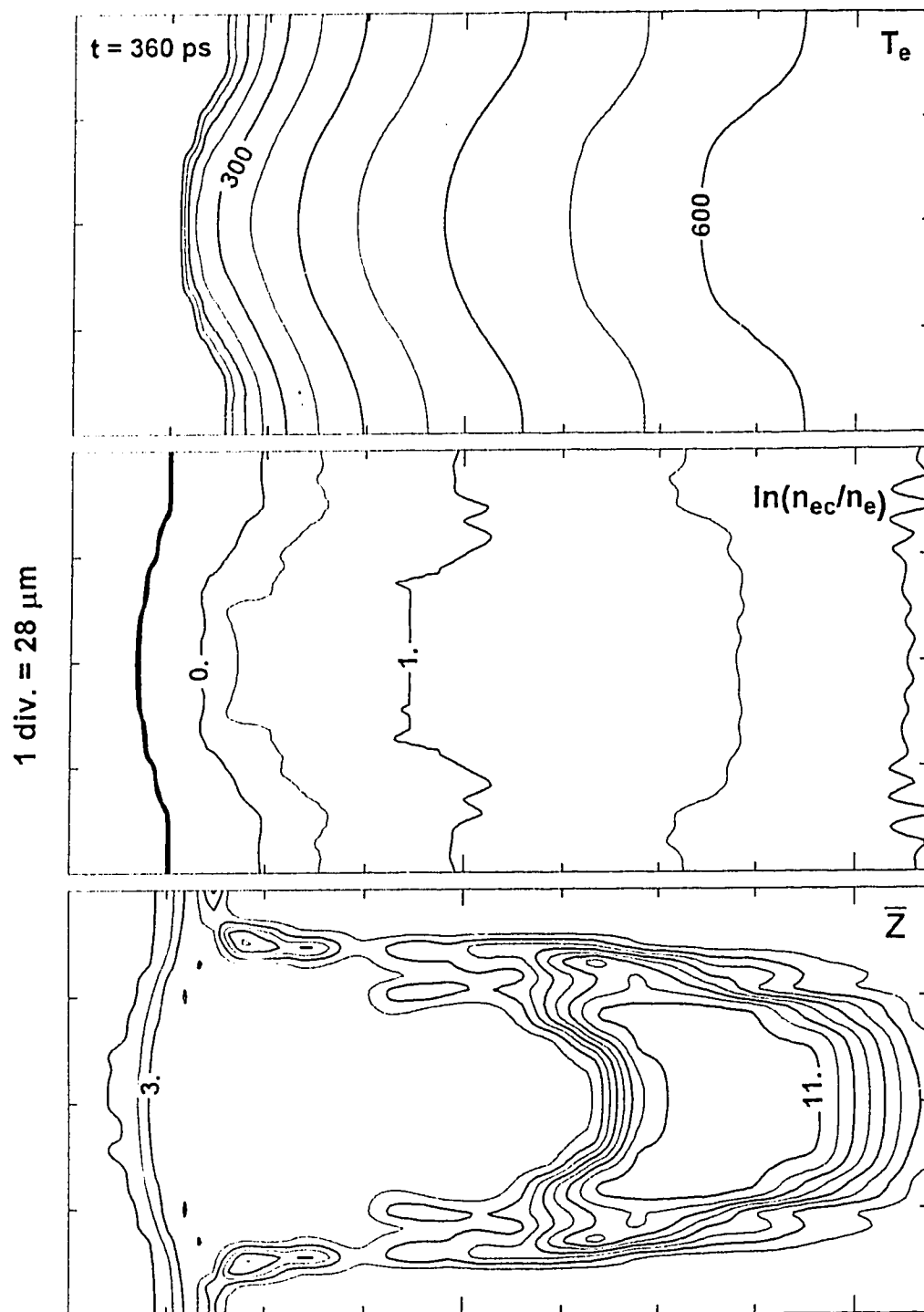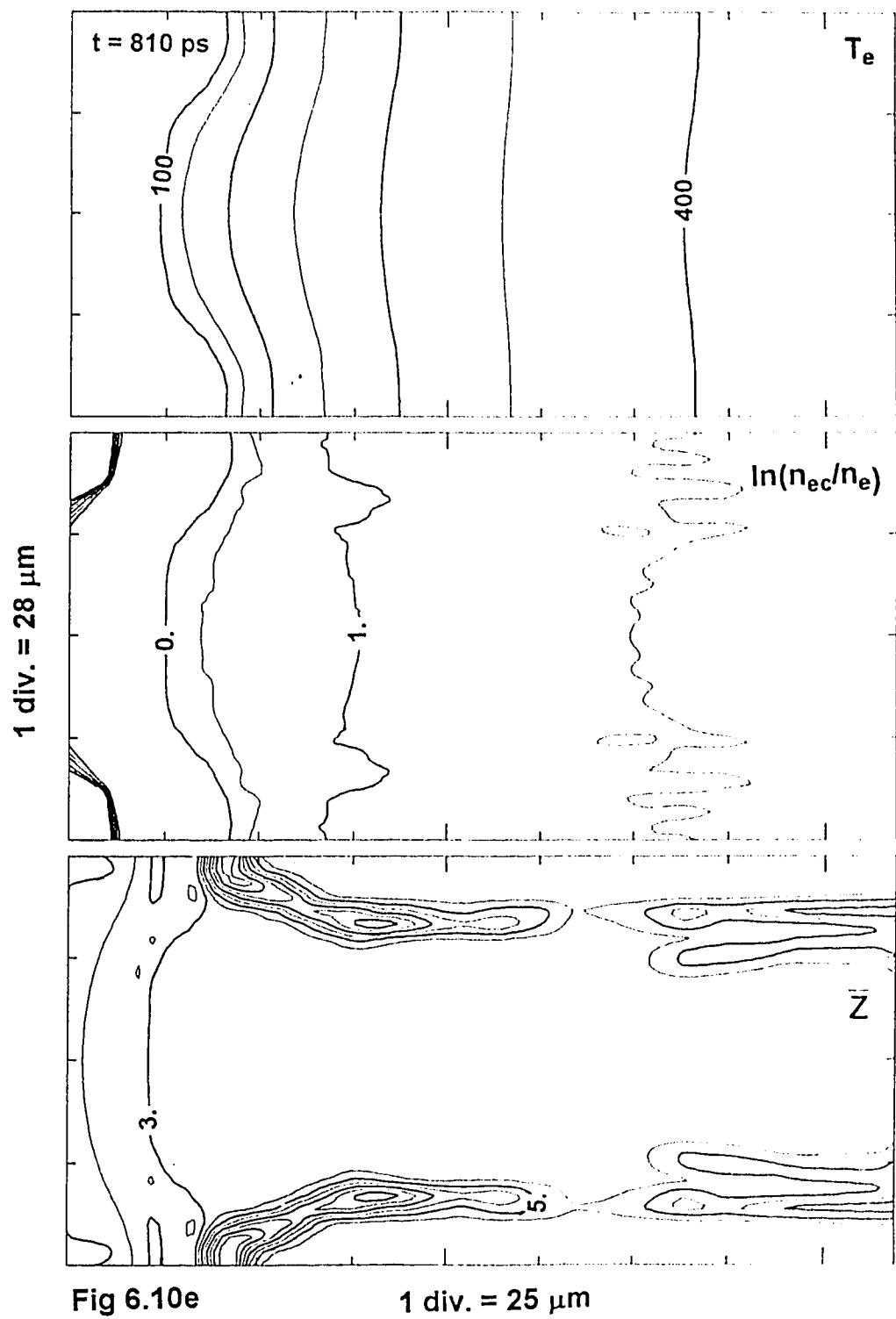that used in this simulation, the expected ablation in the lateral region would be restricted to areal densities below 0.6 gm-μm/cm^3. This is consistent with the experimental e-folding plots of Fig. 6.10(b) which exhibit widening of emission patterns only below this value.

We now turn to an assessment of lateral transport mechanisms. Apart from laser absorption, the transport is dominated by advection and electron thermal conduction. For the typical plasma scale lengths of about 50 μm, most of the laser absorption occurs in the region between 20 to 100 μm downstream from the critical surface. The thermal energy is transported from this region to the target along rather moderate temperature gradients and against the hydrodynamic flow. Since the separation between target and absorption region is comparable to the spatial intensity modulation, one might anticipate that absorbed laser energy could be distributed laterally across the target.

We first look at the laser irradiated ablation region, since the bulk of the inward transport occurs there, and later consider the global picture. In order to assess the role of hydrodynamic transport, the energy advected through the faces of a rectangular subdomain of dimension 56 μm x 28 μm was calculated. The subdomain was located in the central irradiated region and positioned along the laser axis to extend from the ablation surface into the underdense corona. Although this construction is somewhat arbitrary, it allows comparison of the lateral and axial advection through equal surface areas in close proximity to the ablation region. In Fig 6.11 the cell-averaged advection flux $v(\rho e + \rho v^2/2) \cdot \hat{n}$ through the axial and lateral faces of the subdomain is plotted as a function of simulation time. Here $\hat{n}$ is the outward pointing unit vector of the surface. Also plotted is the laser flux $I_{inc}/4$ and the total lateral heat flux through the lateral boundary $q \cdot \hat{n}$ calculated using (3.8).

133
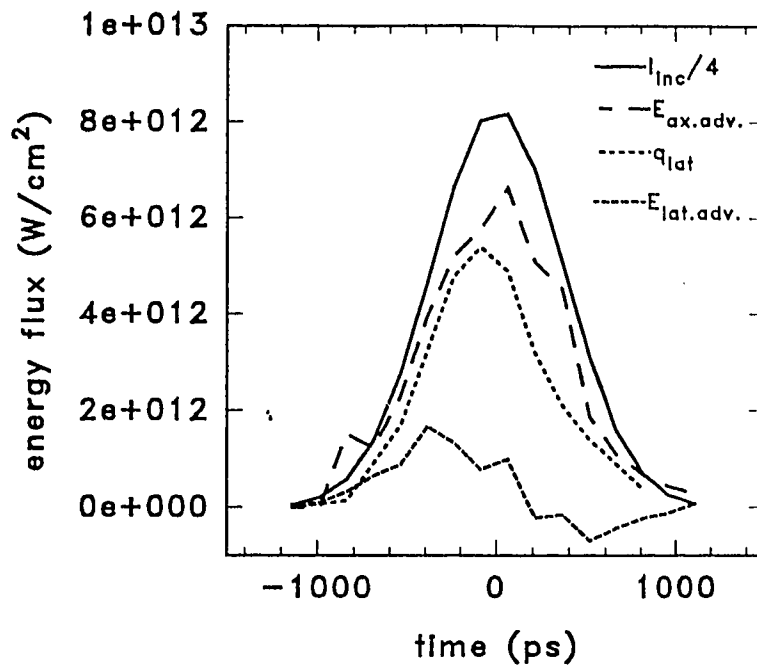
Figure 6.11. Numerical estimates of the axial and lateral energy transport in the vicinity of the ablation surface.

The axial advection dominates over the lateral advection term. The abrupt drop in the lateral advection term after the laser pulse is due to a reversal in the direction of the net hydrodynamic flow in the underdense corona. The dominant lateral transport mechanism throughout the pulse is thermal transport which comparable in magnitude to the axial advection term and represents a significant fraction of the incident laser energy. However, the ensuing plots indicate that the coupling of this energy into the lateral substrate is limited.

With the aid of additional contour plots we are provided with a more global view of the transport processes. First, the growth of the B-fields are illustrated in Fig. 6.12. The field's direction is normal to the plane of the plot; the direction of the field vectors are indicated in the figure. The plots represent the field structure at times $t = -840, -240, +60$ ps. Mass density contours of 0.5 gm/cm^3 are also added to show the approximate position of the target. The fields grow by the $\nabla n \otimes \nabla T$ effect at the boundary between the irradiated and non irradiated regions, and reach peak values of 7×10^5 gauss early in the simulation. These field strengths are not sufficiently strong to seriously effect the transport near the target surface, as is evident in the next series of plots.

The essential characteristics of the energy transport are plotted in Fig. 6.13. All six plots represent the situation at 60 ps. Contours of $n_{e\ crit}$ and $10n_{e\ crit}$ are also shown and densities above critical are lightly shaded. The first two plots (a) and (b) are the inhibition factors along the temperature gradient, namely

$$\frac{1+(\gamma_1'/\gamma_0')(\omega_e\tau_e)^2}{1+(1/\delta_0)\left(\delta_1'(\omega_e\tau_e)^2 + (\omega_e\tau_e)^4\right)} \quad \text{and} \quad \left(1 + \left|\frac{K\nabla T_e}{fq_{fs}}\right|\right)^{-1}.$$ Although the inhibition due to the magnetic fields is considerable in the underdense region of the corona the outward axial flow of plasma effectively decouples the thermal transport of this region from the target. The classical flux inhibition factor influences transport in the ablation regions more strongly. In the lateral ablation region the inhibition factor is moderate with values generally above 0.6.

The axial and lateral components of the heat flux q are plotted in Fig (6.13c) and (6.13d). A significant amount of axially directed heat transport occurs in the shadow regions of the target. However, the degree to which this energy is transported into the target is limited by the hydroflow, as illustrated in the next plots which represent the sum of the advection and heat transport terms in the axial and lateral

directions When the advection terms are summed to the heat transport terms the axial and lateral directions (plots (6.13e) and (f) respectively). In plot (e) the contour of value 0 defines the region of inward transport, may be seen to lie in close proximity to the critical density surface. This region of inward transport is characterized by high electron density, temperature below 300 eV, and inward energy flux below 10^{12} W/cm^3. Under such conditions only a small amount of ablation can be expected in the lateral region.
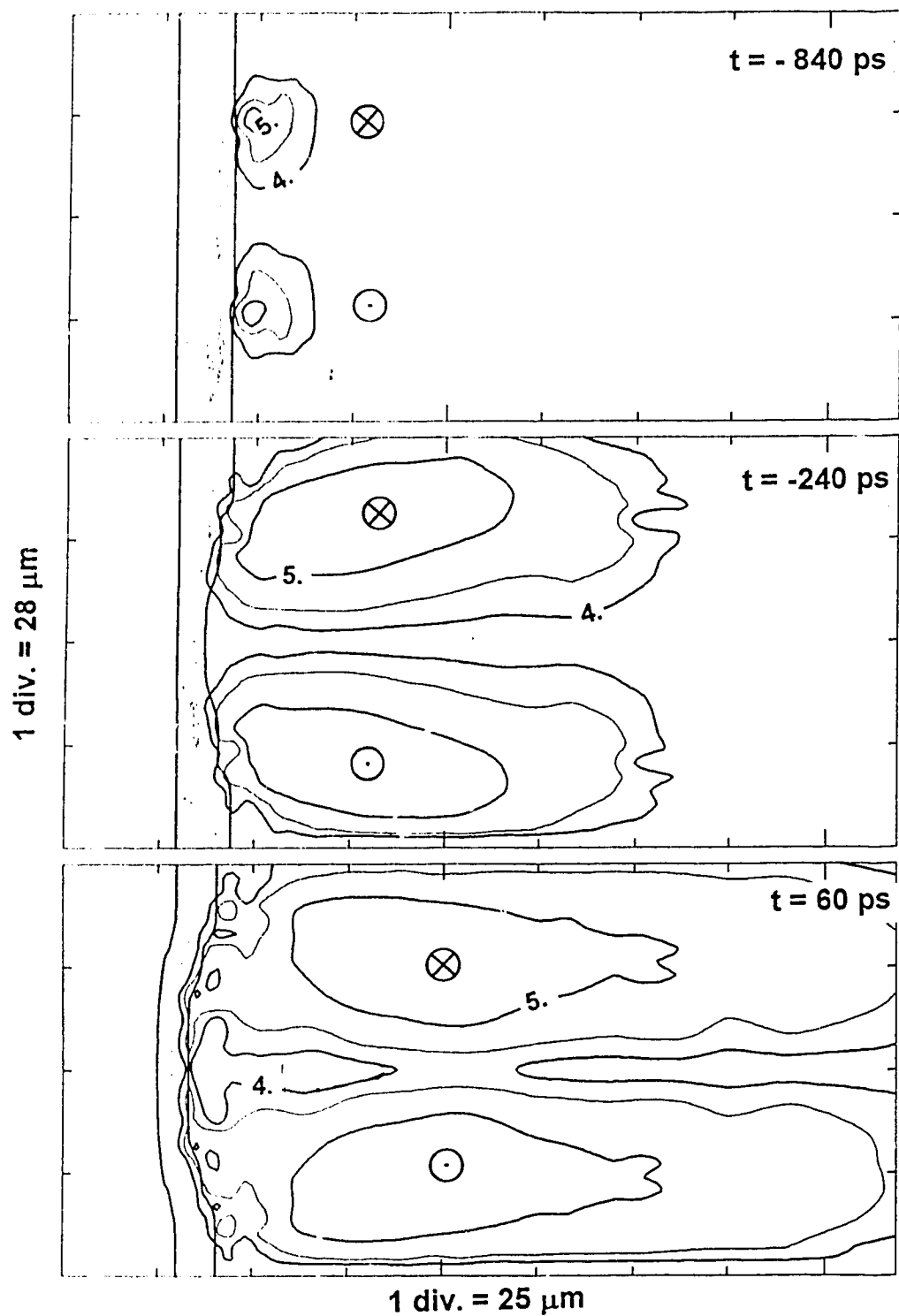
Figure 6.12. Contour plots showing the development of the magnetic fields. The units are log(|B/gauss|).
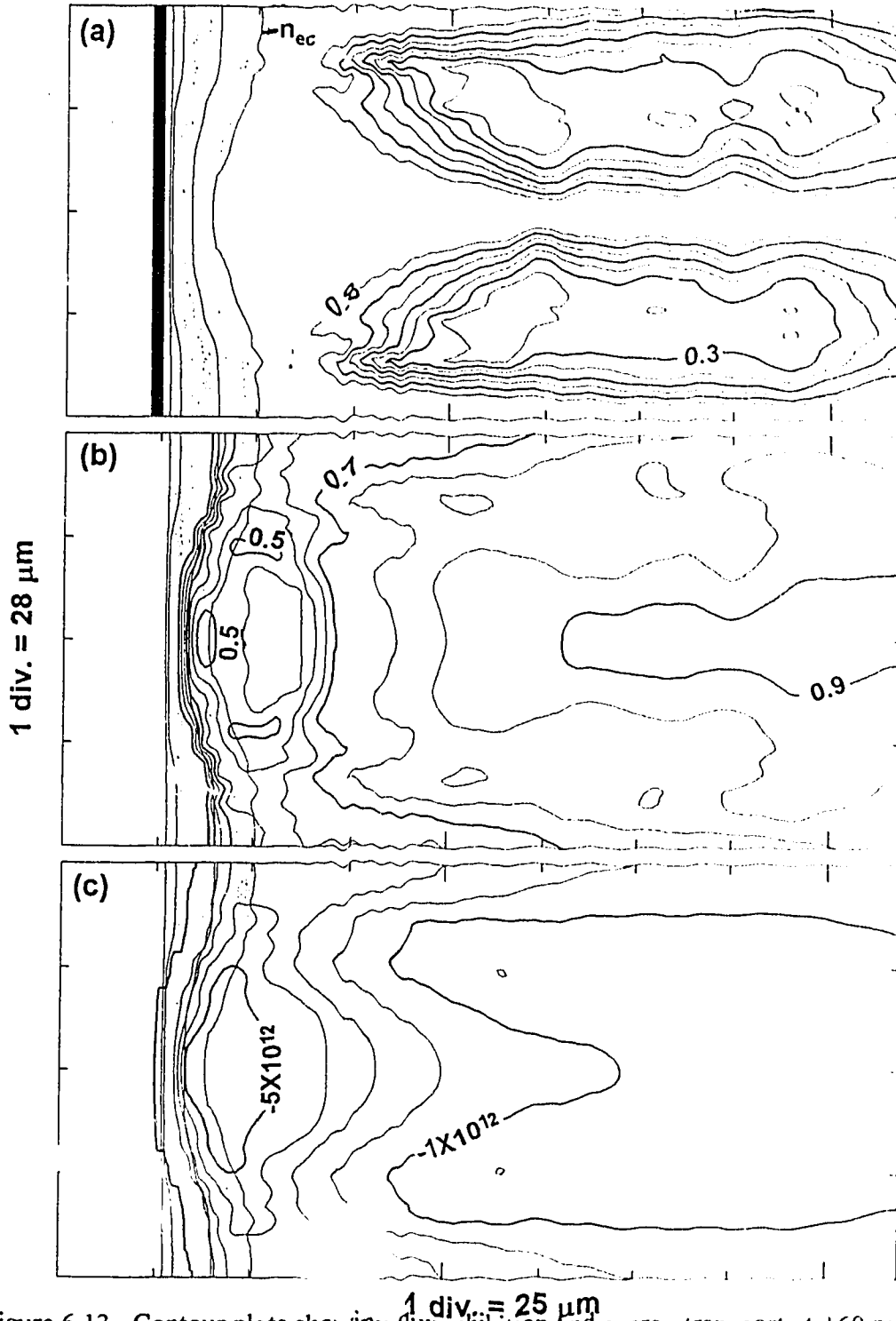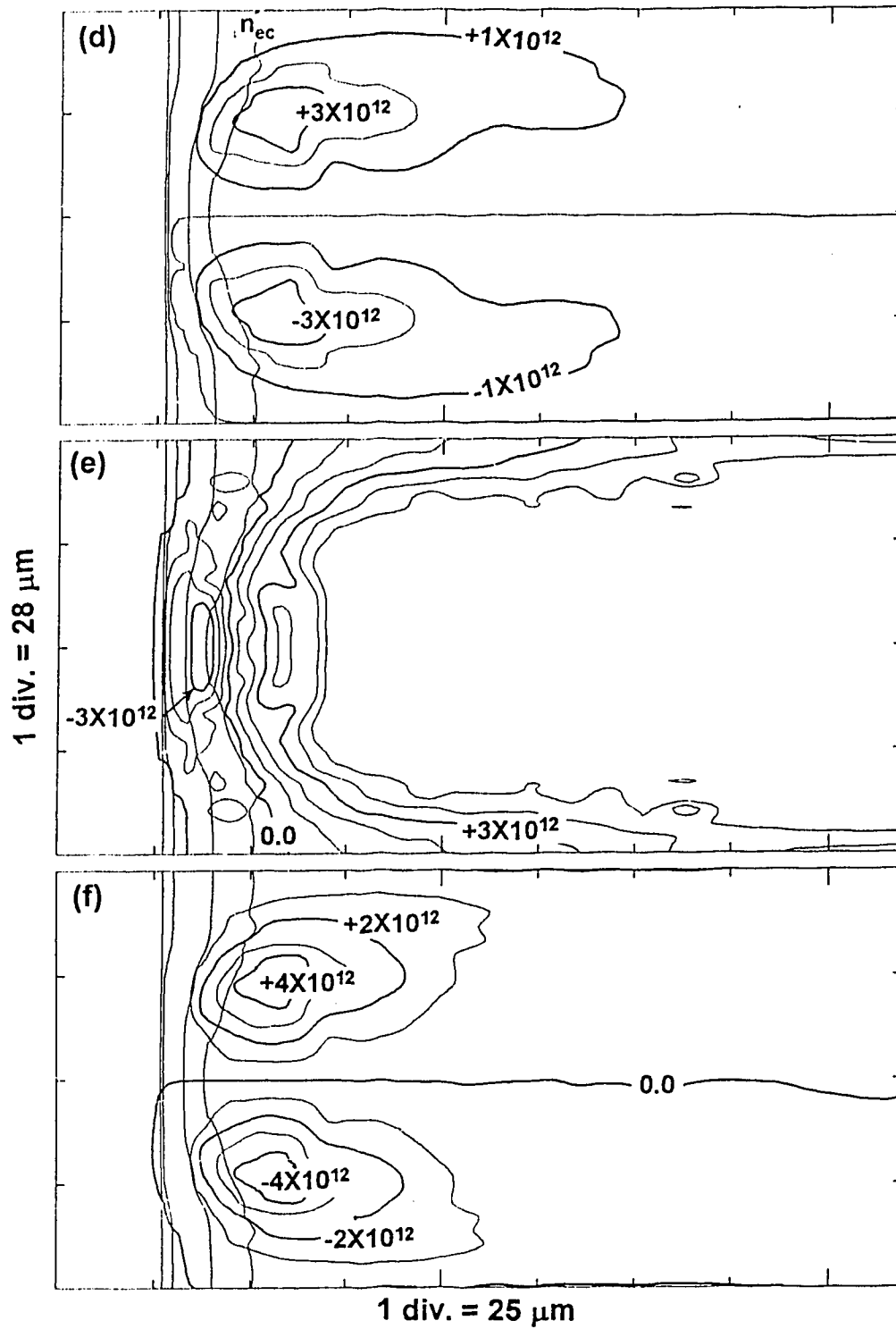
Figure 6.13. Contour plots showing flux inhibition and energy transport at +60 ps: (a) Braginskii inhibition factor; (b) classical inhibition factor; (c)/(d) q_z/q_x in W/cm²; (e)/(f) axial/lateral components of $(q + \rho(e+v^2/2)v)$ in W/cm².

138

139

7. Tight Focus Experiments

Experimental Results

The measurements taken in the tight focus experiments give a somewhat less systematic database, since low signal levels presented a serious obstacle and several revisions in the beam/target conditions were required throughout the course of study. Despite these limitations, evidence for heating of the target in the vicinity immediately surrounding the laser spot was observed. This heating appears to be related to the expansion of a hot plasma sheath along the target surface.

The first tight focus shots were taken on thin CH foil targets of thickness 2 μm upon which tracer bars of aluminum or beryllium were evaporated. The tracers typically consisted of dual parallel bars or annular arcs of areal dimension 50 μm x 200 μm (or 50 μm x 120°) and depth 3000 Å, separated by a distance greater than the focal spot diameter. The laser was focused onto the substrate between the tracers which were consequently not directly irradiated. For some targets a 100 μm diameter 1000 Å layer of gold was evaporated at the focal spot position between the tracers to provide a high-Z ablator. The choice of thin substrate was made in anticipation of high signal levels and with the objective of enhancing the relative emission of the tracers with respect to the directly-irradiated substrate.

The use of thin substrate foils for these shots allowed the rear-viewing pinhole camera (see Fig. 4.7) to be used as a check on the beam positioning and to verify that the tracers were not being directly irradiated. The positioning of the beam was also

checked by firing full energy laser shots through aluminum foils into which apertures had been cut, and recording the x-rays signals thus produced. If the beam was properly aligned, the signal levels recorded by the spectrometers was found to be negligible for the case of 120 μm sized apertures. In contrast, a laser passing through a 100 μm aperture was found to produce a significant signal level , thereby confirming of the value of 110 μm from the focal spot measurements.

Although nominal peak intensities of up to 5×10^{14}W/cm^2 were achieved in these shots, K shell emission as recorded by the crystal instruments was at best very faint and was not recorded at all from targets with a tracer separation greater than 120 μm. The difference between this value and the focal spot size is less than the beam positioning error; therefore these signals may not be interpreted as evidence of lateral transport, since some laser light may have been irradiating the tracers.

The XUV spectrometer data exhibited some evidence of lateral transport, albeit at low signal levels, from the lightup of the tracers on the lateral substrate. The images of Fig. 7.1 are representative of the highest tracer emission signals recorded using the target configurations described above. The spectra at the top represents the accumulated signal from 3 shots of average intensity 2.5×10^{14} W/cm^2 and pulse width 860 ps taken on 2 μm CH foils with Au microdiscs and Al annuli tracers of inner diameter 190 μm. The gold emission from the irradiated gold plasma dominates the signal but the resonance lines of Al^{9+} and Al^{10+} may be discerned along the edges of the spatially-resolved band. The presence of lithium like aluminum as the brightest feature lighting up the tracer suggests that temperatures were above 50 eV in the lateral region, based on the temperature dependence of the fractional populations of the aluminum ionization levels (Duston and Davies, 1980). However, due to the small recorded signal levels, the XUV tracer emission could not be used as a more accurate
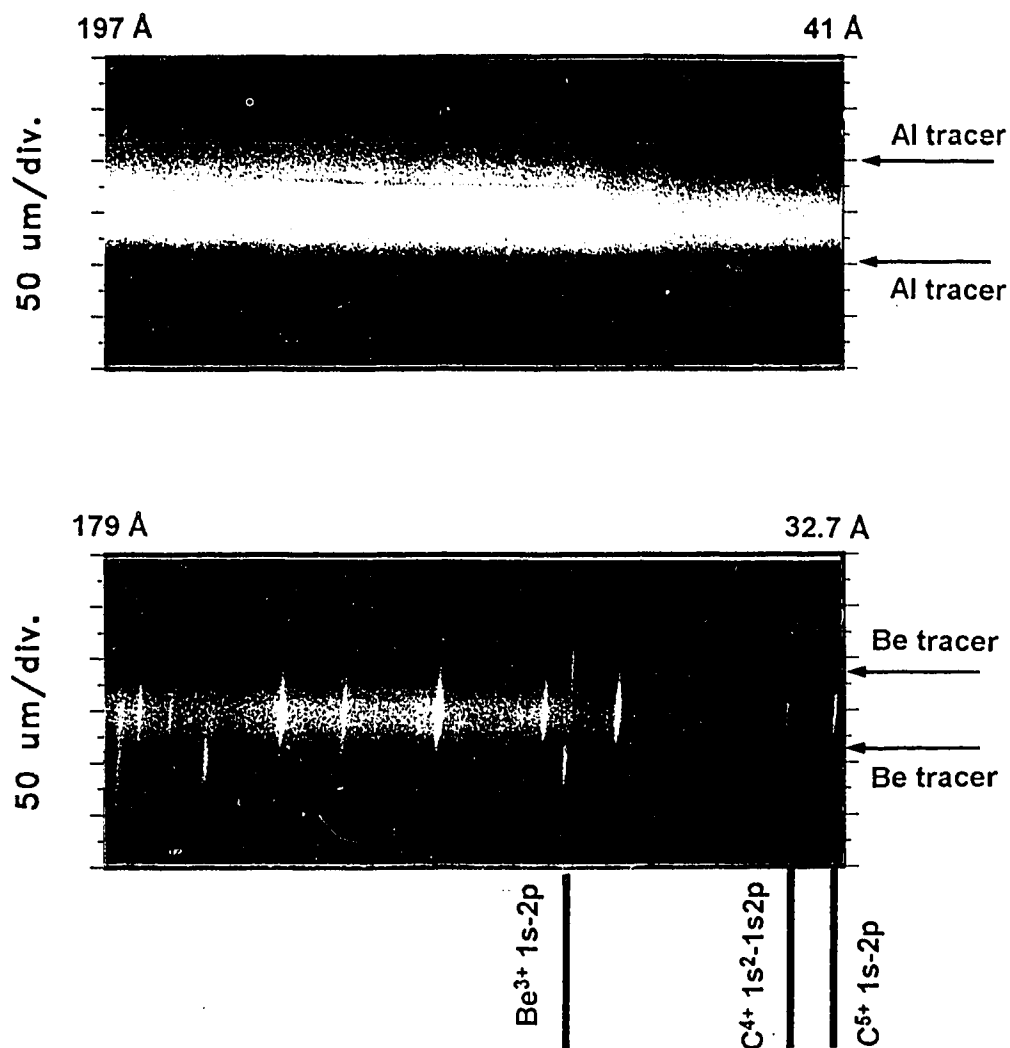
Figure 7.1. Spectra from tracer targets as recorded by the XUV grazing incidence spectrometer. The laser irradiated regions were (top) an Au microdisc on a 2 μm CH foil and (bottom) a 15 μm CH foil. The tracers layers (Al in target at top and Be in the target at bottom) were positioned beyond the laser spot 40 μm and 20 μm from the edge of the focal spot.

142

temperature or density diagnostic. For example, the signal strengths of the temperature or density sensitive lines studied by Duston and Davies (1981) were all below the detection level of the instrument.

A few select shots were taken on thicker substrates with similar results. The bottom spectra in Fig. 7.1 represents a double exposure taken from two 860 ps shots of $I_{peak} = 2.2 \times 10^{14}$ W/cm^2. The first shot was taken through an aluminum foil aperture as an alignment check, and the second was incident upon a 15 μm CH substrate with Be tracer bars of separation 150 μm. The high density plasma of the laser-irradiated region may be identified with the strip of continuum emission. Besides the carbon lines from the substrate, faint tracer emission may also be seen. The brightest feature in the tracer emission is the Be^{3+} 1s-2p line, with the resonance line of Be^{2+} faint but present. This tracer signature is suggestive of temperatures between 50 eV and 100 eV, based on calculations for the fractional populations of the Be ionization levels (House, 1963).

No marked difference in tracer signals could be detected from substrates with high Z targets vs. low Z ablators. However, in a series of shots taken with a 170 ps laser pulse duration and comparable intensity, no tracer emission was recorded for tracer separations greater than 120 μm. These observations suggest that the presence of a laterally expanding plasma sheath, rather than some other mechanism involving remote energy deposition (such as hot electron transport or radiation transport), was responsible for the lateral heating. In the case of the short pulse shots there would have been insufficient time for the plasma expansion to create this sheath.

The remaining database was collected from double tracer targets of the type described in previous chapters, or on solid substrate foils of 15 - 25 μm thickness. For such targets the advection of material from the laser focus may be expected to account for the largest fraction of the x-rays recorded from outside the focal region.

The K shell emission from sodium and aluminum tracers were recorded for a series of 400 ps shots taken at normal incidence on 18 μm CH substrates with double tracer layers and parylene overcoats to depths of 0.9 μm. Nominal peak intensities on target varied from $5 \times 10^{13} W/cm^2$ to $2.3 \times 10^{14} W/cm^2$. Both crystal spectrometer and x-ray pinhole images from this database indicate that emission above 1 keV was confined for the most part to the focal spot region. A set of pinhole images recorded from a shot of peak intensity $2.3 \times 10^{14} W/cm^2$ and overcoat depth 0.1 μm is shown in Fig. 7.2. The four pinholes used to resolve the x-ray emission were separately filtered by 30 μm Be, 30 μm Be + 5 μm Al, 30 μm Be + 10 μm Al, and 30 μm Be + 15 μm Al. The respective transmission e-folding energies for the filter combinations are 1.5, 3.1, 4.0, and 4.7 keV. Most of the recorded x-ray emission comes from the energy band between 1.2 - 3 keV. However, a high energy component may be seen to originate from the central core of the plasma. This pinhole image reveals no evidence of the annular beam structure recorded during the focal spot measurements. This structure was observed, however, in images from targets which had thicker overcoat layers.

In Fig. 7.3 the digitized raw spectrum (top) and processed spectrum (bottom) for a typical high intensity ($I_p = 2.0 \times 10^{14} W/cm^2$) shot is shown. The densitometer scan was taken along the center of the emission band. The dominant emission feature was the Na^{10+} 1s-2p line at 10.0 Å. A Gaussian fit to the profile of this feature resulted ι. an estimated FWHM of 0.02 Å. This value agrees well with the sum of the expected contributions due to the foreshortened plasma source size (0.012 Å) and the crystal dispersion of the instrument (0.009 Å). In comparison, the thermal Doppler broadening expected for this line at an ion temperature of 400 eV is ~.002 Å). The continuum emission is not strongly evident in the plot but was clearly visible on the film, and was always confined to the focal spot size.

144
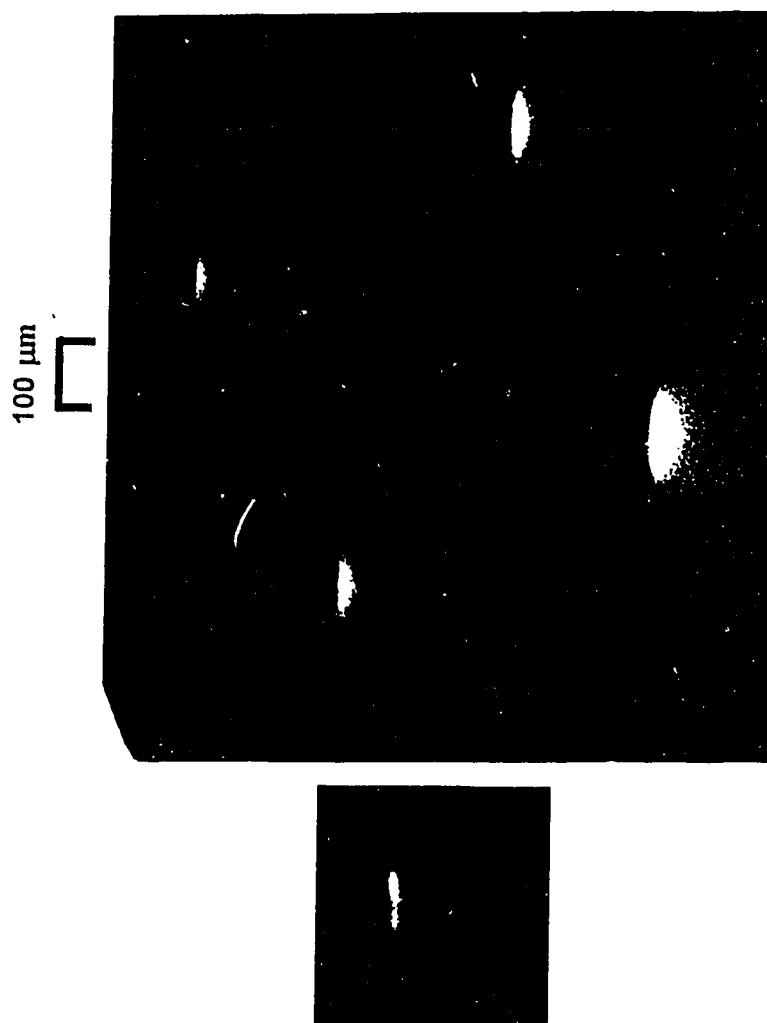
Figure 7.2. TOP: X-ray pinhole images recorded from a shot of peak intensity 2.3×10^{14}W/cm^2 and overcoat depth 0.1 μm. The filtering for the images from brightest to faintest were; 30 μm Be, 30 μm Be + 5 μm Al, 30 μm Be + 10 μm Al, and 30 μm Be + 15 μm Al. BOTTOM: 30 μm Be filtered pinhole image from a shot of intensity 4.1×10^{13}W/cm^2 and overcoat depth 0.53 μm.
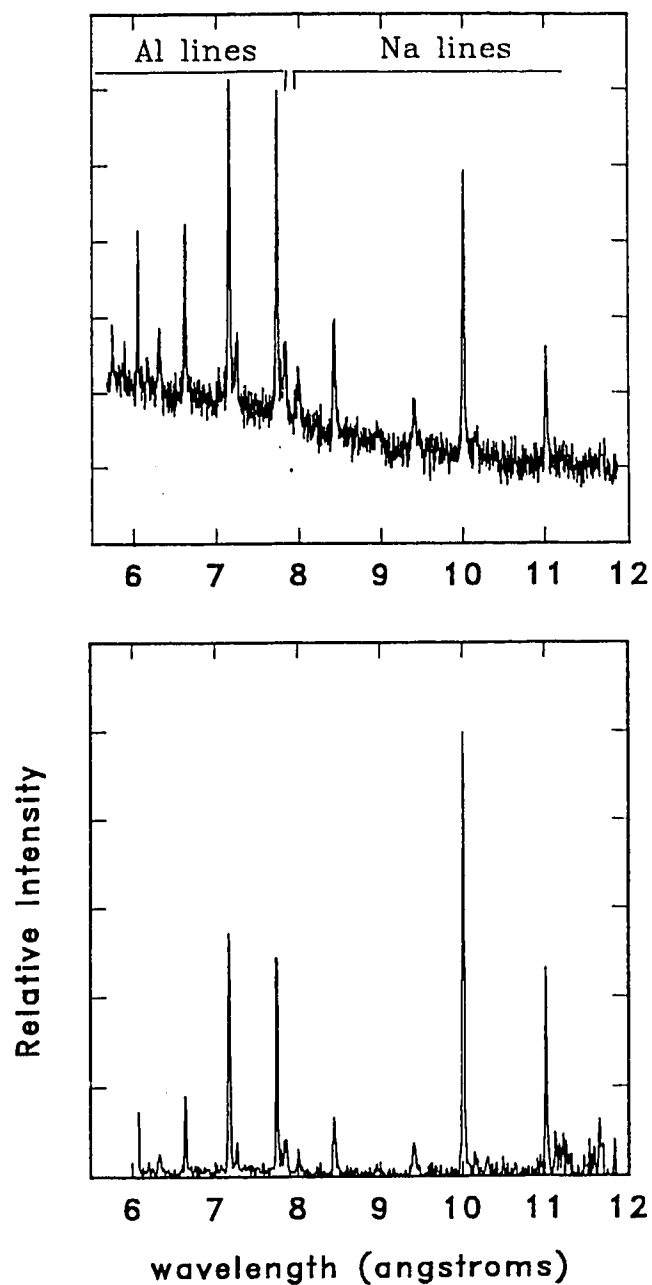
Figure 7.3. Sodium and aluminum K-shell spectra recorded by the crystal spectrometer. Top: raw digitized densitometer scan. Bottom: the same scan converted to relative intensity after subtracting background signal and accounting for the filter, crystal, and film response.

Lateral densitometer scans were taken across the brightest emission lines of each spectrum and converted to relative intensity using the filter transmission, film response, and crystal reflectivity curves. The results of this analysis for two such spectra, after deconvolution of the signal from the instrumental slit function, are shown in Fig. 7.4. The target overcoatings and laser intensities for these shots were 0.9 and 0.1 μm, and 2.0×10^{14}W/cm^2 r. n a later figure the lateral profile from an uncoated target is presented). i n'res the emission levels beyond the focal spot radius of 55 μm is less than of the peak value. Intensity levels above 10 % of peak in the lateral region were observed only from targets with overcoating of less than 0.1 μm. The emission curves originating from the more deeply buried Al layer are invariably narrower than those of the Na emission. The ablation process appears to narrow as it progresses inwards. No significant levels of line emission were recorded beyond a 100 μm radius for any of the targets.

Before we turn to the predictions generated by the IZANAMI simulation, some XUV spectrometer scans will be presented. In Fig. 7.5 another set of lateral profiles, in this case taken through the second order of the Al^{10+} 1s^{2}2p-1s^{2}3d line at 104.5 $\overset{\circ}{A}$, and the adjacent continuum at 100 $\overset{\circ}{A}$ is presented. The laser conditions for the shot (FWHM 300 ps, I_p = 1.5×10^{14}W/cm^2) were comparable to those for the double tracer targets. However the target in this case was 20 μm aluminum foil which required a vertical orientation for accurate positioning, Consequently the laser was incident at 35°, forming an elliptical focus of maximum dimension 135 μm.

A number of interesting features may be seen in this scan. First, the lateral profile of the xuv line extends significantly beyond the focal spot radius. Second, as in the case of the crystal spectrometer data, the region of continuum emission is essentially restricted to within the focal spot. Finally, an asymmetry may be observed
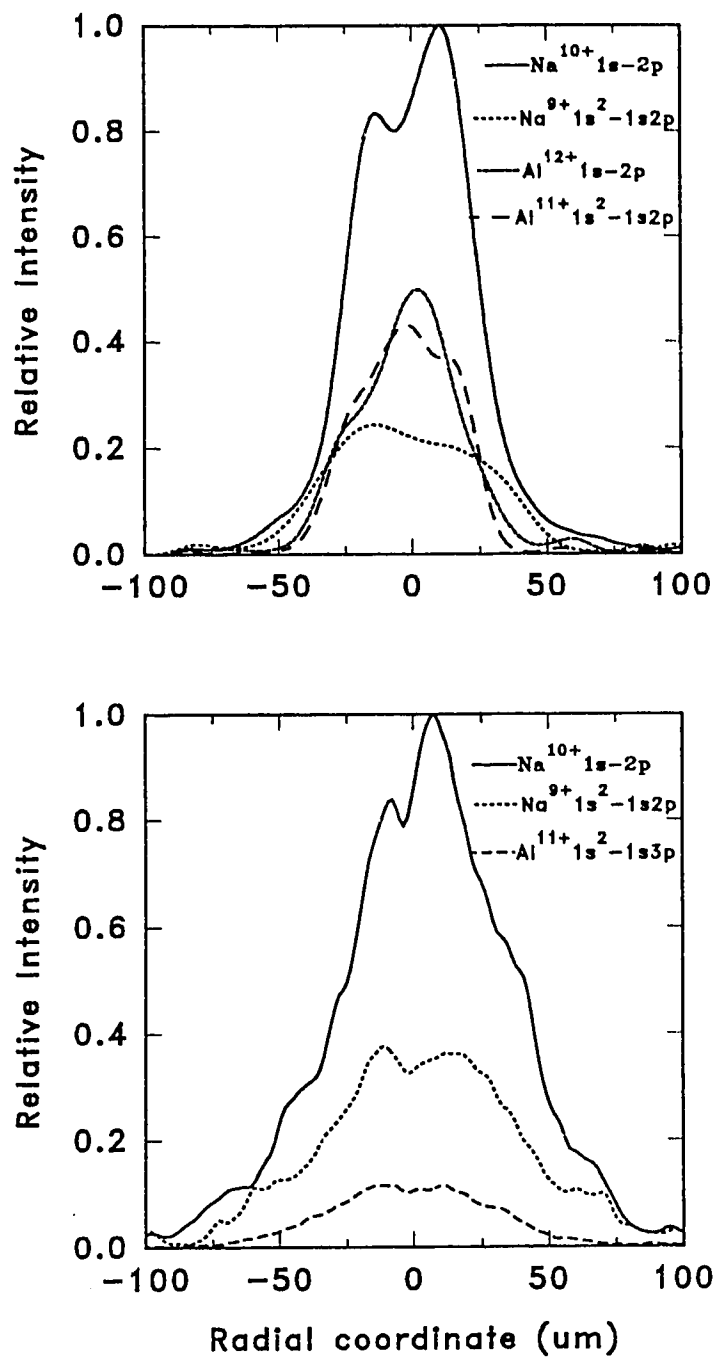
Figure 7.4 Lateral profiles of K-shell lines recorded from double tracer targets with CH overcoats of 0.9 (top) and 0.1 (bottom) μm.

148

1.0

0.8

0.6

Relative Intensity

0.4

0.2

0.0

line + cont.

cont.

−200   −100   0   100   200

Radial coordinate (um)
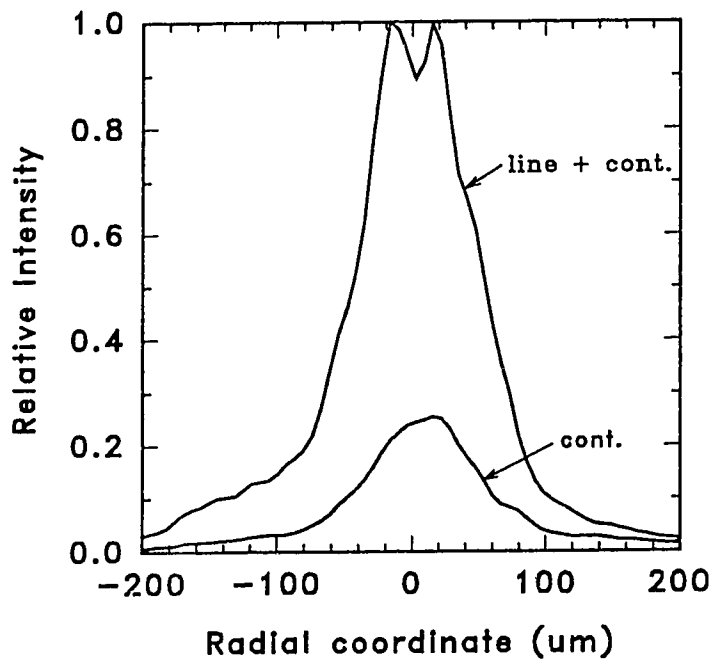
Figure 7.5 Lateral profile of the Al^{10+} $1s^22p$-$1s^23d$ line and adjacent continuum recorded from pure aluminum target.

in the lateral profile. This is thought to be due to the incident angle of the laser axis (the right side of the profile originated from that target half plane nearest to the laser axis) which modifies the characteristics of the hydrodynamic flow away from the focal spot. Also, the plasma expansion may refract some of the beam laterally to heat the target surface outside the focal spot.

In view of the low signal level which was recorded from targets featuring non-irradiated tracers, it is probable that the emission profiles illustrated in Figs. 7.4 and 7.5 were due to a lateral plasma advection from the focal spot. In order to ascertain whether this lateral emission indeed originated from the proximity of the target

surface, some special targets were constructed. They consisted of 20 μm thick aluminum foils onto which 60 μm diameter CH stalks were fastened. The stalks were affixed flush to the aluminum target to present a collision barrier to plasma advecting along the surface. The stalks were positioned outside the focal area with their axes parallel to the horizontal plane of the XUV spectrometer (see Fig. 7.6).

CH stalk   laser

Al foil substrate
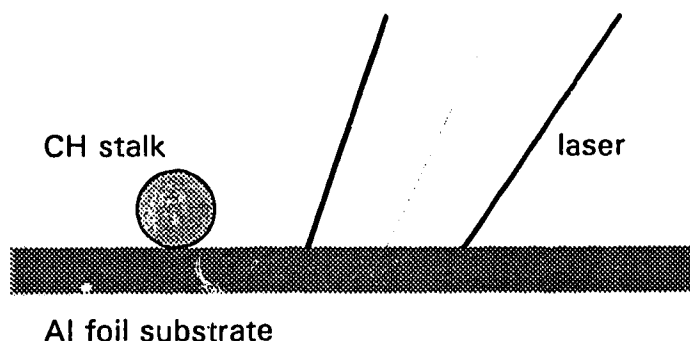
Figure 7.6. Cross sectional diagram of the target configurations used for the data presented in Fig. 7.7.

In Fig. 7.7 the laterally-resolved XUV spectra from three such targets irradiated by 860 ps laser pulses are presented. The locations of the laser focus and stalks are indicated in the figure. The edges of the barrier were positioned 226, 145 and 69 μm from the laser axis and the incident intensities were 1.0, 1.9, and $1.3 \times 10^{14} W/cm^2$. The absence of signal beyond the CH stalk indicates that essentially all of the x-ray emission collected by the instrument originates from a volume lying within 60 μm of the target surface. The corresponding lateral profiles for these spectra, taken through the same wavelengths as Fig. 7.5 are shown in Fig 7.8. The profiles are centered about the position of the laser axis. The observation of enhanced line and continuum emission at the stalk surface barrier is consistent with the presence of a stagnation in plasma flow from the irradiated region.

150

197 Å

42 Å

50 um/div.

laser focus

barrier

50 um/div.

laser focus

barrier

50 um/div.

laser focus

barrier

$1s^22p-1s^23d$ $1s^22s-1s^23p$

Figure 7.7 XUV spectra recorded from three aluminum targets fitted with CH barrier stalks. The positions of the focal spot and stalks are indicated in the figure.
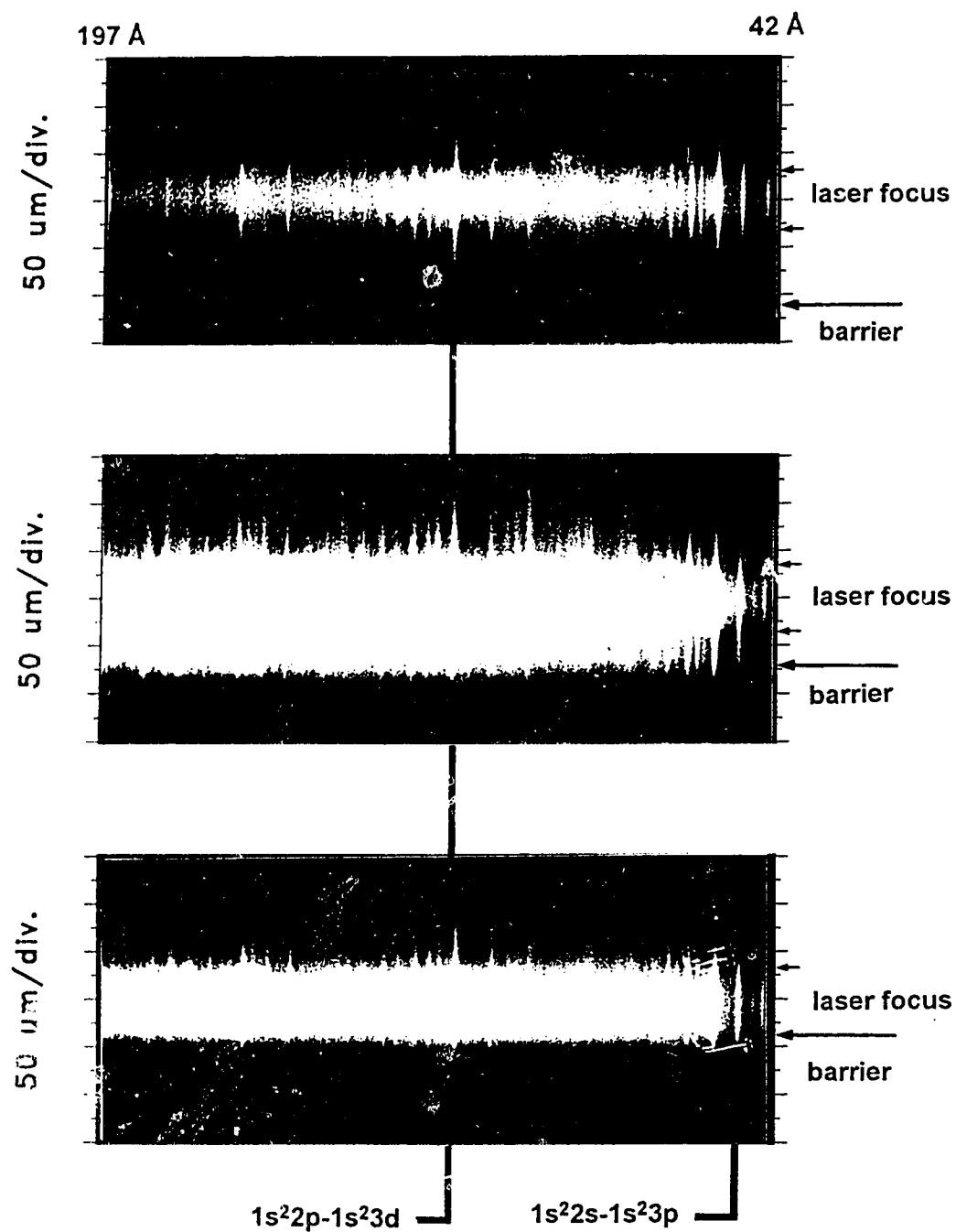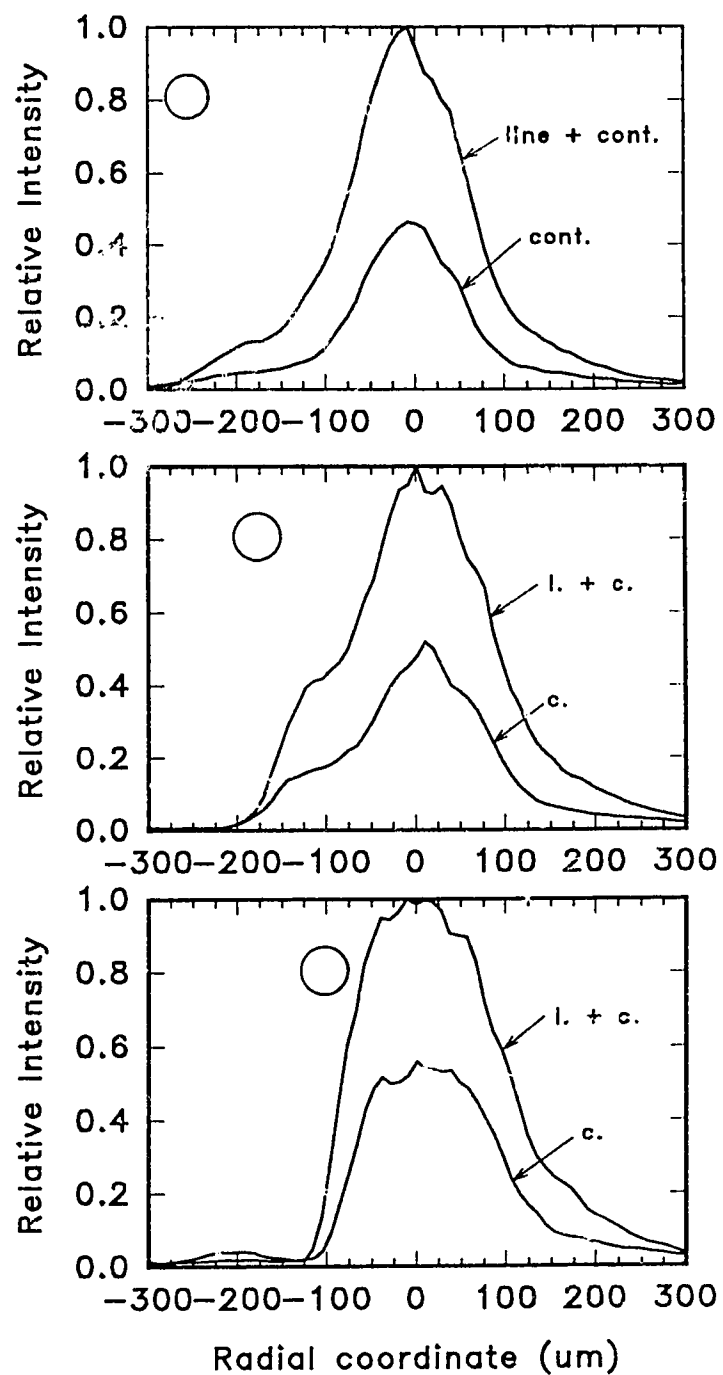
Figure 7.8 Lateral profiles of the Ar^{10+} $1s^2 2p-1s^2 3d$ line and adjacent continuum for the three target spectra of Fig. 7.7. The positions of the barriers are indicated by circles.

152

Simulation Results

In this section the results of an IZANAMI run designed to simulate the conditions of a 6.6 J, 400 ps FWHM laser shot on an uncoated double tracer target is presented. This simulation was run on a cylindrical Eulerian mesh system of r,z dimensions 150 μm x 616 μm, with a reflective boundary condition applied at the laser axis and a free boundary condition (allowing the escape of particles and energy from the simulation domain) at the outer radius of the simulation. Three species of fluid particles representing the CH substrate and the Al and NaF tracers of thickness 0.1 μm were distributed so ι to simulate uncoated double tracer targets, from which the widest K shell line emission profiles were observed. The focal intensity pattern was approximated by a high intensity annulus (inner diameter 60 μm, outer diameter 110 μm) superimposed on a low intensity disc (diameter 110 μm), such that the intensity in the high intensity region was ten times that in the central region.. The peak incident intensity reached in the annulus region was 2.2×10^{14} W/cm^2.

Figures 7.9a to 7.9e illustrate the hydrodynamic history of the interaction, as predicted by an IZANAMI simulation. Electron temperature (top), electron density (center) and average ionization (bottom) profiles are shown for t= -400 ps, -200 ps, 0 ps, +200 ps, and +400 ps, with t=0 again taken at the temporal peak of the laser pulse. The lower horizontal axis represents the central axis and the laser propagates from the right. The hydrodynamic flow exhibits a strong radial component. Thermal transport into the lateral region of the target creates a high density sheath which propagates radially outward along the target surface. Relatively isothermal conditions prevail in the corona throughout the laser pulse, and the electron temperature peaks above 800 eV. This value is significantly higher than the range of 500 - 600 eV suggested by the
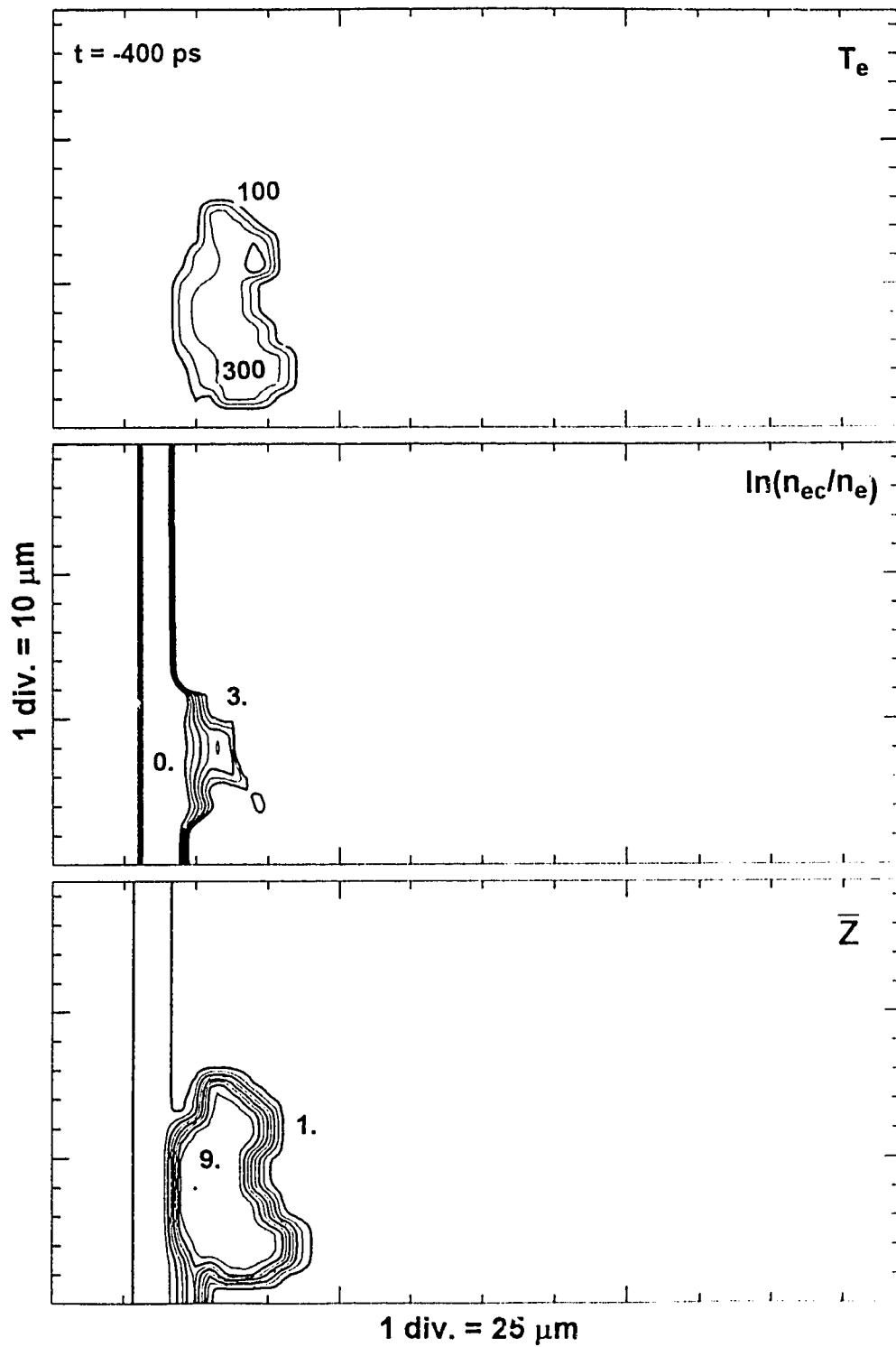
Figure 7.9 IZANAMI predictions for temperature (top), electron density (center), and average ionization (bottom) for an uncoated double tracer target irradiated by a 400 ps 6.6 J laser pulse.

154

Fig. 7.9b

1 div. = 25 μm

Fig. 7.9c

1 div. = 10 μm

1 div. = 25 μm

156

t = 200 ps

T_e

400

700.

$\ln(n_{ec}/n_e)$

2.

0.

1 div. = 10 μm

$\bar{Z}$

.6.

3.

Fig. 7.9d

1 div. = 25 μm

157

t = 400 ps

T_e

$\ln(n_{ec}/n_e)$

300

500

1 div. = 10 μm

0.

2.

9.

3.

$\bar{Z}$

Fig. 7.9e

1 div. = 25 μm

158
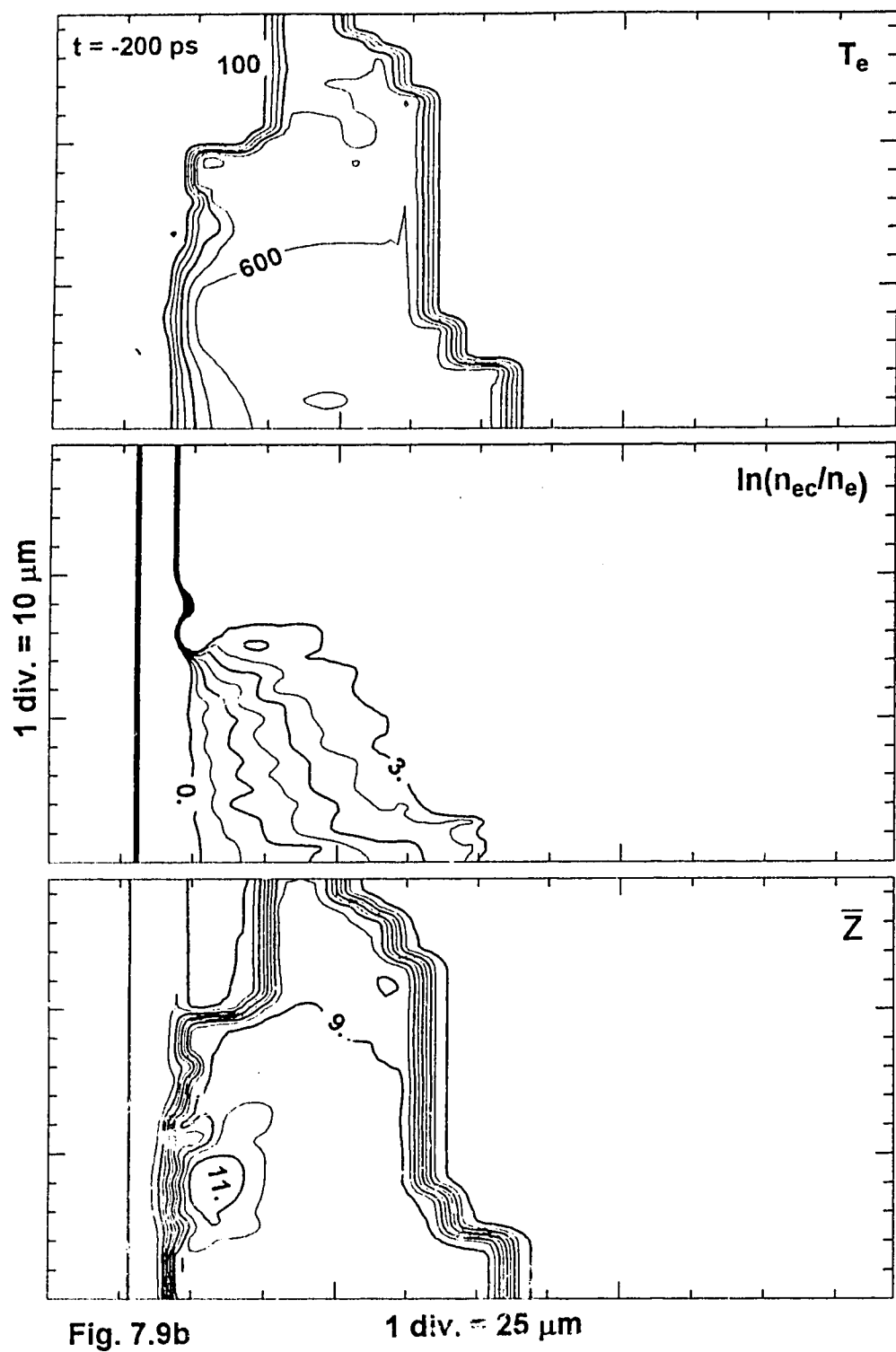
experimental spectra. This discrepancy may be due to the assumption of an ideal gas equation of state in the code. This will underestimate the specific heat of the cold target material. The ablation history is again best illustrated by the ionization contours. Since fully ionized NaF has an ionization of 10, this contour value may be used to estimate the position of the boundary between the tracers, while the Z=4 contour may be interpreted as CH/Al boundary. Both tracer layers have ablated through in the high intensity annulus by the time of the peak of the pulse. A significant amount of ablation also occurs outside the laser focus. By the end of the pulse, both tracers (of combined areal density .54 gm/cm^3 μm) have expanded out to a radius of 85 μm, and the NaF layer has ablated away to a radius of 100 μm.

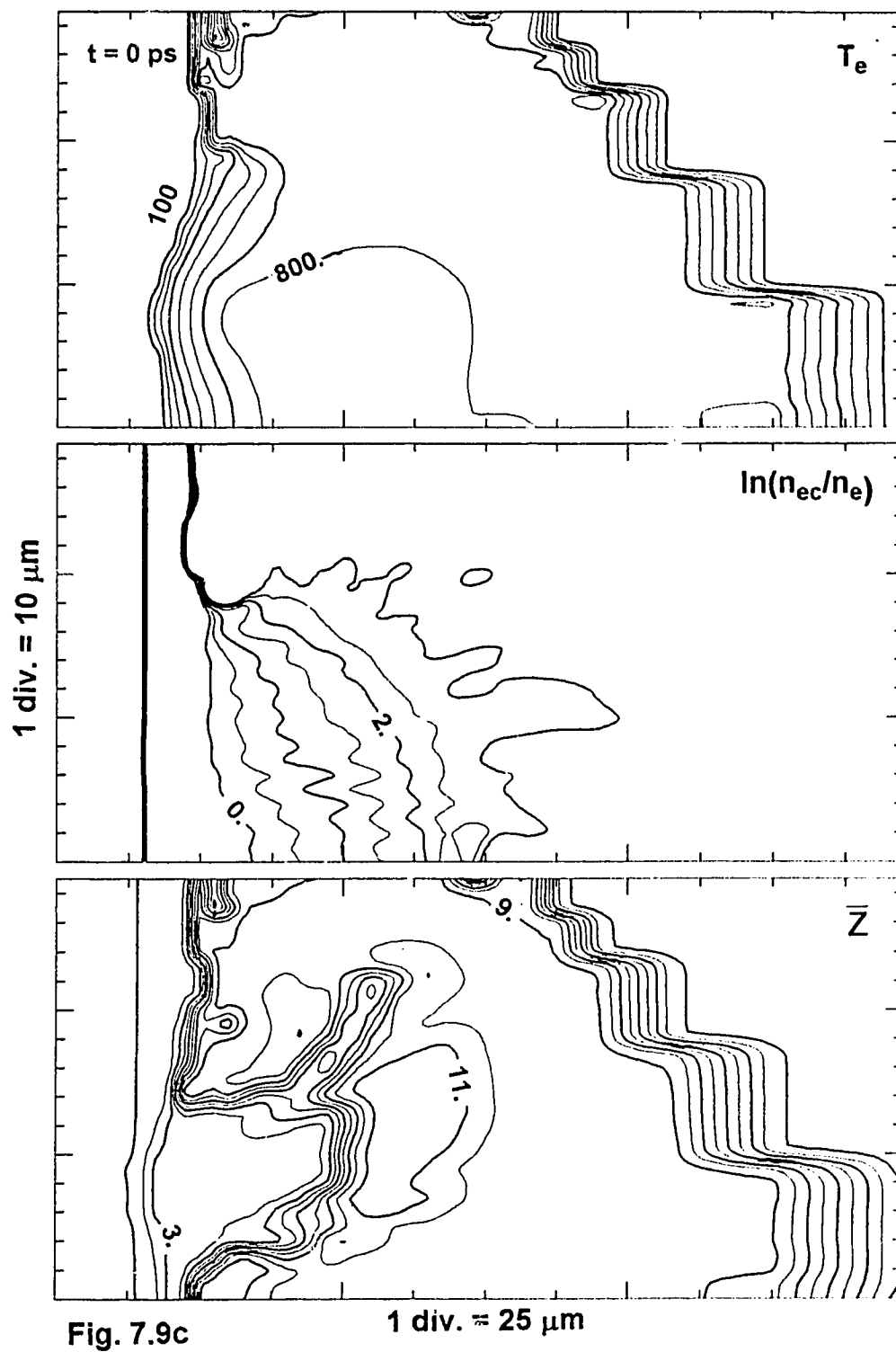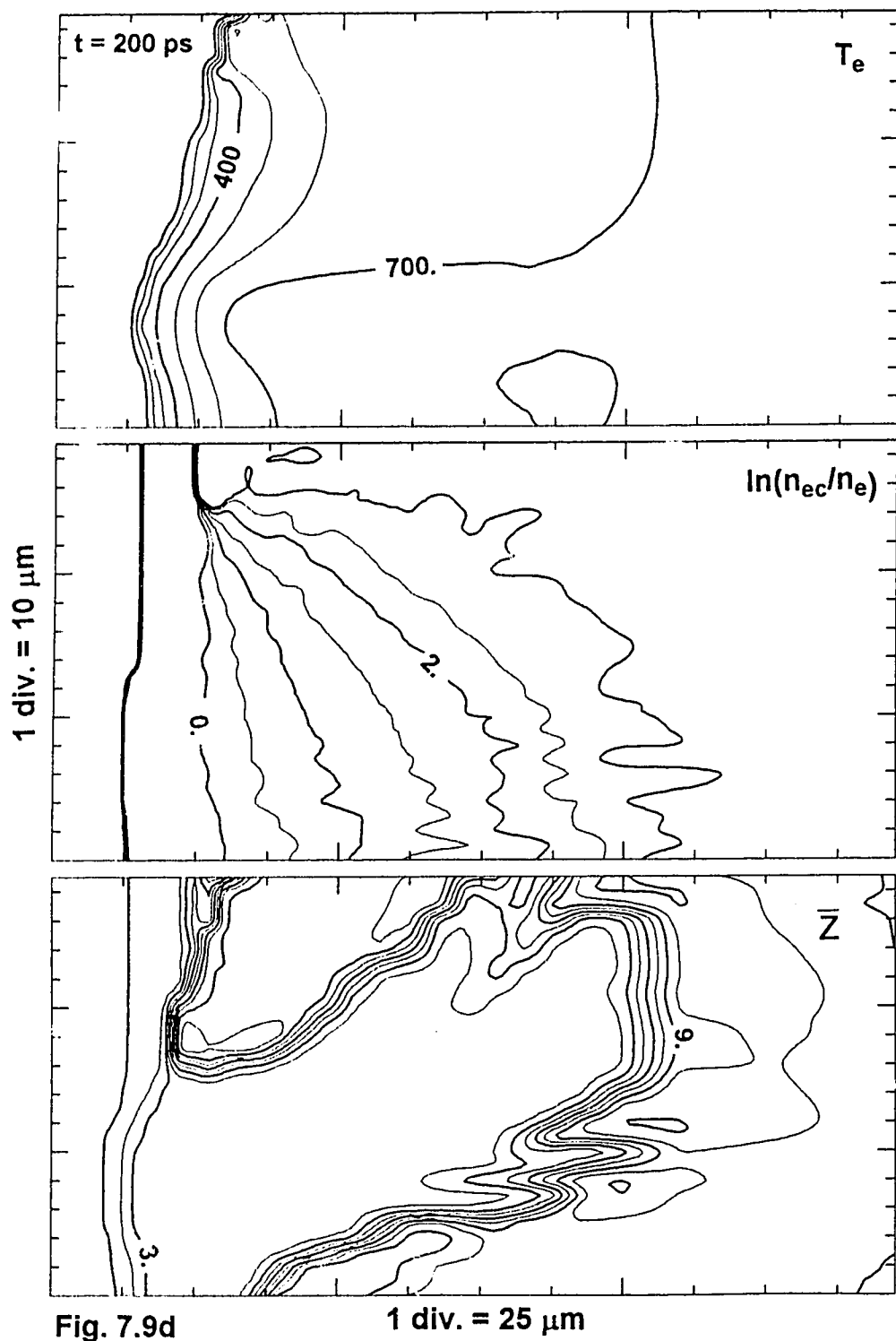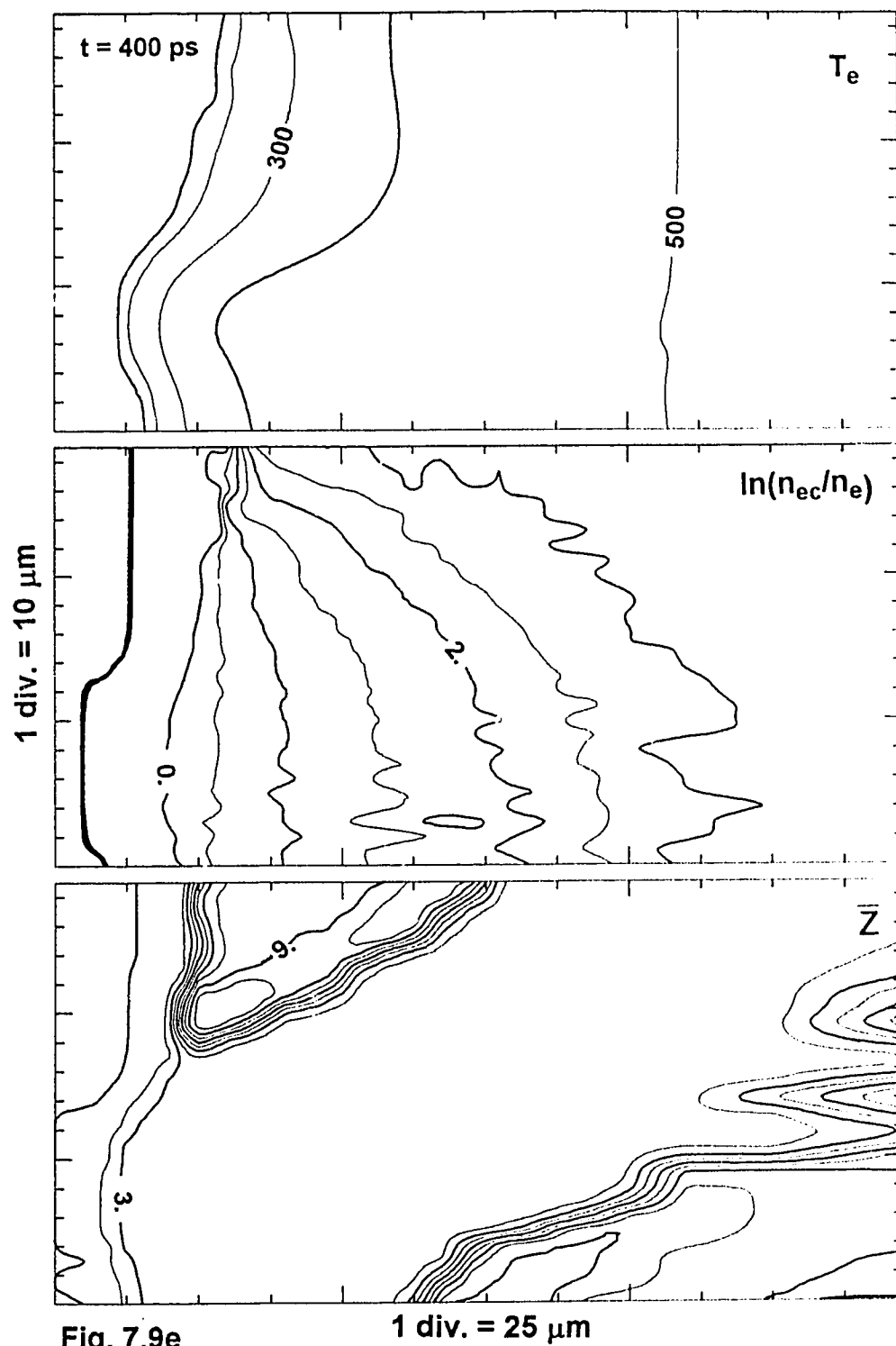The predicted density profiles in the axial direction agree quite favourably with the x-ray pinhole images. The simulation scale length of the plasma at the peak of the pulse, and along the laser axis is about 30 μm. In Fig. 7.10 axial x-ray profiles are presented for two shots of peak intensity $2 \times 10^{14} W/cm^2$ (solid line) and 0.79 $\times 10^{14} W/cm^2$ (dashed line). The solid lines were obtained from the two brightest images seen in Fig. 7.2. The profiles were generated as described previously under suitable assumptions about the characteristic energy of the emitting source. The two profiles obtained from the identically filtered pinhole images were quite insensitive to energy, yielding density e-folding values of 25 and 27 μm.

The growth and generation of magnetic fields is illustrated in the five plots of Figure 7.11a to 7.11e. The fields are generated predominantly at the edge of the spot and at the boundary between the low and high intensity regions of the laser beam. These toroidal structures are oriented in an opposite azimuthal sense and grow to peak values of several megagauss. While the fields strongly inhibit the local thermal
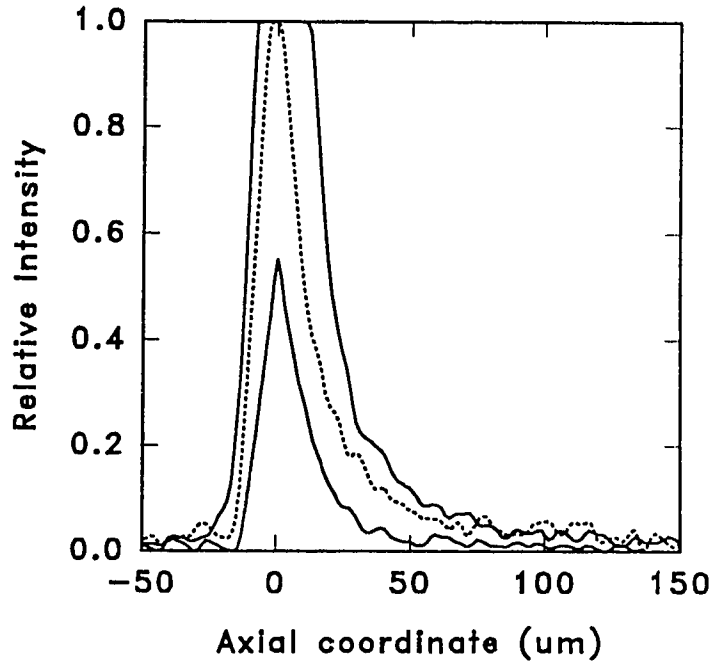
Figure 7.10 Axial x-ray emission profiles calculated from pinhole images for two shots of peak intensity $2\times10^{14}W/cm^2$ (solid line) and $0.79 \times10^{14}W/cm^2$ (dashed line). The solid lines were obtained from the two brightest images seen in Fig. 7.2.

transport; the regions of high field strength and inhibition are localized. The positions of the field maxima are not stationary but may be seen to move radially outwards from the edge of the focus and along the laser axis.

Three effects are chiefly responsible for the evolution of the spatial structure of the field. The first is the $\nabla n \times \nabla T$ effect which is the second source term in (3.7) In the vicinity of the target surface, the location of the maximum effect of this term tends to move outward with the plasma sheath, following the position of the maximum temperature gradients. The first and third terms of (3.7) may be shown to act in a
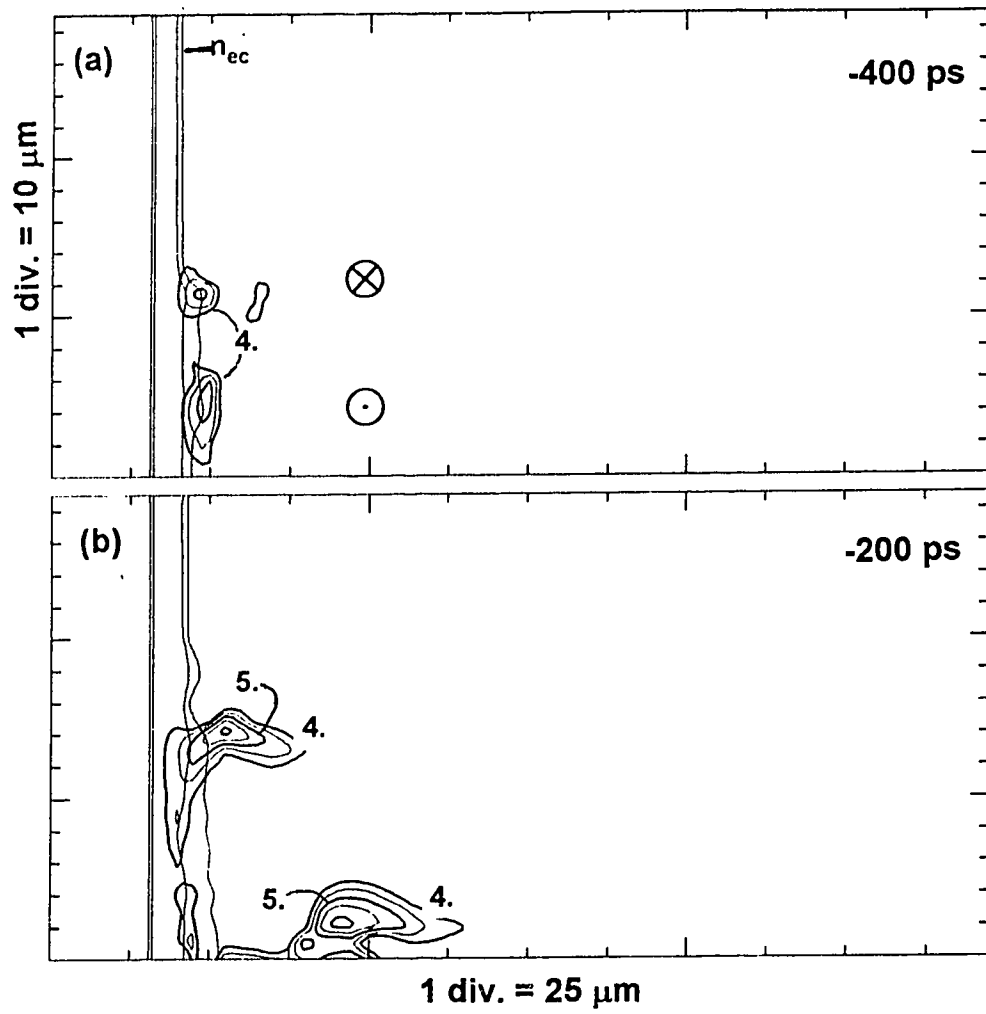
Figure 7.11 The growth and convection of magnetic fields (units log(B/gauss)) under tight focus conditions.

1 div. = 10 μm

1 div. = 25 μm

162
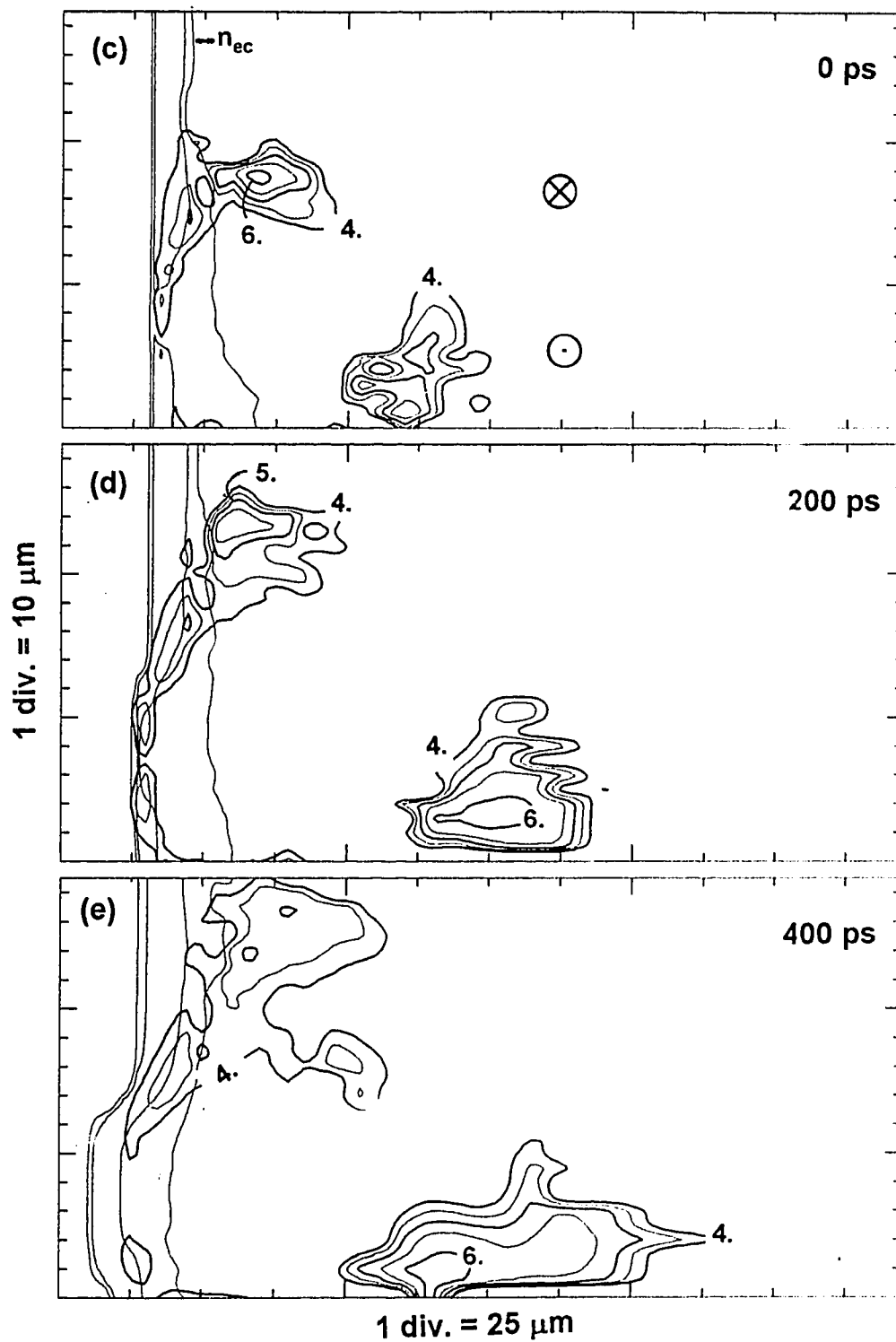
purely azimuthal direction for the two dimensional situation considered here. The other two determinants of the field structure are the pinch effect (Yabe et al., 1982) and the Nernst effect (Nishiguchi et. al, 1984), which arise from the remaining source term of (3.7). The pinch effect works to prevent islands of field structure from expanding, and by implication, also confines the regions of high flux inhibition. The Nernst effect is responsible for the advection of the field with velocity $v + V_T$ where v is the local hydrodynamic velocity and

$$V_T = -\frac{\tau_e}{m_e} \frac{\left(\beta_0'' + \beta_1''(\omega_e \tau_e)^2\right)}{\delta_0 + \delta_1'(\omega_e \tau_e)^2 + (\omega_e \tau_e)^4} \nabla T_e \qquad 7.1$$

where the β coefficients are tabulated by Braginskii (1965) and Nishiguchi (1980b). ...ause of this term the field structures generated in the vicinity of the critical surface tend to break apart at the point where the v and V_T cancel, and drift in two directions toward and away from the surface.

The contour plots describing the energy transport are shown in figures 7.12 and 7.13. The Braginsinkii inhibition factor and classical flux limiting factor κ^*/κ at t= 0 ps are shown in the top and bottom plots of Figure 7.11. The localized nature of the field inhibition is evident in the upper plot. The thermal transport is moderately limited in the corona (the diagonal stepped band of contours in the lower plot is due to the high temperature gradients at the edge of the expanding corona). The plots of Fig. 7.13 are: (top left/right) the axial/lateral components of the heat conduction q and (bottom left/right) the axial/lateral components of the sum of the thermal and advective terms for time t = 0 ps. The areas of inward directed transport may be seen to extend well beyond the spot radius despite the inhibiting effects of the magnetic fields. As in the case of the lower intensity simulations (previous chapter), the critical density surface tends to demarcate the regions of inward and outward net energy

163
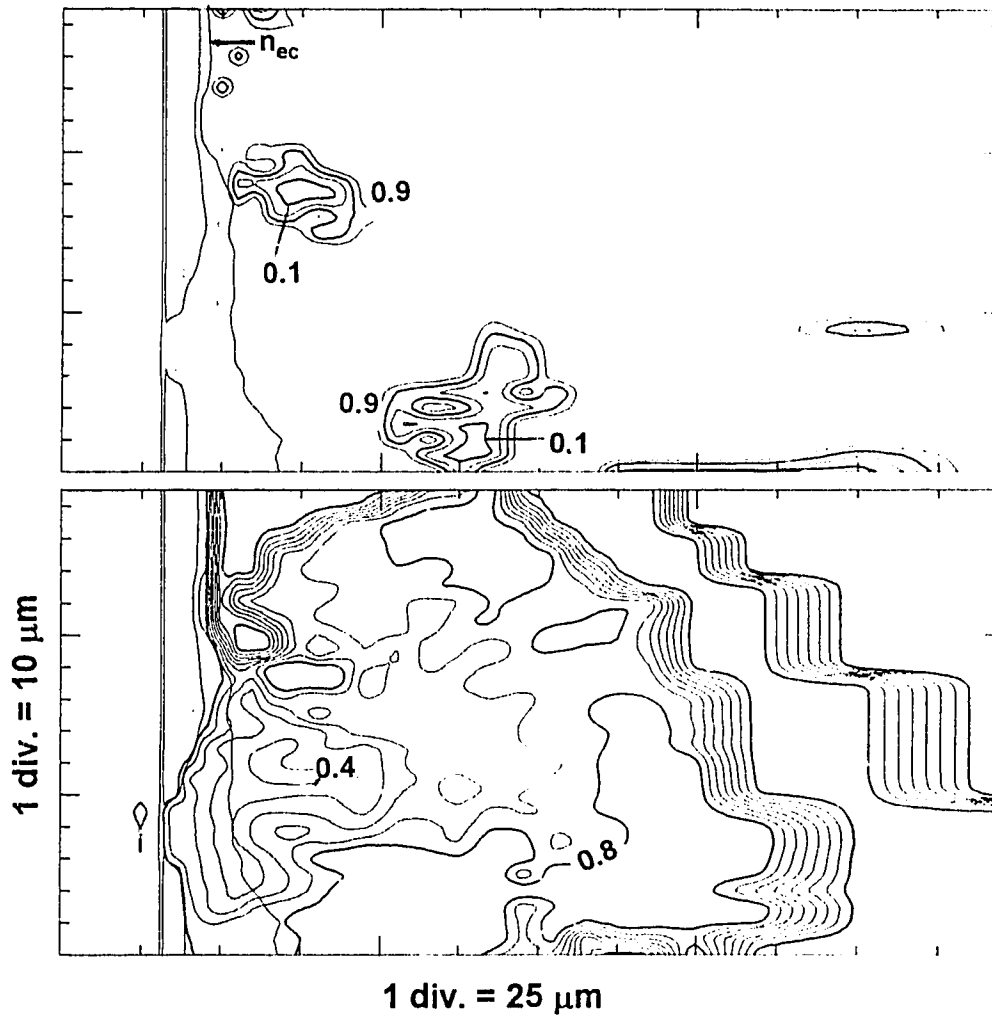
Figure 7.12 The Braginsinkii inhibition factor (top) and classical flux limiting factor κ^*/κ (bottom) at the peak of the laser pulse.

164

1 div. = 10 μm

-n_ec

-10^{12}

-10^{13}

-3.16×10^{13}

10^{13}

3.3×10^{12}

-10^{13}

-10^{11}

-10^{12}

-10^{13}

10^{13}

6×10^{12}

-10^{13}

1 div. = 25 μm
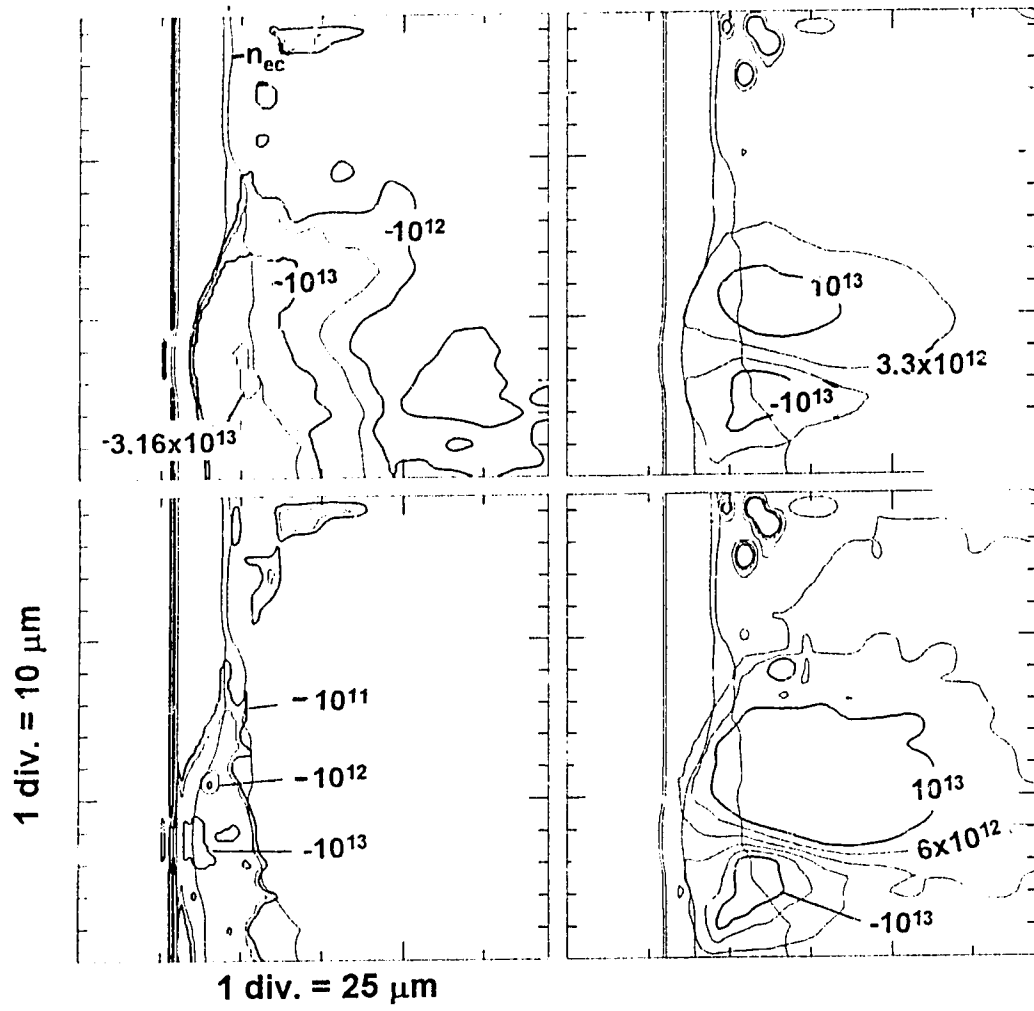
Figure 7.13 Energy transport at the peak of the laser pulse. Top(left/right): the axial/lateral components of the heat conduction q. Bottom(left/right): the axial/lateral components of the sum of the thermal and advective terms. All units are W/cm².

10 μm/div.
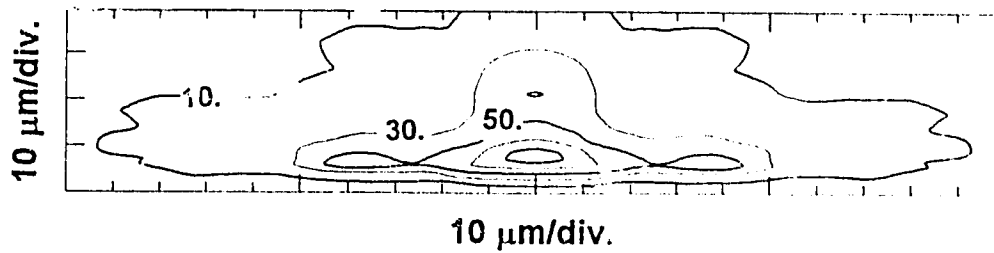
Figure 7.14 Contour plot representing Be filtered x-ray emission integrated along a lateral line of sight normal to the laser axis and over 1 ns of time from the simulation code IZANAMI. The radius of the laser spot is 55 μm.

transport, even beyond the focal spot radius.

When we turn to the x ray emission patterns predicted by IZANAMI, we find fair agreement between the code and the experimental data. A time integrated -ray emission pattern was generated by numerical integration of the total continuum and line emission predicted by the average ion model of the code. An integr .ion along a lateral lines of sight of length 180 μm through the plasma was calculated ic. each r,z coordinate pair. The calculations summed 10 snapshots of the emissivity, temporally separated by 100 ps intervals. The Be filtering of the pinhole instrument is included in the calculation but no accounting was made for opacity effects which, if included, should smooth away some of the features and enhance the relative signal in m the lower density plasma. The resulting contours of Fig. 7.14 reproduce the observed axial scale length of ~25 μm, and, like the pi. ole image from the uncoated target, display little evidence of the annular beam structure. However there is an extended

166

region of 10 %- 30 % of maximum emission strength extending well beyond radius of the focal spot. This feature was not as pronounced in the pinhole images, which suggest somewhat sharper radial profiles. For example, the suggested scale length of the lateral wings of the brightest pinhole image of Fig. 7.2 was ~14 μm, while the corresponding value from the image is ~40 μm.

The K-shell emissivity predicted by the average ion model of IZANAMI was integrated along the positive z direction for each radial coordinate and at 100 ps simulation intervals. The radial emission profiles were then summed and rotated about the laser axis to produce a two dimensional time integrated emission profile in the target plane. Finally this profile was integrated over a strip of width 90 μm which is the expected source size contributing to the densitometer scan.

The resulting normalized profile is shown as the medium dash line in Fig 7.15. An experimental profile of the Na^{10+} 1s-2p recorded from an uncoated target irradiated at a peak intensity of $2x10^{14}W/cm^2$ is shown in solid. The agreement is quite reasonable, although, as in the case of the pinhole image, the emission level predicted in the wings is somewhat greater than that observed.

The small dash line in Fig. 7.15 represents the result of a simple method-of-escape radiation transport calculation for the same feature, which fared worse in predicting the emission profile. A discretized version of equation (2.104) was solved along the positive z direction for each radial coordinate summed as described above. The local electron densities and temperatures were used to obtain the ion populations and opacities for the transition using look up tables generated from the RATION predictions for an NaF plasma. The predicted profile in this case is significantly wider than the observed emission feature.

One possible cause of the discrepancy is the steady state atomic physics model
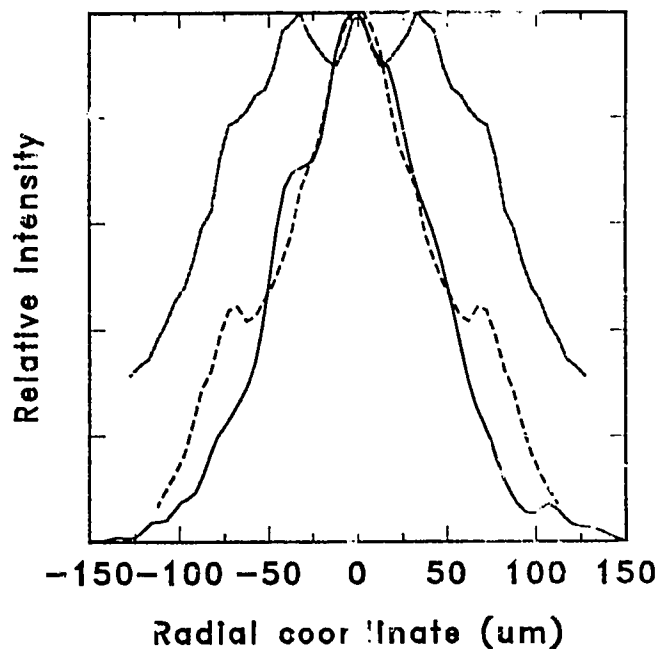
Figure 7.15 Lateral profile of the Na[10+] 1s-2p line recorded from a double tracer target without a CH overcoat (solid line). Also shown (dashed lines) are the predictions of numerical calculations described in the text.

assumed in obtaining the ion populations and opacities used in the transport calculation. In a plasma expansion a non equilibrium condition may prevail in which the upper levels of transitions may depopulate faster than collisional excitation and recombination processes can repopulate them. However, an evaluation of the collisional excitation rates from the ground state to the upper level of the transition in question indicates that, for typical coronal densities ($> 10^{20}$ cm^{-3}) and temperatures (500 -700 eV) predicted by the simulation, depopulation of the upper states would not occur.

A more likely possibility is that the opacity used in the calculation was greatly overestimated due to the wavelength shift caused by motion Doppler broadening

168

effects. At the peak of the laser pulse, for example, the plasma expansion velocity along the line of sight of the instrument varies over a range of 5×10^7 cm/sec. For a line at 10 Å the wavelength shift from two plasma source regions moving with a relative velocity 10^7 cm/sec is 0.0033 Å, which is greater than the thermal Doppler width of 0.00? Å estimated earlier. The effect motion Doppler would be to reduce the self absorption of the line and effectively narrow and steepen the profile in Fig. 7.15. For densities above critical Stark broadening may also be expected to reduce the line opacity.

In summary, coupling of energy into the lateral target substrate (to distances of ~40 µm) was observed. Heating of the substrate to temperatures above 50 eV are suggested but a more accurate assessment of the temperatures could not be made due to small signal levels. The levels suggest that a very small emitting volume is responsible for this emission. The existence of a plasma expanding laterally in close proximity to the target surface is indicated. The presence of this plasma appears to be necessary to create the conditions necessary for energy coupling into the target.

The IZANAMI simulation was able to reproduce reasonably well the densities, temperatures, and x-ray emission features observed from target shots of similar parameters. Most of the x-ray signals recorded from beyond the focal spot were apparently due to the expanding corona rather than the ablating lateral target. Consequently the agreement achieved cannot be interpreted as definite verification of the lateral ablation predicted by the code. In connection with this point, the size of the continuum emission observed by both spectrometers supports the notion that the high density ablation plasma was confined to the focal spot. If this condition in fact holds, there are a number of physical effects which could be responsible. The inhibitory effect of the magnetic field could be much greater in the real interaction for which

perfect azimuthal symmetry did not exist. Small scale high intensity structure in the beam could have created small local cells of magnetic field structure and high local temperature and density gradients. A second possibility is that non-local heat transport, which is not incorporated into IZANAMI, may have also been at work here; for critical electron density and representative temperatures, the equation (3.17) predicts very strong inhibition over scale lengths of 10 -20 μm.

8. Hydrodynamics of Colliding Plasmas*

The study of hydrodynamic structures in the corona of laser-produced plasmas continues to attract the attention of researchers in the field of inertial confinement fusion, r   '· ·h driver uniformity remains a key issue. Radiative cooling instabilities are prime for explaining the relatively cool, high density jets which have been observed ι.. ιlowoff plasma during the later stages of the laser pulse (Dhareshwar et al., 1992). Even more serious for the uniformity issue are structures which exist at or form during the early phase of target compression. Recent simulation studies (Desselberger et al., 1992, and references therein) and x-ray imaging measurements from the ablation region of targets (Emery et al., 1991) indicate that initial beam non-uniformities can create density structures that persist throughout the laser pulse. If such structures extend into the corona, filamentation and self-focusing effects may result (Schmitt, 1988). The related subject of colliding and interpenetrating plasmas has attracted research directed toward the aim of achieving suitable conditions for x-ray amplification or directed x-ray transport.   Previous experiments have incorporated a variety of beam/target configurations including dual beam/parallel planar targets (Glas et al. 1991; Glas and Schnürer, 1991; Bosch et. al, 1992), split beam/single planar targets (Begimkulov et al., 1991), and single beam/internally-irradiated microtubes (Stöckl and Tsakiris, 1991, and references therein). In conjunction with experimental studies, numerical modeling has been able to reproduce observed features of the plasma such as the temperature, density,

---

and emissivity (Begimkulov et al., op. cit.; Berger et al., 1991; Pollaine, Berger, and Keane, 1992).

During the course of the modulated intensity experiments some striking evidence of plasma collisional structures occurring in the non irradiated regions of the corona was recorded. These structures became most evident for targets of very thin or no CH overcoating. In Fig. 8.1 x-ray pinhole images from four targets of varying overcoat thickness are presented. The beam/target configurations for the experiments have already been described in chapter 6. The laser propagates from the right, converging with a beam f# of 2. The recorded energy on target for all of these shots fell within the range 9.6 ± 0.6 J, with corresponding peak intensities of 3.3×10^{13} W/cm^2 in the irradiated areas. The CH overcoat thicknesses for the four range from 0.54 to 0.0 μm; the maximum ablation depth for CH targets under these irradiation conditions was ~1.6 μm, based on the data of Boehly et al. (op. cit.). In the case of the target with thickest overcoat (8.1a), the emission features consist primarily of the hot expansion plumes of the directly-irradiated regions. As the overcoat thickness is progressively decreased, fork-like emission structures are observed in the non-irradiated or "shadow" regions of the target. These features become the three dominant flame shapes in the case of the uncoated target (1d).

The spatial features of the spectrometer data exhibit the same characteristics as the pinhole images. For overcoated targets, the emission features originate primarily from the irradiated regions. The lateral widths of these features increase as the overcoat thickness is decreased. For uncoated targets a bright aluminum spectrum is recorded in the low intensity region. Typical spectra are presented in Fig. 8.2. Spectrum (8.2a) was recorded from the same shot as pinhole image (8.1a) and represents the emission features
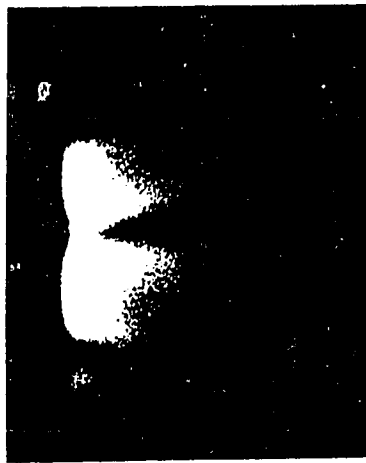
(a)

(b)
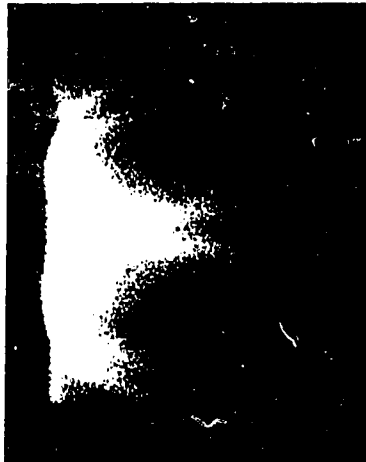
(c)

(d)

Figure 8.1   Time-integrated x-ray pinhole images from four CH/Al/CH layered targets irradiated by a non-uniform laser beam of spatial periodicity 112 μm. The x-ray emission originates primarily from the aluminum layer which was buried at depths of 0.54, 0.24, 0.12, and 0.0 μm for targets (a) to (d) respectively. The laser converged from the right with $I_{peak} = 3.3 \times 10^{13}$ W/cm^2 ±6% and FWHM = 860 ps. Emission from collisional plasmas in the non-irradiated regions become increasingly predominant as the depth of the first CH layer decreases, resulting in the three flame shaped prominences in the case of (d).
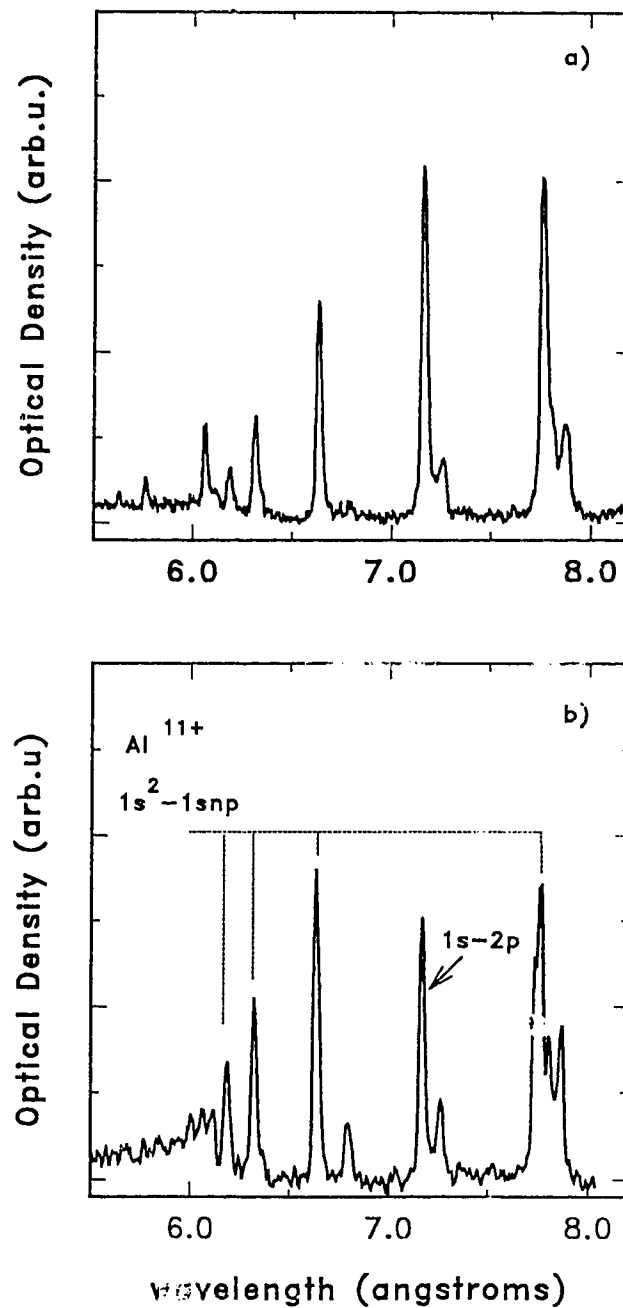
Figure 8.2 K-shell x-ray spectra recorded from the expanding aluminum layer of the targets. Fig. (8.2a) was recorded from the irradiated region of a 0.54 μm overcoated target; spectrum (8.2b) was recorded from the non-irradiated region of an uncoated target, and exhibits strong recombination into the upper levels of highly ionized aluminum ions.

of the laser-irradiated region. Fig. 8.2b shows a spectrum for a 4.9 J shot on an uncoated target. This spectrum originates from the non-irradiated region of the target, and exhibits evidence of strong recombination into the continuum and upper levels of hydrogen- and helium-like aluminum. Using published information for the film sensitivity, crystal reflectivity, and Be filter attenuation, theoretical spectra generated by the RATION code were fitted to the experimental spectra of Fig. 8.2, resulting in characteristic temperature and electron density estimates for the emitting plasma of 580 eV and 4.0×10^{20} cm^{-3} for the case of (8.2a), and 560 eV and 2.0×10^{20} cm^{-3} for the case of (8.2b). The best fit for the latter spectrum was obtained if a plasma length of 50 μm extent was assumed in order to account for opacity effects. This assumption is in accord with the pinhole images, which indicate that this spectrum originates from a comparatively extended region. The temperature and density estimates obtained from (8.2b) must be viewed as tentative only since the equilibrium conditions assumed by the RATION code may not prevail in the shadow region. The emission from the irradiated region of shot (8.2b) was not well characterized by a single temperature or density. This may be expected since the tracer layer progressed through a wide range of density and temperature conditions during the early part of the laser pulse.

The emission features in the non-irradiated areas may be interpreted as evidence for the collision and lateral stagnation of hot coronal plasmas undergoing expansion from the laser-irradiated regions. For uncoated targets, the aluminum tracer layer ablates first, expanding and colliding to produce the flame-shaped features of Fig. (1d). In the case of the CH-overcoated targets the overcoat layer ablates first, forming the dark inner structures of the forks, which widen as the CH overcoating increases; the emission from these structures is filtered out by the instruments.

The boundaries between the dark and bright features of the collisional region are quite distinct. In order to estimate the role that the CH opacity might play in creating this

effect, equations 2.107 and 2.108 were used to estimate the optical depth of a 500 eV plasma at the representative energy 1.6 keV. The CH is essentially fully ionized at this temperature (suggested by the simulations discussed below). For example, RATION predicts a fractional population of 0.996 for the fully ionized C^{6+} ion at a temperature 500 eV and ion density of 10^{20} cm^{-3}. Taking $\overline{Z}$=3.5, $\overline{Z^2}$=17.4, n_i=10^{20} cm^{-3}, the free-free optical depth is 6.4x10^5 cm, and the free bound optical depth, assuming that the absorption edge from the ground state of ground state C^{6+} (E_{ion} = 490 eV) to be the major contributor in (2.107), is 8.85x10^2 cm. It is therefore probable that the sharpness of the Al/CH boundaries is due to a very short mean free path of stopping resulting in little interpenetration of the colliding plasmas.

A few target shots were taken on uncoated targets with very thin tracer layers of thickness 100 Å. Targets with gold tracers were tried as well as the standard ones with aluminum tracers. X-ray images from two such targets are displayed in Fig. 8.3. The target at left made use of an Al tracer; in this image the distinct structure of the directly-irradiated and collisional features is even more evident than in Fig. 8.1. The emission in the image at right originated from a gold layer and illustrates that the collisional structures are also produced from more slowly expanding high Z materials. Since the first 100 Å of the target ablate away very early during the pulse (this is particularly true for the case of the Al tracer), the emission features in the shadow region indicate formation of these structures also occurs at very early stage in the interaction.

In order to support the foregoing interpretation of the data, three simulations were run on IZANAMI for the laser intensities of the shots of Fig. 8.1, with fluid particles of CH and Al initially distributed to simulate the various targets. The simulation parameters were all identical except for the initial distributions of fluid particles, which were positioned to simulate 15 μm CH substrates with 0.1 μm Al tracer layers and CH

176
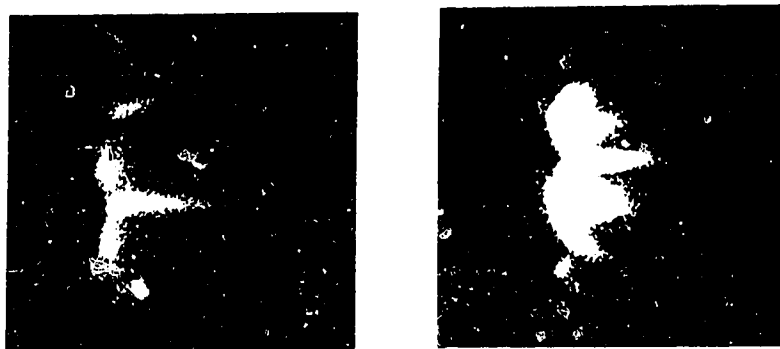
Figure 8.3 X-ray pinhole images from CH targets with 100 Å tracer layers. The shots were of similar peak intensity (3.2 and 3.0 x10^13W/cm^2) but the target tracer at left was inum and that at right gold.

overcoats of 0.54, 0.12, and 0.0 μm. The first of these simulations has already been discussed in Chapter 6; a description of the Cartesian grid and boundary conditions may also be found therein. In all the runs a flux limiter of 0.1 was imposed on the thermal transport along both directions.

The reflective condition was applied at the boundaries parallel to the laser axis, enforcing a stagnation of the lateral component of the hydroflow there. This single fluid approach may be justified by considering the stopping deceleration due to the

counterstreaming of two plasmas α and β, which may estimated by (Berger et al., op. cit.)

$$\frac{dU_\alpha}{dt} = \frac{8\pi n_\beta Z_\alpha^2 Z_\beta^2 e^4 \ln \Lambda (U_\alpha - U_\beta)}{m_i^2 [|U_\alpha - U_\beta|^2 + (T_{i\alpha} + T_{i\beta}) / m_i]^{3/2}}$$ 8.1

where n, m_i, U, Z, and T_i are the ion density, the ion mass, the lateral component of the fluid velocity, the ionization state, and the ion temperature, and the subscripts α and β label the two plasmas. Representative values for the laterally-expanding plasmas approaching the boundary at -8 times during the collision, taken from the simulation of the uncoated target, are $T_i = 115$ eV, $Z = 10$, $n_i = 5 \times 10^{19}$ cm^{-3}, $\ln\Lambda=7.0$, and $U = 1.0\times10^7$ cm/s. Using these values in the expression above, the stopping distance may be estimated to be ~ 0.67 μm, in good agreement with the observed emissivity structures. This single fluid model for the plasma collision should be adequate for distances within 100 μm of the target surface and all but the earliest times of the plasma collision.

Contour plots of the average ionization state at four different simulation times are shown in Fig. 8.4 for a simulation with laser and target parameters of Fig. (1d). The plots have been reflected about one of the stagnation boundaries to facilitate comparison with the pinhole image. The ionization contours from $Z = 2$ to 10 span the range from weakly ionized CH to highly ionized Al; and the region $Z>8$ may be interpreted as the predicted time history of the emitting tracer. Taking as convention t = 0 ps at the moment of peak laser intensity, the plots represent t = -840 ps, -390 ps, +60 ps, and +810 ps respectively. At the beginning of the pulse (t = -1290 ps), the ablated material from the laser-heated region quickly undergoes a 2D expansion and reaches the lateral boundary at -800 ps. After collision, the partially stagnated plasma continues to move away from the target at a slower rate than the plume in the laser - heated region. The relative longevity of the stagnated plasma would account in part for the brightness of this feature as recorded by the time-integrating diagnostics. In simulations of CH overcoated

targets a well defined Al/CH/Al sandwich forms at boundaries, and persists as it flows away from the target.

Emissivity spectra generated by IZANAMI were convolved with the filter response of the pinhole diagnostic, and integrated over energy and time to produce spatial emissivity patterns. In Fig. 8.5 these patterns are shown for each of the three simulations, with target overcoating decreasing from top to bottom. The spatial structure of the patterns are in qualitative agreement with the pinhole images, with the dominant emission feature shifting from the irradiated region to the shadow region as the CH overcoating is decreased. For the case of 0.54 μm overcoated target the 50% emissivity region is enclosed by an unbroken contour of lateral width 43 μm situated in the irradiated region; for the case of 0.12 μm overcoated target the same contour is broken into two curves (combined width 23 μm) lying adjacent to the stagnation boundaries. Predicted density and electron temperature profiles exhibit moderate lateral variation after the collisional plasma has formed. Although the fluid collision results in ion temperatures exceeding 1 keV, thermal transport during the laser pulse is electron dominated since the equipartition time between the two species is several times the laser pulse length. A high degree of lateral thermal smoothing is achieved despite the inhibitory effect of the magnetic field structures. These reach peak values of $\sim 3 \times 10^5$ gauss in the coronal boundary between the irradiation and shadow regions, and reduce the lateral thermal conductivity by 5 - 50%. Electron temperatures in the collisional region are about 100 eV lower during the rising part of the pulse. Lateral thermalization continues throughout the pulse and is established by $t = 500$ ps. Electron temperatures in the directly-heated region peak at about 600 eV at a distance of 100 μm from the target, in good agreement with the estimates obtained from the x-ray spectrum. Interpretation of lateral density profiles requires some care since both tracer and substrate materials are involved in the simulation. At times for which only one species exists in the corona, the

179

density of the collisional region is moderately higher but never exceeds that of the heated region by more than a factor of 1.5.

In summary the technique of tracer layers has been used to study the formation and evolution of coronal structures under non-uniform irradiation conditions. X-ray emission from the non-irradiated region clearly shows a stagnation in the lateral collision of expanding plasmas created in the laser-irradiated regions. Good agreement between experimental measurements and 2D simulations has been demonstrated, consistent with the assumption of lateral stagnation in the collisional region.
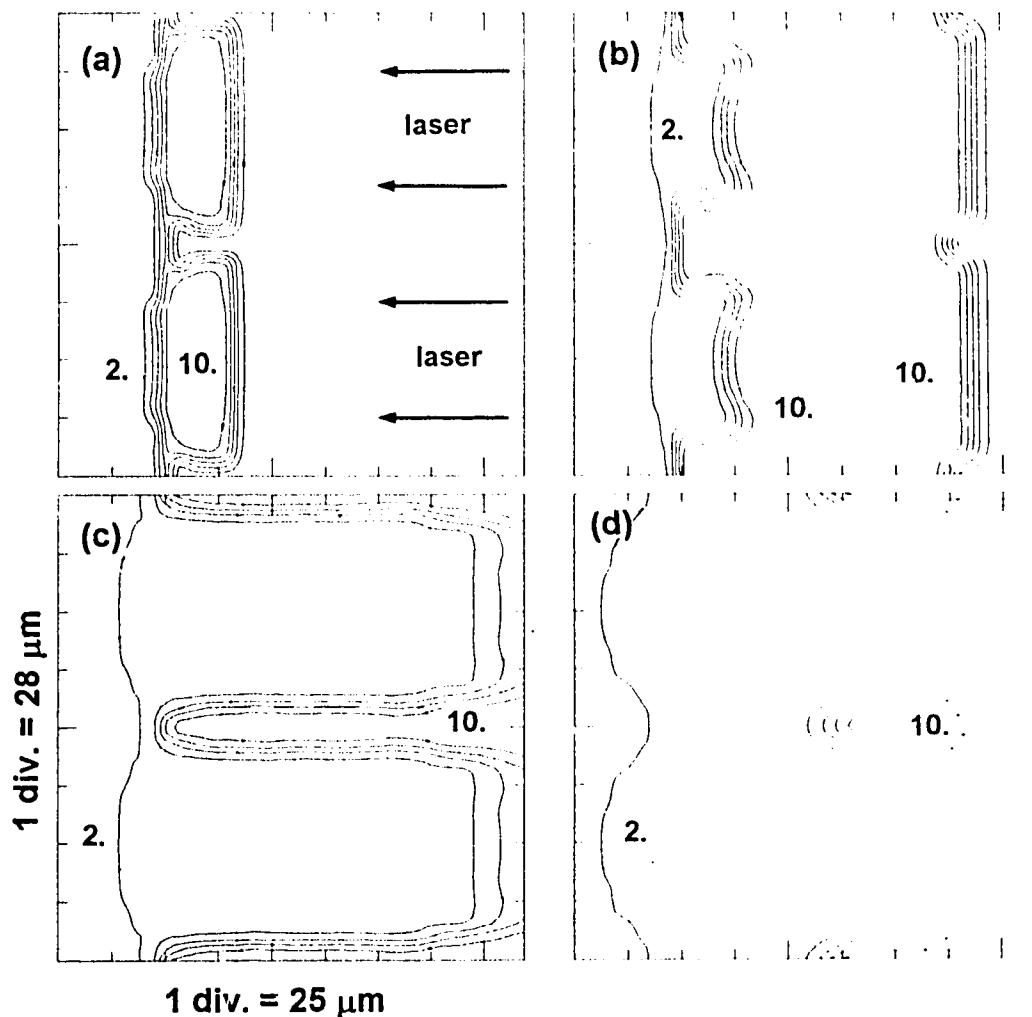
Figure 8.4 Average ionization states from Z=2 to 10 as predicted by the 2D code IZANAMI for the experimental conditions of Fig (8.1d). The simulation times for the plots (a) to (d) are -840 ps, -390 ps, 60 ps, and 810 ps. A region of highly stripped aluminum (Z >8) may be seen to form in the non-irradiated regions early during the pulse, and persist after the laser peak is reached (t = 0 ps). The plots have been reflected about one of the stagnation boundaries to facilitate comparison with the pinhole image and the irradiated regions of the simulation indicated by the arrows in (a).
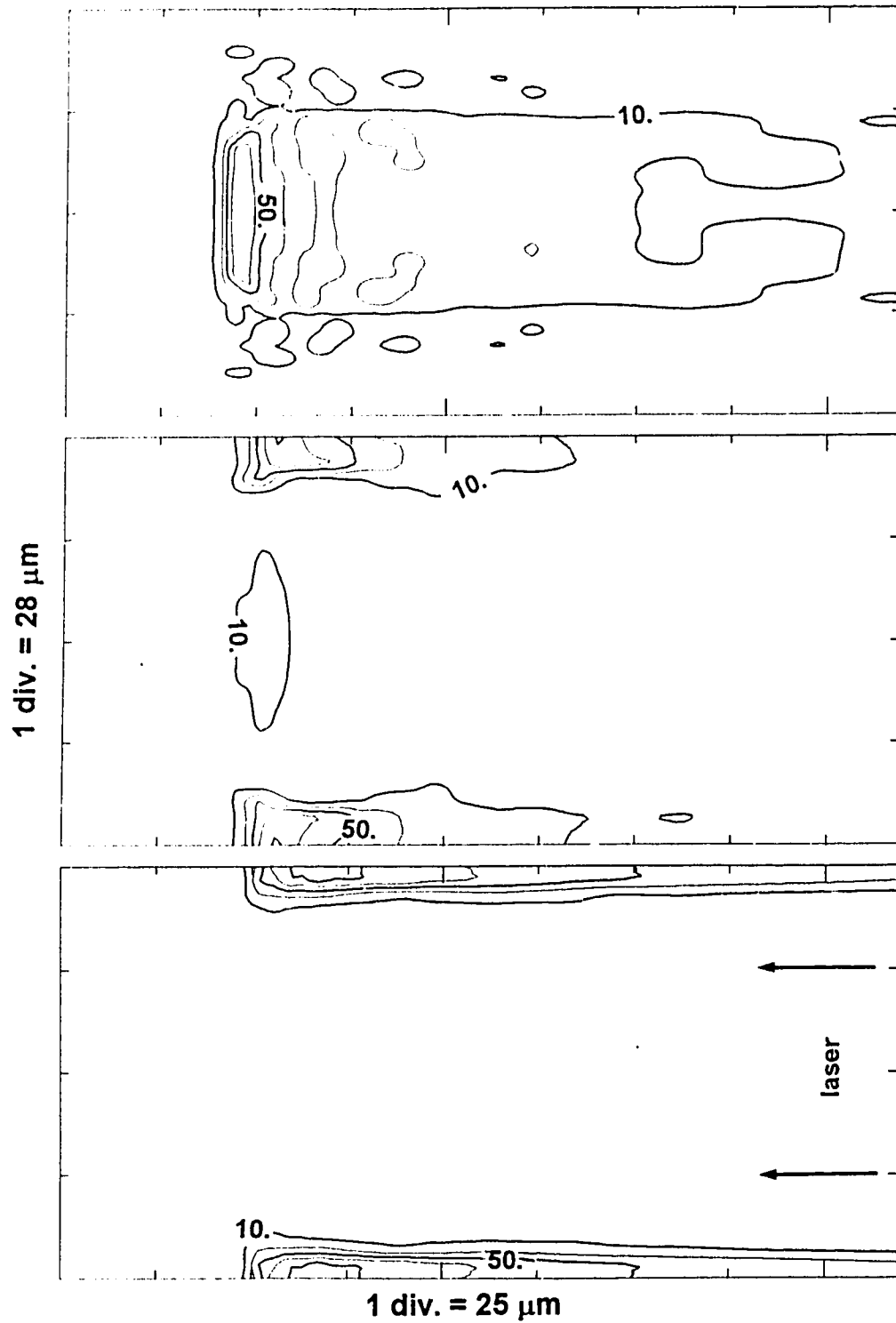
Figure 8.5 Time integrated emissivity patterns predicted by the average ion model for the three IZANAMI simulations. The initial CH overcoats thicknesses assumed in the simulations were from (top to bottom) 0.54, 0.12, and 0.0 μm.

9. Conclusions

In summary, lateral energy transport has been observed in planar targets irradiated by 0.53 μm light over an intensity range of 3×10^{12} to 3×10^{14} W/cm². X-ray pinhole cameras and spectrometers were used to acquire evidence of thermal and convective energy transport away from the directly-irradiated areas of targets for a number of beam/target configurations.

A novel scattering technique was introduced to measure the intensity distribution of the focal spot to 10 μm accuracy. With this method it was possible to set limits upon the fraction of energy incident upon those areas outside nominal focus. For the case of tight focus condition the results of scattering measurements were verified by recording the x-ray levels from aperture targets thus establishing that x-ray signals recorded from the lateral regions of tracer targets were not due to focused ASE nor to residual 1.06 μm light.

A number of interesting x-ray features were seen from multilayer targets irradiated by spatially-modulated beams. The lateral profiles from the lines of highly-stripped tracer ions were obtained from the spectrometer data. These profiles exhibit widening as one progresses from hydrogen-like to lithium-like states, and as the areal density of the overcoat layer is decreased. There is reason to believe that these observations are at least in part due to the heating of tracer material in the lateral region of the target.

X-ray pinhole images indicate moderate widening of ~8 μm of the ablation surface which gives rise to the expansion plume. This indicates a limited degree of

thermal transport at the edges of the laser spots. In some targets a fainter emission was also seen adjacent to the target and beyond the expansion plume which indicated that sufficient energy was laterally transported to heat the tracer layer in the shadow region. The x-ray images indicate that for intensities below 3.3×10^{13} W/cm^2 there is an upper bound of about 0.6 gm$-\mu$m/cm^3 for the areal density of material ablated in this region. If the emission profiles from the hydrogen-like species are taken as being indicative of the conditions which exist in the directly irradiated region, then the crystal spectrometer data indicates that the regions of high ablation rate were confined essentially to the irradiated regions. These profiles exhibit widening only for targets of CH overcoating of areal density less than 0.2 gm$-\mu$m/cm^3. However, for such targets, the emission profiles become dominated by coronal emission from collisional structures in the shadow regions between directly irradiated areas. These structures appear very early in the pulse and effectively restrict the lateral expansion of material which ablates afterwards.

For the case of tight focus data, there is evidence of energy coupling as far as 40 μm beyond the edge of the focal spot. The transport may be explained by the weak coupling of a hot plasma expanding along the target surface. Temperatures reached are high enough to ionize beryllium and aluminum to at least Be^{3+} and Al^{10+} which indicates temperatures exceeding 50 eV. Some widening of the plasma source size due to the expansion of the corona from the laser spot was also observed and is the dominant contribution to the lateral emission. Definitive evidence of K-shell emission from the lateral substrate was not present. This may be due to low signal levels due to a small emitting volume.

The 2D fluid particle code IZANAMI was able to reproduce well some aspects of the modulated intensity interaction, aspects such as density scale lengths, electron temperatures, and hydrodynamic flow patterns of the tracer material for targets of

various overcoat. Contour plots of ionization state indicate a degree of ablation of the lateral substrate which is consistent with experimental observation. X-ray emissivity patterns based on an average ion model exhibited qualitative agreement with the experimental data. However, the forked structures which appear in the pinhole images of Chapter 8 are not well reproduced by the simulation. In part this is due to insufficient mesh resolution in the coronal region of the simulation, and to the imposed Cartesian geometry which precluded proper modeling of the hydrodynamic expansion. Also there is evidence that non-equilibrium atomic physics is occurring in these structures. It may be necessary to make use of time-dependent atomic physics codes to properly describe these emission structures.

Magnetic fields were not predicted to play a major role in inhibiting the transport into the target. For the case of modulated beam conditions, the field structure tends to establish itself in the underdense corona where near-isothermal conditions prevail. In the simulation of tight focus conditions, inhibition regions are very localized and the inhibition is moderated by plasma expanding laterally from the focal spot. Non-local heat transport may be at work in these experiments. However, no definite support for this can be made from the data; the classical flux-limited model assumed here was sufficient to explain the observations.

The amount of energy transported into the lateral regions of the target was limited, first by the advection of material away from the surface, which acted in competition with the inward thermal transport; and second by the low density of the lateral corona, typically two orders of magnitude below solid density of the substrate, which limited the heat content available for coupling into the target. The critical density layer was predicted to coincide well with the boundary of inward vs. outward directed energy transport.

Due to the resource constraints imposed on this study, it must necessarily be viewed as presenting an incomplete description of the lateral transport. Therefore we close with some suggestions for future research.

It would be desirable to repeat the modulated intensity experiments at incident laser intensities above 10^{14} W/cm^2. The expected x-ray signals would then be high enough to allow the apertures of the instruments to be reduced. One could then perform experiments with smaller spatial beam modulations of 10-20 μm for which thermal smoothing effects should become more pronounced. Diffraction effects induced by the beam mask would be more serious in such an experiment. Therefore a shot-to-shot record of the intensity distribution of the focal spot using a calibrated equivalent lens system would be desirable. Also, alignment of the strips parallel to the spectrometer slit becomes more difficult. In an improved target design, a strip tracer would be used instead of a disk, so positioned on the substrate to result in the incident beam overfilling the tracer and creating more uniform plasma conditions along the line-of-sight of the instruments. With such a target, modulated line focus experiments of interest to x-ray laser research could also be undertaken. An additional improvement on the experimental configuration would ensure that the viewing angle and spatial resolving directions of the spectrometers were the same. Finally, the incorporation of a time-resolving x-ray framing camera would be invaluable in investigating the coronal dynamics discussed in Chapter 8.

With respect to the tight focus experiments, a different approach would have to be adopted due to the small signal levels. For the case of experiments involving targets with tracers not directly irradiated, the signal levels could be boosted significantly, at the expense of losing spatial resolution, by replacing the slit of the crystal instrument with a simple light-tight filter and introducing a suitable baffling into the spectrometer to reduce scattering. The XUV spectrometer signals could likewise

be enhanced by eliminating the pinhole, setting a slit at the grating focal position, and using suitable x-ray optics to focus the emission. However, if the spatial resolving capability of the diagnostics was sacrificed, the spectrometers could no longer be used as a check on beam/target alignment. In this case some additional diagnostic would have to be incorporated to fulfill this function.

The incorporation of other diagnostics into the experiment would provide a valuable aid to the interpretation of such experiments. Most desirable of these would be a density diagnostic such as a short pulse, short wavelength optical interferometric probe to characterize the laterally-expanding plasma in the vicinity of the target surface. Time-resolved Faraday rotation measurements could be used to verify the position and dynamics of the magnetic field structure as predicted by the simulations. Finally, it would be informative to investigate the effect that a preformed plasma might have on the results reported here.

REFERENCES

T. Afshar-rad et al. Phys. Rev. Lett. **68**, 942 (1992).

F. Amirinov et al., Phys. Rev. **A32**, 3535, (1985).

S. Avzeni, Plasma Physics and Controlled Fusion **29**, 1535 (1987).

D. M. Barrus et al., AIP Conf. Proc. **75**, 115 (1981).

R. Balescu, Transport Processes in Plasmas vol. 1, North Holland (1988).

U. Sh. Begimkulov et al., Sov. J. Quant. Elec:. **21**, 794 (1991).

R. Benattar and J. Godart, Optics Comm. **51**, 260 (1984).

R. Benattar and J. Godart, Optics Comm. **59**, 272 (1986).

R. L. Berger et al., Phys. Fluids **B3**, 3 (1991).

S. E. Bodner, J. Fusion Energy **1**, 221 (1981).

T. Boehly et al., J. Appl. Phys. **60**, 3840 (1986).

J. L. Bocher et al., Phys. Rev. Lett. **52**, 823 (1984).

V. A. Boiko et al., Journal of Soviet Laser Research **6**, 2 (1985).

D. L. Book (ed.), NRL Plasma Formulary, Naval Research Laboratory (1987).

M. Born and E. Wolf, Principles of Optics, Pergamon Press (1959).

R. A. Bosch et al., Phys. Fluids **B4**, 979 (1992).

T. J. Boyd and J. J. Sanderson, Plasma Dynamics, Barnes and Noble (1969).

D. K. Bradley et al., Laboratory for Laser Energetics Review **41**, 1 (1989).

S. I. Braginskii, "Transport Processes in a Plasma", in Reviews of Plasma Physics **1**, New York Consultants Bureau (1965).

K. A. Brueckner and S. Jorna, Rev. Mod. Phys. **46**, 325 (1974).

C. R. Burch, Proc. Roy. Soc. **59**, 41 (1947).

M. D. J. Burgess, B. Luther-Davies, ans K. A. Nugent, Phys. Fluids **28**, 2286 (1985).

A. J. Campillo, S. L. Shapiro, and B. R. Suydam, Appl. Phys. Lett. **23**, 628 (1973).

M. Chaker et. al., Rev. Sci. Instruments **60**, 3386 (1989).

N. M. Ceglio, J. X-Ray Sci. Tech. **1**, 7 (1989).

N. M. Ceglio, Laser and Particle Beams **1**, 71 (1991).

D. M. Cochrane and R. W. P. McWhirter, Physica Scripta **28**, 25 (1983).

A. J. Cole et al., Rutherford Appleton Laboratory Ann. Rep. **RL-82-039**, 4.13 (1982a).

A. J. Cole et al., J. Phys. **D15**, 1689 (1982b).

D. Colombant and G. F. Tonon, Phys. Fluids **44**, 3524 (1973).

R. S. Craxton and R. L. McCrory, Laboratory for Laser Energetics Rep. No.108, Rochester, N. Y. (1980).

R. S. Craxton et al., IEEE J. Quant. Elect. **QE-17**, No. 9, 1782 (1981).

J. Delettrez, Can. J. Phys. **64**, 932 (1986).

M. Desselberger et al., Phys. Rev. Lett. **68**, 1539 (1992).

L. J. Dhareshwar et al., Phys. Fluids **B4**, 1635 (1992), and references therein.

J. J. Duderstadt and G.A. Moses, Intertial Confinement Fusion, John Wiley & Sons (1982).

D. Duston and J. Davies, Phys. Rev. **A21**, 1664 (1980).

D. Duston and J. Davies, Phys. Rev. **A23**, 2602 (1981).

K. Eidmann, "Emission and Absorption of Radiation in Laser-Produced Plasmas", in Inertial Confinement Fusion, A. Caruso and E. Sindoni (ed.), Int. School of Plasma Physics (1989).

M. H. Emery et al., Phys. Fluids **B3**, 2640 (1991).

E. M. Epperlein, G. J. Rickard, and A. R. Bell, Phys. Rev. Lett. **61**, 2453 (1988).

E. M. Epperlein, Phys. Rev. Lett. **65**, 2145 (1990).

E. M. Epperlein, Phys. Fluids B3, 3082, (1991).

E. M. Epperlein and R. L. Short, Phys. Fluids **B3**, 3092, (1991).

R. Fabbro et al., Phys. Rev. **A26**, 2289 (1982a).

R. Fabbro and P. Mora, Phys. Lett. **90A**, 48 (1982b).

R. Fabbro, C. Max, and E. Fabre, Phys. Fluids **28**, 1463 (1985).

D. W. Forslund and J. V. Brackbill, Phys. Rev. Lett. **48**, 1614 (1982).

E. F. Gabl et al., Phys. Fluids **B2**, 2437 (1990).

A. Gabriel, MNRAS **160**, 99 (1972).

J. H. Gardner and S. E. Bodner, Phys. Rev. Lett. **47**, 1137 (1981).

P. Glas et al., Opt. Comm. **86**, 271 (1991a).

P. Glas and M. Schnürer, Laser and Particle Beams 9, 501 (1991b).

J. W. Goodman, Introduction To Fourier Optics, McGraw Hill, New York (1968).

S. R. Goldman and R. F. Schmalz, Phys. Fluids **30**, 3608 (1987).

T. Harada and T. Kita, App. Opt. **19**, 3987 (1980).

F. H. Harlow in Methods in Computational Physics Vol. 3, Academic Press, New York (1964).

B. L. Henke et al., Atomic Data and Nuclear Data Tables **27**, 1 (1982).

B. L. Henke et al., J. Opt. Soc. Am. **B1**, 818 (1984a).

B. L. Henke et al., J. Opt. Soc. Am. **B1**, 828 (1984b).

B. L. Henke et al., J. Opt. Soc. Am. **B3**, 1540 (1986).

B. L. Henke et al., J. X-ray Sci. Tech. **2**, 17 (1990).

C. Hentschel, Fibre Optics Handbook, Hewlett Packard, Germany (1988).

M. J. Herbst et al., Rev. Sci. Inst. **53**, 1418 (1982).

L. L. House, Ap. J. Supp. Ser. **8**, 307 (1963).

M. Itoh, T. Yabe, and S. Kiyokawa, Phys. Rev. **A35**, 233 (1987).

P. A. Jaanimagi et al., Appl. Phys. Lett. **38**, 734 (1981).

R. N. Jones, R. Venkataraghavan, and J. W. Hopkins, Spectrochimica Acta **23A**, 925 (1967).

M. Kado et al., Japanese Journal of Optics **17**, 234 (1988).

M. Kado et al., Optics Letters **16**, 109 (1991).

M. Kado et al., submitted for publication in Phys. Rev. Lett. (1993).

Y. Kato et al., Annual Progress Report on Laser Fusion Sept.. 1976 - Aug. 1977, Institute of Laser Engineering, 3 (1977).

Y. Kato et al., Annual Progress Report on Laser Fusion Sept.. 1977 - Aug. 1978, Institute of Laser Engineering, 3 (1978a).

Y. Kato et al., Proceedings of the 13th International Conference on High Speed Photography and Photonics, Tokyo, 233 (1978b).

Y. Kato et al., Progress Report on Laser Fusion Sept.. 1978 - Mar. 1980, Institute of Laser Engineering, 5 (1980).

Y. Kato et al., Progress Report on Laser Fusion Apr. 1980 - Dec. 1981, Institute of Laser Engineering, 9 (1982).

C. J. Keane et al., J. Phys **B22**, 3343 (1989).

R. L. Kauffman, R. W. Lee, K. Estabrook, Phys. Rev. **A35**, 4286 (1987).

S. Kaushik and P. L. Hagelstein, Appl. Phys. **B50**, 303 (1990).

R. L. Kelly and L. J. Palumbo, Atomic and Ionic Emission Lines Below 2000 Angstroms, U. S. Govt. Printing Office, Washinton D. C., #0851-00061 (1975).

M. H. Key et al. Phys. Fluids **26**, 2011 (1983).

J. C. Kieffer et al., Phys. Rev. Lett. **50**, 1054 (1983).

J. D. Kilkenny et al., Phys. Rev. **A22**, 2746 (1980).

T. Kita et al., App. Opt. **22**, 512 (1983).

191

S. Kiyokawa, T. Yabe, T. Mochizuki, Jap. J. Appl. Phys. **22**, L772 (1983).

R. Knox, Laboratory for Laser Energetics Review **40**, 185 (1989).

R. Kodama et al., J. Appl. Phys. **59**, 3050 (1986).

R. Kodama, PhD. dissertation, Osaka University (1990).

K. Kondo, J. App. Phys. **67**, 2693 (1990).

R. W. Lee and B. L. Whitten, J. Quant. Spect. Rad. Transfer **32**, 91 (1984).

R. W. Lee et al., RATION Manual, Lawrence Livermore Laboratory (1990).

W. Lotz, Z. Phys. **206**, 205 (1967).

W. Lotz, Z. Phys. **216**, 241 (1968).

W. Lotz, Z. Phys. **220**, 486 (1969).

J. F. Luciani, P. Mora, and J. Virmont, Phys. Rev. Lett. **51**, 1664 (1983).

W. M. Manheimer, D. G. Colombant, and J. H. Gardner, Phys. Fluids **25**, 1644 (1982).

I. Matsushima et al., J. Appl. Phys. **58**, 1674 (1985).

C. E. Max, Theory of the Coronal Plasmas in Laser Fusion Targets Vol. I, Lawrence Livermore Laboratory UCRL-53107 (1981).

R. L. McCrory et al., Nature **355**, 225 (1988).

W. C. Mead et al., Phys. Fluids **27**, 1301 (1984).

R. Mewe, "Satellite Lines as a Diagnostic", Astrophysical and Laboratory Spectroscopy, R. Brown and J.Lang (ed.), Scottish Universities Summer School in Physics (1988).

A. G. Michette, J. X-Ray Sci. Tech **2**, 1 (1990).

D. Mihalas, Stellar Atmospheres, W. H. Freeman, San Francisco (1978).

T. Mochizuki et al., Phys. Rev. **A33**, 525 (1986).

P. Mora and R. Pellat, Phys. Fluids **22**, 2300 (1979).

P. Mora, Phys. Fluids **25**, 1051 (1982).

S. Nakai et al., International Atomic Energy Agency 13th International Conference On

Plasma Physics And Controlled Nuclear Fusion Research, IAEA-CN-53/B-1-3

(Oct., 1990).

N. Nakano, H. Kuroda, T. Kita, and T. Harada, Op. Lett. **23**, 2386 (1984).

A. Nishiguchi and T. Yabe, J. Comp. Physics **52**, 390 (1983).

A. Nishiguchi et al., Phys. Rev. Lett. **53**, 262 (1984a).

A. Nishiguchi, ILE internal document, (1984b).

H. Nishimura et al., Phys. Rev. **A43**, 3073, (1991)

J. Nuckolls et al., Nature **239**, 139 (1972).

K Oades et al. SPIE X-ray Instrumentation **1140**, 94 (1989).

S. P. Obenschain, R. H. Lehmberg, and B. H. Ripin, Appl. Phys. Lett. **37**, 903 (1980).

S. P. Obenschain et al., Phys. Rev. Lett. **46**, 1402 (1981).

G. J. Pert, J. Plasma Phys. **41**, 263 (1989).

S. M. Pollaine, R. L. Berger, C. J. Keane, Phys Fluids **B4**, 989 (1992).

G. C. Pomraning, Radiation Hydrodynamics, Pergamon Press, New York (1973).

R. Popil et al., Phys. Rev. **A35**, 3874 (1987).

M. K. Prasad and D. S. Kershaw, Phys. Fluids **B1**, 2430 (1989).

M. K. Prasad and D. S. Kershaw, Phys. Fluids **B3**, 3087 (1991).

A. Raven, O. Willi, and P. T. Rumsby, Phys. Rev. Lett. **41**, 554 (1978).

A. Raven, et al., Appl. Phys. Lett. **35**, 526 (1979).

P. D. Rockett et al., App. Opt. **24**, 2536 (1985).

M. D. Rosen, Phys. Fluids **B2**, 1461 (1990).

A. J. Schmitt, Phys.Fluids **B3**, 3079 (1988).

M. Seaton, MNRAS **119**, 81 (1959).

I. P. Shkarofsky et al., The Particle Kinetics of Plasmas, Addison Wesley (1966).

D. L. Shealy et al. SPIE X-ray/EUV Optics for Astronomy and Microscopy **1160**, 109 (1989).

J. W. Shearer, Lawrence Livermore Laboratory Report **UCID-15745** (1970); Phys. Fluids **14**, 501 (1971).

C. L. Shepard and P. M. Campbell Phys. Rev. **A39**, 1344 (1989).

K. Shinohara, Proc. SPIE **1140**, 196 (1989).

H. Shiraga et al., Phys. Rev. Lett. **49**, 1244 (1982).

A. E. Siegman, Lasers, Univ. Sci. Bks. (1986).

W. T. Silfvast et al., J. Vac. Sci. Technol. **B10**, 3126 (1992).

H. I. Smith and H. G. Craighead, Physics Today Feb. 1990, p. 24.

L Spitzer, Ap. J. **107**, 6 (1948).

L. Spitzer, Physics of Fully-Ionized Gases, Interscience, New York (1956).

J. A. Stamper and B. H. Ripin, Phys. Rev. Lett. **34**, 138 (1975).

J. A. Stamper, E. A. McLean, and B. H. Ripin, Phys. Rev. Lett. **40**, 1177 (1978).

C. Stöckl and G. D. Tsakiris, Laser and Particle Beams **9**, 725 (1991), and references therein.

T. Tachi, internal communication, Institute of Laser Engineering, Osaka (1990).

K. Terai et al., Appl Phhys. Lett. **46**, 355 (1985).

Y. Tsuchiya, Picosecond **14**, 3 (1983).

G. K. Woodgate, Elementary Atomic Structure, Oxford University Press, New York (1980).

H. Van Regemorter, Ap. J. **136**, 906 (1962).

L. Vainshtein and U. Safronova, At. Data Nucl. Data Tables **21**, 49 (1978).

D. M. Villeneuve et al., Phys. Rev. **A27**, 2656 (1983).

V. Vinogradov, I. Y. Skobelev, and E. A Yukov, Sov. J. Quant. Elec. **5**, 630 (1975).

T. Yabe et al., Phys. Rev Lett. **48**, 242 (1981).

194

.

C. Yamanaka, "Laser Plasma and Inertial Confinement Fusion", in Physics of Laser Plasma, A. Rubenchik and S. Witkowski (ed.), North Holland, New York (1991).

A. Yariv, Optical Electronics, CBC College, New York (1985)

M. A. Yates et al., Phys. Rev. Lett. **49**, 1702 (1982).

P. E. Young et al., Phys. Rev. Lett. **61**, 2336 (1988).

Y. B. Zel'dovich, Y. P. Raizer, Physics of Shock Waves and High-temperature Hydrodynamic Phenomena, Academic Press, New York (1966)

Appendix 1. Target Fabrication

In Fig. A1.1 the steps involved in the target fabrication procedure are illustrated. Most of the substrate foils were between 10 and 25 μm thickness and were fabricated in the following way (production of thinner substrates was done using the parylene coating apparatus described later). A clean flat sheet of glass was positioned under a fume hood on a three point support and adjusted to be level. Vinyl tape was fixed around the border of the glass plate to create a shallow swimming pool structure. Polystyrene beads were dissolved in toluene to produce a solution, and a precalculated amount of this solution was introduced onto the glass. The solution was spread uniformly across the glass plate using a horizontally oriented glass pipette. After 24 hours the toluene evaporated leaving a CH film. At this point the uniformity of the CH film was inadequate and was improved by clamping a second glass surface over the film to produce a sandwich structure. This structure was introduced into an oven at 150° C for several hours and subsequently cooled and separated resulting in good film uniformity. The original glass plate was then sectioned into smaller pieces the shape of microscope slides.

In order to transfer the CH films to the target, support frames of mylar were cut, affixed to double-sided adhesive tape and pressed onto the slides. The foils with frame assembly were then separated from the glass by placing them in a hot water bath for 30 minutes. An array of M2 washers was precleaned in ethanol, dried and affixed to microscope slides by strips of double-sided tape. Small drops of ultra-violet cure
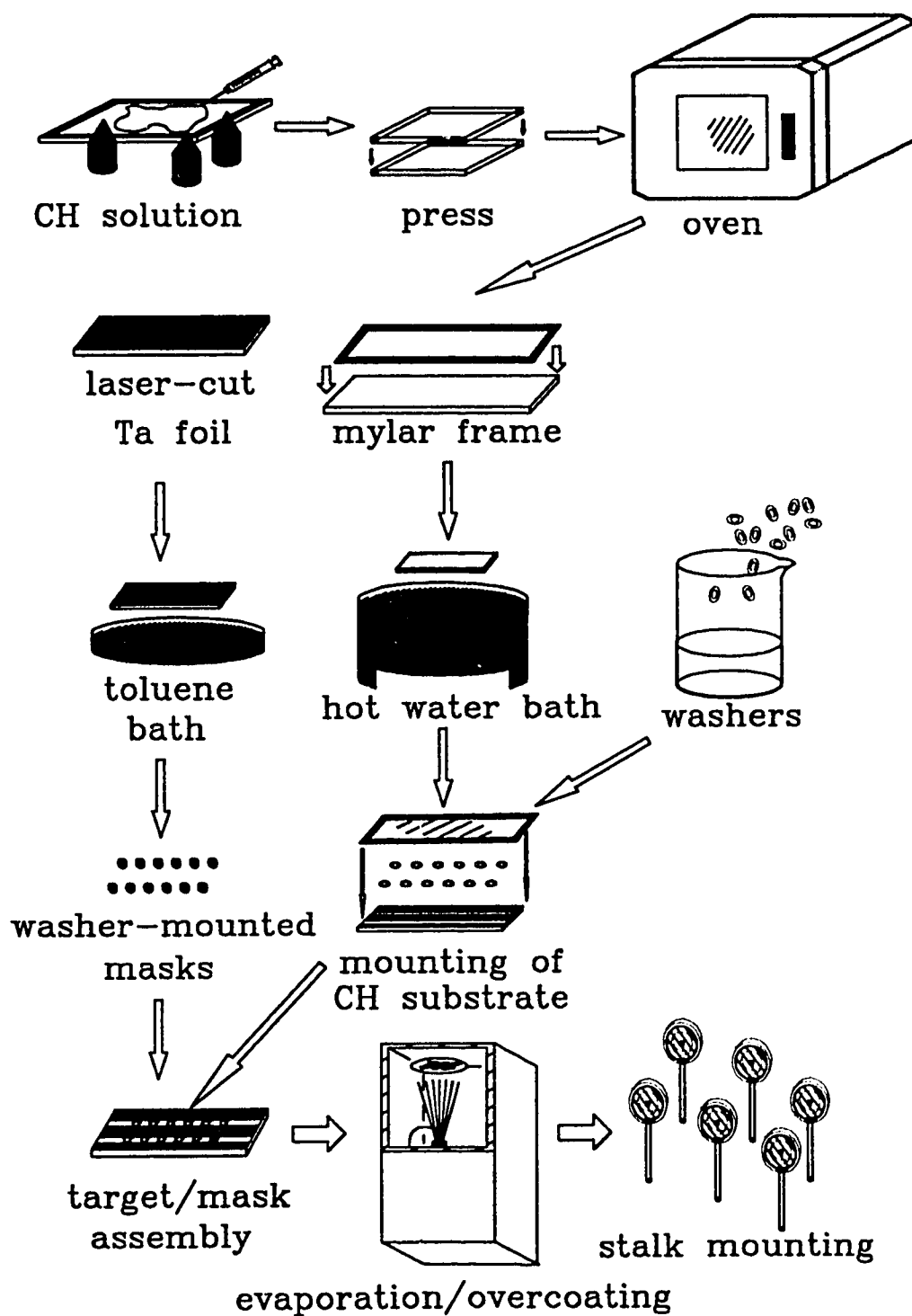
CH solution   press   oven

laser-cut
Ta foil   mylar frame

toluene
bath   hot water bath   washers

washer-mounted
masks   mounting of
CH substrate

target/mask
assembly

evaporation/overcoating   stalk mounting

Fig. A1.1. The various steps involved in the fabrication of targets.

197

epoxy were deposited onto the washer faces and the mylar frame with foil was carefully lowered onto the washer array. After the epoxy was cured by irradiating the entire assembly with a uv source, the CH foil was trimmed away from the washers using a surgical knife. Each target was inspected and any debris on the substrate surface carefully brushed away. For such delicate work, the targets were viewed under a stereo microscope. At this point the targets were now ready for the tracer deposition stage.

In order to introduce tracer patterns specified dimensions onto the targets, evaporation masks had to be created. The desired mask patterns were first cut in 20 μm tantalum foil using a NEC Nd:YAG laser cutter which was slaved off of a computer, allowing the cutting sequence to be programmed. The Ta foils were adhered as flatly as possible by double-sided tape to microscope slides and fixed to the x-y translational stage of the cutter. Although the precise mask shape was in principle programmable to micron precision, the day to day variance in the laser output and lateral transport of energy outside of the laser focus created uncertainties on the order of 10-20 μm. Therefore, in practice, several trial cuts were made and the resulting viewed and photographed under a microscope until the correct mask dimensions were achieved. At this point a run of several masks patterns were done. After the patterns were finished, they were circled by cuts of diameter suitable to allow mounting on M2 washers. To free the foil from the adhesive tape and the waste foil the slide was soaked in toluene for 24 hours. The Ta discs were then carefully separated, cleaned, dried and epoxied to M2 washers. After the epoxy cured, the masks were placed into an ultrasonic cleaner to remove debris from the foil surfaces. After removal and drying the masks were ready.
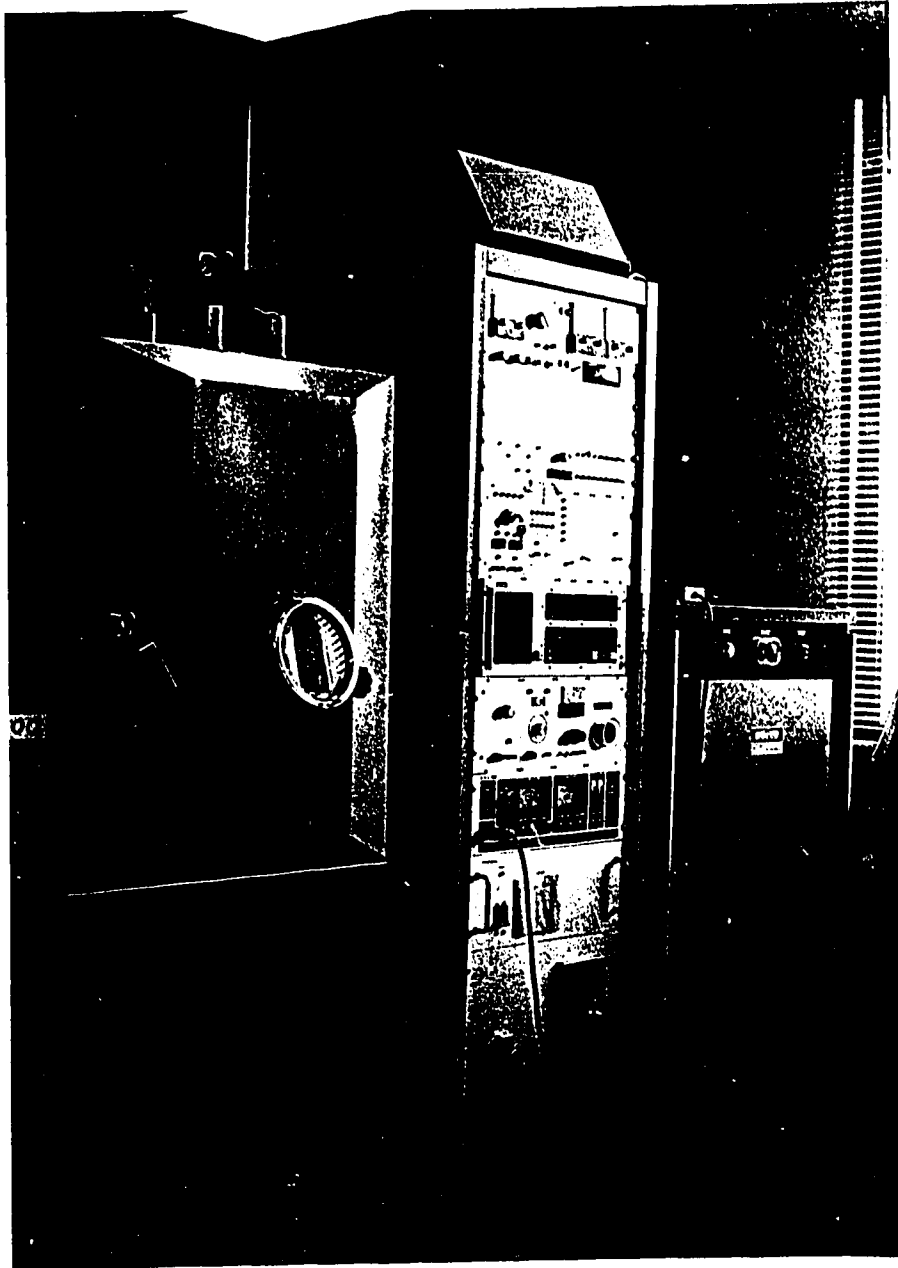
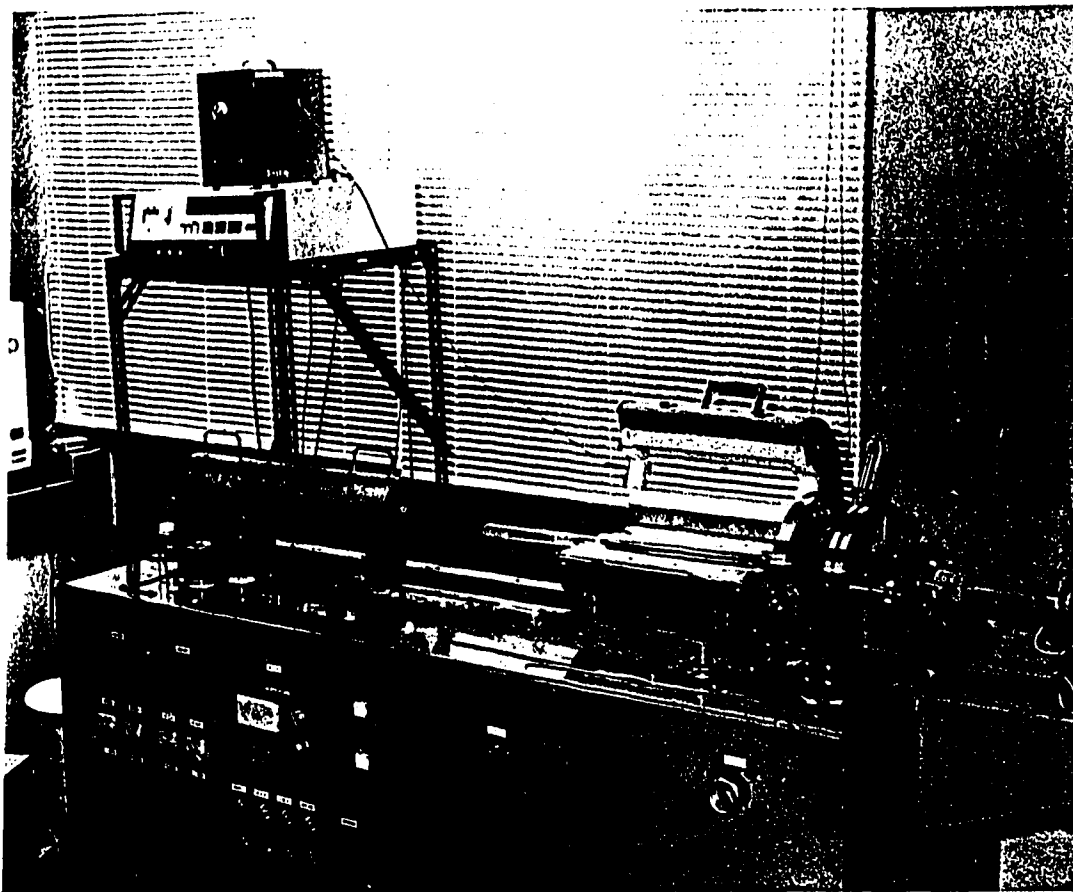Fig. A1.2. The electron beam coating chamber and control system.

199

Fig A1.3. The parylene coating machine.

The masks were next positioned over the mounted targets bringing the Ta foil in contact with the substrates. Strips of heat resistant aluminum tape were used to fix the mask and target washers together and the entire slide assembly was introduced into the electron beam evaporation chamber shown in Fig. A1.2 for deposition of the tracers. The evaporation chamber was cryogenically pumped to 10^{-6} torr. The sample was fixed to a rotating plate situated 50 cm above an electron-irradiated crucible of tracer material; this configuration ensured an even coating rate from point to point on the sample.
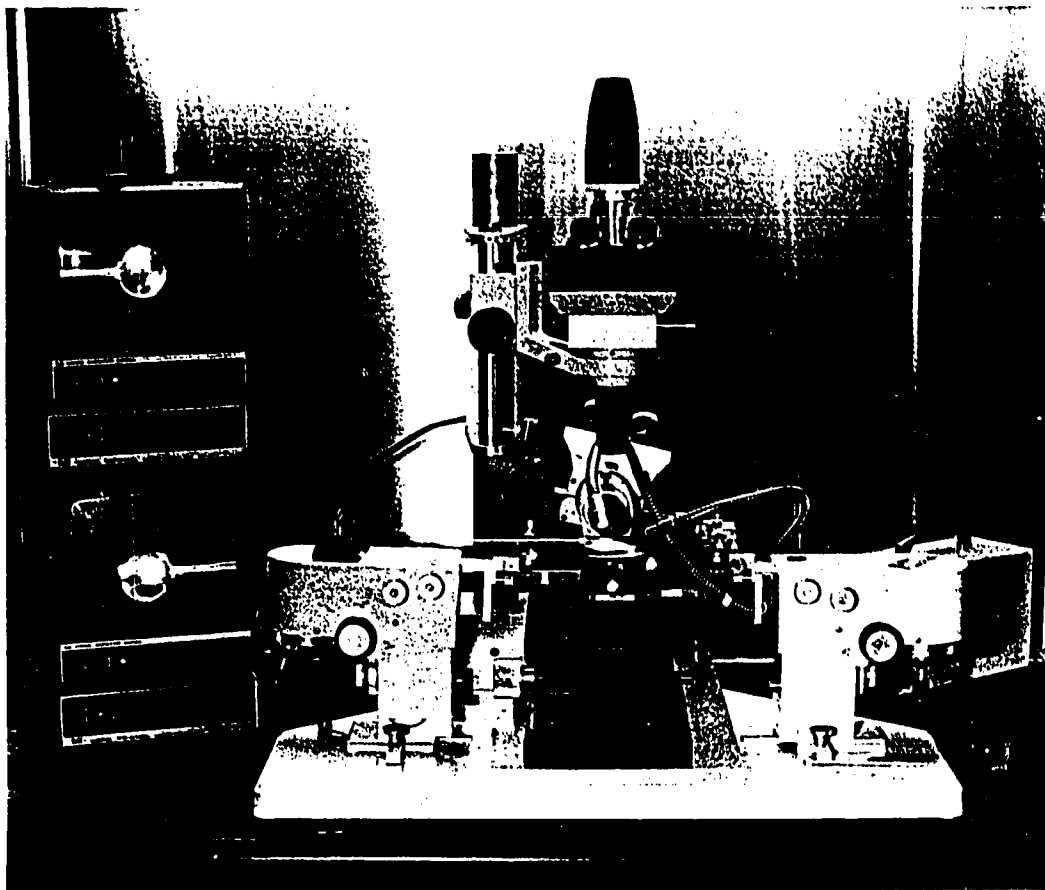
Fig A1.4. The target mounting system features video zooming cameras and precision manipulation devices.

The apparatus was equipped with a crystal oscillating thickness monitor which allowed the tracer deposition rate to be monitored. Prior to each target coating run, a calibration coating run was performed on a blank slide. An interferometric microscope was used to measure the thickness of the coating layer on the slide. In the same manner a blank slide was introduced with each set of targets so that the final tracer thickness could be measured.

After the tracer patterns were deposited, the masks were removed. At this point many of the targets received an additional coating of CH. This was accomplished using the parylene coating apparatus shown in Fig. A1.3. The glass slides were installed in the chamber at the right side of the instrument. This chamber was contiguous with the glass tube to the left, into which a measured amount of parylene was inserted. The apparatus was evacuated down to 0.1 torr by a rotary pump. Two cylindrical ceramic ovens heated the tube for several hours, during which time solid parylene situated at the left end of the tube evaporated, diffused along the tube into the coating chamber, and cooled and resolidified.

The finished targets were mounted on 0.9 mm diameter glass stalks using the setup shown in Fig. A1.4. The target washers were positioned on a central platform and the stalks brought to proximity using one of two $XYZ\theta$ manipulators on either side of the platform. Two orthogonally oriented zooming cameras allowed the targets and stalks to be positioned precisely. The stalks were fixed to the washers by means of uv cure epoxy and were typically oriented at $35°$ with respect to the target surface to ensure normal incidence of the laser during the target experiments.

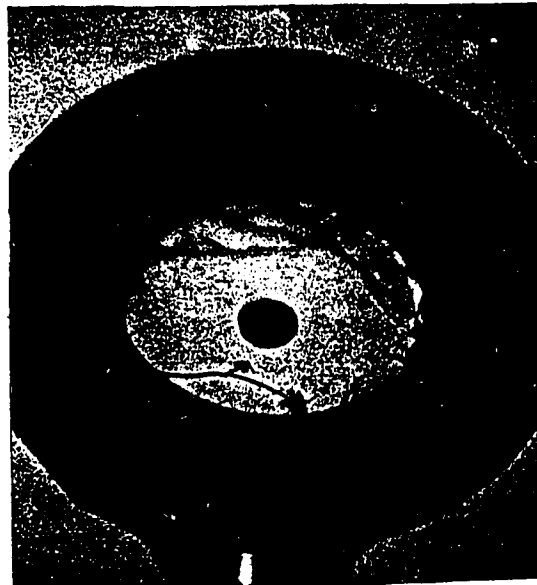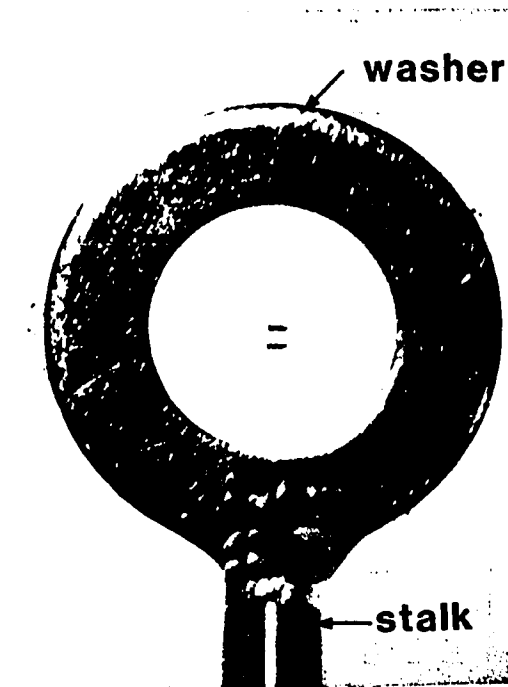In Fig. A1.5 photographs of two finished targets are shown.

Fig A1.5. Photographs of two finished targets showing tracer bars and disc.

Appendix 2. Focal Spot Reconstruction

One option available for the reconstruction of the output intensity profile of laser beam at or near best focus is a 2D Fast Fourier Transform (FFT) technique. The optical field propagating through a thin lens of refractive index n and focal length f undergoes a phase shift of (Goodman, 1968)

$$E'(x,y) = E_{in}(x,y)e^{jk_n\Delta_0}e^{-jk(x^2+y^2)/2f}$$ A2.1

where x,y are the Cartesian coordinates at the input plane normal to the propagation axis, k is the wave number in free space, and the first exponential term accounts for the phase shift through the lens. Under the Fresnel approximation the field at the output plane coordinates x_0, y_0 may be written

$$E_{out}(x_0,y_0) = \frac{e^{jk\ell}}{j\lambda\ell}e^{jk(x_0^2+y_0^2)/2\ell}\int_{-\infty}^{+\infty}\int_{-\infty}^{+\infty}E'(x,y)e^{jk(x^2+y^2)/2\ell}e^{-jk(xx_0+yy_0)/\ell}dxdy$$ A2.2

$$\ell = f + \Delta$$ A2.3.

For small values of the displacement from focus Δ

$$\frac{1}{\ell} \cong \frac{1}{f}\left(1 - \frac{\Delta}{f}\right)$$ A2.4.

Combining these expressions

$$E_{out}(x_0,y_0) = \frac{e^{j(k\ell + k_n\Delta_0)}}{j\lambda\ell}e^{jk(x_0^2+y_0^2)/2\ell}\int_{-\infty}^{+\infty}\int_{-\infty}^{+\infty}E_{in}(x,y)e^{-j\pi\Delta(x^2+y^2)/\lambda f^2}e^{-j2\pi(xx_0+yy_0)/\lambda\ell}dxdy$$

A2.5

The integral will be recognized at a 2D Fourier transform $\mathcal{F}(k_x, k_y)$ with k vectors

$$k_x = \frac{2\pi x_0}{\lambda \ell}, \quad k_y = \frac{2\pi y_0}{\lambda \ell} \qquad \qquad \text{A2.6}$$

The flux is given by

$$E_{out} E_{out}^* = \frac{\mathcal{I}^2 (k_x, k_y)}{(\lambda \ell)^2} \qquad \qquad \text{A2.7.}$$

If the input domain of dimension S_{in} x S_{in} is segmented into 2^N x 2^N cells, then an FFT technique may be used to evaluate $\mathcal{I}$, returning the output field at coordinates

$$x_{0m}, y_{0n} = \frac{\lambda \ell (m, n)}{S_{in}} \qquad m, n = -\frac{N}{2} + 1, \ldots, \frac{N}{2} \qquad \text{A2.8.}$$

The size of the output field is fixed to

$$S_{out} = \frac{\lambda \ell N}{S_{in}} \qquad \qquad \text{A2.9.}$$

This places restriction on maximum allowed value of the shift Δ: if Δ is made too large the beam begins to overfill the output plane resulting in aliasing and non sensible results.

As an alternative approach, a beam propagation routine was written to produce the field structure which results after a specified input field is propagated through a lens and over the distance ℓ. The input field is first expanded in terms of the Hermite Gaussian functions and then propagated by matrix techniques to the output plane where it is reconstructed.

The general solution of the Helmholtz equation for an E field propagating predominantly along the z axis can be written as a superposition eigenfunctions $u_m(x,z)$ and $u_n(y,z)$ (Siegman, 1986)

$$E(x, y, z) = \sum_m \sum_n C_{mn} u_m (x, z) \, u_n (y, z) e^{-jkz} \qquad \text{A2.10}$$

where the normalized basis function $u_m(x,z)$ is

$$u_m(x,z) = \left(\frac{2}{\pi}\right)^{1/4} \sqrt{\frac{\exp\left(+j(2m+1)\left(\Psi(z)-\Psi_0\right)\right)}{2^m \, m! \, \omega(z)}} \; H_m\left(\frac{\sqrt{2}x}{\omega(z)}\right) \exp\left[\frac{-jkx^2}{2q(z)}\right]$$

$$m = 0, 1, 2, \ldots \qquad\qquad\qquad A2.11$$

with an analogous expression for $u_n(y,z)$. Here $\omega(z)$ is the beam radius of the m=0 mode, H_m the Hermite mode of order m, and k is the wave number of the laser. The wave front curvature of the propagating field enters the expression through the definition

$$\frac{1}{q(z)} = \frac{1}{R(z)} + \frac{\lambda}{j\pi\omega^2(z)} \qquad\qquad A2.12$$

and also through the Gouy Phase Shift terms

$$\Psi(z) = \tan^{-1}\left(\frac{\pi\omega^2(z)}{R(z)\lambda}\right) \qquad\qquad A2.13$$

$$\Psi_0 = \tan^{-1}\left(\frac{\pi\omega_0^2}{\lambda}\right) \qquad\qquad A2.14$$

where ω_0 is the beam radius at z=0. The expansion coefficients C_{mn} can be written in terms of the conjugate eigenfunctions

$$C_{mn} = \int\int E(x,y,z)u_m^*(x,z)u_n^*(y,z)dxdy \qquad\qquad A2.15.$$

The beam routine evaluates this integral numerically after the suitable eigenfunctions functions are selected. The eigenfunctions are constructed from a set of pregenerated orthonormal functions

$$f_m(\xi) = \frac{1}{\sqrt{\pi^{1/2} 2^m \, m!}} H_m(\xi) e^{-\xi^2} \qquad\qquad A2.16$$

where H_m is the Hermite polynomial of mode m. The functions f_m were generated using a 4th/5th order Runge-Kutta-Fehlberg algorithm on the differential equation.

206

$$\frac{d^2 f_m}{d\xi^2} + \left(2m + 1 - \xi^2\right)f_m = 0 \qquad\qquad \text{A2.17}$$

Hermite functions of mode 0 to 160 were constructed in this way. There is some freedom for the choice of ω_{in} and the number of modes used in the expansion; these parameters are chosen so that an adequate representation of the input field can be constructed.

The input field is defined over an N x N grid of dimension S_{in} x S_{in}, N and S_{in} being selected by the user. In general it is the intensity profile rather than the E Field profile which is known at the input plane. Since the E Field can not be determined *uniquely* from the flux, the simplest E field consistent with the flux is used. For a Supergaussian this is

$$E_{in} = \exp\left[-\left(\frac{r}{\Theta_r}\right)^{P_r/2} + \frac{j\pi r^2}{\lambda R_{in}}\right] \qquad\qquad \text{A2.18}$$

which reproduces intensity profile (5.3). In addition to the parameters ω_{in} and R_{in}, the mode of supergaussian P_r and the e-folding shoulder radius of the beam Θ_r must be specified. P_r and Θ_r may be obtained experimentally. The wave front curvature in the far field may be written

$$R(z) = z\left(1 + \left(z_R/z\right)^2\right) \qquad\qquad \text{A2.19}$$

where z_R is the Raleigh range

$$z_R = \frac{\pi \omega_0^2}{\lambda} \qquad\qquad \text{A2.20.}$$

.Using the expressions for the far field divergence $\theta_{1/2}$ and z

$$\theta_{1/2} = \frac{\lambda}{\pi \omega_0} \qquad\qquad \text{A2.21}$$

$$z = \frac{\omega(z)}{\theta_{1/2}} \qquad\qquad \text{A2.22}$$

one can express (A2.19) as

$$R_{in} = \frac{\omega_{in}}{\theta_{1/2}}\left[1+\left(\frac{\lambda}{\pi\theta_{1/2}\omega_{in}}\right)^2\right]$$ A2.23

The quantities on the right hand side can in principle be determined experimentally allowing a realistic choice for all of the input parameters for the routine.

After the expansion coefficients C_{mn} have been determined, the complex function q(z) is propagated to the output plane according to

$$q_{out} = \frac{Aq_{in}+B}{Cq_{in}+D}$$ A2.24

The propagation matrix for the system is

$$\begin{bmatrix} A & B \\ C & D \end{bmatrix} = \begin{bmatrix} 1 & \ell \\ 0 & 1 \end{bmatrix}\begin{bmatrix} 1 & 0 \\ -1/f & 1 \end{bmatrix}$$ A2.25

With the new beam radius and field curvature the output field is then reconstructed from (A2.10).